Anti-Drone Drone

DRONE (noun) [drohn]

a remote-controlled pilotless aircraft or missile

Anti-Drone Drone

Final Report
DSE Spring 2016 Group 08

As part of:

Design Synthesis Exercise

at Delft University of Technology

Students:	L. Aerts	4267001
	J. Blom	4306473
	N. Dutrée	4304292
	J. Hagenaars	4297091
	J. Huijing	4281195
	V. de Jonckheere	4135482
	S. Milosevic	4279816
	A. Tiwari-Jones	4181034
	L. Wilkens	4158210
	M. van der Woude	4100379
Staff:	Dr.ir. E. van Kampen	Supervisor
	S. M. Kaja Kamaludeen, MSc	Coach
	Dr.ir. H. G. Visser	Coach

TUDelft

Preface

This document constitutes the fourth and final report in the DSE Anti-Drone Drone project. It was preceded by the Project Plan, Baseline Report, and Mid-term Report. These concluded with a preliminary concept to be designed in detail. Preliminary analysis was conducted in several subject areas already, so as to come up with some estimates for driving characteristics. This report expands on the detailed design and concludes with the final design of the Anti-Drone Drone.

To readers interested in current opportunities in counter UAV systems, it is recommended to read through Chapter 3. Furthermore, complete system analysis is described in Chapter 5 until Chapter 8, including performance, aerodynamics, and structural analysis. Finally, readers might be interested in the future of the product, for which they are referred to Chapter 16.

Abstract

Due to the swift pace of technical innovation, boundaries are pushed in a wide variety of technical fields. Specifically, the increased energy density of batteries has proven to be a fundamental impetus driving the booming business of small and micro unmanned aerial vehicles (UAVs), mainly in terms of amateur drones. With it though, comes an increase in the number of drone incidents in which the vehicle is flown into a restricted area, such as the airspace around an airport or a government building. This sparked the development of ground based anti-drone technologies that focus on removing intruding drones from a specified area by means of nets, lasers, and/or jamming. However, ground based solutions are very costly, whilst also having limited maneuverability as well as long deployment and redeployment times.

DSE group 08 has therefore been tasked with designing a highly maneuverable and flexible anti-drone system, based around an unmanned aerial vehicle that must outspeed, outmaneuver, and ultimately impede any drone with a maximum velocity of 35 meters per second that tries to intrude a specified area of 1 kilometer in diameter. In the previous report, it was concluded that concept HELIADES was the most feasible aerial vehicle for this mission. This is a tiltrotor, fixed wing aircraft, equipped with an integrated removal system consisting of a directional signal jammer, a net launcher, and a kinetic cannon. The purpose of this report was to conduct a detailed analysis on the chosen concept in terms of technical and operational aspects. Moreover, activities for future phases were to be determined.

A detailed analysis was performed in terms of performance, aerodynamics, stability & control, and structure of the aerial vehicle. Furthermore, the operating and logistic characteristics of the entire system were defined in detail, as well as a sustainability approach for the entire development life cycle. Hereafter, the critical risks of the system were identified and its compliance with the requirements set by the stakeholders was analyzed. Finally, a complete post-DSE project plan was developed in order to turn the design into a working prototype.

The result of this report was a fully autonomous aerial vehicle with a total prototype cost of €14,000, operable 24 hours a day in temperatures ranging from -10°C to 50°C. This system consists of a portable ground station and a tiltrotor UAV with a total weight of 9.65kg, a wingspan of 1.70m and a fuselage length of 1.56m. HELIADES can endure a load factor of 20g, and can pitch and roll at a rate of 60°/s and 150°/s, respectively. At an altitude of 600m, it can fly at a maximum continuous velocity of 70.8m/s and perform an instantaneous turn at a rate of 185°/s. The net launcher of the removal system fires 2x2m reusable nets with biodegradable net shells, while ceramics are used as ammunition for the kinetic cannon. The aerial vehicle itself is manufactured from Polylactic Acid (PLA), a biodegradable plastic produced from renewable resources such as corn starch. This means that the structure can be 3D printed and results in a sustainable final product. Its market price for the complete system is estimated at €200,000, making it competitive with existing products due to its increased maneuverability and autonomy.

In conclusion, HELIADES is a unique and sustainable aerial anti-drone system with an estimated removal success rate of up to 89%, through which it may become a fierce competitor of existing anti-drone solutions. The group is confident that HELIADES will experience a successful market introduction due to the design's potential as well as the team's drive to deliver a sound product. This report marked another milestone in the path leading up to this introduction, but certainly not the last one.

Contents

List of Symbols

Symbol	Description	Unit
A	General cross-sectional area (structural analysis)	[m^2]
A	Rotor disk area (performance analysis)	[m^2]
$\bar{A}$	Vector position of anti-drone drone	[-]
A_c	Surface area of convection region	[m^2]
A_{con}	Cross-sectional convection area	[m²]
A_e	Effective area of antenna	[m]
A_I	Enclosed area of upper section	[m^2]
A_{in}	Inlet area	[m²]
A_O	Operational availability	[%]
A_R	Enclosed cross sectional area	[m^2]
AR	Aspect ratio	[-]
b	Wingspan	[m]
B	Distance between camera lenses	[m]
$\bar{B}$	Vector position of target	[-]
B_r	Boom area	[m^2]
c	Mean aerodynamic chord	[m]
c_b	Mean blade chord	[m]
C	Specific cost (structural analysis)	[\$/kg]
C	Antenna circumference (removal system)	[m]
C_{D_0}	Zero lift drag coefficient wing	[-]
$C_{D_{b,0}}$	Zero lift drag coefficient blade	[-]
C_{F_α}	Dimensionless derivative of F with respect to α (stability & control)	[-]
C_l	2D lift coefficient wing	[-]
C_L	3D lift coefficient wing	[-]
$C_{L_{max}}$	Maximum lift coefficient wing	[-]
$C_{L_{\alpha,b}}$	Blade lift coefficient slope	[1/rad]
C_N	Normal coefficient	[-]
C_r	Root chord	[m]
C_{r_t}	Tail root chord	[m]
C_T	Thrust coefficient	[-]
C_T/σ	Normalized thrust coefficient	[-]
C_λ	Wavelength normalized circumference	[-]
D	Drag	[N]
D	Antenna diameter (removal system)	[m]
DL	Disk loading	[N/m^2]
DNL	Day-Night Average Noise Level	[dB]
e	Oswald factor	[-]
E	Young's modulus (structural analysis)	[Pa]
E	Energy	[J]
f	Focal length of camera (control analysis)	[m]
f	Frequency (removal system)	[Hz]
f_e	Equivalent flat plate area	[m^2]
f_n	Natural frequency	[Hz]

Symbol	Description	Unit
F	Force	[N]
F_i	Funnel vector in plane i	[-]
g	Gravitational acceleration	[m/s^2]
G	Shear modulus	[Pa]
G_{Rx}	Receiving antenna gain	[dB]
G_{Tx}	Transmitting antenna gain	[dB]
h	Heat transfer coefficient	[W/(m²K)]
H	Altitude	[m]
i_0	No load current	[A]
I_{aa}	Area moment of inertia around a-axis (structural analysis)	[m^4]
I_{aa}	Mass moment of inertia around a-axis (stability analysis)	[kg m^2]
I_{ab}	Area product of inertia (structural analysis) around the ab-axis	[m^4]
I_{ab}	Mass product of inertia (stability analysis) around the ab-axis	[kg m^2]
J_{mB}	Bessel function of m rotors and N_b blades	[-]
k	Thermal conductivity	[W/(m K)]
K	Induced drag constant	[-]
K	Dimensionless inertia (stability & control)	[-]
K_n	Vibrational constant	[-]
K_v	Specific RPM	[RPM/V]
l_h	Horizontal tail arm	[m]
l_{fus}	Fuselage length	[m]
L	Lift	[N]
L_0	Wire length of helix antenna	[m]
LD_{max}	Maximum lift to drag ratio	[-]
LFS	Free Space Loss	[-]
m	Mass	[kg]
m	Harmonic order (noise)	[-]
M	Moment	[Nm]
$M_{tip,max}$	Maximum tip Mach number	[-]
n	Load factor	[-]
n	Number of turns (removal system)	[-]
n_{BC}	Buckling constant	[-]
N_b	Number of rotor blades	[-]
$N_{day/night}$	Number of day/nighttime operations	[-]
N_r	Number of rotors	[-]
Nu	Nusselt number	[-]
p	Roll rate	[rad/s]
P	Power	[W]
P	Load (structural analysis)	[N]
P_0	Profile power	[W]
P_a	Available power	[W]
P_{br}, P_{shaft}	Shaft power	[W]
P_i	Induced power	[W]
P_p	Parasite power	[W]
P_{ref}	Reference sound pressure	[W]
P_{rms}	Root mean squared sound pressure	[W]
P_{tot}	Total power	[W]
P_{Rx}	Received power	[W]

Symbol	Description	Unit
Pr	Prandtl number	[-]
PS	Power setting engine	[%MCP]
$\dot{Q}$	Heat rate	[W]
q	Pitch rate	[rad/s]
Q_m	Motor torque	[Nm]
q_b	Basic shear flow	[N/m]
q_D	Drag distribution	[N/m]
q_L	Lift distribution	[N/m]
q_s	Shear flow	[N/m]
$q_{s,0}$	Closed section shear flow constant	[N/m]
q_W	Weight distribution	[N/m]
r	Yaw rate	[rad/s]
R	Ideal gas constant air	[J/(K mol)]
R	Reduction ratio (performance analysis)	[-]
R	Radius (gearbox design)	[m]
R_{turn}	Turn radius	[m]
R_b	Rotor radius	[m]
Re	Reynolds number	[-]
R_m	Winding resistance	[Ω]
ROC	Rate of climb	[m/s]
s	Circumference integration parameter	[m]
S	Wing surface area	[m^2]
S	Shear force (structural analysis)	[N]
S	Distance to observer (noise)	[m]
S	Antenna spacing (removal system)	[m]
S_h	Horizontal tail surface area	[m^2]
S_λ	Wavelength normalized spacing	[-]
SEL	Sound Exposure Level	[dB]
SPL	Sound Pressure Level	[dB]
t	Time	[s]
t_D	Skin thickness	[m]
T	Temperature	[°C],[K]
T	Torque	[Nm]
T	Thrust (performance analysis)	[N]
T	Number of gear teeth (gearbox design)	[-]
T_c	Thrust coefficient	[-]
T_f	Flow temperature	[K]
T_w	Surface temperature	[K]
T_{day}	Total day time	[s]
T_{endu}	Endurance time	[s]
T_P	Thrust generated by a single engine	[N]
$\hat{u}$	Relative velocity change	[-]
v	Voltage	[V]
V	Forward velocity	[m/s]
V_h	Horizontal tail volume coefficient	[-]
V_{stall}	Stall velocity	[m/s]
V_{tot}	Total velocity (performance analysis)	[m/s]
V_{turn}	Turn velocity	[m/s]

Symbol	Description	Unit
V_v	Vertical tail volume coefficient	[-]
w	Noise penalty W	[dB]
W	Weight	[N]
W_0	Total wing weight	[N]
W_P	Weight of a single engine and nacelle	[N]
WL	Wing loading	[N/m^2]
WP	Power loading	[N/W]
x	Cross sectional coordinate	[m]
$\bar{x}$	x-coordinate of the centroid	[m]
ΔX	Distance	[m]
$x - x'$	Disparity	[m]
y	Cross sectional coordinate	[m]
x_{LEMAC}	x Position of leading edge of wing mean aerodynamic chord	[m]
$\bar{y}$	y-coordinate of the centroid	[m]
z	Spanwise location (structural analysis)	[m]
z	Distance between camera and object (stability & control)	[m]
α	Helix angle (removal system)	[rad]
α	Helix angle	[°]
α	Angle of attack (stability & control)	[rad]
α_T	Tilt angle	[rad]
β	Side slip angle (stability & control)	[rad]
γ	Specific heat ratio (performance)	[-]
γ	Flight path angle (stability & control)	[rad]
Γ	Dihedral angle	[deg]
δ	Beam deflection (structural analysis)	[m]
δ_3	Kinematic coupling	[°]
δ_{cl}	Left ruddervator deflection	[rad]
δ_{cr}	Right ruddervator deflection	[rad]
δ_a	Aileron deflection	[rad]
δ_{rC}	Conventional rudder deflection	[rad]
ΔG	Dimensionless recoil force from shot gun	[-]
η_{pr}	Propeller efficiency	[-]
θ	Climb angle (performance)	[rad]
θ	Beam angle (structural analysis)	[rad]
θ	Pitch angle (stability & control)	[rad]
$\frac{d\theta}{dz}$	Rate of twist	[rad/m]
κ	Empirical correction factor for momentum theory	[-]
λ	Wavelength (removal system)	[m]
λ	Inflow ratio	[-]
λ_t	Tail taper ratio	[-]
λ_h	Inflow ratio in hover	[-]
Λ_{LE_t}	Leading edge sweep angle	[deg]
μ	Dynamic viscosity	[kg/(ms)]
μ_b	Dimensionless mass	[-]
μ_x	Forward flight ratio	[-]
ρ	(Air) density	[kg/m^3]
σ	Normal stress (structural analysis)	[Pa]
σ	Rotor solidity (performance analysis)	[-]

Symbol	Description	Unit
σ_{yield}	Yield strength	[Pa]
τ	Shear stress	[Pa]
ϕ	Roll angle	[rad]
ϕ_i	Obstacles vector in plane i	[-]
ψ	Yaw angle	[rad]
ω	Turn rate	[rad/s]
Ω_a	Rotor angular velocity in airplane mode	[rad/s]
Ω_h	Rotor angular velocity in helicopter mode	[rad/s]
Ω_m	Angular velocity	[rad/s]
$\oslash$	Pitch circle diameter	[mm]

List of Abbreviations

Abbreviation	Description
3/4G	Third/Fourth Generation
ADD	Anti-Drone Drone
ADS-B	Automatic Dependent Surveillance – Broadcast
ATF	Bureau of Alcohol, Tobacco, Firearms and Explosives
BMU	Battery Management Unit
BUDG	Budgets
CAA	Civial Aviation Authority
CAD	Computer Aided Design
CAGR	Compound Annual Growth Rate
CCU	Cannon Control Unit
CDFC	Communication/Data Flow Chart
CFD	Computational Fluid Dynamics
CFRP	Carbon Fiber Reinforced Plastic
CPS	Cylinder Position Sensor
CPU	Central Processing Unit
C/S/VTOL	Conventional/Short/Vertical Take Off and Landing
CXX	Component number XX
DHBD	Data Handling Block Diagram
DOF	Degrees Of Freedom
DOT	Design Option Tree
DSE	Design Synthesis Exercise
DSSS	Direct-Sequence Spread Spectrum
EBD	Electrical Block Diagram
ESC	Electronic Stability Control
FAA	Federal Aviation Administration
FAQ	Frequently Asked Questions
FAR	Federal Aviation Regulations
FBD	Free Body Diagram
FBS	Functional Breakdown Structure
FCS	Fire Control System
FDM	Fused Deposition Modeling
FEA	Finite Element Analysis
FEM	Finite Element Method
FF(B)D	Functional Flow (Block) Diagram
FHSS	Frequency Hopping Spread Spectrum
FXX	Function number XX
GDI	Gross Domestic Income
GPS	Global Positioning System
GS	Ground Station
GUI	Graphical User Interface
HWBD	Hardware Block Diagram
IMU	Inertial Measurement Unit
IR	Infrared

Abbreviation	Description
ISA	International Standard Atmosphere
ISM	Industrial, Scientific and Medical
LEGN	Legislation
LEMAC	Leading Edge Mean Aerodynamic Chord
LTE	Long-Term Evolution
MCP	Maximum Continuous Power
MDT	Maintenance Down Time
MTBF	Mean Time Between Failures
MTBM	Mean Time Between Maintenance
MTOW	Maximum Take-Off Weight
NACA	National Advisory Committee for Aeronautics
NASA	National Aeronautics and Space Administration
NCU	Net Gun Control Unit
NDI	Nonlinear Dynamic Inversion
NFA	National Firearms Act
NVD	Night Vision Device
N/A	Not Available
OEI	One Engine Inoperative
OTHR	Other
PCD	Pitch Circle Diamter
PEIRP	Peak Effective Isotropic Radiated Power
PID	Proportional Integral Derivative
PLA	Polylactic Acid
PLL	Phased Lock Loop
PPL	Polypropylene
PERF	Performance
RAMS	Reliability, Availability, Maintainability, Safety
REQ	Requirement
RF	Radio Frequency
RMS	Root Mean Squared
RPM	Revolutions per Minute
RTB	Return To Base
RX	Receiver
SAC	Special Airworthiness Certificate
SAFR	Safety and Reliability
SLS	Selective Laser Sintering
SMART	Stanford Multi-Actuator-Receiver Transducer
SMS	Stores Management System
SONAR	Sound Navigation And Ranging
SPDT	Single Pole-Double Throw
SSL	Standard Sea Level
SUST	Sustainability
SWBD	Software Block Diagram
TX	Transmitter
UAS/V	Unmanned Aerial System/Vehicle
U.S.C.	United States Code
VCO	Voltage Controlled Oscillator
VTO/L	Vertical Take-Off and Landing

1. Introduction

The drone market is continuously expanding and a shift has been observed from professional use to amateur use. This has led to difficulties in legislation, which makes it increasingly hard to ensure safe use of these vehicles. Accidents occur at an increasing rate in which amateur drones enter restricted airspace, posing an immediate threat to anyone and/or anything therein. With the exponential increase in drone use as well as drone accidents, the need for anti-drone systems becomes imperative. Several ground-based systems have already been developed in order to address this issue, but these are very expensive while lacking in terms of maneuverability. Therefore, it is important to look for alternatives that perform better in these aspects, so as to ensure adequate protection from drones.

The purpose of this project is to design a system capable of preventing other drones from entering a specified area without entering the area itself: the Anti-Drone Drone (ADD). This system shall consist of at least one unmanned aerial vehicle that is capable of preventing drones whose mass is below 2.5kg and whose velocity is below 35m/s from entering an area of 1km in diameter. The mass of the aerial vehicle shall be no more than 10kg and development cost of a functional prototype shall cost no more than €50,000. This report elaborates on the final design of the selected concept HELIADES following the mission statement: *'DSE Group S08 will design a drone capable of preventing other drones from entering a specified area, whilst doing so in a sustainable way, without entering the area itself.'*

The report is divided in four parts: early concept design, technical analysis, detailed design, and future developments. The former consists of functional diagrams in Chapter 2, that provide an overview of all functions the system has to perform, a market analysis in Chapter 3, in which existing solutions are looked into besides establishing a sales price, and an overview of the current design status in Chapter 4. The latter also includes a budget breakdown in that provides an overview of mass, cost, and power budgets per subsystem. The technical analysis part consists of performance analysis in Chapter 5, stability & control analysis in Chapter 6, and aerodynamic analysis in Chapter 7. Moreover, Chapter 8 focuses on the structural analysis and in Chapter 9 a sensitivity analysis is performed. This is followed by the detailed design part, that starts off with a sustainability analysis in Chapter 11 and a discussion on operations and logistics in Chapter 12. This is followed by a thorough risk analysis in Chapter 13, the complete design configuration and lay-out in Chapter 14, and the requirement compliance matrix in Chapter 15. Finally, the future developments part includes an elaboration on activities that are to take place after the DSE has finished. This is presented in Chapter 16. The report closes with the system technical diagram presented in Appendix A.

2. Functional Flow Diagram & Functional Breakdown Structure

This chapter includes the Functional Flow Diagram (FFD) and the Functional Breakdown Structure (FBS). A first version of the aforementioned was presented in the Baseline Report, which is refined here for HELIADES [66]. Both updated diagrams are shown in Fig. 2.1, Fig. 2.2 and Fig. 2.3. They were used to provide the group with an overview of all the functions that have to be performed, thus ensuring all of them have been thoroughly analyzed and accounted for. Moreover, they were used to set up the list of requirements that is present in Chapter 15. Furthermore, in Fig. 2.2 and Fig. 2.3. Note that these functionalities were used as a baseline and should thus not necessarily be considered as functionalities of the detailed final design.
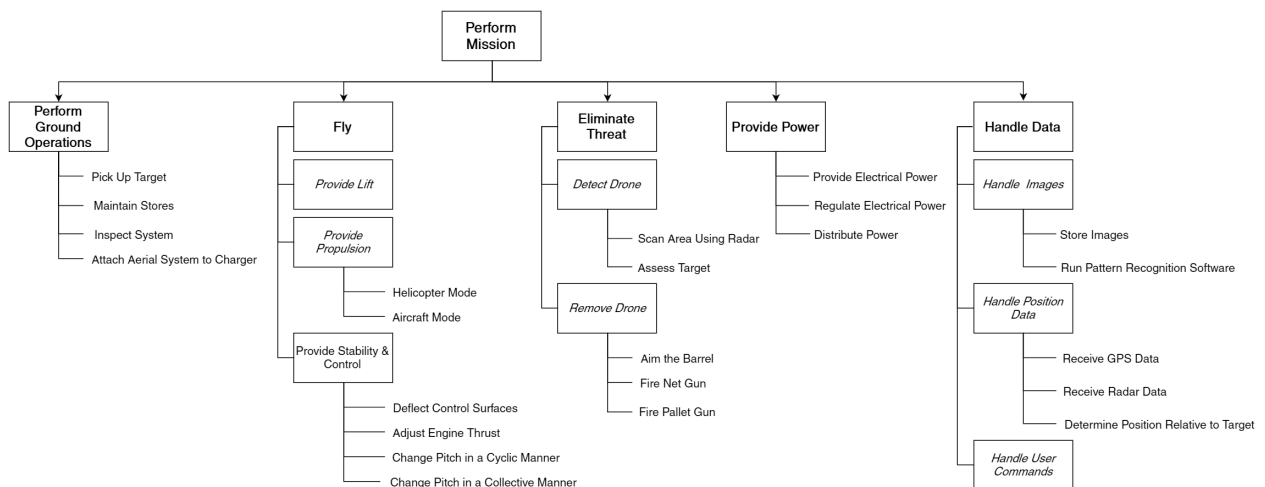

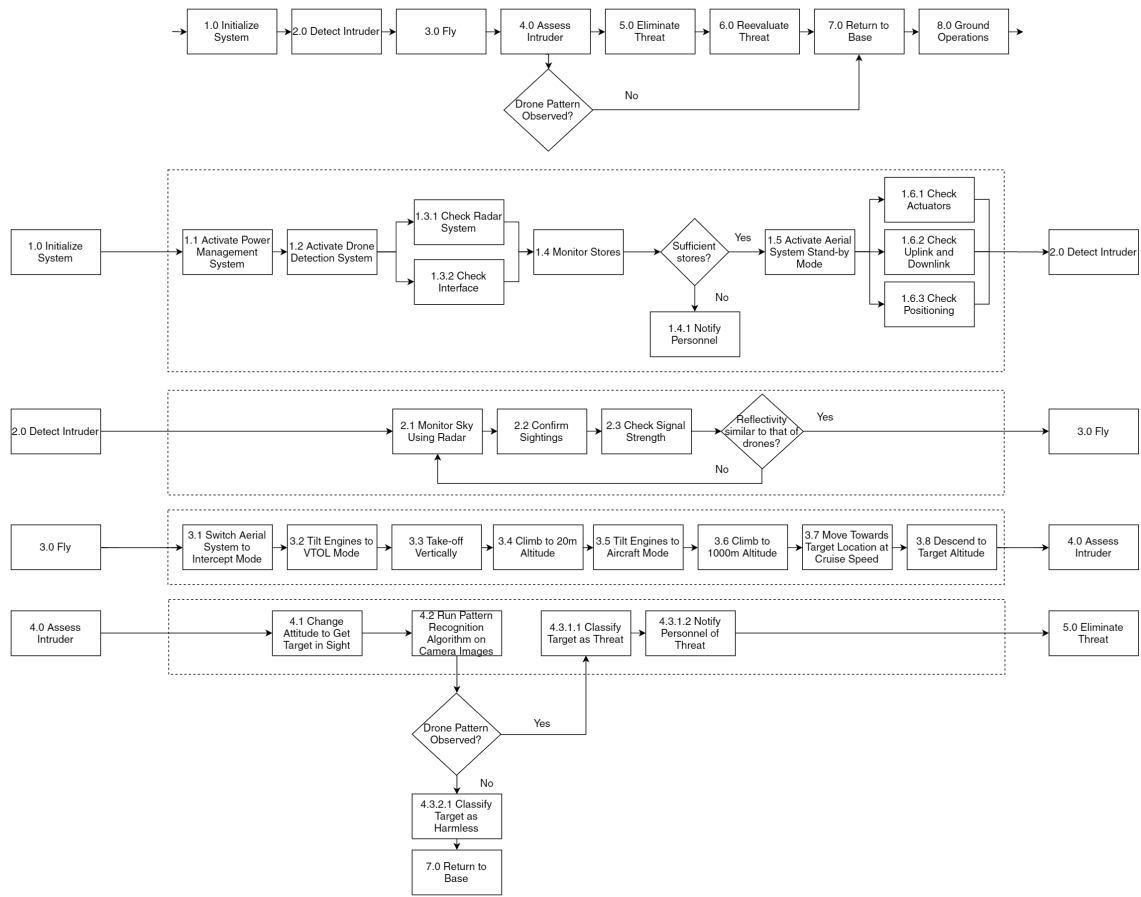Figure 2.1: The Functional Breakdown Structure of HELIADES.

1.0 Initialize System → 2.0 Detect Intruder → 3.0 Fly → 4.0 Assess Intruder → 5.0 Eliminate Threat → 6.0 Reevaluate Threat → 7.0 Return to Base → 8.0 Ground Operations

Drone Pattern Observed? — No → 7.0 Return to Base

1.0 Initialize System → 1.1 Activate Power Management System → 1.2 Activate Drone Detection System → 1.3.1 Check Radar System / 1.3.2 Check Interface → 1.4 Monitor Stores → Sufficient stores? — Yes → 1.5 Activate Aerial System Stand-by Mode → 1.6.1 Check Actuators / 1.6.2 Check Uplink and Downlink / 1.6.3 Check Positioning → 2.0 Detect Intruder

Sufficient stores? — No → 1.4.1 Notify Personnel

2.0 Detect Intruder → 2.1 Monitor Sky Using Radar → 2.2 Confirm Sightings → 2.3 Check Signal Strength → Reflectivity similar to that of drones? — Yes → 3.0 Fly

Reflectivity similar to that of drones? — No → (back to 2.1 Monitor Sky Using Radar)

3.0 Fly → 3.1 Switch Aerial System to Intercept Mode → 3.2 Tilt Engines to VTOL Mode → 3.3 Take-off Vertically → 3.4 Climb to 20m Altitude → 3.5 Tilt Engines to Aircraft Mode → 3.6 Climb to 1000m Altitude → 3.7 Move Towards Target Location at Cruise Speed → 3.8 Descend to Target Altitude → 4.0 Assess Intruder

4.0 Assess Intruder → 4.1 Change Attitude to Get Target in Sight → 4.2 Run Pattern Recognition Algorithm on Camera Images → 4.3.1.1 Classify Target as Threat → 4.3.1.2 Notify Personnel of Threat → 5.0 Eliminate Threat

Drone Pattern Observed? — Yes → 4.3.1.1 Classify Target as Threat

Drone Pattern Observed? — No → 4.3.2.1 Classify Target as Harmless → 7.0 Return to Base

Figure 2.2: First part of the Functional Flow Diagram of HELIADES.

5.0 Eliminate → 6.0 Re-evaluate → 7.0 Return to Base → 8.0 Ground Operations

5.1 Determine Threat Distance → Camera in Range? — Yes → First Elimination Attempt? — Yes → 5.3.1 Aim Net Gun → 5.4 Determine Shooting Distance → Drone in Range? — Yes → 5.5.2 Fire Gun → 5.6 Reload Gun

Camera in Range? — No → 5.2.1.1 Calculate Required Trajectory → 5.2.1.2 Fly Trajectory

First Elimination Attempt? — No → First Attempt Missed? — Yes → 5.3.2 Aim pallet gun

First Attempt Missed? — No → (to 5.2.1.1 Calculate Required Trajectory)

Drone in Range? — No → 5.5.1 Maneuver Closer to Threat

6.1 Re-detect Threat → Still Flying? — Yes → 5.0 Eliminate

Still Flying? — No → 6.2 Predict Landing Coordinates → 6.3 Notify Personnel for Pick-up

7.1 Determine Returning Trajectory → 7.2 Ascend/Descend to 1000m Altitude → 7.3 Cruise Towards Ground Station → 7.4.1 Descend to 20m Altitude / 7.4.2 Slow Down to Transition Speed → 7.5 Tilt Rotors to Helicopter Mode → 7.6 Check Landing Position → 7.7 Align Position with Landing Station → 7.8 Land Vertically → 7.9 Turn Propulsion System Off → 7.10 Activate Standby Mode

8.1.1 Attach Drone to Charger → 8.2 Inspect Structural Integrity → Inspection fine? — Yes → 8.3 Check Stores → Sufficient stores? — No → 8.3.1 Notify Personel for Resupply

Inspection fine? — No → 8.2.1 Perform Repairs
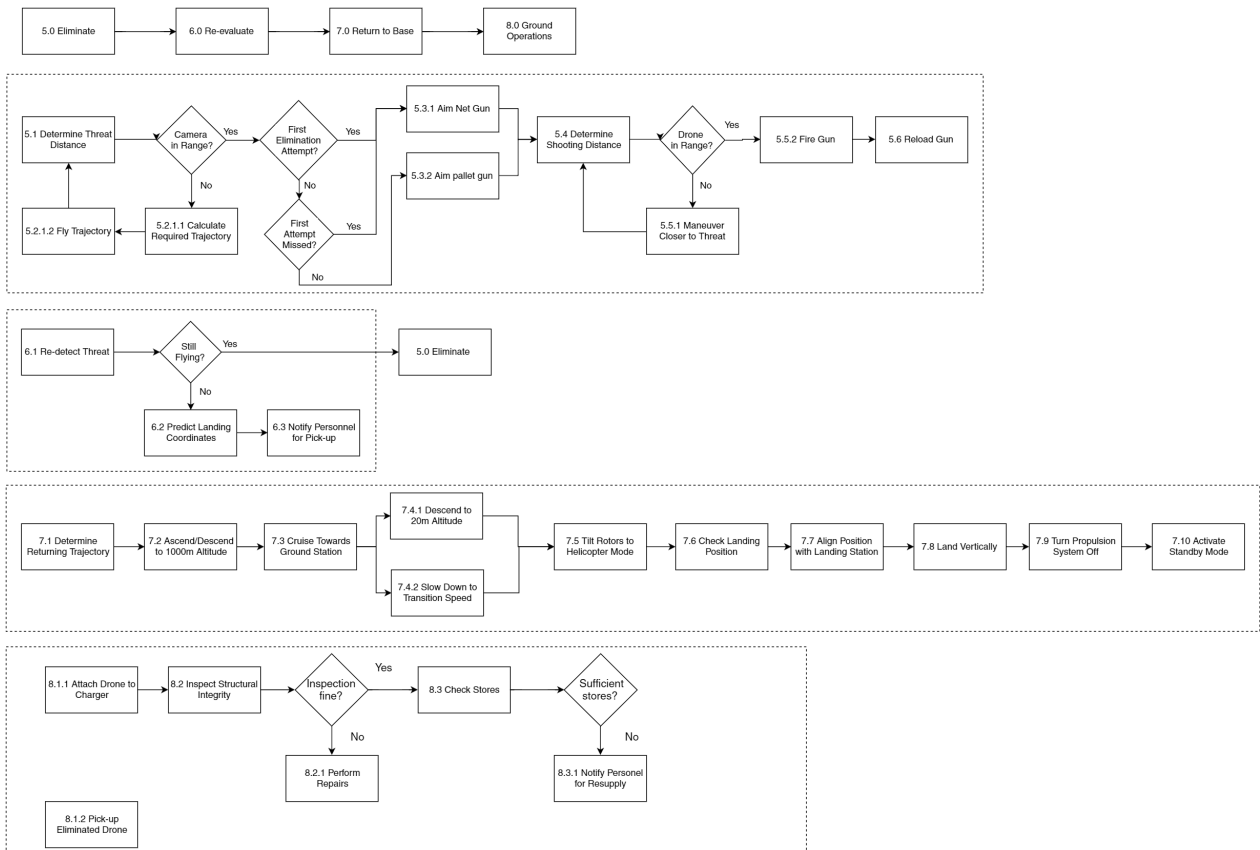
8.1.2 Pick-up Eliminated Drone

Figure 2.3: Second part of the Functional Flow Diagram of HELIADES.

3. Market Analysis

A good product is not necessarily a successful product. Innovative solutions can experience failure if, for example, they are launched prematurely (i.e. the market does not yet exist), or if the product is not targeted to the right consumer base. This chapter serves as a basis for further design, as the right market and its composition need to be determined prior to conducting the actual design.

The current anti-drone development is dominated by military and governmental organizations. However, as potential customers arise, being government premises, prisons, nature reserves, security services, emergency services, and the general public, the anti-drone market will shift to a more commercial sector. With a more widespread availability of consumer drones, legislative bodies will have to reconsider current laws, and see the benefit of a countermeasure such as an anti-drone system. Airports present a good initial customer base, as they are willing to innovate in the name of safety, and in addition have existing radar systems, which can be adjusted to be used alongside the ADD as a detection system.

The cumulative annual growth rate of the anti-drone market is estimated to be 23.89% for 2017-2022; North America is expected to obtain the largest market share, and the Asia-Pacific region is expected to have the largest growth rate in this period. Therefore, these regions are selected as potential market [124].

3.1 Competitor Analysis

Capturing a significant market share can be made possible by outperforming the existing products offered on said market. Therefore, the current products offered were analyzed, in order to determine their strengths and weaknesses.

Figure 3.1: MPI-200 capturing a drone [27].

Figure 3.2: DroneCatcher capturing a drone [10].

Aerial Systems

Table 3.1: Comparison between competing drone removal systems.

Category	MPI-200	DroneCatcher	HELIADES
Battery	N/A	6S Li-Po	Li-Po
Purchase price [€]	25,000	N/A	TBD
Range [km]	1	1	5
Maximum velocity [m/s]	27.79	10	50
Endurance [min]	N/A	10-15	10
Weight [kg]	5.4 (excl. batteries)	5.5 (incl. batteries)	10.0 (incl. batteries)

The **MALOU MPI-200** serves as a great reference, as it is currently one of the only aerial anti-drone drones available on the civil market. It uses a rectangular net that deploys by dropping a straight bar, which is attached to the bottom of the net, see Fig. 3.1 [27]. The drone is controlled by a human operator, which can use virtual reality goggles if deemed necessary as there is a camera attached to the MPI-200. The downfall of this product lies in its operator

dependence, as well as its lack of detection capabilities. The latter means that the detection must be done visually, thus limiting the surveillance area.

The **DroneCatcher** from Delft Dynamics is also an important competitor. The company participated in the 'Small Business Innovation Research' and ended up receiving governmental grants to develop the product. For this competition, where off-the-shelf products were used, a quadcopter and a net gun were combined into one system. Currently, the net gun and corresponding software are being further developed into a more effective product. In Fig. 3.2, the DroneCatcher is shown shooting its net towards a target drone [10]. As Delft Dynamics is a Dutch company, its focus is primarily on the Dutch market. Therefore, Dutch legislation is taken into account [9]. This has a major impact on the specifications of the DroneCatcher - for example, the maximum allowable altitude is 120m and the maximum range is 500m. This provides it with limited drone catching opportunities, considering that an intruding drone might not abide by the rules. From a meeting with Elwin Rath from Delft Dynamics more information was gathered as shown in Table 3.1.

Lastly, **Theiss UAV** has been working on an anti-drone drone system, featuring an attachable net gun that can be used in combination with either multicopters or winged drones. Their ultimate goal is to develop a fully autonomous system, though they are still in the research phase of the project, hence a price is yet to be determined. The net gun is named Excipio, meaning 'I capture' in Latin, and can be seen in Fig. 3.3 [52]. A disadvantage of their system is the inability to continue the pursuit after firing the net, since there is only one net carried onboard.

Figure 3.3: Theiss UAV's Excipio net gun, mounted on a hexacopter [52].

Figure 3.4: Blighter's Anti-UAV Defense System. The radar detection system on the left, and the RF jammer on the right [6].

Ground systems

Apart from the aerial solutions examined above, ground based anti-drone solutions are also available. These are limited in performance due to their immobility and ineffectiveness to deal with evasive targets (in case a target hides behind buildings and other objects). The detection-only systems exist, but were not considered, since it is the removal aspect that the ADD will be competing against.

The **Blighter AUDS Anti-UAV Defence System** is a ground-based anti-drone system that combines detection, tracking, and disruption [6]. Although the cost is significant - $1.2 million (€1.07 million)- the system is aimed at government agencies and other large scale organizations that can afford said price. Its effective range extends up to 10km, although the downfall of the system is in stopping autonomous flying vehicles which do not rely on the radio frequency (RF) spectrum for control (i.e. they use pre-programmed GPS for navigation). It is shown in Fig. 3.4 [6].

A similar system has also been developed by Selex ES, called **Falcon Shield Counter-UAV System** [43]. The major difference between the Falcon Shield and Blighter's system is the price - the Falcon Shield comes in at $250,000 (€225,000). Moreover, the Falcon is a compact system, which can easily be mounted on a tripod, making it convenient for one-time events or quick deployment.

Finally, OpenWorks' answer to the anti-drone system is a handheld, manually operated net launcher, which shoots nets at incoming targets. It is called the **OpenWorks SkyWall 100** and, as of the writing of this report, the price and launch date are still unavailable [35]. This system has its own niche, but will not fit into the market that the group aims for - there is a lack of autonomy, and a limited detection range. What SkyWall 100 does feature though, is an advanced target tracking system, and a quick reload time of 8 seconds.

3.2 Product Cost

The high price points of ground-based solutions are justified by the research and development required to implement new technologies into these products. Selecting a suitable price point for the anti-drone system can be based on current competition, though it should be taken into consideration that HELIADES provides autonomy and maneuverability. These are aspects that the aerial and ground competitors, respectively, do not offer.

The cost of building a prototype of €50,000 provides a reference point for the final product price. If the demand is large enough though, the price does not have to be limited by the manufacturing and development costs. For example, an airport might be interested in acquiring an ADD system in order to prevent future shutdowns due to drone-related interruptions. Dubai Airport recently experienced such an interruption, which ended up costing roughly €40 million [61]. Hence, if the system being sold can save the customer millions, a higher price would still ensure a remunerative business.

Due to HELIADES' autonomy, another important consideration to factor in is the cost of having an operator. Therefore, other anti-drone systems are at a disadvantage, especially when an average employee salary is considered. In Table 3.2 one can see the average income for different countries [51]. This data can be used to calculate average cost of employing an operator for a specified period of time. What this represents is the additional cost of operating the competitors' products. As the only employee necessary for keeping HELIADES running can be an existing employee with a small additional task of conducting maintenance and servicing as required (not more than an hour a day, on average).

Table 3.2: Average Gross Domestic Income (GDI) per capita in Euros. The yearly budget is for the human labour only, does not include spare and replacement parts.

Country	Monthly GDI (2011-2015) [€]	Estimated yearly operational budget [€]
Australia	4,820	57,840
Canada	3,852	46,224
China	552	6,624
India	117	1,404
Japan	3,314	39,768
Korea	2,021	24,252
Netherlands	3,869	46,428
United States	4,121	49,452

Considering the above mentioned product and labour costs, as well as competitors' product costs, **HELIADES can still remain competitive if priced at €200,000**, including the radar detection system. This is due to the aerial competitors lacking functionality in terms of autonomy, and the ground-based solutions having a significantly higher price. Moreover, as airports can save millions using this product, this price is low compared to the potential losses.

4. Preliminary Design

In the Mid-term Report, the trade-off of conceptual designs has been presented, where HELIADES is continued to the detailed design phase. The following chapter serves as a quick reminder of the chosen concept used in the remainder of the Design Synthesis Exercise.

4.1 Aerial Vehicle

HELIADES is a tiltrotor aircraft equipped with a modular removal system consisting of a kinetic cannon, a net launcher and a RF jammer. A sketch of the initial design of the aerial vehicle is displayed in Fig. 4.1.

Figure 4.1: Initial design of the aerial vehicle concept HELIADES.

System Features

The initial design of the anti-drone system utilized the following technologies and systems within its aerial vehicle.

- Propulsion System: Tilting rotors; nacelles mounted at the wing tips, spinning open rotors. They possess cyclic and collective pitch control for helicopter-like maneuverability and the blades may be folded away for compactness.
- Navigation System:
  - GPS Antenna for navigation via GPS waypoints.
  - IMU re-calibrated with GPS.
  - Pitot tube for airspeed measurement.
- Communication System: Communication antenna dorsally mounted. Used for two-way communication with the GS.
- Detecting System: Camera used for targeting enemy drone at engagement distances and a radar system on the ground for preliminary detection.
- Removal System:
  - RF cannon: This is a high-gain directional antenna for use in jamming or disabling the target via EM interference.
  - Dual-purpose launcher: The modular removal system entails a dual-purpose launcher, capable of firing non-lethal ammunition through its kinetic cannon or by firing expanding nets with drogue chutes for ensuring a safe descent of the captured target.
  - Mesh: This is a deployable, towed, aft mounted filament mesh. The filaments would ensnare target propulsion systems, then snap off from the removal system.

Interception

The sequence of events for a target ingress intervention are outlined as follows:

1. Initial State: HELIADES is fully supplied waiting on the ground.
2. Detection: The radar detects a target, HELIADES takes off and is guided to the target area for interception.

3. Visual Contact: The optical camera can now track the target, bringing HELIADES close to the target.
4. Elimination: The RF cannon is fired, after which the net gun is used. If the net gun is not successful, the pellet gun is used instead.
5. Loiter or Landing: Depending on the remaining stores, HELIADES may loiter till the next engagement or land for resupply.

4.2 Ground station

The ground station comprised of a necessary communication system that relays information to the drone, and the computer interface for it. Another point of communication was the operator, who needs to be informed when the drone needs maintenance or resupplying. The system was designed to be autonomous up to that point, so the operator does not have to be at the ground station at all times. This way, existing employees can still do their regular work, and assist the drone when necessary.

Furthermore the ground station features a radar detection system, which is crucial for detecting an intruding drone. Since the focus of the initial design was mainly the aerial vehicle, the radar system is to be designed at a later stage. At this phase of the design, it was assumed that the radar system had a detection range of 3-9km, with a classification range of 1.1km[1].

The position estimate and velocity of the intruding drone outputted by the combination of the radar system and GPS receiver was to be put into an algorithm in the ground station CPU, calculating the time needed for the target drone to get to a certain location. This information would then be communicated to the ADD which then determines the desired Euler angles and thrust settings.

4.3 Mass and Cost budget

The mass and cost allocation budgets that were devised in the Mid-term Report for HELIADES are displayed in Table 4.1. The cost pertained only the cost of materials. The mass of the ADD was set at exactly 10kg and cost of the system was specified at €8900. This cost budget did not include the cost of the radar system, since it had not been determined in the initial design.

Table 4.1: Mid-term Report mass and cost allocation.

	Group	Component	Mass [kg]	Cost [€]	Power [W]
Aerial vehicle	Structure	Wing	1.0	1000	-
		Fuselage	2.0	1000	-
		Landing gear	0.1	100	-
		Tail	0.3	100	-
	Removal system	Launcher	1.5	2000	1.0
	Propulsion	Motor	1.4	1000	3051
	Electronics	CPU	0.1	158	2.0
		Battery	2.8	800	-
		Transceiver	0.1	76	1.0
		GPS receiver	0.1	60	1.0
		IMU	0.1	75	1.0
		Jammer	0.2	224	3.0
		Camera	0.2	400	3.8
		Actuators	0.1	480	129.6
	Subtotal		**10**	**7473**	**3193**
Ground station		Computer	5.0	1200	150
		Recharger	0.2	100	2740
		Radar	N/A	N/A	N/A
		Transceiver	0.1	76	1.0
		GPS receiver	0.1	60	1.0
	Subtotal		**5.4**	**1436**	**2892**
	Total		**15.4**	**8909**	**6085**

---
[1]Classification range is the range at which the system can identify a flying object as a drone

5. Performance Analysis

In this chapter, a performance analysis of HELIADES is performed. The structure of this chapter is as follows. First, Section 5.1 introduces the approach that was taken, graphically illustrated through a flow diagram and mission profile. Then, Section 5.2 list and explains the primary and secondary assumptions that were made. Section 5.1 states and explains the three mission profiles that were used for the performance analysis.

Next, Section 5.3 explains the analysis and the optimization of the design, resulting in a required battery mass. After this, the theory and numerical model is verified and validated in Section 5.4. The propulsive system is sized in Section 5.5. Finally, Section 5.6 deals with heat generation within the aerial vehicle.

5.1 Approach

The approach for the performance analysis is illustrated in Fig. 5.1. Continuing from the initial design parameters derived in the Mid-term Report [67], the defined mission profiles and the required maneuvers, an iterative process can be started that results in a certain mass of the propulsive system. The propulsive system includes the battery and all systems in the nacelles. These are the rotors and rotor hubs, the actuators, the motors, the electronic speed controllers and the gearboxes.
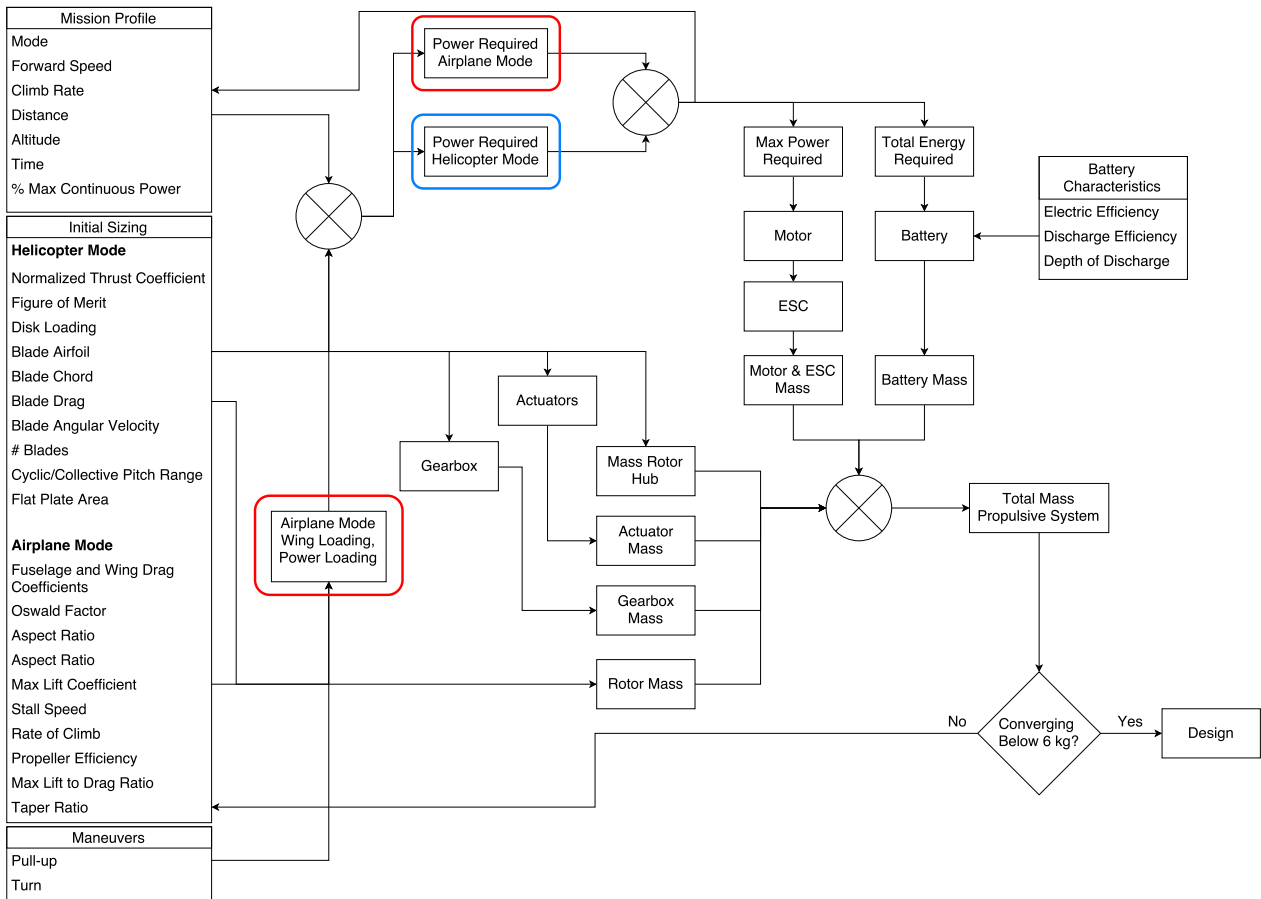
Figure 5.1: Flow diagram for the performance analysis. Denoted in blue are the parts for the power required and performance estimation procedure in helicopter mode, described in Section 5.3.1. Denoted in red are procedures in airplane mode, described in Section 5.3.2.

If the resultant mass is higher than 6kg, the initial design parameters and/or the mission profiles should be adjusted until there is convergence below 6kg.

Mission Profile

After several iterations, the mission profile of HELIADES has been finalized and has resulted in an acceptable battery mass. The final mission profile is displayed in Fig. 5.2 and the segments are explained below, as well as the

battery calculations. The total distance covered is 3500 meter.
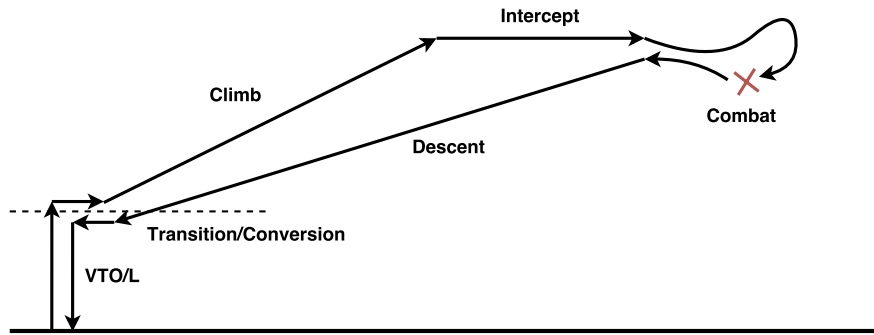
Figure 5.2: The finalized mission profile of HELIADES
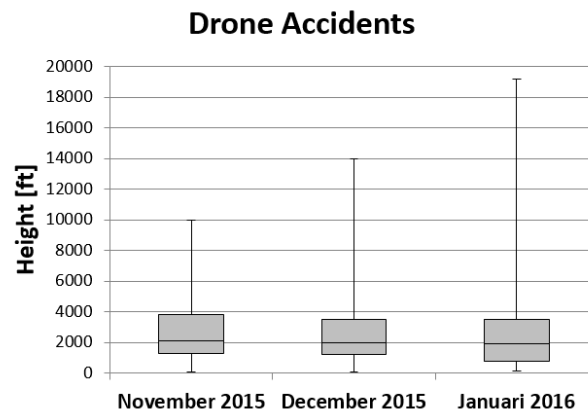
Figure 5.3: FAA database of drone accident altitudes [17].

VTOL: since HELIADES is a VTOL (Vertical Take-Off and Landing) aircraft, the first part of the mission consists of an axial climb of 50m in helicopter mode in order to ascend above any obstacles, apart from large buildings. This climb must be performed at a climb rate of at least 8m/s (**REQ-PERF-03**).

Conversion: afterwards, the aircraft performs a horizontal conversion to airplane mode and continues its mission. For this conversion, the forward speed in helicopter mode must exceed the stall speed of the wing in order to not drop out of the sky. This conversion is done at 50m, in steady flight.

Forward Climb: then, the aircraft climbs to the design altitude and distance. The design altitude is taken at 600m, which corresponds to the mean accident height of 2000ft in Fig. 5.3 [17]. The total horizontal distance covered, including conversion, is set at 1500m, leaving 250m for intercepting the enemy drone. The required climb rate is again at least 8m/s (**REQ-PERF-03**).

Interception: after reaching the desired altitude of 600m, the aircraft cruises for 250m to intercept the target. The total horizontal distance covered with the conversion, climb and intercept is then 1750m (**REQ-PERF-09**). The minimal interception velocity shall be 50m/s (**REQ-PERF-02**).

Combat: after intercepting the drone, the drone has to be taken out. This may involve a conversion back to helicopter mode in case of a hovering target or it may result in a high-speed chase and highly loaded maneuvers for an evasive target. The minimum load factor to be overcome is 20 (**REQ-PERF-23**). The mission assumes a 30 second combat at full power is enough to dispose of the drone.

Descent: with the enemy drone taken out, the aircraft must now descend back to the ground station. The descent from 600m to 50m altitude is then initiated at the desired transition speed, to avoid having to decelerate for the transition. For the descent, a steady powerless glide is initiated, requiring no propulsive power.

Transition: after the descend to 50m altitude, the aircraft converts back to helicopter mode. To do this successfully, the aircraft must decelerate as to not exceed the maximum forward flight speed achievable in helicopter mode. This conversion is also estimated to take 100m.

Landing: a powered landing occurs in helicopter mode after a successful conversion and the aircraft descends from a 50m altitude to the ground station.

5.2 Assumptions

The assumptions made during the performance analysis have been classified as either primary or secondary assumptions and are elaborated below.

5.2.1 Primary Assumptions

- **Steady symmetric flight**: for all mission segments apart from the unpredictable combat mode, steady symmetric flight has been assumed. This eliminated any accelerations present and allowed an analysis based on free-body diagrams and momentum theory. The dynamics involved during accelerated flight are beyond the scope of this report.
- **Uniform inflow**: in order to justify the use of momentum theory in helicopter mode, uniform inflow is a requirement[118]. This requires an ideally twisted blade, which in reality is impossible to manufacture. By using high values of linear twist ($< -20°$), which is generally used in aircraft but avoided for helicopters [132], the inflow resembles that of an ideally twisted blade and the assumption is justified.
- **No interaction between modes**: in helicopter mode, it is assumed that the wing does not generate any lift as the forward speed increases, and the effects of transition during forward flight may be neglected. This is done because the analysis of the dynamic problems encountered during transition and conversion are beyond the scope of this report.
- **No viscious losses**:

5.2.2 Secondary Assumptions

- **Constant blade profile drag coefficient**: in helicopter mode, the profile drag coefficient $C_{d_{b,0}}$ of the blades has been modeled as a function of the obtained C_T/σ in hover, while in reality, it also increases slightly with forward flight velocity [129]. This change has been deemed negligible, given the already marginal contribution of profile power to the resultant required power.
- **Constant equivalent flat plate area**: in reality, the equivalent flat plate area f_{e0}, relevant for the parasitic drag in helicopter forward flight, increases quadratically as angle of attack α increases [100]. The magnitude of this increase is impossible to quantify unless a full-scale wind tunnel test is performed. Given the moderate angle of attack range of the helicopter (Fig. 5.6), f_{e0} is therefore assumed constant.
- **Constant propeller efficiency**: in reality, the efficiency of a propeller varies slightly with motor RPM[40]. For the RPMs encountered in HELIADES, the propeller presumably lies within the range of 70% to 95%, hence a conservative value of 80% is chosen.

5.3 Analysis

This section elaborates on the necessary theory to satisfy the performance requirements as well as to calculate the required battery energy. The performance analysis starts with an analysis in helicopter mode, resulting in the maximum attainable forward flight speed. Then the aircraft mode is analyzed, resulting in the maximum attainable forward speed and turn rates.

5.3.1 Helicopter Mode

The procedure used to calculate the power required for axial and forward flight in helicopter mode is described in Fig. 5.4, which is a zoomed-in part of the performance flow chart Fig. 5.1. The rotor disk loading that is picked initially (orange rectangle) is constrained by the maximum attainable disk loading in airplane mode, see Fig. 5.5.

Determination of Inputs

The input parameters for the power required and performance optimization for helicopter mode are given in Table 5.1. The initial values have been taken from the Mid-term Report [67]. The determination of these parameters is explained in the following paragraphs.

Disk Loading
The disk loading DL was initially at 200N/m^2 but has been decreased to 135N/m^2. A lower disk loading increases the hover performance of HELIADES [118], which was deemed necessary to ensure the axial climb power remained below 1.5kW (Equation (5.13).

$$R_b = \sqrt{\frac{\frac{W}{2DL}}{\pi}} \qquad (5.1)$$

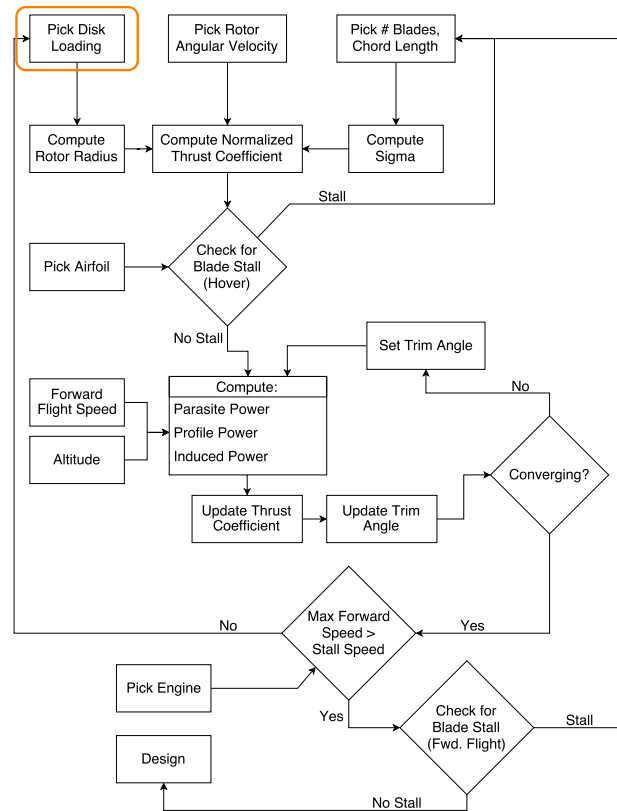$$\sigma = \frac{N_b c_b R_b}{\pi R_b^2} \qquad (5.2)$$

Figure 5.4: Flow diagram of the computations for helicopter mode.

Rotor Dimensions and Solidity

The rotor solidity σ (not to be confused with normal stress, Chapter 8), is defined as the ratio of actual blade area to disk area and is given by Equation (5.2). The selection of solidity consists of a trade-off between rotor stall and profile drag. An increase in solidity, achieved by either adding blades or increasing rotor chord, results in an increase in rotor profile drag (Equation (5.11)), while a decrease in solidity reduces the stall margin of the rotor (Equation (5.3)). The latter is deemed more critical, since the contribution of profile power is marginal (<10%) compared to the overall power required.

The rotor chord dimension is a compromise between the usual rotor aspect ratio in helicopters and aircraft. According to [130], a blade aspect ratio between 14 and 20 is desirable for helicopters, while a blade aspect ratio between 5 and 8 is usual for propeller aircraft [72]. As a compromise, an aspect ratio of 10 has been chosen, which is comparable to the aspect ratio of the XV15 (10.75). A three-blade configuration has been chosen, in line with tiltrotor aircraft such as the AW609, V22 Osprey, Bell Eagle Eye and the previously mentioned XV15). Filling in Equation (5.2), this leads to a solidity of 0.0955.

Rotor Airfoil

The rotor airfoil chosen is the NACA 23012, due to its high maximum lift coefficient and relative simplicity [132] compared to other airfoils. The $C_{l_{max}}$ for this airfoil is 1.5. Most helicopters use linear twist in the range of -5 to -16°, while aircraft propellers utilize higher negative values of twist [132]. A linear twist of -20° has been chosen, which has the closest inflow resemblance compared to ideal twist [118]. This way uniform inflow can be assumed and the use of momentum theory is validated.

Rotor Angular Velocity

The lower bound of rotor RPM is constrained by blade stall (Equation (5.3)), while on the high side, rotor RPM has an upper bound of 3000RPM (based on comparable RC helicopters and their blades [21]). Since the blade stall is again deemed critical, a rotor RPM of 3000, equivalent to 314rad/s, has been chosen.

Hover Correction Factor

The hover correction factor κ accounts for the imperfections of the helicopter caused by the induced velocity of the rotor on the body. For most helicopters, this value lies between 1.12 and 1.25 [118]. For HELIADES, a value of 1.15 is chosen.

Blade Profile Drag Coefficient

The mean blade profile drag coefficient is the dimensionless drag experienced by the blades during flights and must be estimated from references. Its mean value is 0.006 for a C_T/σ of 0.08 and increases as C_T/σ increases [129]. For HELIADES, the value has been set at 0.009.

Equivalent Flat Plate Area

f_{e0} is defined as the product of the equivalent wetted fuselage area and average fuselage drag coefficient. Its exact value can only be determined in a full-scale wind tunnel test. Since these resources were unavailable, the value had to be estimated from reference data. According to [137], f_{e0} lies between 0.046 and 0.19m^2 for UAVs. With a mass of approximately 10kg, HELIADES is classified as a small UAV, and its flat plate area has thus been estimated as 0.08m^2, on the low end of the spectrum.

Table 5.1: Design inputs for the analysis of helicopter mode.

Parameter	Symbol	Unit	Value
Aerial vehicle mass	m	[kg]	10
Disk Loading	DL	[N/m^2]	135
Rotor Radius	R_b	[m]	0.340
# of Blades	N_b	[-]	3
Blade Aspect Ratio	AR_b	[-]	10
Blade Twist	ϕ	[deg]	-20, linear
Blade Chord	c_b	[m]	0.0340
Rotor Solidity	σ	[-]	0.0955
Rotor Angular Velocity Helicopter	Ω_h	[rad/s]	314
Blade Lift Coefficient Slope	$C_{l_{\alpha,b}}$	[1/rad]	5.959
Hover Correction Factor	κ	[-]	1.15
Mean blade drag coefficient	$C_{d_{b,0}}$	[-]	0.009
Equivalent Flat Plate Area	f_{e0}	[m^2]	0.08

Calculation of Outputs

With the required parameters known, the outputs of helicopter mode can now be calculated. The results of the calculations in helicopter mode are displayed in Table 5.3.

Thrust Coefficient and Blade Stall

From the parameters in Table 5.1, the normalized thrust coefficient C_T/σ can be computed [118]. In steady inviscid axial flight, the thrust of the tiltrotor equals half the weight, thus $T = W/2$ per rotor. A is the disk area per rotor (πR_b^2).

$$C_T/\sigma = \frac{T}{\sigma \rho A (\Omega_h R_b)^2} \tag{5.3}$$

At the ceiling of 4000m, $\rho = 0.819$kg/m^3 (ISA) and C_T/σ is calculated to be 0.151. To check whether the blades will not suffer from blade stall in hover, the following has to apply: $6C_T/\sigma < C_{l_{max}}$ [132]. Here, $C_{l_{max}}$ is the maximum lift coefficient of the rotor airfoil. Performing this calculation yields a C_l of 0.907, which ensures that no blade stall occurs during flight.

Forward Flight Power

In steady symmetric horizontal flight, the total power required in helicopter mode is the sum of the required induced power, profile power and parasite power. Induced power P_i is the power used per rotor to accelerate the air going through the rotor and produce thrust. Profile power P_0 is the power that is needed by the rotor to overcome the viscous losses of its blades. Parasite power P_p is the power required to overcome the drag of the body of the aircraft. The total power required can then be computed for different forward speeds and altitudes and is defined as $P_{tot} = 2P_i + 2P_0 + P_p$.

Tilting the Disk

In forward flight, the thrust produced by the rotors has to be tilted in such a way that $T\cos\alpha_T = W$ and $T\sin\alpha_T = D$, where α_T is the tilt angle defined with respect to the rotor axis (vertical) and D the total drag of HELIADES. For a

first estimation of α_T, steady inviscid flight may be assumed [118], reducing the drag to just the parasitic drag, $\frac{1}{2}\rho f_{e0}V^2$.

Combining these relations, this leads to Equation (5.4), where α_T is purely a function of airspeed and altitude. In order to calculate the angle more accurately, a complete state-space system of HELIADES in helicopter mode would be required, which is beyond the scope of this report. Nonetheless, the estimated α_T does give a more realistic view of the increase in drag with α_T, compared to the ideal case where $\alpha_T=0$.

$$\alpha_T = \tan^{-1}\left(\frac{\frac{1}{2}\rho f_{e0}V^2}{W}\right) \tag{5.4}$$

Dimensionless Coefficients
Continuing the analysis, it is convenient to make the airspeeds non-dimensional. The induced inflow ratio λ_i is defined in Equation (5.5) and is a dimensionless parameter of the induced velocity. Similarly, the advance ratio can be defined as the dimensionless forward speed (Equation (5.6)).

$$\lambda_i = \frac{v_i}{\Omega_h R_b} \tag{5.5} \qquad\qquad \mu_x = \frac{V\cos\alpha_T}{\Omega_h R_b} \tag{5.6}$$

Induced Power
To calculate the induced power in forward flight, the inflow ratio λ must be computed, which is a function of both induced inflow and advance ratio. Since the induced velocity on the rotor varies with flight speed, λ must be solved iteratively using Equation (5.8) [118]. Here, λ_h is the inflow ratio in hover and is defined in Equation (5.7).

$$\lambda_h = \sqrt{\frac{(C_T)_{hover}}{2}} \tag{5.7} \qquad\qquad \lambda = \mu_x\tan\alpha_T + \frac{\lambda_h^2}{\sqrt{\mu_x^2 + \lambda^2}} \tag{5.8}$$

The validity of Equation (5.8) is discussed in [118]. This equation is valid in stationary flight and climb, but a non-physical solution will be obtained if the axial descent velocity is less than two times the induced rotor velocity. In this case, the aircraft enters the so-called vortex ring state, which causes the airflow around the rotor to no longer be uniform, thus invalidating the momentum theory.

$$(P_i)_{hover} = \frac{\kappa T_{hover}\sqrt{T_{hover}}}{\sqrt{2\rho A}} \tag{5.9} \qquad\qquad P_i = \frac{\lambda}{\lambda_h}(P_i)_{hover} \tag{5.10}$$

The induced power in forward flight can now be related to the hover case by Equation (5.10). The induced power in hover (Equation (5.9)) can be obtained using momentum theory, where the rotor thrust equals half the weight. κ is the empirical correction factor from Table 5.1, ρ is the air density and A is the rotor disk area.

Profile Power
The profile power P_0 (Equation (5.11)) slightly increases with forward flight due to the $\left(1 + 4.65\mu_x^2\right)$ term. It is also dependent on rotor solidity, density and tip speed. $C_{d_{b,0}}$ is the blade zero lift drag coefficient and can be found in Table 5.1.

$$P_0 = \left[\frac{1}{8}\sigma\rho(\Omega r)^3 A C_{d_{b,0}}\right]\left(1 + 4.65\mu_x^2\right) \tag{5.11} \qquad\qquad P_p = \frac{1}{2}\rho f_{e0}V_{tot}^3 \tag{5.12}$$

Parasite Power
Finally, parasite power P_p is computed using Equation (5.12) [118]. It increases cubically with forward flight speed and is thus the main limiter in forward flight. f_{e0} is an initial estimate of the equivalent flat plate area and can be found in Table 5.1 and $V_{tot} = \sqrt{V^2 + ROC^2}$, where V is the forward velocity and ROC is the rate of climb.

Conversion Corridor
As a result, the total power required as well as the angle of attack to remain in equilibrium, can be obtained for a given forward flight speed. By evaluating this procedure for various altitudes in combination with the stall speed in airplane mode V_{stall}, a so-called 'conversion corridor' can be constructed. This corridor shows the range of speeds in which conversion can be performed without stalling the wing or overloading the rotor.

Axial climb and Descent
For a set climb rate ROC, the new induced power in climb can be computed in Equation (5.13). While climbing, the power induced per rotor increases with the climb rate ROC, as per Equation (5.13), while the profile power can be assumed constant [100]. The total power is then given by $P_{tot} = 2P_{i_c} + 2P_0$.

$$P_{i_c} = \frac{1}{2} \frac{W}{2} ROC + \frac{W}{4} \sqrt{ROC^2 + \frac{W}{\rho A}} \qquad (5.13) \qquad V_{i,c} = -V_{i,h} \left[\frac{ROD}{2V_{i,h}} - \sqrt{\left(\frac{ROD}{2V_{i,h}}\right)^2 - 1} \right] \qquad (5.14)$$

For axial descent, it gets more complicated. Here, the method to compute the induced velocity while descending is dependent on the ratio of ROD over $V_{i,h}$, the induced velocity in hover. If $\frac{ROD}{V_{i,h}} < -2$, momentum theory is valid and Equation (5.14) can be used to compute the resulting induced velocity. For less negative rates of descent, the vortex ring state is entered, and the induced velocity must be computed from experimental data, given by Equation (5.15). In both cases the required power can be computed from Equation (5.16).

$$V_{i,c} = V_{i,h} \left[\kappa - 1.125 \frac{ROD}{V_{i,h}} - 1.132 \left(\frac{ROD}{V_{i,h}}\right)^2 - 1.718 \left(\frac{ROD}{V_{i,h}}\right)^3 - 0.655 \left(\frac{ROD}{V_{i,h}}\right)^4 \right] \quad (5.15) \qquad P_{i_d} = P_{i_h} \frac{ROD + V_{i_c}}{V_{i_h}}$$
$$(5.16)$$

Stall in Helicopter Mode

Before continuing to the analysis of aircraft mode, different types of stall encountered in helicopter mode have to be identified, quantified and analyzed. The types of stall most likely to be encountered in this state are summarized below.

Rotor Airfoil Stall
As explained in Section 5.3.1, the value of thrust-weighted solidity C_T/σ can be related to the 2D-lift coefficient of a wing airfoil. The selected NACA 23012 airfoil has a $C_{l_{max}}$ of 1.5 in hover, and with a maximum C_T/σ of 0.151 at the operational ceiling, this stall is avoided.

Retreating Blade Stall
In forward flight, the helicopter tilts its shaft, thus increasing its angle of attack, in order to produce sufficient thrust in forward direction. When the aircraft flies forward in helicopter mode, its maximum tip speed is experienced by the advancing blade while the retreating blade experiences a minimum in tip speed.

Due to the assumed uniform inflow, the induced velocity is constant for each rotor blade element. On the retreating blade, the induced velocity is thus higher compared to the forward velocity, resulting in a higher angle of attack on the retreating blade compared to the advancing blade. At high enough Mach numbers ($M_{tip} > 0.8$ [118]), the outer portion of the retreating blade will stall, hence it is named retreating blade stall.

Drag Divergence
As the Mach number on the propeller tip increases, its drag increases as well. At tip Mach numbers approaching the speed of sound, the drag suddenly increases rapidly. This phenomenon is called drag divergence and should be avoided. To simplify the analysis, it is usually assumed negligible for a tip Mach number $M_{tip} < 0.8$ [118].

In helicopter mode, the rotor tip speed is given by Equation (5.17). Here, a is the speed of sound, γ is the specific heat ratio, R is the ideal gas constant of air and T is the air temperature.

$$M_{tip,h} = \frac{V_{tip,h}}{a} = \frac{\Omega_h R_b + V \cos \alpha_T}{\sqrt{\gamma R T}} \qquad (5.17)$$

The critical case occurs at the operation ceiling of 4000m at maximum forward flight speed. By substituting the values for Ω_h and R_b from Table 5.1, as well as $V = 28.7$m/s and $\alpha_T = 15.4°$, a maximum tip Mach number of 0.414 has been found. This is well below the cut-off for drag divergence and retreating blade stall thus its effects on the performance of HELIADES can be neglected.

5.3.2 Airplane Mode

The procedure used to calculate the power required and maneuver performance in airplane mode is described in Fig. 5.5, which is a zoomed-in part of the performance flow chart Fig. 5.1. The orange part is the maximum disk loading. The rotor disk loading used for the helicopter mode will have to be checked against this one. If it is higher than allowed, another iteration will have to be performed.

Determination of Inputs

The input parameters for the power required and performance optimization for airplane mode are given in Table 5.2. Again, some are taken from the Mid-term Report [67] and are still identical, and some parameters have been updated in the meantime.
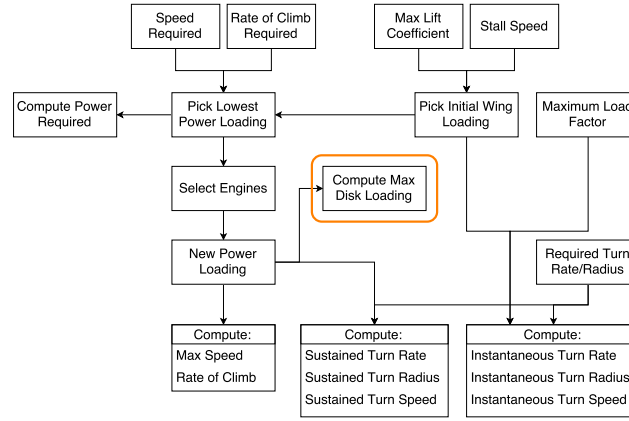
Figure 5.5: Flow diagram of the computations for airplane mode.

Wing Sizing

The wing loading, WL, was initially at 138N/m^2, based on the constraint plot in the Mid-term Report. Too reduce the wing surface area, and thus the weight of the wing, the wing loading was raised to 170N/m^2. This decreases the performance of the aircraft, but was necessary to comply with the weight requirement (**REQ-BUDG-01**).

Raising the aspect ratio AR would also benefit performance, but this was not desirable due to structural constraints, and thus it remained at 5. For a wing with no taper, the wing area, wingspan and chord have been calculated from these parameters.

Maximum Lift-to-Drag Ratio

The zero lift drag coefficient C_{D_0}, maximum lift coefficient $C_{L_{max}}$ and Oswald efficiency factor e have been updated in the aerodynamic analysis chapter (Chapter 7). The maximum lift-to-drag ratio LD_{max} can then be calculated according to Equation (5.18) [72]. In this equation, $K = \frac{1}{\pi ARe}$ is the induced drag constant. This ratio is thus independent of flight speed or altitude and has been tabulated in Table 5.2.

$$LD_{max} = \frac{1}{\sqrt{4C_{D_0}K}} \qquad (5.18) \qquad\qquad V_{stall} = \sqrt{\left(\frac{2}{\rho}\right)\left(\frac{1}{C_{L_{max}}}\right)WL} \qquad (5.19)$$

Stall Speed

The stall speed can be calculated using Equation (5.19) [72], at sea level conditions, $\rho = 1.225\text{kg/m}^3$ (ISA). With the updated values of $C_{L_{max}}$ and WL it is found to be 13.2m/s at SSL conditions. At the ceiling altitude of 4000m and ISA conditions, V_{stall}=16.1m/s

Rotor Tip Speed and Efficiency

The rotor tip speed has decreased slightly compared to hover mode, and is set at 2400RPM, since most aircraft propeller RPM are between 2050RPM and 2700RPM [40]. The propeller efficiency has been estimated at 0.9, which is on the high side for propeller airplanes (0.75 - 0.95) [72]. This is due to the variable speed control of HELIADES, enabling the aircraft to fly at an advance ratio close to one. This improves the efficiency of the propeller [40].

Power Loading

From the Mid-term report [67], the power loading, WP, has been computed both for required maximum speed $V_{max,r}$ (Equation (5.20)) [72] and rate of climb ROC_r (Equation (5.21)) [72], the latter of which uses a small angle approximation.

$$WP_{Vmax,r} = \frac{\eta_{pr}}{\frac{1}{2}\rho V_{max,r}^3 \frac{C_{D_0}}{WL} + \frac{2K}{\rho V_{max,r}}WL} \qquad (5.20) \qquad WP_{ROC,r} = \frac{\eta_{pr}}{ROC_r + V_{ROC,r}\frac{2\sqrt{3}}{3LD_{max}}} \qquad (5.21)$$

Filling in these two equations with the updated aerodynamic parameters leads to $WP_{Vmax,r}$ =0.126 and $WP_{ROC,r}$ =0.0968. This corresponds to a minimum required power of 1014W to satisfy the cruise and climb requirements in aircraft mode. After a motor selection, it became clear that the available power would be 2kW, resulting in a power loading WP=0.049, as seen in Table 5.2.

Calculation of Outputs

With the inputs specified in Table 5.2, the outputs can now be calculated and are listed in Table 5.3.

Maximum Disk Loading

From the engine selection, a new power loading results, which is first used to compute a minimum rotor radius

Table 5.2: Design inputs for the analysis of airplane mode.

Parameter	Symbol	Unit	Value
Wing Loading	WL	[N/m^2]	170
Power Loading	WP	[N/W]	0.049
Wing Area	S	[m^2]	0.577
Wing Aspect Ratio	AR	[-]	5
Wingspan	b	[m]	1.70
Wing Chord	c	[m]	0.340
Zero Lift Drag Coefficient	C_{D_0}	[-]	0.015
Max Lift Coefficient	$C_{L_{max}}$	[-]	1.60
Oswald efficiency factor	e	[-]	1.0
Induced drag constant	K	[-]	0.0636
Propeller Efficiency	η_{pr}	[-]	0.9
Rotor Angular Velocity Airplane	Ω_a	[rad/s]	251
Max Lift to Drag Ratio	LD_{max}	[-]	16.18
Stall Speed (SSL)	$V_{stall,0}$	[m/s]	13.2
Stall Speed (ceiling)	$V_{stall,c}$	[m/s]	16.1

$R_{b_{min}}$ by relating the amount of power able to absorbed by a propeller to its radius. For a 3-bladed rotor, this relation is given in Equation (5.23) [72]. This is then converted into a maximum value for disk loading DL_{max} (Equation (5.22)) which must be obeyed in helicopter mode. With an available power of 2kW, this results in a DL_{max} of 258N/m^2 and a minimum rotor radius $R_{b_{min}}$ of 0.246m. As shown in Table 5.1, HELIADES satisfies these requirements.

$$DL_{max} = \frac{W}{2\pi R_{b_{min}}^2} \quad (5.22) \qquad\qquad R_{b_{min}} = \frac{0.0254 \cdot 18 \frac{P}{2 \cdot 745.7}^{1/4}}{2} \quad (5.23)$$

Maximum Cruise Velocity

The new power loading from Table 5.2 is used to compute the maximum achievable speed V_{max} for a propeller aircraft (Equation (5.24), [72]). In this equation, V appears on both sides of the equation and must thus be solved numerically. This results in a maximum attainable velocity of 70.78 m/s at an altitude of 600m.

$$V = \sqrt{\frac{\frac{\eta_{pr} WL}{V \cdot WP} + WL \sqrt{\left(\frac{\eta_{pr}}{VWP}\right)^2 - 4C_{D_0} K}}{\rho C_{D_0}}} \quad (5.24)$$

New Climb Rate

In the Mid-term Report, the maximum rate of climb was solved by making use of the small-angle assumption. However, this assumption cannot be justified in this analysis. In the new equation (Equation (5.25) [72]), both V_{tot} and θ appear on each side of the equation and this requires solving for climb angle θ for a given airspeed. Note that the V_{tot} in this equation is the total airspeed, not the forward speed.

$$ROC = V_{tot} \sin\theta = V_{tot} \left[\frac{\eta_{pr}}{WP} - \frac{1}{2} \frac{C_{D_0} \rho V_{tot}^2}{WL} - WL \frac{K}{\frac{1}{2}\rho V_{tot}^2} \cos^2\theta \right] \quad (5.25)$$

Maximum Load Factor

The maximum load factor is constrained by the minimum WL (Equation (5.26) [72]), maximum WP (Equation (5.27) [72]) and the structural constraint n_{max}=20. The maximum achievable sustained load factor can be determined from Equation (5.27), while the maximum achievable instantaneous load factor is determined from the intersection of (Equation (5.26) and the structural constraint.

$$n_{max,WL} = \frac{1}{2}\rho V^2 \frac{C_{L_{max}}}{WL} \quad (5.26) \qquad\qquad n_{max,WP} = \frac{\frac{1}{2}\rho V^2 \frac{\eta}{V \cdot WP} - \frac{1}{2}\rho V^2 C_{D_0}}{K \cdot WL} \quad \frac{}{WL} \quad (5.27)$$

Turns and Pull-ups

The sustained and instantaneous turn characteristics (turn rate ω and turn radius R_{turn}) can now be computed and updated using the new values for wing and power loading and the found V_{turn}. Note that Equation (5.28) [72] assumes level turns. The pull-up is only relevant using the obtained instantaneous turn rate and can be calculated with Equation (5.29) [72]. The turn rate for both maneuvers can be related to the turn speed and turn radius by $\omega = \frac{V_{turn}}{R_{turn}}$. Note that both these radii approach the same value at large load factors.

$$R_{turn} = \frac{V_{turn}^2}{g\sqrt{n_{max}^2 - 1}} \qquad (5.28) \qquad\qquad R_{\textbf{pull-up}} = \frac{V_{turn}^2}{g(n_{max} - 1)} \qquad (5.29)$$

Aircraft Stall

Like in helicopter mode, stall must also be taken account in aircraft mode. In airplane mode, wing stall and drag divergence of the propeller must be taken into account.

Wing Stall

Wing stall occurs when the maximum angle of attack is exceeded and the aircraft starts to lose lift. The minimum speed that the aircraft is able to fly depends on altitude, wing loading and its maximum 3D lift coefficient. It can be calculated with Equation (5.19).

Drag Divergence

The rotor tip speed in aircraft mode differs slightly from that in helicopter mode and is given in Equation (5.30) since the propellers are now tilted horizontally. The maximum tip Mach number in aircraft mode can be found by substituting Ω_a, R_b and the maximum cruise velocity calculated from Equation (5.24) at an altitude of 4000m. This results in a maximum tip Mach number in aircraft mode of $M_{tip,max,a}$=0.359 at the operational ceiling.

$$V_{tip,a} = \sqrt{\Omega_a R_b^2 + V_\infty^2} \qquad (5.30)$$

To conclude, the found tip Mach numbers are well below the cut-off for drag divergence in both helicopter and aircraft and its effects on the performance of HELIADES can thus be neglected.

Results

The results of the optimization in terms of performance are summarized in Table 5.3. Also, various figures are supplied that show results of the performance analysis as well as the results of the computation of power required.

Fig. 5.6 displays the variation of rotor tilt angle with airspeed. The power required in helicopter mode for various forward speeds has also been calculated at an altitude of 50m. The results are plotted in Fig. 5.7. When compared to the 'ideal' case, where $\alpha_T = 0$, the increase in angle of attack leads to an increase in induced drag at higher forward velocities.
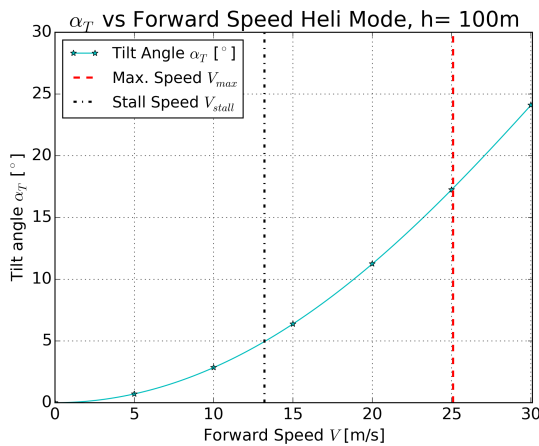
Figure 5.6: Tilt angle in forward flight in helicopter mode, computed at an altitude of 50 meter.
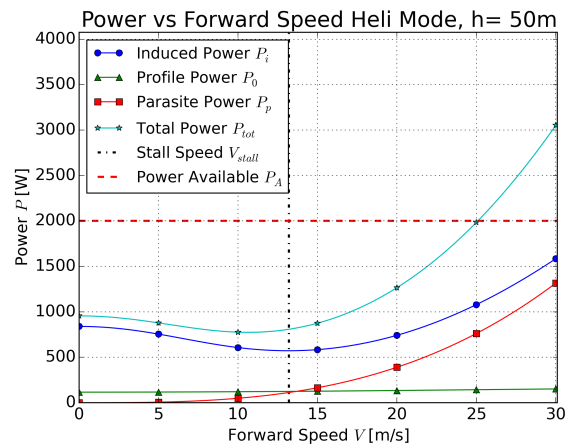
Figure 5.7: Power required in helicopter mode as a function of forward speed. All parameters have been calculated at an altitude of 50 meter.

From these plots, the maximum forward speed in helicopter mode is determined as $V_{max,h} = 25.1$m/s, resulting in an α_T of 17.4 °. When in axial climb, all of the available power can be used, leading to maximum axial climb

Table 5.3: Optimization results for helicopter and airplane mode.

Parameter	Symbol	Unit	Value	Altitude
Helicopter				
Max Rate of Climb (Take-off)	$ROC_{max,h}$	[m/s]	13.9	SSL
Max Forward Speed	$V_{max,h}$	[m/s]	25.1	50m
Forward Speed for Min Power	$V_{Pmin,h}$	[m/s]	10.6	50m
Max Tip Mach Number	$M_{tip,max,h}$	[-]	0.414	4000m
Normalized Thrust Coefficient	C_T/σ	[-]	0.153	4000m
Conversion				
Conversion Speed	V_{conv}	[m/s]	15.2	50m
Airplane				
Max Forward Speed	$V_{max,a}$	[m/s]	70.8	600m
Stall Speed	V_{stall}	[m/s]	13.6	600m
Max Rate of Climb	$ROC_{max,a}$	[m/s]	41.3	600m
Max Tip Mach Number	$M_{tip,max,a}$	[-]	0.359	4000m
Turn Rate, Sustained	ω_{sus}	[rad/s]	2.38	600m
Turn Rate, Instantaneous	ω_{ins}	[rad/s]	3.23	600m
Turn Radius, Sustained	R_{sus}	[m]	18.82	600m
Turn Radius, Instantaneous	R_{ins}	[m]	18.76	600m
Turn Speed, Sustained	$V_{turn,sus}$	[m/s]	44.81	600m
Turn Speed, Instantaneous	V_{corner}	[m/s]	60.63	600m

rate in helicopter mode $ROC_{max,h}$ of 13.9m/s. The minimum power required is $P_{min,h}$=774.4W, at an airspeed $V_{Pmin,h}$=10.6m/s.

For airplane mode, the power required can also be computed as a function of forward speed. This is shown in Fig. 5.8. In combination with a power available P_a =2000W, which is determined in Section 5.5.2, this leads to a maximum forward speed in airplane mode $V_{max,a}$ =70.78m/s at a cruise altitude of 600m. Note that the minimum speed in airplane mode is the stall speed, $V_{stall,cruise}$ =13.6m/s at cruise altitude (600m).

The rate of climb in airplane mode as a function of forward speed at an altitude of 600m has been plotted and is shown in Fig. 5.8. Note that at low speed there is a straight line in the plot, hence the maximum climb rate is straight up (90°). This is possible due to the excess power (500W) in the engines combined with the low C_{D_0}. Similarly, the rate of climb vs. the total speed has been plotted in Fig. 5.9.

In Fig. 5.10 the maximum load factor for several limiting cases is plotted. The maximum structural load factor $n_{max,struct}$ = 20 results from **REQ-PERF-23**. Furthermore, the maximum load factor is computed for limiting wing and power loadings.

The load factors and speeds at the intersection points in Fig. 5.10 can be substituted into Equation (5.28) to get the instantaneous and sustained turn characteristics, where $\omega = \frac{V_{turn}}{R_{turn}}$.

The conversion corridor in Fig. 5.11 shows the range of speeds for a certain altitude in which transition from helicopter to airplane mode or transition from airplane to helicopter mode can take place, based on airplane mode stall speed and maximum forward velocity in helicopter mode. The actual conversion speed is set equal to the stall speed + 2m/s. For the conversion altitude of 50m, this will be V_{conv} = 15.2m/s.

Critical Cases

Table 5.4 displays the critical cases from the performance analysis, which will be used in the aerodynamic and structural analysis.
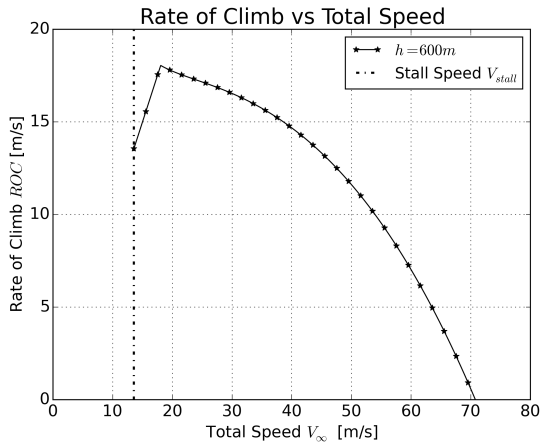
Figure 5.8: Rate of climb in airplane mode as a function of forward speed at an altitude of 600m.
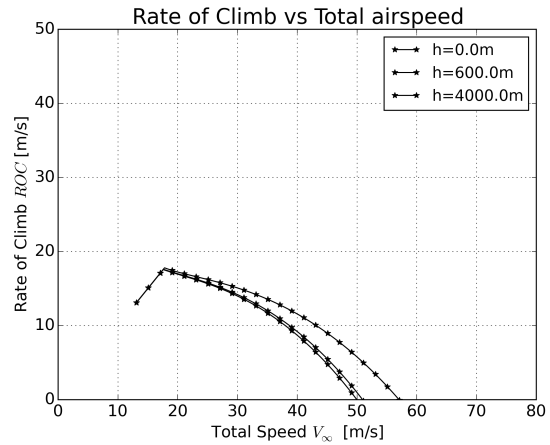

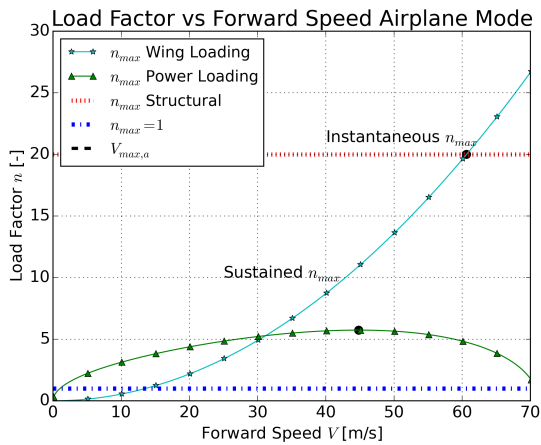Figure 5.9: Rate of climb in airplane mode as a function of airspeed at an altitude of 600m.

Figure 5.10: Maximum load factor n_{max} for wing loading, power loading and structural limiting cases. The load factors, as well as the maximum speed $V_{max,a}$, are calculated at 600m altitude.
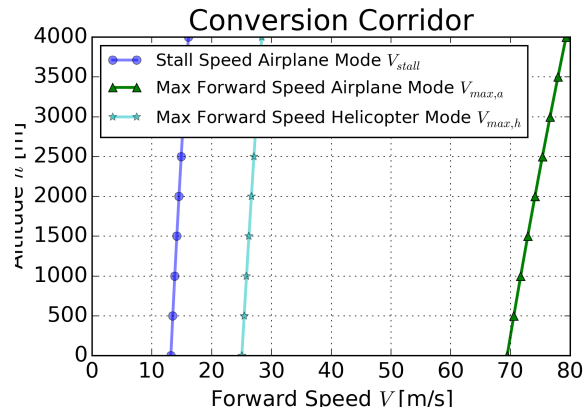

Figure 5.11: The conversion corridor for conversion from helicopter to airplane mode and vice versa for a range of altitudes.

Table 5.4: Critical Cases for the Aerodynamic and Structural Analyses

Mode	Helicopter	Helicopter	Aircraft	Aircraft	Aircraft
Segment	Hover	Tilted	Turn	Cruise	Max. Speed
T [N]	49.05	51.394	22.32	6.62	14.12
α_T [deg]	0	17.36	90	90	90
V_i [m/s]	7.44	2.145	1.17	0.314	0.474
V_∞ [m/s]	0	25.09	44.81	50.0	70.78

Mission Segment Analysis

The battery weight can be determined when the total battery energy for each mission profile is known. The energy of each segment can be calculated by multiplying the required power per mission segment with the time required to complete it. The total capacity of off-the shelf batteries is given in milliampere-hour (mAh).

$$EmAh = \frac{3600}{1000} \frac{E_J}{V_{batt}} \tag{5.31}$$

By using the theory explained in Section 5.3.1 and Section 5.3.2, the energy required for each mission segment defined in Section 5.1 can be calculated. For every segment, the acceleration to steady flight is assumed to occur instantaneously. The result per mission segment is shown in Table 5.5.

Take-Off: the take-off is done at a rate of climb of 8 m/s. Substituting for *ROC* in Equation (5.13) and integrating over a height of 0 to 50 meters, the average power required is 1435W. The time to climb is then 6.3s, resulting in a required energy of 641.2mAh.

Transition and Conversion in Steady Flight: conversion from helicopter to aircraft mode, as well as conversion from aircraft to helicopter mode, is only possible within the conversion corridor in Fig. 5.11. The conversion is done in level flight, since a forward climb in helicopter mode is not power efficient. The conversion speed is taken 2m/s above the stall speed of the wing (Equation (5.19)) as a safety margin against minor disturbances.

At an altitude of 50m, the stall speed is 13.2m/s and the conversion speed is thus 15.2m/s. Substituting this into Equation (5.10) to Equation (5.12) leads to a required power of 885W. The total time to tilt the rotor has been determined in Section 5.5 and is two seconds. The total energy expended is then 126.5mAh

Climb at Maximum Power: Climbing at a rate of 8 m/s up to 600m altitude for a horizontal distance of 1469.6 meter, results in an airspeed of 22.8m/s at an angle of 20.5°. The average power required during this climb is 1076W and the time required to climb is 68.8s. This results in a total battery energy of 5285.0mAh.

Intercept Target: the interception of the target drone is done at 50.0m/s for a distance of 250 meters, at an altitude of 600m. By solving Equation (5.24), the power required has been computed as 735.7W. The time to cover this distance is then 5.0s, resulting in a required battery capacity of 262.7mAh.

Combat: the calculation of the combat segment per mission is simply multiplying the required power and assumed time. The given mission profile assumes a combat phase at full power (2kW) that lasts 20 seconds. The combat phase then requires 2857.1 mAh of energy and the maximum attainable airspeed is 70.8m/s. An instantaneous 20g turn can be performed at an airspeed of 60.6m/s.

Descent: the descent is assumed a steady powerless glide back to the base. The horizontal and vertical distance covered during the glide is equal to that during the intercept and climb, being 1719.6 and 550 meter, respectively. This results in a rate of descent of -4.7m/s at an airspeed is 15.6m/s for a C_L of 0.00479.

Landing: the landing occurs in helicopter mode after transitioning from aircraft mode. The rate of descent during landing is 5 m/s, requiring an average of 972.24W of power. At this descent rate, HELIADES is operating in the vortex ring state. The required energy is then 696mAh.

Table 5.5: Energy required for each mission segment

Segment	h [m]	dx[m]	Vinf [m/s]	U [m/s]	RoC [m/s]	Pavg [W]	t [s]	E [mAh]
Take-off	**0-50**	0	8	0	**8.0**	1434.46	6.3	641.2
Conversion	50	30.4	**15.2**	15.2	0	884.97	**2.0**	126.45
Climb	**50-600**	1469.6	22.8	21.4	**8.0**	1076.02	68.8	5285.0
Intercept	600	**250.0**	**50.0**	50	0	735.68	5.0	262.7
Combat	600	-	62.9	-	-	**2000.00**	**20.0**	2857.1
Descent	**600-50**	1719.6	15.6	14.8	-4.7	0	116.0	0
Transition	50	30.4	**15.2**	15.2	0	884.97	**2.0**	126.45
Landing	**50-0**	0	5.0	0	**-5.0**	972.24	10.0	695.85
Subtotal	-	-	-	-	-	590.3	-	9701.6
Total	-	3500	-	-	-	663.2	240	10899.3

Battery Selection

Since the nominal voltage of the motors is 50.4V (see Section 5.5.2), a '12S' class battery is necessary. This can be accomplished by installing one 12S class battery or by installing 2 6S batteries in series.

From Table 5.5 it can be concluded that the required battery capacity shall be at least 10900mAh, thus a 12000mAh battery is required. Since most high-capacity batteries from hobby stores have a capacity of either 10000mAh or 16000mAh, not many different options were available. The chosen battery configuration consists of three Lumenier 12000mAh 4S battery packs. Their combined weight and cost is 2820g and $419.97, respectively. Its dimensions are 3x (182 mm x 74 mm x 32 mm).

5.4 Verification & Validation

To conclude the performance analysis, the applied theory must be verified and validated. Verification can be split up into two parts, namely code verification and calculation verification. Code verification involves getting rid of programming bugs while calculation verification ensures the formulas are correctly implemented. Finally, validation ensures that the theoretical solutions are applicable to the real-life problem.

Verification

Code Verification

The syntax errors in the code are noted by the compiler and thus do not require much effort to discover. Next, the code must be verified by adding 'print' statements throughout each file to ensure that the methods have been implemented correctly and display the correct results. In this way, mistakes such as missing pairs of brackets are quickly noticed since the outputs deviate by orders of magnitude from the expected values.

Calculation Verification

Calculation verification verifies each module by performing calculations by hand for each of the following modules in the program.

Stall
The equations used to account for stall are Equation (5.17) and Equation (5.30) for the drag divergence and Equation (5.3). The wing stall speed has been calculated using Equation (5.19). The calculation verification consisted simply of calculating the values by hand and comparing these with the numerical model.

Helicopter Mode: Forward Flight Power
The equations used to calculate forward flight power are Equation (5.8), Equation (5.10), Equation (5.11) and Equation (5.12). The latter equations can be solved for a given flight speed, while the former three had to be solved simultaneously.

Helicopter Mode: Axial Flight Power
The equations used to calculate axial flight power are the same as for forward flight, with the forward velocity component set to zero. This simplified the verification, since no iterative processes were required. The increase in axial climb speed was accounted for by Equation (5.13). The found values could then quickly verified by hand.

Aircraft Mode: Maximum Velocity
The maximum cruise velocity has been calculated in Equation (5.24). The iterative solver in the numerical model could be verified by manually inserting the found maximum airspeed for various values of power loading and then comparing the values on the left- and right-hand side of the equation.

Aircraft Mode: Rate of Climb
With the amount of excess power that is able to be supplied to HELIADES, the small-angle approximation assumed in the theory had to be discarded. This turned the procedure of the rate of climb into an iterative process, instead of an analytical one.

Like the trim procedure, this iterative process was verified by putting the found values for V_∞ and γ on both the left- and right-hand side of equation Equation (5.25) and checking whether these values matched.

Aircraft Mode: Maneuvering
The maneuvering performance consisted of the maximum turn rate and minimum turn radius in level turns and pull-ups. These equations were straightforward to solve, and could be verified by estimating the plot intersections in Fig. 5.10 and then calculating the resulting turn rate and turn radius manually.

Apart from the unit tests, the inputs of each technical analysis have to be verified and updated with respect to each other, in order to avoid conflicting inputs and thus inconsistent and invalid results.

Validation

Validation of Theory

With a verified numerical model, it must now be validated. The theory used in helicopter mode has been derived from the equations of motion and momentum methods applicable to a conventional helicopter, consisting of a main rotor and a tail rotor. These had to be altered in order to be valid for a side-by-side configuration like a tiltrotor. A consequence is that the weight carried, and thus thrust produced, by the rotor had to be divided by two. Care had to be taken to be consistent in this approach.

Additionally, the equation for ceiling sizing had to be altered. Normally these equations take into account the decrease in available engine power at higher altitudes, but this could be ignored for the case of electric motors. This also resulted in different power available-altitude curves than for fuel consuming aircraft.

The theory used during the performance analysis is mainly from textbooks, lecture slides, as well as the theory of the NASA NDARC program [129]. Prouty [132] and Leishman [118] were the main sources for the helicopter analysis, with Filippone [100] for the rotor disk angle trim procedure. For analysis of airplane mode, Anderson [72] and Filippone [100] were used and their results were compared to validate their theory.

To ensure the validity of the results, it was necessary to keep track of all the assumptions made by the authors of the theory. These have been stated in Section 5.2.

Validation of Numerical Model

Now that the theory is validated, it has to be determined whether the theory applied in the numerical mode is valid for this particular real-life problem. The only way to do this is to construct a prototype and perform a flight test. The results of this test, such as the achievable rate of climb per altitude and velocity, can then be measured and compared with the predictions of the numerical model and the numerical model can be validated or tweaked accordingly. Additionally, this would also give insight into the validity and practical impact of each assumption stated earlier. Performing such a test, however, is beyond the scope of this report.

5.5 Propulsive System Design

In this section, the design of the HELIADES propulsive system is described. First, Section 5.5.1 deals with the design of the rotor. Next, Section 5.5.2 describes the rationale of engine choice and determining its best operating point. As the best operating point for the motor and Rotor are different, a gearbox is necessary. Its design is detailed in Section 5.5.3. Finally, in Section 5.5.4, the design of the rotor tilting gearbox is detailed.

5.5.1 Rotor

Blade Flap and Damping

Blade flapping is an up and down motion of the blade, which combined with cyclic feathering helps to mitigate asymmetry of lift. As the advancing blade's relative velocity increases due to the addition of the flight velocity vector, it will produce more lift, and flaps upwards. The upwards velocity from the flap reduces the induced angle of attack and decreases the lift. In HELIADES' rotor, flapping is achieved by a hinge located at the base of the spindle. Damping is provided by simple elastomer dampers, whose stiffness may be tuned to increase or decrease the damping ratio. This is shown in Fig. 5.12, a semi-section view, with the elastomer dampers in blue. Additionally, the stack of thrust and radial bearings is shown. Thrust bearings are placed at the distal and proximal end of the stack so as to resist thrust forces in the rotor plane, due to centripetal force and preload, while the radial bearings resist forces normal to the rotor plane, such as lift and out of plane forces such as drag.

Swashplate-Rotorhead Phasing

The blade grips are actuated via links terminated in rod end bearings. These semi-rigid linkages are necessary to provide the level of articulation necessary for cyclic and collective control, however, they may twist with the upper swash about the main shaft due to inertial effects. This leads to out-of phase cyclic responses. In order to prevent this, an articulated 2DOF (degree of freedom) rigid driving link-the scissor link is used. This linkage couples the rotorhead and upper swash plate, maintaining the phase relationship, but folding with collective/cyclic inputs, as shown in Fig. 5.13.

Whirl-Mode stability and Delta-3

The Delta-3 angle, δ_3, refers to the kinematic coupling between the rotor blade's flapping motion and changes in its pitch, due to a difference in position between the blades flapping hinge axis and the control horn effector. A positive value results in a nose down pitching moment upon an upwards blade flapping. From literature, a negative δ_3 confers stabilisation for the flap-lag coupling, however too much is detrimental to the cyclic response [122] [102]. Further, δ_3 is constrained by the physical geometry of the rotor. Indeed the XV-15 has a nominal δ_3 of $-15°$ [8].

With these needs for reasonable damping ratios in fast forward flight, as well as fast cyclic response, a nominal δ_3 of $-11.88°$ at $0°$ collective was achieved. This is shown in Fig. 5.14.
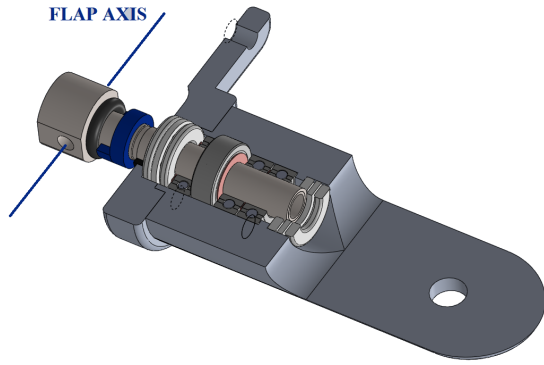
5.5.2 Motor Sizing

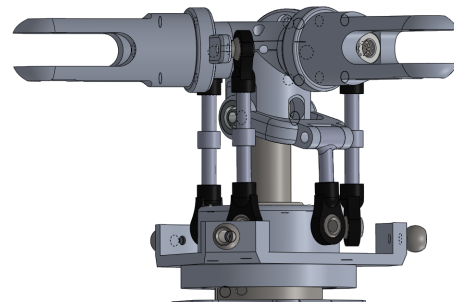Figure 5.12: HELIADES' spindle and blade grip, showing spindle, dampers and bearings.

Figure 5.13: An isometric view of HELIADES' rotor head and swash, showing the scissor link.
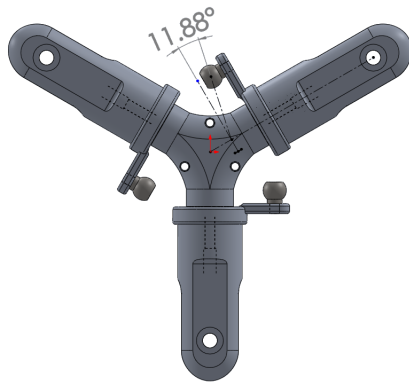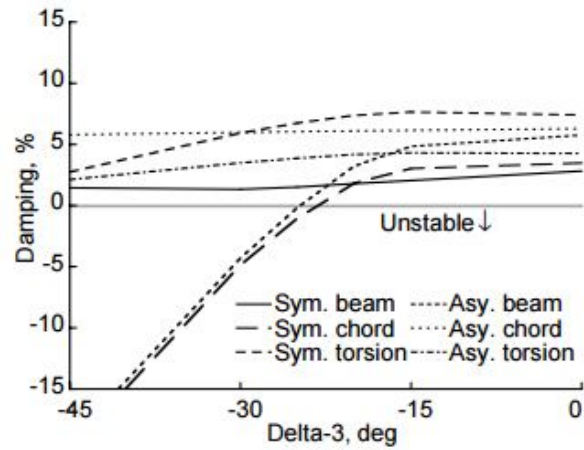

Figure 5.14: HELIADES rotor, $\delta_3 = -11.88°$.

Fig. 4. Variation of damping with δ_3 for the XV-15 and unmodified rotor at 300 knots.

Figure 5.15: Damping vs δ_3 for XV-15 at 300kts [8].

Power Required

One of the key results from the performance analysis is the power required for various flight conditions. It was found that for intercept speed, a power of 3kW was necessary, or 1.5kW per engine. A survey of the highest efficiency brushless motors was carried out. Two 2kW motors were found, each having a mass of 220g, however for an increase of 70g, 3kW motors could be used. Theoretically this would allow the mission to be performed with one engine out, while increasing the maximum power to weight ratio would be beneficial from a general performance standpoint, costing only 0.7%. Hence the higher powered motors were chosen. The specification of the motor, as obtained from the manufacturer [114], are shown in Table 5.6.

Table 5.6: General motor specifications.

Motor	Mass [g]	K_v [RPM/V]	Max RPM [RPM]	Continuous Power [W]	Efficiency [%]	Price [$]
Kontronik Pyro 640-62-L	290	620	30,000	3,000	90	355.90

Operating Point

The efficiency of the brushless motor varies with its angular velocity, it is therefore desirable to operate the motor at or around this point. Using a standard 3 parameter motor model, shown in Fig. 5.16, equations relating the performance of the motor may be derived, namely motor torque, angular velocity, shaft power and efficiency. The

3 constant parameters in the model are the specific RPM K_v, no load current i_0, and the winding resistance R_m. For the chosen motor, these are 620RPM/V, 1.9A, and 57mΩ.
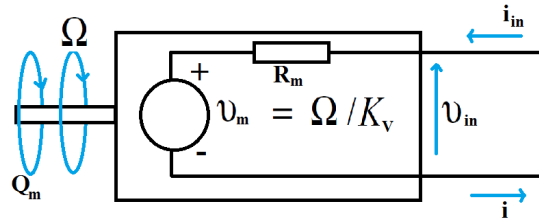
Figure 5.16: 3 Parameter electric motor model for a brushless motor.

From this model, equations giving the motor torque, Q_m, angular velocity, Ω_m, shaft power, P_{shaft} and efficiency η_m may be written as in Equation (5.32) - (5.35).

$$Q_m = \frac{i_{in} - i_0}{K_v} \qquad (5.32)$$

$$\Omega_m = (v_{in} - i_0 R_m) K_v \qquad (5.33)$$

$$P_{shaft} = Q_m \Omega_m \qquad (5.34)$$

$$\eta_m = \frac{P_{shaft}}{v_{in} i_{in}} \qquad (5.35)$$

The first step is to determine the operating voltage of the motor for best efficiency. This is achieved by plotting Equation (5.35) for a range of voltages between the minimum and maximum manufacturer rated voltages. As lithium polymer cells are used, the voltage increment is the voltage of a single cell, namely 4.2V. The chosen voltages therefore are 42V, or 10S, 46.2V or 11S, and 50.4V or 12S.

From Fig. 5.17, it can be seen that a higher voltage yields a higher peak efficiency of 89% at a lower current of 47A, this is because power losses scale with the square of the current. From Fig. 5.18, The peak efficiency occurs at 29550RPM, 450RPM below the maximum. These results were then verified against results from the software DriveCalc [15], which contains databases of experimentally measured data. It was found that the peak efficiency was 87%, achieved at 28798RPM at 48A. This is shown in Fig. 5.19.
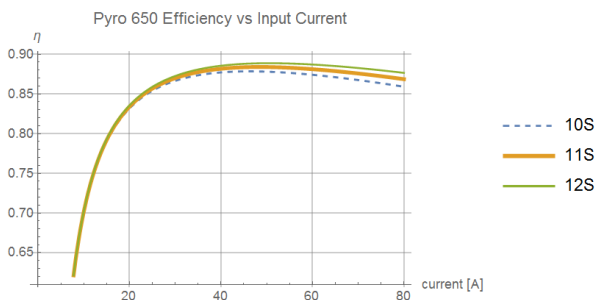
Figure 5.17: Efficiency versus input current for the Pyro 650.
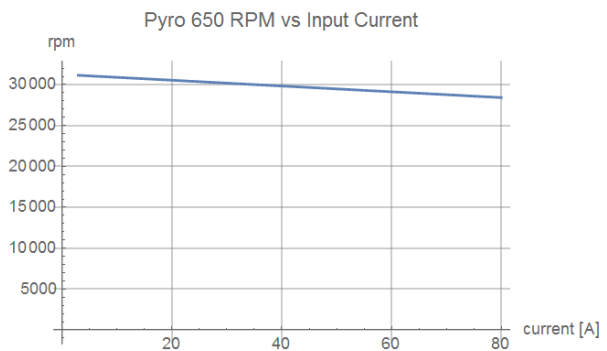
Figure 5.18: Motor RPM versus input current for the Pyro 650.

As the results of both methods are in good agreement, the design point is to run the motor at 12S, and 29000RPM. This places the operating point near the flat of the efficiency curve, and so excursion from this point will not result in significant decreases in efficiency.

In conclusion, two 3kW motors were chosen, giving a total installed power available of 6kW. These motors should have their rotation opposite to each other, such that the motor on the Left nacelle rotates anticlockwise, while the one on the right nacelle rotates clockwise. This has the beneficial effect of canceling the resulting torques, as well as reducing the wingtip vortices.
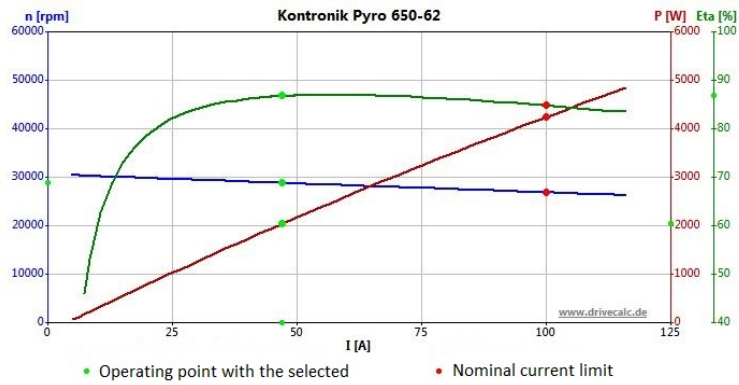
Figure 5.19: Kontronik Pyro 650 performance data from DriveCalc.

5.5.3 Main Gearbox

From the previous performance calculations in Table 5.1, the maximum operating RPM of the main rotor was found to be 3000RPM. It is clear that there is a mismatch between the motor and rotor speeds, hence from the need to operate both within the regions at which they are most efficient, a gearbox must be used.

Reduction Ratio and Gearbox Tradeoff

First the reduction ratio, R, is calculated in Equation (5.36).

$$R = \frac{rpm_{motor}}{rpm_{rotor}} = 10 \tag{5.36}$$

Hence a 10:1 reduction is necessary. There are many ways to achieve this, the most common being either an epicyclic planetary gearbox, or a parallel shaft spur gear box. For the latter, although it is simpler to manufacture, a single tooth of each gear must bear to the total torque, which would necessitate larger gears with a commensurate increase in weight, whereas in a planetary gearbox, the torque is shared among the planet gears. A simple trade-off (Table 5.7) is performed in order to make the appropriate choice.

Table 5.7: Qualitative comparison of epicyclic planetary gearboxes and plain parallel shaft spur gear gearboxes.

Property	Planetary Gearbox	Parallel Shaft Spur Gearbox
Load Capacity	Higher	Lower
Operating Speed	Higher	Lower
Backlash	Lower	Higher
Efficiency	Higher	Lower
Noise	Higher	Lower
Volumetric Efficiency	Higher	Lower
Cost	Higher	Lower
Verdict	Positive	Negative

From the trade-off, an epicyclic planetary gearbox is selected. Although a reduction ratio of 10:1 is the largest practical reduction in a single planetary stage, this would require a very small pinion given the maximum envelope of the nacelle. Hence two cascaded 3:1 stages are used for a total reduction of 9:1. This does not result in a significant shift in the motor operating point from an efficiency standpoint.

Further, the overall power efficiency of epicyclic gearboxes has been estimated to be 99.055% [3].

Planetary Gearbox Design

In order to produce a reduction with a planetary gearbox, the ring is held fixed, with the sun as the input gear and the planet carrier as the output. With this in mind, it is possible to derive equations relating the pitch circle diameters of the sun and ring gears to the reduction ratio, as shown in Equation (5.37).

$$R = 1 + \frac{\varnothing_{PCD,ring}}{\varnothing_{PCD,sun}} \tag{5.37}$$

A pitch circle diameter of $\varnothing_{PCD,ring}$ = 40mm is chosen for the ring gear so as to fit within the nacelle envelope, as this diameter drives the gearbox size. This results in a sun gear with a pitch circle diameter of $\varnothing_{PCD,sun}$ = 20mm. It follows from geometry that each planet gear will have a pitch circle diameter of $\varnothing_{PCD,planet}$ = 10mm. The mating pitch circle geometries are shown in Fig. 5.20.

Subsequently, the *module* of the gears is chosen. This quantity is the ratio between the pitch circle diameter and the number of teeth. With a selected module of 1M, the number of teeth of the ring and sun gears respectively is 40 and 20, and the planet gears will hence have 10. The design of the gearbox is shown in Fig. 5.21, and the properties of the gearbox and its components are summarized in Table 5.8.
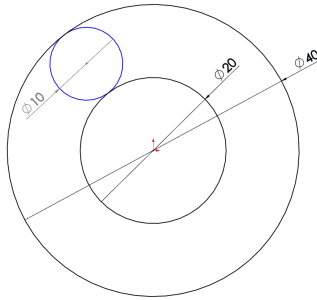
Figure 5.20: Pitch circle diameter geometry.
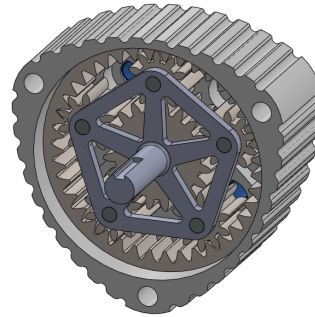
Figure 5.21: Isometric view of the gearbox.

Table 5.8: Properties of a main gearbox single stage (2 stages per gearbox).

Property	Value		Property	Value
Reduction Ratio	3:1		# Planets	5
$\varnothing_{PCD,ring}$	40mm		Gear Material	4140
$\varnothing_{PCD,sun}$	20mm		Shaft Material	303
$\varnothing_{PCD,planet}$	10mm		Housing Material	Delrin®
Module	1M		Mass	36g
T_{ring}	40T		Depth	25mm
T_{sun}	20T		Height	55mm
T_{planet}	10T		Width	55mm

5.5.4 Tilt Gearbox

Unlike most extant tiltrotor aircraft, HELIADES does not rotate the entire nacelle, but the forward portion ahead of the engine, thus preventing the exhaust from the motor and ESC cooling air from being blown directly on the ground.

Reduction Ratio and Gearbox Trade-Off

The purpose of the tilt gearbox is not to provide reduction or overdrive, but to facilitate the transfer of the shaft power from the main gearbox to the rotor, as the nacelle angles change. As such, the ratio is 1:1.

With regards to the function of transmitting the rotation, there are several methods available, for example, coiled springs, universal joints and constant velocity joints all allow torque to be transmitted through some angle. Unfortunately, these mechanisms do not possess the articulation necessary for the HELIADES' nacelles, thus an alternative has been designed.

In common practice, bevel gears are used to transfer rotational motion through an angle, and for three gears meshed together, with the central one fixed, the outer two may be moved relatively to the middle one. This forms the basis for the tilt gearbox. First the rotation of the motor is transmitted through 90°by a bevel gear pair. A spur gear locked coaxially with the take off bevel gear transmits the motion through a train of two more spur gears, the last member of which is coaxially locked to another bevel gear. Finally, this bevel gear mates to the rotor shaft, transmitting the motion back through 90°. The functioning of the tilt gearbox is shown in Fig. 5.22 and Fig. 5.23.

As designed the tilt gearbox allows for mast angles of 90°to -10°. The tilting mechanism is actuated by two linear actuators, the model chosen is the Firgelli L12-R.

From experience, the mechanical losses of the tilting gearbox are estimated to be less than 1%, similar to the planetary gearbox in the nacelles.
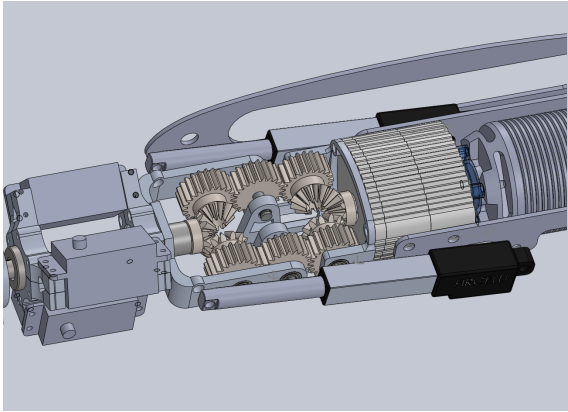
Figure 5.22: Gearbox Tilted to 0°.   Figure 5.23: Gearbox tilted to 45°.
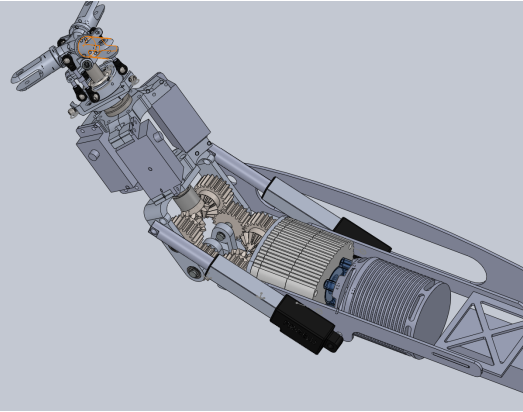
5.6 Heat

The issue of global warming demands for sustainable designs that limit heat and gas emissions. As HELIADES' propulsive energy is electrical energy, heat is a critical concern. According to Burmeister [82] heat is defined as 'energy flowing across a boundary as a result of a temperature difference across that boundary'. In this chapter, different major heat sources are identified and possible cooling options are stated.

5.6.1 Heat Sources

Keeping the conservation of energy in mind, all energy which is not converted to work will be converted to heat. This means that efficiency losses for propulsion will directly be converted into heat. Moreover, computing power requires power as well, where the internal resistance of the component will produce heat as well. These two sources are considered as the most important sources creating thermal energy, or heat. Other heat sources, such as skin friction of the fuselage, rotors and wing is neglected as their influence is assumed to be negligible.

5.6.2 Cooling

To prevent damage to materials due to heating, cooling is necessary. If HELIADES is in airplane mode, this can be easily achieved by convection. High and low pressure points can be chosen to be the starting and ending stage of the flow respectively, flow via the battery, sensors or processor to absorb thermal heat. This can even lead to a small amount of thrust as air is slightly expanded due to the heat, but this is assumed to be negligible. The cooling for the engines is taken care of by small fans which are added to the shafts of HELIADES. These fans have to provide relatively more cooling during helicopter mode, as the forward velocity is zero.

To determine the amount of drained heat, Newton's Law of Cooling [82] could be used, see Equation (5.38). h is the heat transfer coefficient and T_f and T_w are the object surface temperature and flow temperature respectively. If the surface area of the component is known, a relationship between the battery surface temperature and inlet area can be estimated.

To find this relationship, Equation (7.2), Equation (5.38), Equation (5.40) and Equation (5.39) should be used to determine the inlet area [5]. The inputs used for this estimation are listed in Table 5.9.

Though, some assumptions had to be made for this analysis. First of all, the average (forward) mission velocity is used, which is derived from Section 5.1. For the combat speed, the stall speed is used. Mission 3 is the mission with
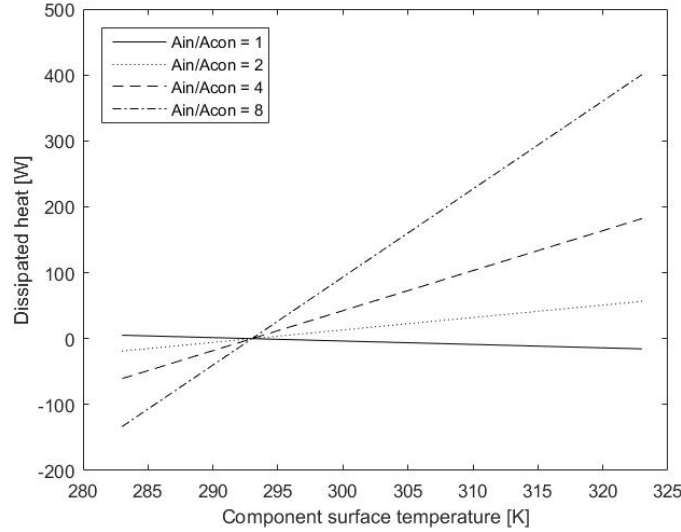
Figure 5.24: Dissipated heat at different for battery surface area at different area ratios, computed using Equation (5.38), Equation (5.39), Equation (5.40) and the inputs from Table 5.9.

the lowest average speed of 24m/s. Furthermore, a turbulent airflow is assumed over the components surface area. Lastly, air properties are all taken at 293K, but will differ as the flow temperature changes.

Table 5.9: Inputs for the heat equations.

Variable	Symbol	Value	Unit	Comment
Heat transfer coefficient	h	-	[W/(m^{2}K)]	Derived from Equation (5.40)
Convection area	A_c	-	[m^2]	Component dependent
Surface temperature	T_w	-	[K]	Variable value
Flow temperature	T_f	293	[K]	Assumed constant value
Density	ρ	1.225	[kg/m^3]	Assumed constant, ISA
Air velocity	V	-	[m/s]	Average mission velocity
Convection distance at surface	x		[m]	Length of component
Dynamic viscosity	μ	1.82E-5	[kg/(m s)]	Taken at 293 K [50]
Prandtl number	Pr	0.713	[-]	Taken at 293 K [49]
Thermal conductivity	k	0.0257	[W/(m K)]	Taken at 293 K [49]

$$\dot{Q} = h A_c (T_w - T_f) \qquad (5.38)$$

$$\rho V A = \text{constant} \qquad (5.39)$$

$$\text{Nu} = \frac{0.3387 \cdot \text{Re}^{1/2} \text{Pr}^{1/3}}{\left[1 + (\frac{0.0468}{\text{Pr}}^{2/3})\right]^{1/4}} = \frac{h \cdot x}{k} \qquad (5.40)$$

Results for the battery convection are shown in Fig. 5.24, where the area is twice the battery area as two batteries are placed next to each other, and convection is assumed to take place at both sides. For different ratios of inlet area over convection area (A_{in}/A_{con}), the dissipated heat is shown.

If one takes a closer look at Fig. 5.24, the influence of the assumption of the turbulent flow is probably visible for the case where the area ratio is 1. Here, the flow is partly laminar over the component surface, leading to an inaccurate result, as negative heat is produced by the convection, meaning that the battery is heated by the colder air.

The same method describe above can also be applied for other components, for example the ESC. Furthermore, if more cooling has to be acquired, a conductive metal could be used to increase the convective surface area, rather than increasing the inlet over convection area.

During the post-DSE phase, experiment tests should be done to determine the component temperature. From this, the inlet areas can be adjusted according the aforementioned method.

The program is verified by looking at different input variables and their behavior. As can be seen in Fig. 5.24, zero heat is dissipated if the battery and outside temperature have the same value, which was expected. Lastly, unit tests are performed to verify equations.

Other methods such as water cooling are practically not possible, or at least not incorporated in the aerial vehicle, due to the significant increment of weight. A water cooling element might be possible on the ground station for quick cooling.

6. Stability & Control Analysis

The goal of this chapter is to describe the tail sizing process, control surface design, the resulting maneuverability and stability of HELIADES and control algorithms used for interception and removal. Section 6.1 Describes the steps from preliminary design to determining the PID control specifications. Section 6.2 shows all assumptions which are used in this chapter. The design of the components which influence the stability and control of the ADD and the calculation of stability and control derivatives is discussed in Section 6.3 and Section 6.4, the latter resulting in an update of the first. Section 6.7 describes the research and analysis done for the command center of the autopilot, a description of which is given in Section 6.1. Section 6.7 elaborates on the verification and validation procedures for the preliminary and initial design described in Section 6.3 and Section 6.4.

6.1 Approach

To get an overview of the different control and stability cases to be analyzed, a mission modes diagram is shown in Fig. 6.1.
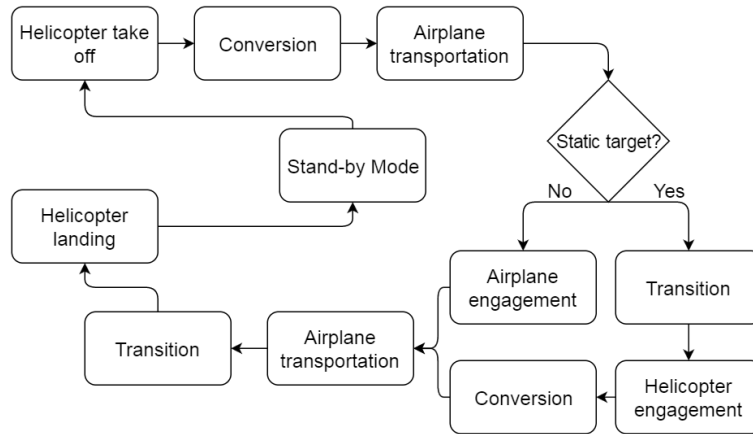
Figure 6.1: Mission modes diagram.

Control in airplane mode is accomplished through actuation of ailerons and ruddervators. While helicopter mode control is done using cyclic and collective pitch, differential thrust, and inverse tilting of the rotors.

The design and analysis of the stability and control of HELIADES was done using the structure shown in Fig. 6.2. With the two larger blocks representing the design and analysis described in Section 6.3 and Section 6.4.

A separate block was created in Fig. 6.2 to make the maneuver requirements more constraining, since the presented analysis of the state space only yields an estimate of the required time to actuate to a set angle or rate. Time should however, also be allocated for the settling of the aircraft under the final angle or rate. Helicopter mode stability and control is analyzed in Section 6.4.2, where it is checked whether the design is stable and controllable in hover mode, after which the design is updated if necessary. The aircraft mode stability and control design is discussed in Section 6.4.1.

Control definition

Since HELIADES has autonomous flight control, it needs positional control with inputs from the command center in the CPU. The information flow is shown in Fig. 6.3, which is modeled in MATLAB as Fig. 6.4. These diagrams describe the process of moving from the initial position to the desired position, as received from the Command Center, of which the features are described in Section 6.6. This is the part of the CPU where the navigation part of the autopilot is situated, while the rest of the diagram describes the flight controller with sensors.

In the positional control block, the desired velocity and attitude is determined from the desired position and is compared to measured position. In the attitude control block, control surface deflections are determined from the desired and measured attitude. This is a proven method for UAV control [134].

The control blocks described are linear control blocks, which is the most used form of control. Although other options are available, such as backstepping [65] and Nonlinear Dynamic Inversion (NDI) with adaptive controls
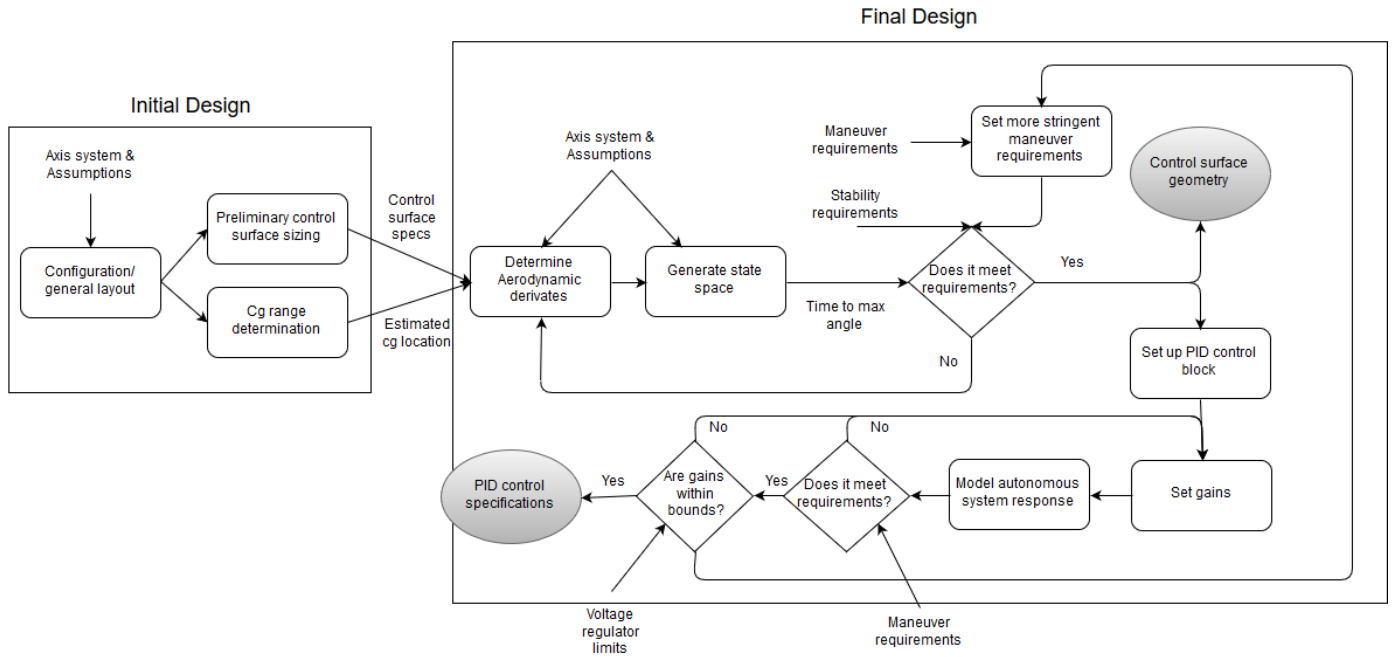
Figure 6.2: WFD for airplane mode analysis.

[64]. These systems are more accurate and, as opposed to linearized systems, they can be used at large angles, at any point in the flight envelope, and when the system is not functioning properly. However, these systems require a lot of processing power to function and expertise to develop.

6.1.1 Axis system

In the design of the stability and control properties of the ADD, the body axis system is used. This is a right-handed axis system with origin at the center of mass of the ADD. Positive x-axis is defined towards the forward longitudinal direction of the fuselage, positive y is pointed in the extension of the right wing and positive z towards the bottom of the ADD. It is chosen such that I_{xy} and I_{yz} can be assumed zero. In the model, the forces parallel to the body axes x, y and z are X, Y and Z respectively. Velocities are u, v and w respectively. Moments around the body axes are L, M and N respectively. Roll rate is p, pitch rate is q and yaw rate is r.
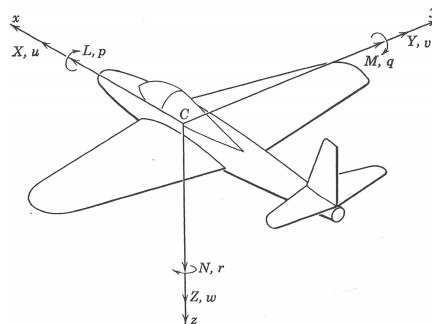
Figure 6.5: Body axis system of the ADD [85].

6.2 Assumptions

In this section the assumptions which are used throughout the chapter are stated. Assumptions are required to reduce the computational complexity and workload while retaining the significance of the result. Assumptions are divided into primary and secondary assumptions where primary assumptions have a major impact on the result while secondary assumptions only have a minor effect.

Primary assumptions

- **Quasi steady flight:** During maneuvers it is assumed that steady flight occurs, or $dV/dt = 0$. In fact, flight
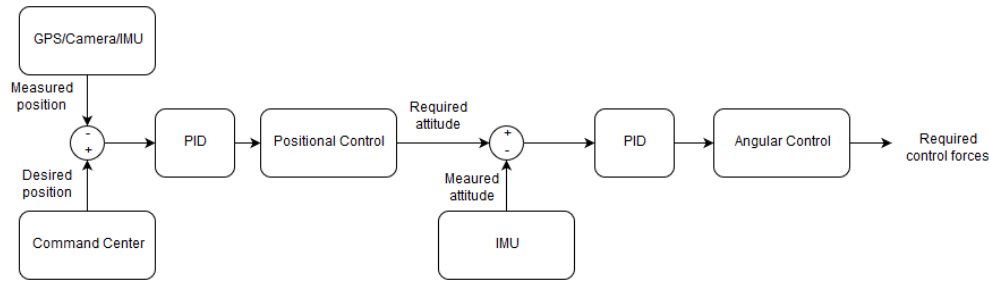
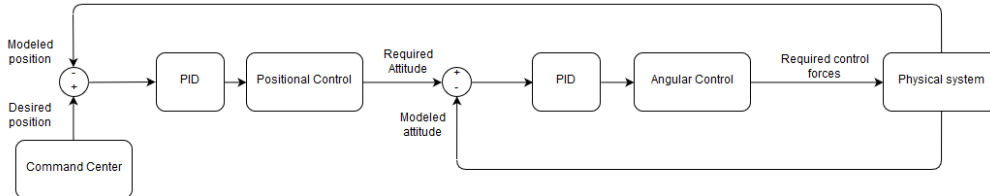Figure 6.3: Control block diagram.

Figure 6.4: Block diagram for the MATLAB control model.

velocity differs throughout the maneuver, however for the short-time maneuvers flight velocity is assumed not to vary significantly.

- **Quasi rectilinear flight:** The flight path angle is assumed small, thus $\sin(\gamma) \approx \gamma$ and $\cos(\gamma) \approx 1$. This is required for the validity of the model for steady symmetric flight. This assumption can have a big impact on the results if the flight path angle becomes large [128].
- **Small angle of attack:** This assumption results in $C_L \approx C_N$. This assumption can have a significant impact on the results if the angles of attack become large [128]. The reason for this assumption is to linearize the system, so it can be modelled by a state space model.
- **Tail surface projection:** In the preliminary tail design it is assumed that the stability and control performance of a V-tail is equivalent to a conventional tail with the same projected surface area. As the V-tail only deflects one of its ruddervators compared to two control surface deflections of the conventional tail for a certain maneuver, it is under-designed. However, designing for relaxed static stability allows under designing when projecting the surfaces of a conventional tail.

Secondary assumptions

- **ADD mass is constant:** As the motors consume energy with batteries as source, the mass does not vary. External mass influences such as dirt and rain water are neglected. This does not have a significant influence on results.
- **ADD is a rigid body:** The aircraft is assumed not to deform and thus no aero-elastic effects occur. This assumption is not expected to have a big impact on the results.
- **Symmetric aircraft:** The aircraft is assumed to be symmetric. This results in I_{xy} and I_{yz} being zero. This will simplify the equations of motion. The ADD is designed to be symmetric, even though the net launcher and kinetic cannon are not symmetrical with respect to the xz-plane, this assumption will not result in large errors.
- **Thrust plane intersects the c.g. of the ADD:** The thrust plane is defined as the plane spanned by the thrust vectors of both engines. This plane intersects the c.g. such that the thrust forces do not provide a pitching moment. This assumption simplifies the analysis. The c.g. of the ADD is designed such that this is true, however moment arm can differ slightly due to misalignment during manufacturing.
- **Resultant thrust vector is parallel to the symmetry plane:** This means that the thrust vector does not influence the body force Y. this assumption simplifies the equations used. The Moment arm can differ slightly due to misalignment during manufacturing.
- **Earth is flat:** Since the traveled distances are small, the curvature of the Earth does not play an important role. The vector of the gravitational force is perpendicular to this surface.
- **Earth is non-rotating:** Since the measurements times are small compared to the time a full Earth rotation takes place, this assumption is expected to not have a big impact.
- **Standard atmosphere:** The International Standard Atmosphere (ISA) is assumed. This way the atmospheric properties at a certain altitude can be calculated. In reality the properties can deviate but these are assumed to be negligible.
- **Zero wind velocity:** It is assumed that there is no wind, this means that the kinematic velocity is equal to the

aerodynamic velocity. This assumption gives rise to errors in case of heavy winds.

- **Constant gravitational acceleration:** The gravitational acceleration is assumed to not vary on the Earth's surface, neither in altitude. Due to the relatively low operating altitude, the output will not differ significantly.
- **Effects of rotating masses are neglected:** Gyroscopic precession of the rotating ADD causes coupling between rotation around the principle axes. This does not have a significant effect on the dynamic maneuvers of the ADD since rolling, yawing or pitching at the same moment is not considered.
- **Non existent P-Factor:** In propeller aircrafts, an air inflow which is not perpendicular to the propeller plane, causes an asymmetrical thrust. One half of the propeller disk generates more thrust as its effective air velocity is higher. Nevertheless, symmetric thrust is assumed (P-factor = 0) which does not affect the solution significantly.
- **The system is continuous time invariant:** The the state space model does not change during simulations. Deviations from the starting condition are sufficiently small so that the state-space equations are valid throughout the time interval of the measurements.

6.3 Initial design

As described in Section 6.1, an initial design on a stability and control basis will be performed for the HELIADES. It entails a determination and sizing of the fuselage, wing placement, cg location, empennage design and control surface design, based on sizing methods from literature.

6.3.1 Fuselage design

In this section the overall shape and geometry of the fuselage is explained. In modeling the hull, the part of the fuselage under the main wing is considered as the central part of the aircraft. The longitudinal geometry of the fuselage is extrapolated from the root chord distance of the wing, required tail arm and components which are housed inside the fuselage. The side view of the fuselage is designed as an airfoil to slightly increase its lifting capability. The final design is modeled using Rhino [138], which is preferred due to its easy surface modeling capabilities. See Fig. 6.6 for a top view wire frame of the fuselage.
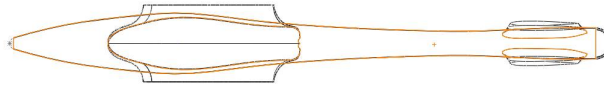

Figure 6.6: top view wireframe picture of the fuselage.

Central: The central part starts at the intersection of the leading edge of the wing and ends at the intersection of the trailing edge of the wing. The central part houses mainly the removal system, flight electronics and battery. Its cross-section is approximated as an ellipse with a longer vertical semi-major axis which adds to the 'Weathervane-effect'[135], which increases the directional stability due to side slip.

Nose: The nose is the portion of the fuselage in front of the leading edge of the main wing. The main components inside the nose are the camera sensors and pitot tube. Its general shape is approximated by a spherically blunted tangent ogive with base cross section equal to the central part. The nose is blunted for ease of manufacturing and resistance to handling and flight damage [90].

Tail cone: The tail cone starts at the trailing edge of the main wing. Its cross-section is approximated by an ellipse throughout, with the horizontal semi-major axis as the larger axis. The cross-section morphs into the cross-section of the central part of the fuselage. It has a flat shape as this benefits longitudinal stability and reduces drag during turning flight. Its length is governed by the tail arm needed from the tail sizing.

6.3.2 Wing placement

To determine the placement of the wing, a trade-off is performed to decide whether it is mounted as a low wing, mid wing or high wing. Four criteria are chosen: dynamic stability, mass, moment of inertia and portability. Each criteria is given a weight factor ranging from 1-5, 1 being least important and 5 most important. Each wing configuration is given points from 1-5 according to its performance with respect to each criterion. Table 6.1 shows the trade-off of the wing placement.

Dynamic stability: A high wing increases the dihedral effect, which has a negative C_{l_β} contribution and thus makes the aircraft more laterally stable [128]. A low wing has a positive C_{l_β} contribution, which can be mitigated by applying a dihedral angle Γ. A mid wing has a neutral C_{l_β} contribution. The flight controller can handle a certain degree of instability, thus weight is set at 2.

Mass: Applying dihedral increases the complexity of the design and stresses in the wing due to increased moments, in turn increasing mass. Mass is a driving requirement, weight is set at 4.

Rolling moment of inertia: Having the wing placed other than at the mid of the fuselage increases the rolling moment of inertia I_{xx}. However, its effect is moderate, weight is set at 2.

Portability: To have a transportable UAV, the wings must be designed to be detachable. A high or low placement of the wing enables easy detachment of the wing. Weight is set at 4.

Table 6.1: Trade-off table for the wing placement.

	Weight	Low wing		Low wing + Γ		Mid wing		High wing	
		Points	Score	Points	Score	Points	Score	Points	Score
Dynamic stability	2	2	4	4	8	3	6	4	8
Mass	4	3	12	2	8	3	12	3	12
I_{xx}	2	2	4	3	6	4	8	2	4
Portability	4	4	16	4	16	2	8	4	16
Total			36		38		34		40

As Table 6.1 shows, the high wing placement without dihedral has the best characteristics. Thus a high wing placement is chosen.

6.3.3 Empennage design

Before the dynamic analysis in Section 6.4.1 can be performed, the design of the empennage and control surfaces must be specified. In this section the design of the empennage is described. This design is used to check the maneuvering requirements and is subsequently iterated to arrive at the final design for the empennage.

Empennage trade-off

In the design of the empennage, different layouts were examined and compared in a trade-off. These layouts are conventional tail, T-tail, H-tail, V-tail, inverted V-tail and inverted Y-tail. The V-tail is a horizontal tail with a dihedral angle, the inverted V-tail is a horizontal tail with an anhedral angle, see Fig. 6.7.

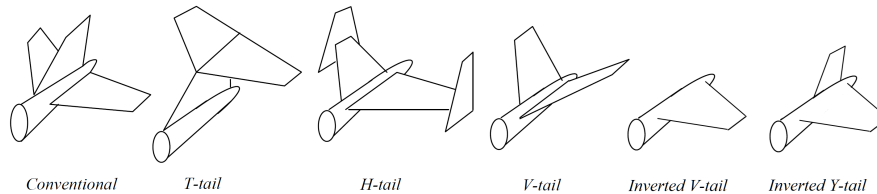*Conventional*   *T-tail*   *H-tail*   *V-tail*   *Inverted V-tail*   *Inverted Y-tail*

Figure 6.7: Tail empennage options [143].

The trade-off criteria are the wetted surface area, stall performance, mass, complexity, maneuverability, rolling moment of inertia (I_{xx}) and feasibility. Each criterion is given a weight from 1-5, with 1 as least important and 5 of highest importance.

Wetted surface area: This is the amount of wetted surface which is needed to adequately provide stability and control. Higher area leads to higher profile drag and more control surfaces lead to higher interference drag. As drag is an important performance aspect, importance is set at 3.

Stall performance: During flight at a high angle of attack, the elevator should be able to provide a pitching moment to recover from deep stall. To recover from spin, the rudder should be able to provide a sufficient yawing moment. As the ADD shall be performing frequent high angle of attack maneuvers during its pursuit, stall performance importance is regarded at 3.

Mass: The mass of the empennage must be as low as possible, including actuators. For instance having a control surface at the end of another control surface, as is with the T-tail and H-tail, increases the structural weight. Mass must always be minimized, importance set at 3.

Complexity: This is related to the amount of actuators and connections needed to deflect the control surfaces. More actuators increase the amount of connectors to actuate the control surfaces. Importance set at 2.

Control dynamics: The properties of the control surfaces during flight in relation to the dynamics of the aircraft are compared in control dynamics. Lateral and directional control derivative characteristics like ad-verse and pro-verse yaw are evaluated. Pro-verse yaw is advantageous as positive yawing moments are accompanied by positive rolling moments which aid to maneuvering the aircraft in the right direction. Also, lateral and directional aerodynamic derivative characteristics are taken into account. Maneuverability was a key criterion in the trade-off in the mid-term, with the empennage playing a significant role in its performance. Thus its importance is set at 5.

Rolling moment of inertia: For attaining high angular accelerations, having a low I_{xx} is beneficial. Importance is set at 3.

Each design option is given points between 1-5 according to its performance with respect to the criterion. See Table 6.2 for the trade-off of the empennage.

Table 6.2: Trade-off table for the empennage design.

Criterion	Weight	Conventional		T-tail		H-tail		V-tail		Inverted V-tail		Inverted Y-tail	
		Points	Score	Points	Score	Points	Score	Points	Score	Points	Score	Points	Score
Wetted surface	3	2	6	5	15	5	15	4	12	4	12	3	9
Stall performance	3	3	9	2	6	3	9	4	12	5	15	4	12
Mass	3	4	12	2	6	2	6	3	9	3	9	3	9
Complexity	2	4	8	3	6	2	4	5	10	5	10	4	8
Control dynamics	5	3	15	3	15	3	15	3	15	4	20	4	20
I_{xx}	3	4	12	4	12	5	15	2	6	2	6	3	9
Total			62		60		64		64		72		67

Wetted surface: The wetted surface area of the T-tail and H-tail is less than the conventional tail due to the end plate effect. On the T-tail, the vertical surface can thus be made smaller and on the H-tail, the horizontal surfaces can be made smaller. The V-tail only has two surfaces, but they have to be scaled up to provide the same control forces. In the end, the area is 5% lower than that of the conventional layout [131] and has a lower drag compared to a conventional empennage [84]. The Y-tail has a wetted area surface between the V-tail and conventional tail.

Stall performance: The T-tail has the worst deep stall performance as its horizontal part is situated inside the wake of the wing and fuselage during stall. Therefore, its elevator becomes ineffective and the aircraft incontrollable [155]. The inverted tails demonstrate the best deep stall performance as its elevators are situated lower than the wing and fuselage. The conventional tail and inverted Y-tail has to be designed properly to let the rudder be effective during spin. The H-tail has a partial disadvantage in spin as only one half of each rudder is inside the wake of the horizontal stabilizer. The V-, inverted V- and inverted Y-tail demonstrate good spin recovery characteristics.

Mass: For mass, the wetted surface area can be used as indication. Lower areas relates to lower mass. Besides this, structural mass is taken into account. Tails with end-plate configuration have increased structural mass. V-tails also have slightly higher structural mass as the moments generated are higher.

Complexity: The amount of actuators and connection rods are taken into account. Higher amount of control surfaces increases complexity. Actuators are situated inside the fuselage, thus tails with end-plates have to have a more intricate design of connectors to move the end-plate control surfaces.

Control dynamics: Horizontal and vertical tails show moderate coupling of rolling and yawing moments during control surface deflection. V-tails however provide a significant rolling moment during yawing and vice-versa. Advantageous would be a positive rolling moment accompanied with a positive yawing moment, or pro-verse yaw. This is the case in horizontal tails with an anhedral angle, like the inverted V-tail and inverted Y-tail, see the right two tails in Fig. 6.8. For the left tail in Fig. 6.8, the tail goes to the right and nose is pointed to the left, the rolling moment rolls the airplane clockwise, which opposes the maneuver of yawing the aircraft to the left. Also considered is the lateral stability due to side slip, dihedral decreases C_{l_β}, which is favorable. Anhedral increases C_{l_β}, which is unfavorable. This however plays a smaller role as the flight controller is designed to counter instability.

Rolling moment of inertia: Larger vertical and horizontal tail span combined with higher mass increase moment of inertia. Span is the most important indicator. The H-tail has low horizontal span due to the end-plate effect. The T-tail has lower vertical span, but has its horizontal surface at a distance from the centroid. This negates the benefit of shorter vertical span. The tails with dihedral or anhedral have longer spans than the conventional tail, thus perform less for this criterion.
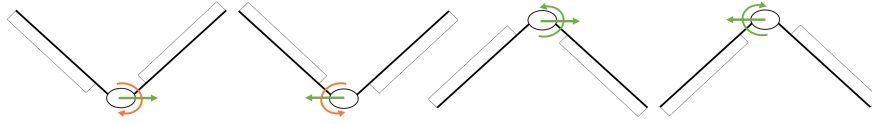
Figure 6.8: Yaw-roll coupling of V-tail and inverted V-tail.

Conclusion

The inverted V-tail wins by an adequate margin of 5 points. The main contributors to the high score are the good wetted surface area, stall performance, control dynamics and low complexity. The inverted Y-tail is in second place. If however it turns out that the inverted V-tail stretches too far down, such that the landing gear must be lengthened, the inverted Y-tail will be chosen instead. This because it retains similar control dynamics and imposes lower requirements on the free area beneath the fuselage tail cone. This will be decided upon after complying the tail surfaces with the maneuver and aerodynamic requirements.

Preliminary empennage design

The preliminary geometry of the empennage is calculated using a scissor plot overlaid with a center of gravity range plot, as described in Torenbeek [155]. The geometry for the inverted V-tail is calculated for a conventional tail and is projected onto the axes of the inverted Y-tail [135]. This way, the vertical and horizontal components of the tail are equivalent. The horizontal component geometry is calculated using the aforementioned plots. The longitudinal position, taper and root chord of the vertical component is set equal to that of the horizontal component.

The aircraft is designed for a relaxed static longitudinal stability. This is due to the autonomous control, which does not require inherent stability. By designing the aircraft for relaxed static longitudinal stability, the control inputs yield a quicker response and the tail does not need to provide negative lift during trim, reducing needed lift and drag and weight of the main wing and drag of the tail. In fighter aircrafts, this has been proven to reduce the mass of the aircraft by $\approx 15\%$ [159].

In the scissor plot, $\frac{S_h}{S}$ is shown as function of $\frac{x_{cg}}{\bar{c}}$ for a number of constraints which are plotted inside the graph. x Values normalized by $\bar{c}$ will be referred to by a bar above the x, $\bar{x}$. The constraints used in determining the empennage geometry are longitudinal stick-fixed stability and controllability at V_{stall}. Longitudinal stick-free stability is regarded by adding a margin of 5% on the stick-fixed stability curve[117]. All derivative coefficients are derived according to the formulas in Torenbeek. The 3D lift curve coefficients are calculated using the DATCOM method for the lift-curve slope of a straight tapered wing for subsonic velocities [107].

The controllability at V_{stall} line is dictated by Equation (6.1). This equation is the result of summing to 0 of longitudinal moments around the c.g.. $C_{m_{ac}}$ is the moment coefficient of the wing, $C_{L_{A-h}}$ is the lift coefficient of the aircraft minus the horizontal tail. C_{L_h} is the lift coefficient of the horizontal tail. S_h is the surface area of the horizontal tail, l_h is the length from the aerodynamic center of the wing to the aerodynamic center of the horizontal tail. $\frac{V_h}{V}$ is the ratio of airspeed of the horizontal tail with respect to the main wing.

$$C_{m_{ac}} + C_{L_{A-h}}(\bar{x}_{cg} - \bar{x}_{ac}) = \frac{C_{L_h} S_h l_h}{S\bar{c}}\left(\frac{V_h}{V}\right)^2 \tag{6.1}$$

The stick-fixed stability line in the scissor plot is dictated by Equation (6.2). This equation is the result of equating the sum of longitudinal moments to 0 around the c.g. after a change in angle of attack. $C_{L_{\alpha_h}}$ is the lift curve coefficient of the horizontal tail, $C_{L_{\alpha_{A-h}}}$ is the lift curve coefficient of the wing and fuselage combined. $\frac{d\epsilon}{d\alpha}$ is the downwash gradient of the horizontal tail.

$$\bar{x}_{cg} = \bar{x}_{ac} + \frac{C_{L_{\alpha_h}}}{C_{L_{\alpha_{A-h}}}}\left(1 - \frac{d\epsilon}{d\alpha}\right)\frac{S_h l_h}{S\bar{c}}\left(\frac{V_h}{V}\right)^2 \tag{6.2}$$

The intersection of the two constraint lines gives the optimal S_h with S of the wing given, and optimal $\bar{x}_{cg}$ given this optimal S_h. The output optimal $\bar{x}_{cg}$ is used as input in the center of gravity range plot, which gives the optimal x position of the leading edge of the mean aerodynamic chord of the wing, normalized by the fuselage length, $\frac{x_{LEMAC}}{l_{fus}}$. To determine the center of gravity range plot, the components of the aircraft with their longitudinal position and mass are divided into a fuselage and wing group. The wing group shifts along with the wing, this way the center of gravity changes significantly with changing wing position. The origin of the right-handed axis system for modeling the components is at the tip of the nose, with x-axis positive to the aft and z-axis positive upwards. The leading

edge of the wing is assumed $1\bar{c}$ from the tip of the nose. This plot is comprised of just one line as its x_{cg} does not change during operation. See Fig. 6.9 for the scissor plot overlaid with the center of gravity range plot. As shown in Fig. 6.9, the optimal $S_h/S = 0.131$ and $\frac{x_{LEMAC}}{l_{fus}} = 0.243$ for a $\frac{x_{cg}}{\bar{c}} = 0.222$.
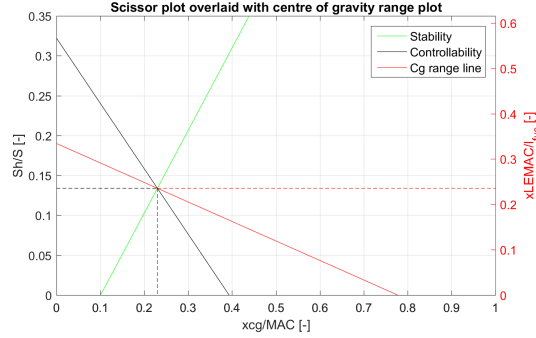

Figure 6.9: Scissor plot overlaid with center of gravity range plot.

The steps in determining the preliminary empennage horizontal component is shown the flow diagram of Fig. 6.10. It is comprised of three iteration loops. The first checks the input V_h to the output V_h of the scissor plot, the second loop checks the placement of the wing along the fuselage after the center of gravity range plot and the third checks the tail arm with the input tail arm.
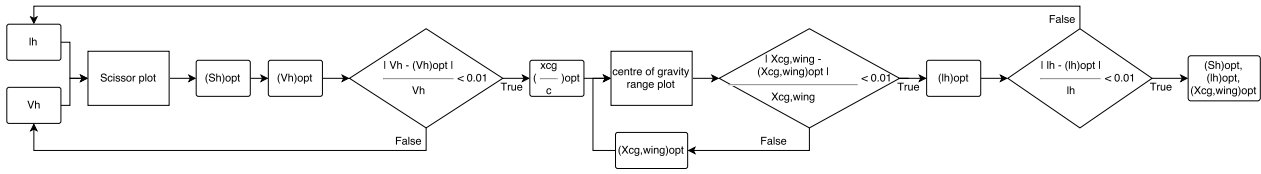

Figure 6.10: Horizontal tail component sizing flow diagram.

For the input l_h and V_h, averaged data of reference fighter aircrafts is used, as high maneuverability is considered. For l_h, an initial estimate of 55% of l_{fus} is used [135]. For V_h, an initial estimate of 0.4 is used [135]. After performing the loops in Fig. 6.10, the vertical span is calculated by using the same root chord and taper of the horizontal part, combined with vertical tail surface area derived from vertical tail volume coefficient of 0.07 [135].

Knowing the tail volumes and setting the aspect ratio of the horizontal tail at 4 and vertical tail at 2 [143], the span of the tail segments are calculated. The remaining unknown variable to determine the preliminary tail planform is taper ratio λ_t. λ_t Is set at 0.8, to increase the 3D lifting efficiency of the airfoil and reduce the control force arm. The profile of the tail is a symmetric profile, because during trim no lift has to be generated. An airfoil with 12% thickness is chosen, the NACA0012. A thicker profile can be chosen when the stresses turn out to be too large. The leading edge sweep angle Λ_{LE_t} is taken such that the trailing edge has a sweep angle of 0°. This results in $\Lambda_{LE_t} = 17.35^o$.

This concludes the preliminary design of the empennage. This design will be adjusted according to the maneuvering requirements from the dynamic analysis. Table 6.3 shows the data for the empennage after iteration.

Table 6.3: Preliminary empennage geometry.

l_h [m]	V_h [-]	V_v [-]	Γ [deg]	C_{r_t} [m]	λ_t [-]	A [-]	l_{fus} [m]	Wing x_{LEMAC} [m]
0.975	0.369	0.07	34.5	0.1834	0.4	5.15	1.564	0.368

l_h In Table 6.3 is 13% longer than the estimate of 55% of l_{fus}, which is reasonable due to the short l_{fus} in comparison to wing span. A larger $\frac{l_h}{l_{fus}}$ assures adequate tail arm when l_{fus} is relatively short. V_h is 0.369, which is smaller than the initial value of 0.4. this is due to the relaxed static stability criterion which permits a smaller tail and hence smaller tail volume. Aspect ratio is 5.15 which is higher than 4 of the horizontal tail. This is reasonable as the tail span is larger due to the projection of both horizontal and vertical tail components, retaining the chord geometry of only the horizontal tail.

6.3.4 Control surface design

To calculate the maneuvering forces of the control surfaces, the area and maximum deflection of the surfaces need to be determined. In this section a preliminary design for the ailerons and ruddervators is shown. The data of this planform is used in checking the maneuvering requirements in the dynamic analysis of section Section 6.4.1 and iterated to reach the final planform.

Aileron design

For the preliminary design, the ailerons are set at a span of 50-90% of the semi span [135]. They are situated maximally outboard to increase the force arm for rolling. The ailerons do not extend to the wing tips because the last 10% does not add to much control effectiveness due to vortex flow at the wing tips [135]. However, the engine nacelles are an extension to the wing, thus increasing the maximal aileron extension. Additionally, the propellers rotate with the inboard part up, thus mitigating the wing tip vortices and increasing the lift coefficient at the end of the wings [158]. The chord of the ailerons are set at 25% of the chord of the wing and constant-percent along the span [135]. The ailerons are designed as plain flaps as they are simple and cheap to manufacture. The maximal deflection of the ailerons is set at 20° upwards and 15° downwards, to counter adverse yaw. See Fig. 6.11 for the planform of the wing with ailerons, dimensions are in mm.

Having the primary roll control surfaces at the end of the wing requires a control system with high resolution to precisely control the UAV at high velocity. If the resolutions turns out to be insufficient, gearing can be used to increase precision.

Ruddervators

The ruddervators are set at a span of 30-100% of the tail span and have a constant chord length of 30% C_{r_t} [135]. An all moving tail just as a full span ruddervator is not possible due to the close placement of the two tail surfaces. Like the ailerons, the ruddervators are designed as plain flaps. Deflection of the ruddervators is limited to 20° upwards and downwards. See Fig. 6.12 for the planform of the tail surface with ruddervator, dimensions are in mm.

If the dynamic requirements analysis requires a larger surface, a notched ruddervator can be considered. A notched ruddervator also decreases the stresses in the tail due to the moment generated by the ruddervator.
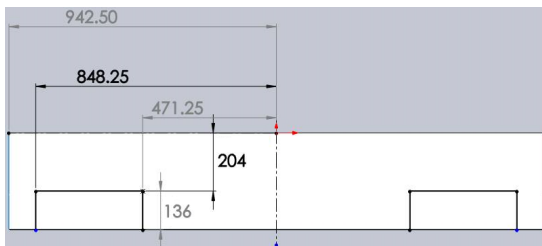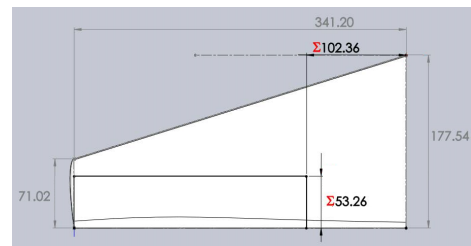

Figure 6.11: Planform of the wing.

Figure 6.12: Planform of the tail surface.

6.4 Final design

This section is describes the analysis and design done in the second large block in Fig. 6.2, the final design phase of the stability & control analysis. The initial design from Section 6.3 is tested and altered based on whether or not the design meets the requirements in Chapter 15. Aircraft and helicopter mode are treated in Section 6.4.1 and Section 6.4.2 respectively.

6.4.1 Aircraft mode

The physical system of the aircraft can be modeled as in Equation (6.3). This differential equation can be linearized and put in state space form as in Equation (6.4).

$$\boldsymbol{F} = M\ddot{\boldsymbol{x}} + C\dot{\boldsymbol{x}} + K\boldsymbol{x} \qquad (6.3) \qquad\qquad \dot{\boldsymbol{x}} = A\boldsymbol{x} + B\boldsymbol{u} \qquad (6.4)$$

For conventional aircraft, the physical system is usually separated into two independent state spaces for analysis: a symmetrical and asymmetrical state space. But since for V- or Y-tail aircraft pitch and yaw are controlled using the same control surface, the two are not decoupled. So for HELIADES only one state space system is created for rotations and accelerations around all axes.

The state vector x for the system is given by Equation (6.5). The input vector u is given by Equation (6.6). To this input vector an additional ΔT_c is added to analyze the one engine inoperative (OEI) case or a ΔG when the effect of a shot being fired is modeled.

$$\boldsymbol{x} = \left[\hat{u}, \alpha, \theta, \frac{qc}{V}, \beta, \phi, \frac{pb}{2V}, \frac{rb}{2V}\right]' \quad (6.5) \qquad\qquad \boldsymbol{u} = [\delta_{cl}, \delta_{cr}, \delta_a, \delta_{rC}]' \quad (6.6)$$

In equation 6.6, δ_{cl} and δ_{cr} are deflections of the left and right control surfaces on the tail, where downward is a positive deflection. δ_a resembles an upward deflection of the left aileron and equally large downward deflection of the right aileron. δ_{rC} is a deflection of the rudder on the conventional vertical tail in the negative y-direction. Since the tail sizing concluded that the conventional vertical tail of the Y-tail can be dropped, this input will always be zero, until the vertical tail is deemed necessary for either stability or control.

The A-matrix is constructed as shown in Equation (6.9), where A_{sym} and A_{asym} can be found in Equation (6.7) & Equation (6.8), these are taken from the Flight Dynamics reader [128].

$$A_{sym} = \begin{bmatrix} \frac{V}{\bar{c}} \frac{C_{X_u}}{2\mu_c} & \frac{V}{\bar{c}} \frac{C_{X_\alpha}}{2\mu_c} & \frac{V}{\bar{c}} \frac{C_{Z_0}}{2\mu_c} & \frac{C_{X_q}}{2\mu_c} \\ \frac{V}{\bar{c}} \frac{C_{Z_u}}{2\mu_c - C_{Z_{\dot{\alpha}}}} & \frac{V}{\bar{c}} \frac{C_{Z_\alpha}}{2\mu_c - C_{Z_{\dot{\alpha}}}} & -\frac{V}{\bar{c}} \frac{C_{X_0}}{2\mu_c - C_{Z_{\dot{\alpha}}}} & \frac{2\mu_c + C_{Z_q}}{2\mu_c - C_{Z_{\dot{\alpha}}}} \\ 0 & 0 & 0 & 1 \\ \frac{V^2}{\bar{c}^2} \frac{C_{m_u} + C_{Z_u}\frac{C_{m_{\dot{\alpha}}}}{2\mu_c - C_{Z_{\dot{\alpha}}}}}{2\mu_c K_Y^2} & \frac{V^2}{\bar{c}^2} \frac{C_{m_\alpha} + C_{Z_\alpha}\frac{C_{m_{\dot{\alpha}}}}{2\mu_c - C_{Z_{\dot{\alpha}}}}}{2\mu_c K_Y^2} & \frac{V^2}{\bar{c}^2} \frac{C_{X_0}\frac{C_{m_{\dot{\alpha}}}}{2\mu_c - C_{Z_{\dot{\alpha}}}}}{2\mu_c K_Y^2} & \frac{V}{\bar{c}} \frac{C_{m_q} + C_{m_{\dot{\alpha}}}\frac{2\mu_c + C_{Z_q}}{2\mu_c - C_{Z_{\dot{\alpha}}}}}{2\mu_c K_Y^2} \end{bmatrix} \quad (6.7)$$

$$A_{asym} = \begin{bmatrix} \frac{V}{b} \frac{C_{Y_\beta}}{2\mu_b} & \frac{V}{b} \frac{C_L}{2\mu_b} & \frac{1}{2} \frac{C_{Y_r} - 4\mu_b}{2\mu_b} & \\ 0 & 0 & 1 & 0 \\ 2\frac{V^2}{b^2} \frac{C_{l_\beta} K_Z^2 + C_{n_\beta} K_{XZ}}{4\mu_b(K_X^2 K_Z^2 - K_{XZ}^2)} & 0 & \frac{V}{b} \frac{C_{l_p} K_Z^2 + C_{n_p} K_{XZ}}{4\mu_b(K_X^2 K_Z^2 - K_{XZ}^2)} & \frac{V}{b} \frac{C_{l_r} K_Z^2 + C_{n_r} K_{XZ}}{4\mu_b(K_X^2 K_Z^2 - K_{XZ}^2)} \\ 2\frac{V^2}{b^2} \frac{C_{l_\beta} K_{XZ} + C_{n_\beta} K_X^2}{4\mu_b(K_X^2 K_Z^2 - K_{XZ}^2)} & 0 & \frac{V}{b} \frac{C_{l_p} K_{XZ} + C_{n_p} K_X^2}{4\mu_b(K_X^2 K_Z^2 - K_{XZ}^2)} & \frac{V}{b} \frac{C_{l_r} K_{XZ} + C_{n_r} K_X^2}{4\mu_b(K_X^2 K_Z^2 - K_{XZ}^2)} \end{bmatrix} \quad (6.8)$$

$$A = \begin{bmatrix} A_{sym} & O_{4x4} \\ O_{4x4} & A_{asym} \end{bmatrix} \quad (6.9)$$

The input response matrix can be found in Equation (6.16). This matrix is based on the B-matrix for conventional aircraft and adjusted for an inverted Y-tail configuration. It has been taken into account, for this matrix and all its derivatives, that the rudders act as both ailerons and elevators, as is explained in Section 6.3.3.

For the analysis it is assumed that $(\frac{V_v}{V})^2 = (\frac{V_h}{V})^2 = 0.95$ which is common for fuselage mounted tails [128]. The aerodynamic derivatives are taken from the CFD analysis performed by the aerodynamics group, see Chapter 7 and external sources [141],[128],[144] & [83]. The mass moment of inertia is taken from the CAD model in Chapter 14 as can be seen in Table 6.4.

$$\mu_b = \frac{m}{\rho S b} \quad (6.10) \qquad\qquad \mu_c = \frac{m}{\rho S c} \quad (6.11)$$

$$\frac{I_{xx}}{mb^2} \quad (6.12) \qquad \frac{I_{yy}}{mc^2} \quad (6.13) \qquad \frac{I_{zz}}{mb^2} \quad (6.14) \qquad \frac{I_{xz}}{mb^2} \quad (6.15)$$

$C_{X_0} = 0$ [128] $\quad C_{Z_0} = -0.39$ [128] $\quad C_{m_0} = 0$ [128]

$C_{X_u} = -0.16$ [128] $\quad C_{Z_u} = -0.79$ [128] $\quad C_{m_u} = 0$ [128]

$C_{X_\alpha} = 0.21$ [128] $\quad C_{Z_\alpha} = -3.77$ [128] $\quad C_{m_\alpha} = -0.087$ [128]

$C_{X_{\dot\alpha}} = 0$ [128] $\quad C_{Z_{\dot\alpha}} = -0.14$ [128] $\quad C_{m_{\dot\alpha}} = -0.42$ [128]

$C_{X_q} = 0$ [128] [141] $\quad C_{Z_q} = -2.09$ [128] [141] $\quad C_{m_q} = -3.3$ [128] [141]

$C_{X_{\delta_{cl}}} = 0$ [141] [128] $\quad C_{Z_{\delta_{cl}}} = -0.063$ [141] [128] $\quad C_{m_{\delta_{cl}}} = -0.17$ [141] [128]

$C_{X_{\delta_{cr}}} = 0$ [141] [128] $\quad C_{Z_{\delta_{cr}}} = -0.063$ [141] [128] $\quad C_{m_{\delta_{cr}}} = -0.17$ [141] [128]

$C_{Y_\beta} = -0.12$ [128] Chapter 7 $\quad C_{l_\beta} = -0.046$ [128] Chapter 7 $\quad C_{n_\beta} = 0.11$ [128] Chapter 7

$C_{Y_p} = 0$ [128] [141] [133] $\quad C_{l_p} = -0.39$ [128] [141] $\quad C_{n_p} = 0.01$ [128] [141]

$C_{Y_r} = 0.20$ [128] [141] [133] $\quad C_{l_r} = 0.59$ [128] [141] [133] $\quad C_{n_r} = -0.11$ [128] [141] [133]

$C_{Y_{\delta_a}} = 0$ [141] [144] $\quad C_{l_{\delta_a}} = 0.29$ [141] [144] $\quad C_{n_{\delta_a}} = 0.029$ [141] [144]

$C_{Y_{\delta_{cl}}} = 0.13$ [141] [128] $\quad C_{l_{\delta_{cl}}} = -0.0014$ [141] [128] $\quad C_{n_{\delta_{cl}}} = -0.077$ [141] [128]

$C_{Y_{\delta_{cr}}} = -0.13$ [141] [128] $\quad C_{l_{\delta_{cr}}} = 0.0014$ [141] [128] $\quad C_{n_{\delta_{cr}}} = 0.77$ [141] [128]

$\mu_c = 42$ Equation (6.11) $\quad \mu_b = 8.32$ Equation (6.10) $\quad K_{XZ} = 3.74 \cdot 10^{-4}$ Equation (6.15)

$K_X^2 = 0.051$ Equation (6.12) $\quad K_Y^2 = 0.3311$ Equation (6.13) $\quad K_Z^2 = 0.063$ Equation (6.14)

Table 6.4: Aerodynamic coefficients.

$$B = \begin{bmatrix} \frac{V}{\bar{c}}\frac{C_{X_{\delta_{cl}}}}{2\mu_c} & \frac{V}{\bar{c}}\frac{C_{X_{\delta_{cr}}}}{2\mu_c} & 0 & 0 \\ \frac{V}{\bar{c}}\frac{C_{Z_{\delta_{cl}}}}{2\mu_c - C_{Z_{\dot\alpha}}} & \frac{V}{\bar{c}}\frac{C_{Z_{\delta_{cr}}}}{2\mu_c - C_{Z_{\dot\alpha}}} & 0 & 0 \\ 0 & 0 & 0 & 0 \\ \frac{V^2}{\bar{c}^2}\frac{\frac{C_{m_{\dot\alpha}}C_{Z_{\delta_{cl}}}}{2\mu_c - C_{Z_{\dot\alpha}}} + C_{m_{\delta_{cl}}}}{2\mu_c K_Y^2} & \frac{V^2}{\bar{c}^2}\frac{\frac{C_{m_{\dot\alpha}}C_{Z_{\delta_{cr}}}}{2\mu_c - C_{Z_{\dot\alpha}}} + C_{m_{\delta_{cr}}}}{2\mu_c K_Y^2} & 0 & 0 \\ \frac{V}{b}\frac{C_{Y_{\delta_{cl}}}}{2\mu_b} & \frac{V}{b}\frac{C_{Y_{\delta_{cr}}}}{2\mu_b} & \frac{V}{b}\frac{C_{Y_{\delta_a}}}{2\mu_b} & \frac{V}{b}\frac{C_{Y_{\delta_{rC}}}}{2\mu_b} \\ 0 & 0 & 0 & 0 \\ 2\frac{V^2}{b^2}\frac{C_{l_{\delta_{cl}}}K_Z^2 + C_{n_{\delta_{cl}}}K_{XZ}}{4\mu_b(K_X^2 K_Z^2 - K_{XZ}^2)} & 2\frac{V^2}{b^2}\frac{C_{l_{\delta_{cr}}}K_Z^2 + C_{n_{\delta_{cr}}}K_{XZ}}{4\mu_b(K_X^2 K_Z^2 - K_{XZ}^2)} & 2\frac{V^2}{b^2}\frac{C_{l_{\delta_a}}K_Z^2 + C_{n_{\delta_a}}K_{XZ}}{4\mu_b(K_X^2 K_Z^2 - K_{XZ}^2)} & 2\frac{V^2}{b^2}\frac{C_{l_{\delta_{rC}}}K_Z^2 + C_{n_{\delta_{rC}}}K_{XZ}}{4\mu_b(K_X^2 K_Z^2 - K_{XZ}^2)} \\ \frac{V^2}{b^2}\frac{C_{l_{\delta_{cl}}}K_{XZ} + C_{n_{\delta_{cl}}}K_X^2}{4\mu_b(K_X^2 K_Z^2 - K_{XZ}^2)} & \frac{V^2}{b^2}\frac{C_{l_{\delta_{cr}}}K_{XZ} + C_{n_{\delta_{cr}}}K_X^2}{4\mu_b(K_X^2 K_Z^2 - K_{XZ}^2)} & \frac{V^2}{b^2}\frac{C_{l_{\delta_a}}K_{XZ} + C_{n_{\delta_a}}K_X^2}{4\mu_b(K_X^2 K_Z^2 - K_{XZ}^2)} & \frac{V^2}{b^2}\frac{C_{l_{\delta_{rC}}}K_{XZ} + C_{n_{\delta_{rC}}}K_X^2}{4\mu_b(K_X^2 K_Z^2 - K_{XZ}^2)} \end{bmatrix}$$

(6.16)

Maneuverability requirements

The aileron is sized based on a roll rate of $p = 150°/s$, which is generally a requirement for fighter aircraft [159]. The rudder is sized based on the OEI mode. The elevator is sized based on a required pitch rate $q = 60°/s$ from Chapter 15. Moreover, the aircraft should stabilize after firing the gun. All requirements are simulated at the lowest maneuver velocity since at this velocity it is hardest to maneuver the aircraft due to less effective control surfaces. This airspeed is taken at 20m/s.

The maximum control deflections are as specified earlier in this chapter. The maximum aileron deflection is taken as 17.5°, which is the average absolute deflection of the left and right aileron described in Section 6.3.4. The maximum ruddervator deflections for maneuvers are taken as 75% of the maximum deflections defined in Section 6.3.4, since it should be possible to control the yaw angle of the HELIADES in maximum pitch actuation and vice versa.

Update to the design

After the dynamic analysis of the aircraft, with initial tail size found in Section 6.3.3, it was found that the relaxed static stability was approached closely with a $C_{m_\alpha} = -0.0867$. see table Table 6.5 for the update of the tail data.

During the roll analysis it was found that due to the engines being situated on the wingtips, combat worthy roll performance is hard to accomplish. The aileron span is increased to $10 - 90\%$ of the wing span, which is possible because the HELIADES does not have flaps. The percentage of chord is kept at 30% of the wing chord. The percentage of span and chord used by the ruddervators is the same as described in Section 6.3.4.

Table 6.5: Final empennage geometry.

l_h [m]	Γ [deg]	C_{r_t} [m]	λ [-]	A [-]	l_{fus} [m]	Wing x_{LEMAC} [m]
0.975	34.5	0.183	0.4	5.15	1.564	0.368

Dynamic behavior

The results of the analysis can be found in Fig. 6.13-6.16. In the OEI analysis the case of having a malfunctioning right engine causing a positive moment around the z-axis, which should be corrected for using a positive rudder deflection. As can be seen in Fig. 6.13, the yaw moment generated by the rudder is larger than the moment caused by the engine.

The aircraft can get into the required pitch rate within 0.2s as is shown in Fig. 6.14 and into the required roll rate in 0.24s Fig. 6.15. Since after these short time intervals the aircraft attitude can still be described in small Euler angles ($\theta_{act} = -7.5°, \phi_{act} = -20°$), the model and its response are valid.

Fig. 6.16 shows that without deflecting any surfaces, the maximum change of pitch of the HELIADES due to recoil is only 3.5°, based on the z offset of the barrel w.r.t the cg from the CAD drawing in Chapter 14.
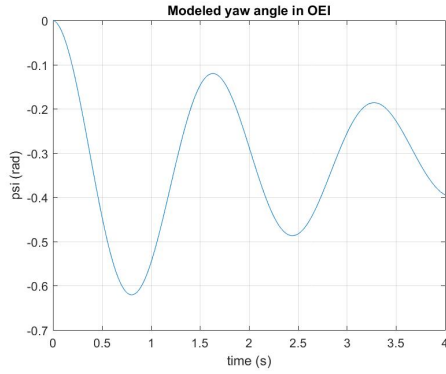

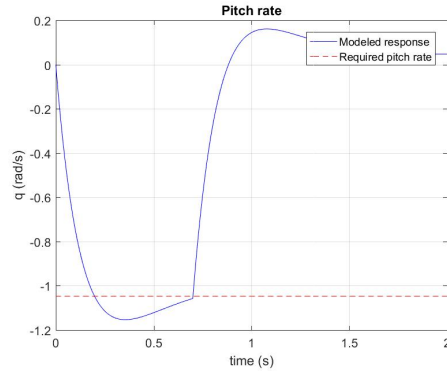Figure 6.13: Model yaw response to positive rudder deflection in OEI mode.

Figure 6.14: Model pitch rate response to a 0.2s maximum positive elevator deflection.
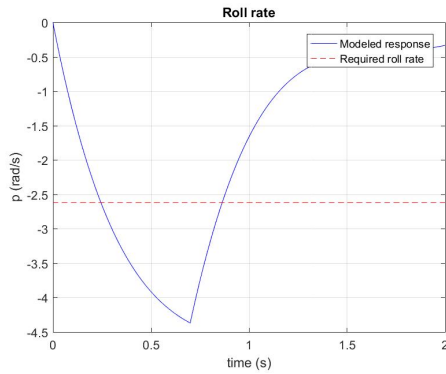

Figure 6.15: Model roll rate response to a 0.2s maximum positive aileron deflection.
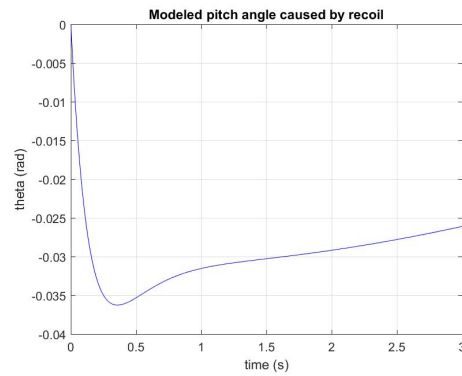

Figure 6.16: Model pitch angle response to a shot.

Stability

For the lateral stability, the behavior of the HELIADES in spiral and Dutch roll are analyzed, through the Routh-Hurwitz criteria: E > 0 for spiral and R > 0 for Dutch Roll. These are the critical stability criteria [128], calculated using Equation (6.17) - (6.22).

$$A = 16\mu_b^3 K_X^2 K_Z^2 \tag{6.19}$$

$$B = -4\mu_b^2(2C_{Y_\beta}(K_X^2 K_Z^2 - K_{XZ}^2) + C_{n_r}K_X^2 + C_{l_p}K_Z^2 + (C_{l_r} + C_{n_p})K_{XZ}) \tag{6.20}$$

$$E = C_L(C_{l_\beta}C_{n_r} - C_{n_\beta}C_{l_r}) \qquad (6.17) \qquad\qquad R = B \cdot A \cdot D - A \cdot D^2 - B\dot{E} \qquad (6.18)$$

$$C = 2\mu_b((C_{Y_\beta}C_{n_r} - C_{Y_r}C_{n_\beta})K_X^2 + ((C_{Y_\beta}C_{n_p} - C_{n_\beta}C_{Y_p}) + (C_{Y_\beta}C_{l_r} - C_{l_\beta}C_{Y_r}))K_{XZ} +$$
$$(C_{Y_\beta}C_{l_p} - C_{l_\beta}C_{Y_p})K_Z^2 + 4\mu_b C_{n_\beta}K_X^2 + 4\mu_b C_{l_\beta}K_{XZ} + \frac{1}{2}(C_{l_r}C_{n_p} - C_{n_r}C_{l_p}) \qquad (6.21)$$

$$D = -4\mu_b C_L(C_{l_\beta}K_Z^2 + C_{n_\beta}K_{XZ}) + \frac{C_{Y_p}}{2}(C_{l_\beta}C_{n_r} - C_{n_\beta}C_{l_r})2\mu_b(C_{l_\beta}C_{n_p} - C_{n_\beta}C_{l_p}) +$$
$$\frac{C_{Y_\beta}}{2}(C_{l_r}C_{n_p} - C_{n_r}C_{l_p}) + \frac{C_{Y_r}}{2}(C_{l_p}C_{n_\beta} - C_{n_p}C_{l_\beta}) \qquad (6.22)$$

For the final configuration the stability criteria, E = 0, R = 4.63 & C_{m_α} = -0.0867 are found. Also from simulations it can be seen that the aircraft recovers from disturbances, like the recoil, gusts and control deflections. From all this it can be concluded that HELIADES possesses the relaxed stability aimed for.

PID Design

Proportional Integral Derivative (PID) control is used to correct inputs to a controller using its past, current, and expected value, as opposed to just its current value. Having high values for the inputs derivative gain usually leads to faster convergence, but makes the controller more sensitive to noise.

The preliminary gain tuning was performed using MATLABs sisotool library. The remainder of the tuning is done manually by changing the gains until the actuation and settling time requirements are satisfied.

Stability and control analysis

When the horizontal tail area is decreased below S_h = 0.0690m^2, the aircraft becomes longitudinally unstable. When the elevator span is decreased to 65% of the tail span, HELIADES is only able to get into a pitch rate of q = 60°/s at θ = 30°, an angle too high for the model to be valid. The same goes for the aileron and its roll requirement of p = 150°/s, when its span is decreased to 85% of the wing span.

Tail Control Forces

The maximum control forces generated by the ruddervators are calculated using the control surface derivatives and their maximum angles. This results in an F_z = -14.8N & F_y = -19.1N per ruddervator, these are used in Chapter 8 to analyze the strength of the tail.

6.4.2 Helicopter mode

The helicopter mode of the aircraft is assumed to only be initiated during take-off, landing or to take care of stationary targets. For these modes the stability and control will be described in this section.

Control actuation

Since 333N excess thrust is present in hover, as determined in Chapter 5, rpm rather than collective pitch will be used to control HELIADES in this mode. In helicopter mode, yaw control is done by tilting of the rotors in opposite direction with a thrust angle, (α_T). This generates a moment around the z-axis. During the maneuver the rpm has to be increased to ensure vertical equilibrium.

Roll control is done by varying the differential thrust between the left and right propeller, through varying the rpm. Since the large excess thrust is present making roll control easy, the roll control will not be further described in this report, other than the pitch control, which is more difficult to control for tilt rotor aircraft.

Pitch control is done by using cyclic pitch, thus increasing the angle of attack at one side of the shaft and decreasing it on the other side. This generates a moment around the c.g., since the propeller shaft is aligned with the c.g., causing the aircraft to pitch.

Required stability characteristics

In order to capture a stationary target, the removal mechanism must be used in helicopter mode. HELIADES must be able to generate excess torques over winds up to 15m/s, as specified inChapter 15, to be able to accurately aim the kinetic cannon or net gun.

The moment caused by the recoil of the shotgun found in Chapter 5 causes a pitch down moment of $M_{shot} = 20$Nm during 1.5 ms.

The moment generated around the c.g. during either a vertical or a lateral gust of 15 m/s can be calculated by modeling the ADD as a flat plate mounted on two cylinders of different size, which represents the wing and the fuselage respectively. With this method, it is calculated that the maximum pitching moment to be overcome is $M_y = 0.4882Nm$. The maximum yawing moment is found to be $M_z = 4.40$Nm.

Control moments generated

The thrust angle (α_T) required to generate a yawing moment large enough to counteract M_z is calculated using Equation (6.23) and is found to be $\alpha_T = 3°$. So angles used to control HELIADES are small, requiring accurate actuation from the tilt gear box.

$$M_z = \frac{Wb}{2}\tan(\alpha_T) \tag{6.23}$$

For the cyclic pitch control around the y-axis, the blades stall angle $\theta_{cyc_{stall}} = 20°$, the mechanical limit of the actuator $\theta_{cyc_{mech}} = 10°$, nominal pitch angle $\theta_{prop_{nom}} = 8°$ and the maximum angle for yaw control are limiting factors. The fact that helicopter control does not use collective pitch, relieves the pitch control of another limitation on the pitch angle.

The maximum achievable pitch control moment $M_{cyc_{max}} = 3.52$Nm is calculated using Equation (6.24), where $d\theta_{prop} = \theta_{cyc_{mech}} - \theta_{prop_{nom}}$. This leads to a maximum instant angular pitch acceleration of $\ddot{\theta} = 2.89$rad/s^2. The formula can be used because the propeller is aligned with the c.g. of HELIADES.

$$M_{cyc_{max}} = C_{L_{\theta_{prop}}} d\theta_{prop} r_{prop} \tag{6.24}$$

The value found for $M_{cyc_{max}}$ shows that HELIADES is stable in gusts, but to see whether or not it can correct for recoil, Equation (6.25) is used, where angular displacements due to recoil (rec) and actuation (act) are set equal. Using this equation it was found that HELIADES can correct for the pitch angle caused by the impuls from the gun within 0.03 s.

$$\theta_{rec} = \frac{1}{2}\alpha_{rec} t_{rec}^2 = \theta_{act} = \frac{1}{1}\alpha_{act} t_{act}^2 - \alpha_{rec} t_{rec} t_{act} \tag{6.25}$$
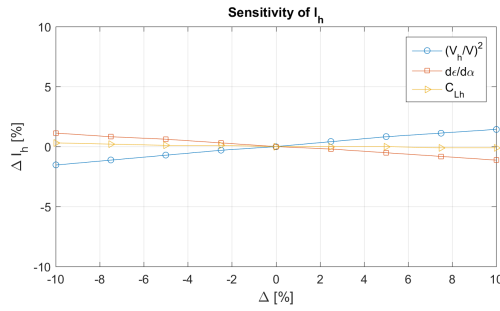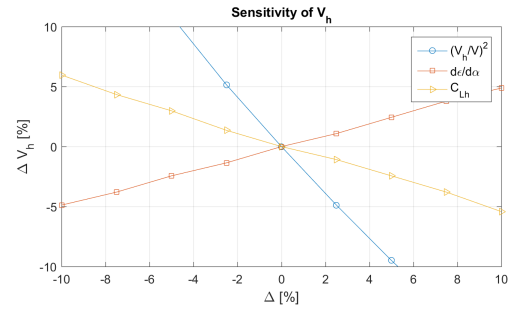
6.5 Sensitivity analysis

6.5.1 Preliminary tail design

In this section the robustness of the preliminary tail design is tested with a sensitivity analysis. A few system parameters which have a probability of uncertainty will be varied to investigate their effect on l_h and V_h. This way the validity of the results can be quantified. The following parameters will be varied:

- **Horizontal tail/wing airspeed ratio** Horizontal tail/wing airspeed ratio $(\frac{V_h}{V})^2$ is used as an horizontal tail effectiveness parameter in both scissor plot lines. Torenbeek assigns a value of 0.95 for a fin-mounted horizontal stabilizer [155]. This value is used in the design since the geometric center of the horizontal component of the V-tail is situated half-way the fin.
- **Distance between the horizontal tail and the vortex shed plane** This distance is used in the calculation of the downwash gradient of the horizontal tail, which is used in calculating the stick-fixed stability line in the scissor plot. The average height of the V-tail is used as reference to calculate this distance.
- **3D lift coefficient of the horizontal tail** C_{L_h} Is used in the line of the scissor plot which depicts the controllability at stall speed constraint. Torenbeek assigns a value of -0.8 for an adjustable horizontal tail [155].

Each parameter is varied in steps of 2.5% from -10% to +10%, every time iterating until l_h and V_h are converged. Final l_h and V_h values are plotted in Fig. 6.17 and Fig. 6.18 respectively.

- **Sensitivity of l_h** Fig. 6.17 shows that all parameters do not affect the tail arm greatly. The maximum deviation of tail arm is -1.53% at -10% deviation of $\frac{V_h}{V}$. The design of l_h is thus not very sensitive.
- **Sensitivity of V_h** Fig. 6.18 shows that V_h is more sensitive to changes of input variables. Increasing $d\epsilon/d\alpha$ increases the tail volume as the tail experiences a lower angle of attack due to higher downwash. Its effect on V_h is moderate at ±5%. Increasing C_{L_h} decreases V_h moderately at ±5%. Higher tail lift coefficient increases

Figure 6.17: Sensitivity of l_h

Figure 6.18: Sensitivity V_h

tail effectiveness an hence decreasing needed V_h. Increasing $(V_h/V)^2$ decreases the tail volume significantly. To determine $(V_h/V)^2$ most accurately, detailed flow analysis must be done. However, the uncertainty of design validity due to this sensitivity is mitigated by the dynamic requirement analysis, which will produce the final design.

6.6 Command

This section will elaborate on the command part of the control flow diagram in Fig. 6.3. The command center of HELIADES feeds a desired position and speed to the autopilot which consists of the positional and angular control block described in the first part of this chapter.

6.6.1 Hardware

Apart from the hardware necessary to make the aircraft fly, i.e. motors, propellers and actuators, the drone also requires hardware equipment for control, positioning, and vision. Removal mechanisms are examined in Chapter 10 and are thus left out in this discussion.

Vision

The drone uses its optical system for both visual identification of the environment as well as measuring distances en route. In order to use it as such, it requires a stereoscopic camera system, i.e. a system with two cameras thus simulating human binocular vision. An alternative solution is using a single camera and an optical flow algorithm [93]. This method is more suited for smaller drones that have stringent weight limitations for which shedding the mass of one of the cameras makes a grand difference. Nonetheless, it was ruled out due to the required calculation time and the immaturity of the technology involved.

The stereoscopic system is used to determine distances to objects ahead of the drone whilst in flight; elaborated on in more detail in Section 6.6.3. Potential vision system components were looked into, leading to the initial selection presented in Table 6.6.

Table 6.6: Trade-off of the visual system.

Model	Bumblebee XB3 [37]	Stereolabs Zed [48]	Mega DCS [32]
Resolution	$1280 \times 960 px$ @ 16 FPS	$1920 \times 1080 px$ @ 30 FPS	$1280 \times 960 px$ @ 7.5 FPS
Field of view/ Focal length	$97°/2.5 mm$	$110°/2.8 mm$	interchangeable lenses - varies
Power consumption	4W @ 12V	1.9W @ 5V	1W
Dimensions ($L \times W \times H$)	$277 \times 41.8 \times 37 mm$	$175 \times 33 \times 30 mm$	$125 \times 25 \times 37.5 mm$
Weight	$505g$	$159g$	N/A

Due to the combination of low weight, high resolution and timeframe, the final choice of the visual system went to Stereolabs' Zed. Moreover, it is a more modern alternative to the above mentioned choices, offering higher

resolution and better development support. The dimensions seemed to pose a problem, since the initial estimate of the fuselage width was in the range of 80mm. In order not to introduce any additional drag, the visual system will be mounted in the fore fairing of the wing, on top of the fuselage. The field of view will be slightly decreased due to the fuselage body, though this decrease is localized and does not obstruct the view ahead. Another downside is the price. At $449, it is not exactly cheap, although worth the price for a system component as critical as the vision system.

Other Sensors

The sensors required for conducting operations include the following:

- Laser range finder: *Lightware SF11/C* - used to determine the distance to target [25].
  - Range of 120m, with an accuracy of 0.1m.
  - Lightweight design (35g), with low average power consumption (15mW).
- Ultrasonic range finder: *LV-MaxSonar-EZ2* - shortsighted ultrasonic range finder mounted on the bottom of the fuselage, used for more accurate altitude determination during landing [31].
- Infra-red (IR) sensors: (3x)*Sharp GP2Y0A21YK* - one at each nacelle, and one located at the tail, to be used for collision avoidance [45].
- Barometer: *Bosch BMP180* - altitude determination unit [7].
- IMU: *9 Degrees of Freedom - Razor IMU* - inertial measurement unit comprising of a magnetometer, an accelerometer and a gyroscope. The power consumption was provided in terms of individual components, which has current draws in the range of hundreds of microamperes. The total power consumed by the IMU system (in combination with a 5V battery) is approximately 5mW [46].
- GPS: *LS20030-3* - 66-channel GPS receiver with a pointing accuracy of 2.5m. Higher accuracy would involve using Real Time Kinematic (RTK) navigation, which introduces a source of dependency, since this method of navigation requires a ground base for position corrections. Furthermore, visual guidance is used once the target is approached, deeming further increase in pointing accuracy redundant [26].
- CPU: *BeagleBone Black* - an ARM Cortex-powered board, with enough input-output ports (46 in total) for the required components, with additional ones in case more components are to be added [47].
- Pitot Tube: *PixHawk PX4 Airspeed Sensor* [36]- A small pitot tube unit, designed for drones specifically; used to get an accurate speed reading .
- ADS-B: *uAvionix pingRX* [56] - a miniature automatic dependant surveillance-broadcast device, used to help identify the drone in the vicinity of airports, so as to avoid collision with other (un)manned aircraft. A more expensive and power-consuming option would have been the Ping2020, a transceiver that provides 2-way communication. Instead, PingRX is able to identify other aircraft and avoid them accordingly, though it does not enable ADD to emit any signal. Having this device on-board will also make the ADD compliant with the proposed FAA's regulations that will become effective in 2020, allowing unmanned aerial vehicles to operate in controlled airspaces below the altitude of 6000ft [28].

The selected components were chosen based on their performance figures as well as cost. For some components, such as the IR sensors, the accuracy and quality are less pertinent than, for example, the power consumption. In other components, such as the laser range finder and the camera, the precision and range required justify the costs. The mass and power budgets of all the sensors mentioned above are provided in Table 6.7. In here, the power budget is estimated at 5V. Note that the prices are in dollars due to the suppliers mostly targeting the American market, the provided price in Euros was found using the average exchange rate, 02-Jun-2016 [99]. For the sake of brevity, the visual system is included in the table to encompass the general power and mass requirements of the command system. Furthermore, some of the components' mass specifications were unavailable (marked with 'N/A' in Table 6.7).

6.6.2 Hardware Integration

The visual components presented in Section 6.6.1 need to be integrated in one system, in order to provide any useful information. The BeagleBone CPU serves as an intermediary between the hardware components and software used to conduct real-time analysis of the surrounding. The CPU also provides the interface between the awareness system (i.e. visual and sensory equipment) and the flight control system. The data is then processed on-board using Linux-based OpenCV platform, which is a visual data processing package capable of real-time image processing. Disparity maps can be created from the stereoscopic image feed provided by the Zed camera, which are then to be used to determine any potential threats in the direction of heading of the drone [33]. IR sensors are primarily used for detection avoidance when in hovering flight, as they provide one-dimensional output, which is only to be used to inform the ADD that it is apporaching an obstacle from the sides or tail, as these are blind spots for the camera system. The main camera unit, on the other hand, captures and analyzes the environment in front of the drone, and is to be used primarily in horizontal flight mode, but also during hover (in combination with the rest of the

Table 6.7: Mass, power, and cost budgets for the electronic hardware components necessary for the operations.

Component	Power	Mass	Cost
Camera	1.9W	159g	$449
Laser range finder	20W (peak), 15mW (average)	(3x)35g	$249
Ultrasonic range finder	10mW	4g	$28
IR sensors	(3x) 1W (peak), (3x) 18mW (average)	3.5g	(3x)$14
Barometer	$25\mu W$	N/A	$10
IMU	5mW	5g	$75
GPS	0.135W	10g	$60
CPU	2.3W (max), 1.7W (average)	40g	$55
Pitot Tube	15mW	3g	$65
ADS-B	150mW	1.5g	$175
Total	**4.02W** (average), **27.5W** (max)	**269g**	**$1208 = €1063**

sensors).

6.6.3 Guidance & Tracking

The following section presents methods for conducting the mission, with a starting point of the ground station detecting an intruder. Firstly the drone is activated and launched from the vicinity of the ground station. Once it approaches the target drone it switches from absolute radar-guided position determination to relative positioning based on the visual system. Finally, the ADD needs to make a decision about the removal method used, when to use it, and how to proceed in case the intruder tries escaping capture.

Phase 1: Initial Response

The target drone is firstly identified using ground station's radar system. The message is relayed to ADD's on-board communication system, commanding it to deploy. Following the take-off maneuver, the ADD climbs to cruise altitude, above any obstacles that might present a collision risk. Nearing the target, whose coordinates are continuously relayed from the ground station, the ADD drops in altitude so as to match target drone's altitude.

In the context of the remained of this chapter, $\hat{A}$ is used to represent the absolute position vector of the ADD, whilst $\hat{B}$ denotes the intruding drones position vector. Once the ground station communicates $\hat{B}$, the ADD exits the standby mode and prepares for take-off. The take-off is done in the vertical hover mode, and the ADD stays in said mode until it reaches conversion altitude, since the climb rate is higher than in the conventional horizontal flight mode. Once the altitude is achieved, the ADD accelerates forwards (i.e. in the direction of the $\hat{B}$ position), and once the velocity of 23.2m/s is reached, it transitions into the horizontal flight mode.

The cruise altitude is based on the altitude of the intruding drone; if the intruder is flying at an altitude of less than 100m, the cruise altitude will be set at 100m. This height ensures that the fixed obstacles such as buildings are avoided during cruise flight, which omits the need for extensive obstacle avoidance processing, and allows the ADD to achieve its maximum speed. Any higher than that, and the ADD will assume the altitude of the intruding drone as its cruise altitude. In case there are buildings present in the surrounding area that are more than 100m in height, those can be marked as no-fly zones and can be avoided thereafter.

Obstacle Avoidance

It is crucial to remember that, as of the writing of this report, the global airspace is shared by both manned and unmanned vehicles. It is therefore of major importance to design an intelligent navigation system, especially considering that the drone in question is autonomously controlled. The drone should therefore not only be able to identify objects, but also react accordingly by changing its flightpath so as to avoid collisions. This entails a robust real-time information processing of the surrounding environment.

Different techniques have been explored in the field of object avoidance and trajectory planning. Most recently, methods have been developed that utilize Probabilistic Road Maps and Rapidly Exploring Random Trees [161]. These methods rely heavily on using probability theory to determine the next move, meaning that the system needs to determine as many possible outcomes. This requires significant computational power that cannot always be guaranteed against low cost and in a small enough form factor to be used on-board the ADD. An alternative

recently published technique circumvents this using so-called 'funnel libraries'. This technique sees the possible trajectories ahead as funnels, each funnel representing a summation of collision-free pathways [123]. This method also takes into account flight deviations such as cross-winds and navigational inaccuracies introduced by GPS, since it heavily relies on the data provided by the camera. An example of a possible trajectory plan scenario is presented in Fig. 6.19.
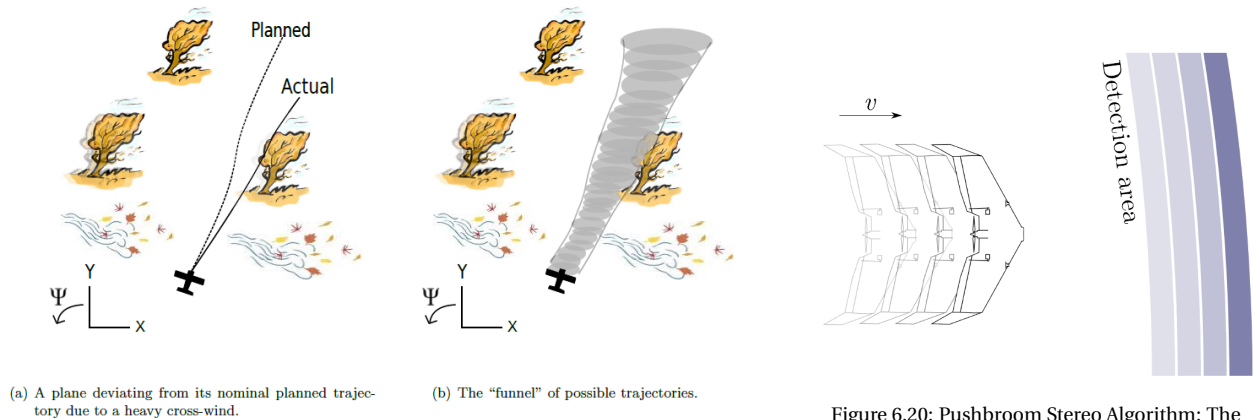
(a) A plane deviating from its nominal planned trajectory due to a heavy cross-wind.

(b) The "funnel" of possible trajectories.

Figure 6.19: Example of a possible flight scenario, (a) representing an undesirable outcome and (b) the funnel library solution [123].

Figure 6.20: Pushbroom Stereo Algorithm: The planes shown in blue are scanned consecutively, forming a full map of the drone's surroundings [77].

While the funnel libraries allow the drone to conduct calculations autonomously, trajectory guidance can be further improved by using an algorithm that scans for obstacles in only a single plane, equidistant to the drone. The scanning method is called the Pushbroom Stereo Algorithm, and is illustrated in Fig. 6.20 [77]. The continuously scanned areas ahead of the drone are combined with the drone's telemetry system information to provide a visualization of obstacles. These obstacles are then used to construct the previously mentioned funnels of possible trajectories. The Pushbroom Stereo Algorithm is superior to other methods due to its per plane analysis. This means that there is less data to process instantaneously when compared to other 3D visualization platforms, while still achieving the same result, as the un-scanned space will eventually be scanned as the drone flies forward.
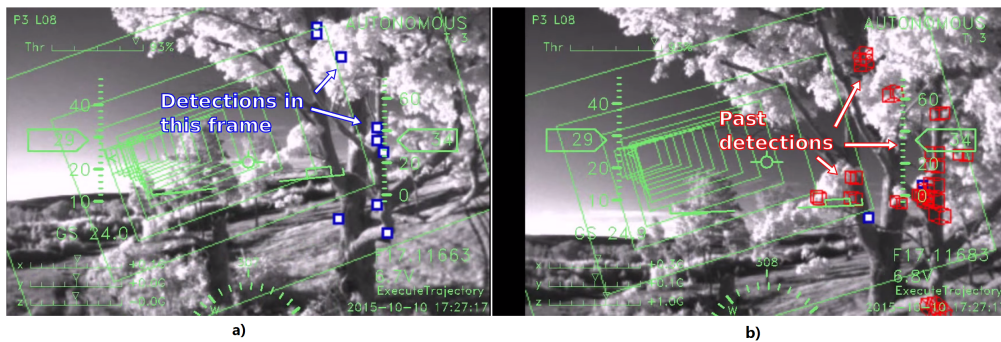

Figure 6.21: Pushbroom Stereo Algorithm: (a) Blue boxes present identified obstacles in the current plane being analyzed, (b) red boxes represent cumulative obstacles found in previous planes [77].

The above described software can be seen in Fig. 6.21, in combination with the discussed funnel libraries [77]. The travel 'funnel' can be seen in green. Notice the subtle shift of the trajectory due to the drone having to navigate around the tree branches, i.e. identified obstacles.

Phase 2: Visual Detection

Once the target drone is within range for the camera, the system switches to visual detection. This camera range is specified at 15m [48]. With the camera activated, the priority is to lock onto the target and initiate tracking of it. To this end, use is made of Linux-based OpenCV software, which is a visual data processing package capable of real-time image processing [33]. Contrast maps can be created from the stereoscopic image feed provided by the Zed camera using the OpenCV's *findContours* function. These maps can then be used to discern the target from the environment, thus allowing for a lock-on. This is illustrated in Fig. 6.22.

With the target being tracked, HELIADES will then maneuver such that the drone is kept in the center of the camera image. This means that, if the target moves to the right on the camera image, HELIADES initiates a positive yaw

---

Algorithm 1 Trajectory Planning

1: inputs: $\hat{B}$ - target destination vector, relayed from ground station, $\hat{A}$ - drone location vector, from GPS
2: initialize Pushbroom algorithm
3: load funnel libraries
4: **while** $|\hat{B} - \hat{A}| > 200m$ **do**
5:     climb to cruise altitude
6:     transition hover $\rightarrow$ horizontal flight mode
7:     accelerate to max speed
8:     update $\hat{B}, \hat{A}$
9:     recalculate $|\hat{B} - \hat{A}|$
10: **while** in flight **do**
11:     **if** $altitude(\hat{A}) \neq altitude(\hat{B})$ **then**
12:         align altitude $\Rightarrow$ increase/decrease
13:         update $\hat{B}, \hat{A}$
14:         recalculate $|\hat{B} - \hat{A}|$
15:     $\hat{A} \rightsquigarrow \hat{B}$ set heading towards target
16:     **for** plane i **do**
17:         identify obstacle (disparity map)
18:         get telemetry
19:         append obstacle and telemetry, **return** Φ_i = obstacles in plane i
20:         initialize current planned funnel F_i
21:         update current position $\hat{A}$
22:         update obstacle positions Φ_i
23:         **if** $\hat{A} \not\subset F_i$ **then**
24:             update flight heading
25:         **if** $F_i \cap \Phi_i \neq 0$ **then redo** funnels
26:             find funnel F_{i+1} such that $\hat{A}$ is contained in its inlet and has no intersection with Φ_i
27:             refresh F_i, Φ
28:     $i \leftarrow i + 1$ % next plane
29:     **if** speed $< 25m/s$ **then**
30:         transition $\rightarrow$ hover mode
31:     **else**
32:         transition $\rightarrow$ horizontal flight mode

---

through control surface deflections until the target is centered again.

Nevertheless, this does not yet address the issue of moving closer to the target to allow for removal. In order to accomplish this, the stereoscopic vision is again used. As the Zed camera delivers two images of the same object from different angles, the distance towards this object can be determined from the principle of equivalent triangles in a so called depth map [34]. The principle is depicted schematically in Fig. 6.23 [34].

Equation (6.26) holds due to the equivalent triangles present in Fig. 6.23.

$$x - x' = \frac{Bf}{z} \tag{6.26}$$

Here, $x - x'$ is the difference in distance of corresponding image points and their camera centers, B is the distance between the camera lenses, f is the focal length of the cameras, and z is the distance between the camera and the object X. As B and f are known, the distance of the object is inversely proportional to the disparity $x - x'$. Several algorithms exist that use this principle to determine the distance to an object [163]. By incorporating these algorithms in HELIADES, the relative distance to the target drone can be determined. Moreover, as images are generated perpetually by the Zed camera, the relative velocity of the target with respect to the ADD can be determined using the known frame rate (60fps at a resolution of 1280x720) and the difference in distance between two subsequent images [48].

The combination of the maneuvering to center the target in the image and the disparity positioning allows for tracking and chasing of the intruding drone. With the relative distance to and the relative velocity of the target drone known, the thrust can be adjusted accordingly to minimize the distance between the two vehicles to eventually
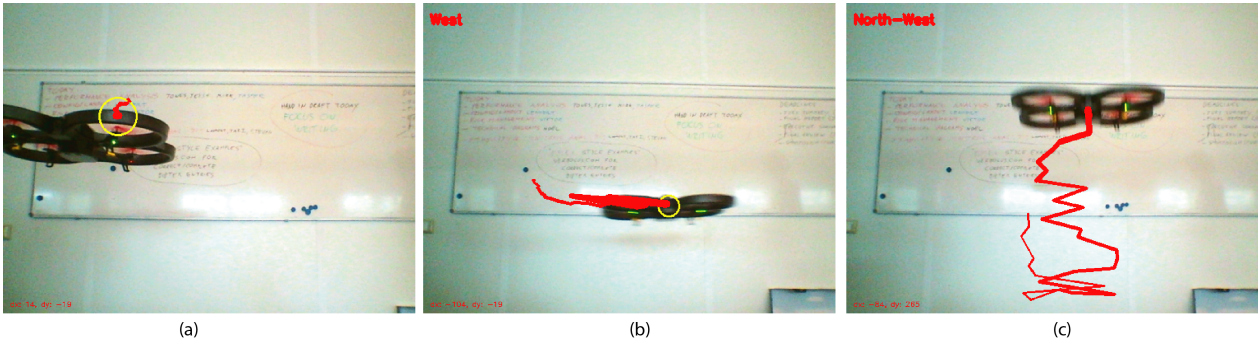
Figure 6.22: Test of the target tracking algorithm, (a) shows a drone in a fixed position, (b)&(c) show the drone maneuvering around the visual perimeter. Notice the hectic movements of the red track due to the camera picking up individual parts of the drones to track, and not the drone as a whole. This will not pose a problem with contrast maps as opposed to regular video camera feeds, in which the color discrepancy is based on the distance and not the lighting of the surroundings.
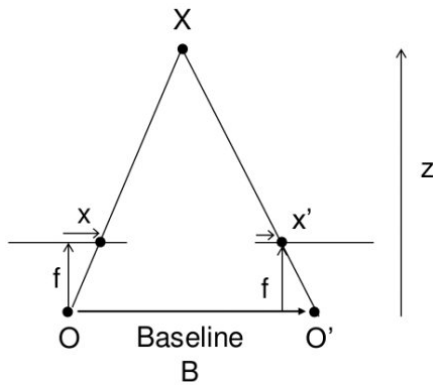

Figure 6.23: Schematic representation of the triangle existing between object X, camera one O and camera two O'.
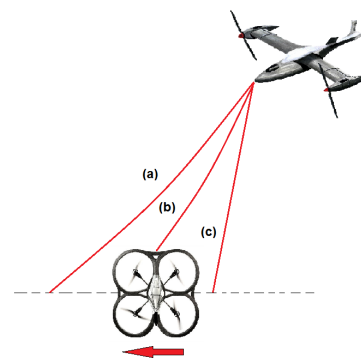

Figure 6.24: Aiming principles: (a) lead, (b) pursuit, (c) lag.

come within range to initiate removal. The aforementioned range is specified as 5m [1]. The approach used once this range is achieved is described in the next subsection. It should also be noted that the trajectory planning described in the previous section remains active in Phase 2.

Phase 3: Target Interaction

Phase 3 is initiated when the distance between HELIADES and the target is less than 5m away. This phase uses the same visual tracking methods as used in Phase 2 (centering using contrast maps and positioning/tracking using disparity maps). In the previous phase though, it was attempted to minimize the relative distance to the target, whereas in this phase the relative distance is kept constant by adjusting the thrust accordingly. This is done to avoid potential collisions, whilst still ensuring a sufficient distance for the removal system to be effective. The process is visualized in the flow diagram in Fig. 6.25. Note that Phase 2 elements are also present at the beginning of this flow diagram.

As seen in Fig. 6.25, the net is the preferred method of removal due to its non-destructive aspect. As long as nets are available, these are to be used for removal. When HELIADES is in this 'net'-mode, it will position itself slightly above the target. This is accomplished by adju1sting the centering algorithm such that the target is centered horizontally, whilst being located in the bottom half of the image. The desired position is chosen due to the weight of the net causing it to lose altitude. Besides, it also makes it more likely that the net will entangle the target's propellers, as these tend to be located at the top of most drones.

If the net ammunition has been depleted or if the target manages to evade HELIADES for more than 10 seconds, the secondary removal system is activated: the kinetic cannon. This cannon uses a different approach due to it firing destructive shells that experience limited gravitational pull. Aforementioned aspects make it more favorable to fly below the target and fire upward in a pull-up maneuver, as this limits potential danger on the ground and increases the likelihood of hitting the target due to the increased hit area. The latter is due to most drones having a greater top/bottom area than side area as the largest components are located in the body frame. The centering algorithm is adjusted for this 'kinetic cannon' mode in a similar way as described in the previous paragraph, only with the

---

[1] According to Delft Dynamics, a typical net gun takes approximately 3 meters to deploy fully.
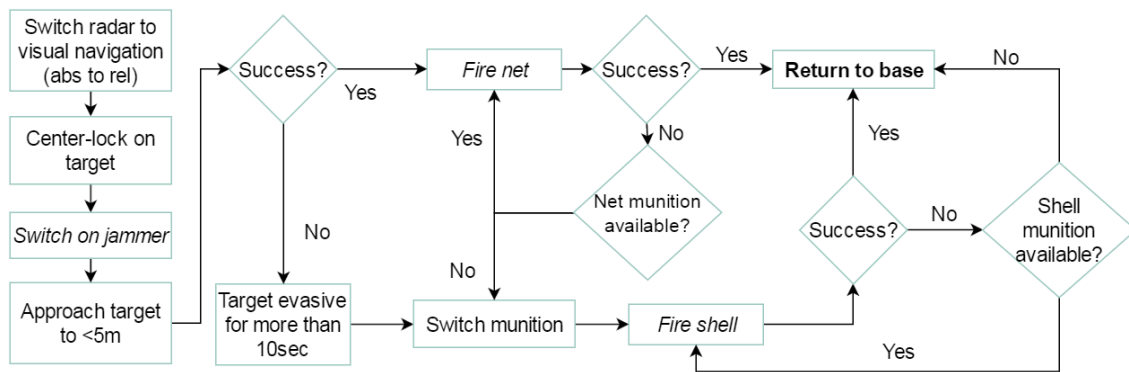
Figure 6.25: Flow Diagram of the target elimination process.

centering being performed in the top half instead of the bottom half of the image. Note that the kind of pull-up maneuver described previously does require excess thrust due to the conversion of kinetic and potential energy. Following the analysis from Chapter 5 though, this excess thrust can be delivered by the engines, thus negating this issue. Moreover, the fact that 'hail' bullets are used, meaning that multiple pellets fire out of a bullet, increases the chance of hitting the target.

To hit the target though, leading fire has to be delivered, meaning that the system aims slightly in front of the target rather than at the target. This is essential for successful removal due to the relative velocity at which the intruding drone is traveling. The situation is illustrated in Fig. 6.24.

The relative distance and velocity of the target are known, and by saving the deviation from the center of the camera image each frame, the direction of flight of the other drone can be determined. To clarify the latter: if the is located to the right on consecutive camera images, it can safely be assumed that the drone has a velocity component perpendicular to HELIADES' trajectory. Using this information, the firing mechanism is initiated by first adjusting the attitude such that the target is located at the mirrored position through the center of the camera image after which the cannon is fired. Illustrating this using the previous example of the target moving to the right on the camera image with a final position of (x,y) with the origin located at the center of the image, HELIADES changes its attitude to locate the target at position (-x,-y) at which it fires the shot. When the target is at this position, the barrel is aiming slightly in front of the other drone. This combined with the shell speed of 535m/s, as determined in Section 10.1, as well as the spread of the pellets, should lead to a sufficiently reliable removal system. However, this should be validated in the post-DSE phase once a complete prototype has been developed.

6.7 Verification and validation

6.7.1 Preliminary tail design

This section describes the verification and validation procedures to give an insight in the quality of the results of the preliminary tail design. The scissor plot overlaid with the center of gravity range plot is calculated in one file which contains 4 parts. One part calculates the values for the controllability at V_{stall} line, one part calculates the values for the stick-fixed stability line, one part calculates the center of gravity range values and the last part compares the input values with the output values.

For verification, all calculations to set up the scissor plot and center of gravity range plot were recalculated by hand in individual units and as blocks. Variables of the plotted lines were considered individual units and the line co-efficients were considered blocks. As this file is taken from an existing file which was composed and verified for a previous course AE3211-I, no errors were found in unit calculations and block calculations which were not altered from the original file. However, the file was edited to read out variables from a text file, resulting in a few mis-referrals. And the structure of the center of gravity range plot part was altered to accommodate different components, which lead to a few mis-placements of geometry. All were amended after thorough re-calculating. Another block verification was done by checking the linearity of the center of gravity range line. This line must be linear as shifting the wing group longitudinally has no effect on the total mass of the aircraft.

For validation, the resulting V_h and l_h from the existing file were checked against specifications of an existing aircraft, a Fokker F100 [87]. Since no definite component distribution information of the Fokker F100 or any other existing aircraft has been found, the precision of the center of gravity range plot can not be validated. Still, the resulting V_h and l_h were within 8% deviation.

6.7.2 Stability and control analysis

Aerodynamic derivatives are found from different sources and compared. It can be concluded that only the aileron derivatives from [144] differed with more than 10% from those found in other sources. The state space as a whole was verified using a validated state space of a Cessna Citation II from [80]. The model as a whole is validated by checking the reactions to various inputs and comparing the behavior with the expected one from [128].

The calculations of the control and aerodynamic moments are verified by hand. Validation of the procedure is done by comparing it to control actuation from [136].

7. Aerodynamic Analysis

This chapter describes the aerodynamic analysis of the anti-drone drone and a preliminary noise analysis. First, the approach for both analyses is discussed in Section 7.1. Then, Section 7.2 lists the used assumptions to simplify the models. Thirdly, Section 7.3 elaborates on the analyses with obtained results. Finally, the methods and results are verified and validated in Section 7.4.

7.1 Approach

7.1.1 Airfoil selection

The first step in the aerodynamic design process was the trade-off for the airfoil selection. From the performance analysis, a required wing loading of 170N/m^2 was retrieved, see Table 5.2. With this wing loading, a design lift coefficient $C_{l_{design}}$ has been calculated using Equation (7.1). This equation used to have a factor of 1.1 in front of it to account for the reduction in lift by the downwash of a complete 3D wing. However, it was found that a propeller placed at the tip of the wing, when spinning in the opposite direction of the expected wingtip vortices, increases the lift coefficient by a factor of approximately 1.1, depending on the propeller thrust setting [96]. Therefore, this factor could be omitted.

In Equation (7.1), Λ refers to the sweep angle of the wing. An advantage of sweep is that it reduces the effective velocity over the airfoil and therefore increases the free stream velocity at which supersonic flow occurs. Therefore, wing sweep is usually applied to aircraft that fly near a Mach number of 1. A disadvantage of wing sweep, however, is that the spanwise flow caused by the wing sweep lowers the stagnation point on the leading edge. This causes the effective angle of attack to be higher at wing sections further to the rear of the plane. This then leads to a lower stall angle, which is unfavorable. To avoid this phenomenon, and since the aircraft will be operating at low Mach numbers, the wing sweep has been set to zero.

With the previously mentioned wing loading of 170N/m^2, the value of $C_{l_{design}}$ is 0.11. This is the value of the 2D lift coefficient at which the airfoils were compared. The other parameter that needed to be known to be able to compare the airfoils to each other is the Reynolds number, given by Equation (7.2). Here μ is the dynamic viscosity, V is the velocity, taken at the required 50m/s (REQ-PERF-02), and $\bar{c}$ is the mean aerodynamic chord. With a chord of 0.34m (Table 5.2), the Reynolds number is 1,300,000.

$$C_{l_{design}} = \frac{1}{\frac{1}{2}\rho V^2 cos(\Lambda)} \frac{W}{S} \qquad (7.1) \qquad\qquad Re = \frac{\rho V \bar{c}}{\mu} \qquad (7.2)$$

7.1.2 Aircraft

The first step that was done to get an analysis of the complete aircraft was to import the airfoils of the main wing and the tail. The tail airfoil is a NACA 0012, as will be elaborated upon in Section 6.3.3. These airfoils needed to be analyzed in 2D before interpolating it to 3D. This 2D analysis has been to be done for a range of Reynolds numbers the wing can experience at the cruise Mach number. The Reynolds numbers that were analyzed were in the range from 30,000 up to 6,000,000. Once the 2D airfoil data was analyzed for a large range of angles of attack (-10° up to 25°) the aircraft dimensions could be defined for analysis.

The first step of defining the aircraft geometry was to select the airfoil of the main wing. After that the span, chord (Table 5.2)and the sweep value were inputted. Then, the tail and body dimensions that have been determined in Chapter 6 were inputted and all the components were given a mass, from which the resulted moment of inertia is retrieved that is used for the stability analysis. Once this was all done the method and analysis could be chosen. The method that was chosen for this case is the horseshoe vortex method. Two other methods available in the software tool are the ring vortex method and the lifting line theory method. The lifting line theory has limitations its limitations since it assumes incompressible flow, inviscid flow and can't be used for swept and low aspect ratio wings [73]. The horshoe and ring vortex method cannot be used for large angles of attack and require an inviscid, incompressible and irrotational flow. The ring vortex method gave results similar to the horseshoe vortex method, but the horseshoe gave more realistic results at higher angles of attack when compared to real data [95]. The Lifting line theory was not used since it did not converge and made the program crash for unknown reasons. For more details on these methods the reader is referred to [73]. For this analysis the assumption of in-viscid flow gives accurate enough results for this stage of design.

The type of analysis that was chosen was a constant lift analysis and a constant speed analysis depending on the type of output data that was needed. The constant lift analysis runs through a range of angles of attack and then calculates the required speed that is needed to fly at this angle this means that the data that is then retrieved is the complete range of speeds at which the aircraft can operate.

To model the influence of the propellers, a piece of symmetric wing with a relatively high thickness was attached at the wingtip to represent the nacelle. Next to that the propeller induced velocity was calculated and by multiplying the lift distribution with the relative change in velocity a new lift distribution could be made. The same approach has been taken for the drag coefficient.

The effect of the propeller on the wing tip vortices was hard to calculate and required complex software. Due to the limited amount of time and resources available this analysis could not be performed. Therefore, experimental data of wingtip placed propeller wing interaction wind tunnel experiments had to be used as a reference [158]. What could be concluded from these experiments is that the tip placed propellers counteract the wing tip vortices that normally occur and with that lower the induced drag that is normally experienced. The propeller creates a downwash which locally reduces the angle of attack and therefore also reduces the angle at which $C_{L_{max}}$ is achieved. Because the velocity is increased locally however the value of $C_{L_{max}}$ is higher than without the propeller because of the increased velocity. These findings were implemented into the lift drag polars by multiplying the lift and drag coefficients by their relative velocity. Since XFLR5 already underestimates the drag coefficient the reduction of the induced drag was neglected to compensate for this underestimation.

7.1.3 Noise

Noise is defined as 'sound that is unwanted by the observer' [142]. Noise is an important issue considering the sustainability of the UAS and is closely linked to aerodynamics, as noise is caused by vibrating air. To perform computational aeroacoustic procedures, thorough CFD analyses have to be performed. This is outside of the scope of this project as it would simply take too much computational time and power. Therefore, other methods have been addressed to estimate the amount of noise produces by the ADD. In this section, the maximum allowable amount of daytime and nighttime operations are determined considering the noise requirement. First, methods are described and hereafter the results and discussions are elaborated upon.

Before stating the different methods that are used, first is determined what should be analyzed. The noise requirement (REQ-SUST-06) states that the Day-Night Average Sound Level (DNL) should not exceed 65 dB. In order to determine this, the Sound Pressure Level (SPL) is determined, which gives an indication of the level of noise heard by an observer. If the SPL is zero or less, the noise is inaudible for humans. Furthermore, the SPL at distance S can be determined if the SPL at 1m is known according Equation (7.3).

$$\text{SPL}|_S = \text{SPL}|_1 - 20\log S \tag{7.3}$$

Different noise sources are distinguished. Aerodynamic noise can be divided in two main sources, which are periodic and broadband noise. Most noise analyses distinguish blade slap, rotational and vortex sources as the most important sources regarding rotor noise [121].

Two different methods were used to determine the SPL. The first one is elaborated on in Elements of Aviation Acroustics by G.J.J. Ruijgrok [142]. It is an empirical method, based on numerous conventional propeller aircraft and their experimental data. The maximum SPL from a distance of S meter from the observer was estimated using Equation (7.4). These parameters are the shaft power P_{br}, rotor radius R_b, tip Mach number M_{tip}, number of blades N_b and number of rotors N_r. All of these parameters have been calculated in Chapter 5.

$$SPL_{max}(r) = 83.4 + 15.3\log P_{br} - 20\log 2R_b + 38.5M_{tip} - 3(N_b - 2) + 10\log N_r - 20\log S \tag{7.4}$$

However, as noise is mostly not equally distributed from the source, the maximum SPL level is higher in certain directions. For this analysis, the worst case scenario was considered, which is at an emission angle of approximately 105° [142].

The second method is based on theoretical work from Gutin, described by J. Marte and D. Kurtz in 'A Review of Aerodynamic Noise From Propellers, Rotors, and Lift Fans' [112]. This method provides two equations, one for the rotational source and one for the vortex source. However, as the tip Mach number region of the ADD is significantly lower than for a conventional helicopter, vortex noise has been neglected. The root mean squared rotational noise pressure in dynes per squared centimeter is found using Equation (7.5) [112], where the argument of the Bessel function (J_{mN_b}) is $x = 0.8M_{tip}mN_b\sin\theta$. Furthermore some differences in units are present. S is the distance to

the observer in ft, R_b propeller radius in ft, A propeller disc area in ft^2, P_h shaft power in horsepower and T thrust in lb. Other parameters follow from the list of symbols. Using Equation (7.6) the pressure in Pascals is obtained.

$$P_{rms} = \frac{169.3 m N_b R_b M_t}{SA}\left[\frac{0.75 P_h}{M_{tip}^2} - T\cos\theta\right] J_{mN_b}(x) \qquad\qquad P\,[\text{Pa}] = 0.1 \cdot P\,[\text{dyn/cm}^2] \qquad (7.6)$$
$$(7.5)$$

The SPL in decibel can be calculated using Equation (7.7). Here, the root mean squared sound pressure from Equation (7.5), P_{rms}, and the reference sound pressure, P_{ref}, of 20 μPa [150] are used.

$$\text{SPL} = 10\log\left(\frac{P_{rms}^2}{P_{ref}^2}\right) = 20\log\left(\frac{P_{rms}}{P_{ref}}\right) \qquad\qquad (7.7)$$

According to Marte and Kurtz [112], reasonable results are obtained in the first few harmonic orders, so $m = 1, 2, 3, 4$. The overall sound pressure can be calculated by summation of the square root of the sum of the squares of the solution. The sound pressure level can be determined using Equation (7.7).

For both methods, the Day-Night Average Noise Level (DNL) can be calculated using Equation (7.8) [148]. The Federal Aviation Administration (FAA) has set a penalty for the time between 10pm and 7am, where w(t) is equal to 10 [148]. For the remaining time, w(t) equals 1. Furthermore, for L_a the worst case is assumed to be with an endurance of 363s, derived in Chapter 5. The integral of Equation (7.8) can be approximated by a summation and is therefore suitable for programming [148], with N the amount of operations per day, SEL the sound exposure level and w_i the penalty in decibel.

$$\text{DNL} = 10\log\left(\frac{1}{T_{day}}\int_0^{T_{day}} w(t) 10^{\frac{L_a(t)}{10}}\,dt\right) = 10\log\left(\frac{1}{T_{day}}\sum_{i=1}^{N} 10^{\frac{SEL_i + w_i}{10}}\right) \qquad (7.8)$$

With the requirement of the maximum DNL of 65 dB, the maximum amount of daytime and nighttime operations can be determined, as all parameters are known except for N as the SEL can be calculated using Equation (7.9). The SEL is assumed constant and equal to the SPL, which makes this a worst case scenario analysis.

$$\text{SEL} = 10\log\left(\frac{1}{T_1}\int_0^{T_{endu}} 10^{\frac{SNL}{10}}\,dt\right) = 10\log\left(\frac{1}{T_1} 10^{\frac{SNL}{10}} \cdot T_{endu}\right) \qquad (7.9)$$

For this analysis, the A-weighted sound pressure level has been assumed to be equal to the SPL, which is the most widely used because it is a good measure for perceived noise level [148].

7.2 Assumptions

7.2.1 Airfoil selection

- **Air properties:** All air properties are taken at sea level for all cases. This is not always the case since operation altitudes can get upto 4km altitude. This results in an underestimation of the Reynolds number, which in case leads to an underestimation of the aerodynamic performance of the airfoil.
- **Deviations from reality:** The error in the analysis is the same for all airfoils analyzed and can neglected in the comparison. This might obviously not be the case which might lead to the case that not the best airfoil has been selected.

7.2.2 Aircraft

- **Air properties:** All air properties are taken at sea level for all cases. This is not always the case since operation altitudes can get upto 4km altitude. This results in an underestimation of the Reynolds number, which in case leads to an underestimation of the aerodynamic performance of the airfoil.
- **NACA 0030 airfoil to represent the nacelle:** The nacelles can be modeled as NACA 0030 airfoils with increased chord length. This results in an overestimation of the lift they produce especially since the nacelle does not tilt completely but
- **Influence of rotors:** The influence of the rotors on the wing can be estimated by scaling the lift and drag coefficients with the relative velocity they experience due to the induced velocity from the rotors. Making this assumption is neglecting the fact that the rotors wake creates an increase of angle of attack on the wing.

This results in an underestimation of the lift coefficient and an overestimation of the maximum angle of attack.

- **Induced drag:** The assumption of the reduction of the induced drag coefficient depends on the propeller setting and therefore does not hold for all situations. This could therefore be either an under or overestimation of the drag coefficient.
- **Imperfections:** The effect of small imperfections in the wing and fuselage due to hatches and gabs between aileron and main wing are neglected. This results in an overestimation of the lift coefficient and an underestimation of the drag coefficient.
- **The fuselage can be simplified:** The approximate fuselage shape can be imported into the software to resemble the real shape. The complexity of the wing fairing and removal system parts sticking out of the fuselage cannot be resembled in the program.

7.2.3 Noise

- **Only rotors are considered as noise sources:** HELIADES is relative small compared to conventional aircraft and therefore, drag forces can be neglected.
- **A-weighted sound level is measured:** This is the most widely used sound level because it is a good measure for perceived noise level [148].
- **The A-weighted sound pressure level has been assumed to be equal to the SPL:** This serves as a worst-case scenario, as the sound pressure level is usually lower than the A-weighted sound pressure level.
- **Fly-over time is equal to the total combat time:** As this is the most time extensive part of the mission which could potentially take place at more less the same location.
- **Combat power is constant 3 kW:** Therefore, the integral from Equation (7.8) can be easily derived. This might be a wrong assumption, but the fly-over time should amply compensate for this.
- **Observer angles are 90°and 105°[142]:** These are the worst case scenario for both methods.

7.3 Analysis

7.3.1 Airfoil selection

Airfoil trade-off

To ensure that the optimal airfoil is chosen, a large number of different airfoils [2] were selected and their coordinates were gathered and imported into the XFLR5 software tool. Once imported an analysis was run for the Reynolds number of 1,300,000, considering a range of angles of attack from -10° to 25° with a step of 0.1°. After all airfoils were analyzed, the data was collected in an excel sheet which determined the cruise angle of attack; the angle at which the appropriate $C_{l_{design}}$ was reached.

The proper airfoil was then selected by performing a trade-off. Three trade-off criteria were selected and given weights. The efficiency at cruise ($\frac{C_l}{C_d}$), the maximum lift coefficient ($C_{l_{max}}$) and the range of angles of attack at which it can operate. The latter was determined by calculating the difference between the maximum angle of attack and the cruise angle of attack. The weights that were assigned to each criterion can be found in the second row of Table 7.1. The $C_{l_{max}}$ is the most important factor since it allows for both easy transition as well as high maneuverability, which are vital for the combat stage. It has therefore been given a weight factor of 4. Also important is the efficiency during cruise, but since it is not as critical for mission success or failure as the combat stage, the efficiency during cruise is granted a weighting factor of 3. Finally, the angle of attack range is not a critical factor but does have an effect on the possible operating possibilities and is therefore granted a weighting factor of 2. The airfoils that are in the table are a small selection of a database of 40 different airfoils, the 15 airfoils that were selected had the best trade-off values.

After the trade-off, a sensitivity analysis was performed by changing the weight factors to see how the results change. It was concluded that when the weight factors were changed by 1 or 2 points, it did not affect the top rated airfoil. The wing loading was also changed by 50%, but this also did not affect the trade-off winner. Thus, it became clear that the NASA/Langley ms(1)-0.317 was the best airfoil. It is a medium speed airfoil designed for general aviation. It has a maximal thickness of 17% at 37.5% chord and a camber of 1.7 at 72.5% chord.

Airfoil Sensitivity

The last thing that needed to be checked to make sure the airfoil is appropriate for the job is the sensitivity to roughness caused by dirt or bugs. A wind tunnel test of the airfoil done by NASA is taken as reference[125]. In this wind tunnel test the airfoil is tested with and without a roughness strip. This roughness strip placed at the leading edge of the airfoil is causing similar effect as, for example, dirt or bugs that hit the wing during flight. As can be seen in Fig. 7.1, the influence of the roughness strip on the lift curve and the drag polar is negligible.

Criteria	$C_{l_{max}}$-Score	$\frac{C_L}{C_d}$-Score	α-range-Score	Total Score
Weight	4	3	2	
S2060 8%	4.084	3.528	1.478	9.090
NACA 63-412	4.002	3.279	2.320	9.601
NACA 23012	4.552	3.159	1.828	9.539
NACA 22112	4.721	3.153	2.113	9.987
NASA/Langley ms(1)-0317	4.747	3.068	2.696	10.511
NACA 23112	4.639	3.017	2.022	9.678
NACA 63-215 modB	4.746	3.007	2.009	9.762
MH 93 15.98%	4.306	2.987	2.307	9.600
NACA 24112	4.538	2.919	1.945	9.402

Table 7.1: Airfoil trade-off at Re=1,300,000. The scores assigned to each airfoil were found by dividing the specific values of $\frac{C_L}{C_d}$, α-range and $C_{l_{max}}$ by the average of all airfoils selected. All these factors were then multiplied by the weighting factors and added up to get a final trade-off grade.
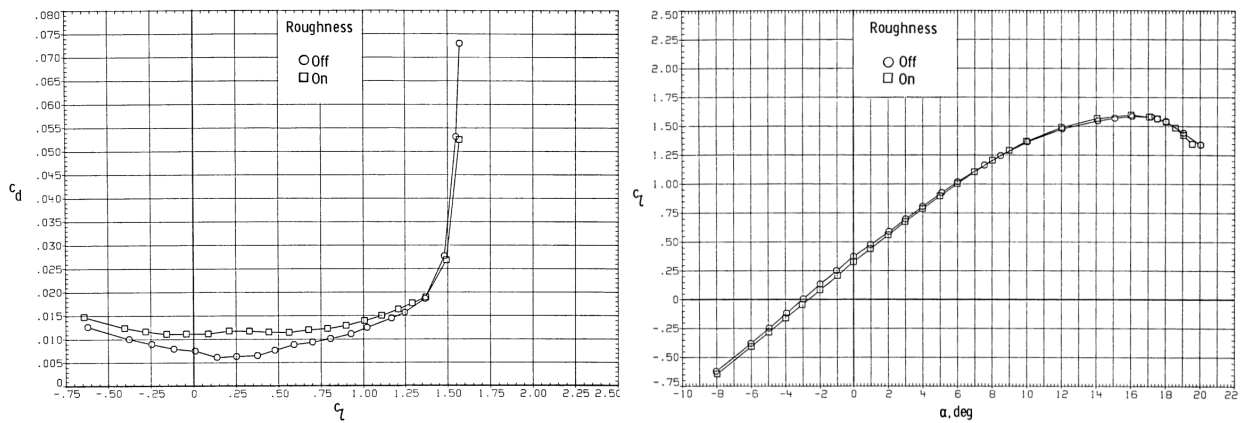

Figure 7.1: Results of wind tunnel test of the NASA/Langley MS-(1)0317 airfoil performed by NASA at Re=$2 \cdot 10^6$, M=0.15

The only difference that can be spotted is that the characteristic laminar bucket is not present anymore since the flow becomes turbulent due to the roughness strip. This means that the airfoil is insensitive to dirt regarding the maximum lift coefficient but does lose some efficiency in cruise condition. This is confirmed by the software tool used. It showed a transition from laminar flow to turbulent flow at large angles of attack at the leading edge of the wing. This phenomenon leads to the roughness having a little effect on the lift curve and $C_{l_{max}}$ values.

7.3.2 Aircraft

The aerodynamic forces could now be calculated for three different cases. The first case is horizontal flight in aircraft mode at 50m/s. The second is forward flight in helicopter mode at 25m/s with the rotors tilted to an angle of 73.6° with respect to the wing chord. Finally the aerodynamic forces are calculated in full vertical flight, where the rotors have an angle of 90° with respect to the wing chord. The final result with all the aerodynamic forces can be found in Table 7.2

Horizontal flight

For the first case the lift and drag polar was constructed by first analyzing the aircraft without propellers in XFLR5 Fig. 7.3. Then the pressure drag coefficient was multiplied by the relative velocity it experiences to get a drag distribution that is adapted for the propeller influence. For the horizontal flight at 50m/s, an induced velocity of 0.314m/s is produced by the propeller. An approximation of the induced velocity distribution was made based on reference data [158] and can be found in Fig. 7.6. The effect of the propeller on the induced drag was also estimated on reference data and showed that the drag coefficient is reduced by 0.01 if the propeller is turning in the opposite direction of the wing tip vortices. With these adjustments, the new lift and drag polars could be plotted, which are shown displayed in Fig. 7.4.

It should be noted that the data is not accurate at high angles of attack. This is because the program did not con-

verge at these higher angles of attack. According to the program, the wing keeps producing more and more lift up to an angle of attack of 40° which is impossible in practice. The maximum lift coefficient that can be achieved has been assumed to be similar to that of the airfoil. A full 3D wing has a lower maximum lift coefficient than the airfoil, a $C_{L_{max}}$ that is about 90% [72] of the $C_{l_{max}}$ that of the airfoil. Since the propeller increases the maximum lift coefficient again by about 10% this effect the maximum lift coefficient has been determined to be 1.6. The lift distribution in cruise can be found in Fig. 7.2

Tilted flight

The second case that is analyzed is vertical tilted flight where the drone has a forward velocity of 25m/s and the propellers are tilted forward with an angle of 73.5° Chapter 5. The induced velocity from the propellers in this case is 2.145m/s. The effective velocity and angle of attack experienced by the wing then is 21.0m/s at an angle of attack of -17.6°. To analyze the effect the part of the wing that is influenced by the propeller is analyzed under the conditions described previously. This data is than added to rest of the wing analyzed at 25m/s and 0° angle of attack. The lift distribution for tilted flight can be found in Fig. 7.2.

Vertical flight

For vertical flight the drag coefficient is determined differently than for the horizontal flight. This is because the program did not give accurate results for high angles of attack. At an angle of attack of 90°, the program calculated a lift coefficient of -1.5 and a drag coefficient of the same magnitude as for 0°, which is not expected. Therefore an approximation has been made to say that there is no force in the fuselage direction and only a force in the vertical direction. Furthermore, it is assumed that each wing section has a drag coefficient of 0.8 which is the drag coefficient of the airfoil at an angle of attack of 90°. This coefficient is then scaled with the relative velocity just as has been done in horizontal flight, see Fig. 7.2.

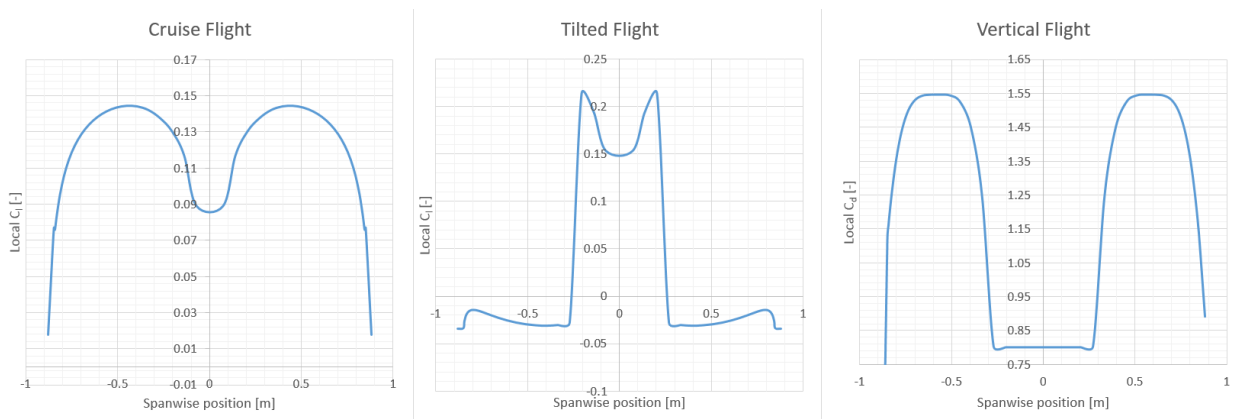

Figure 7.2: Spanwise lift distribution for 3 cases: Cruise flight 50m/s, α = -1.2°; tilted flight 20m/s, flight angle = 0°; vertical flight 8m/s
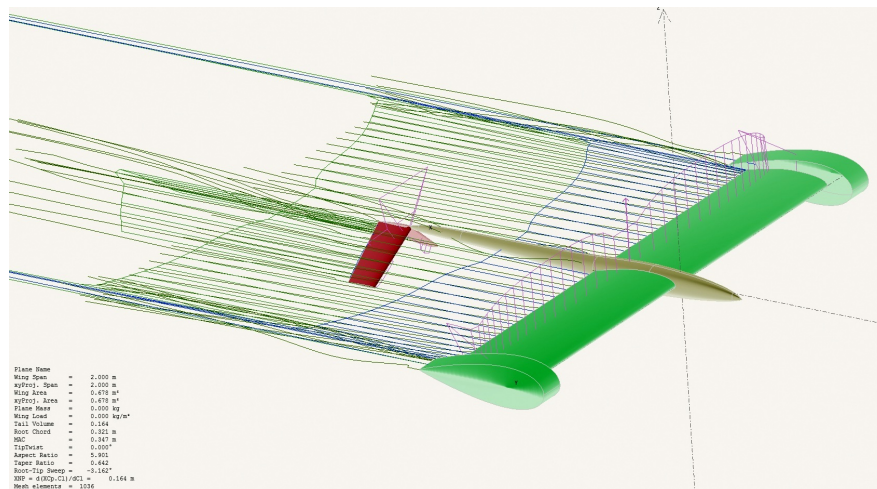

Figure 7.3: The lift and drag forces calculated using XFLR5 graphically visualized. Forces are for the aircraft without propellers, the propeller interaction is modeled afterwards as explained in Section 7.1.2.
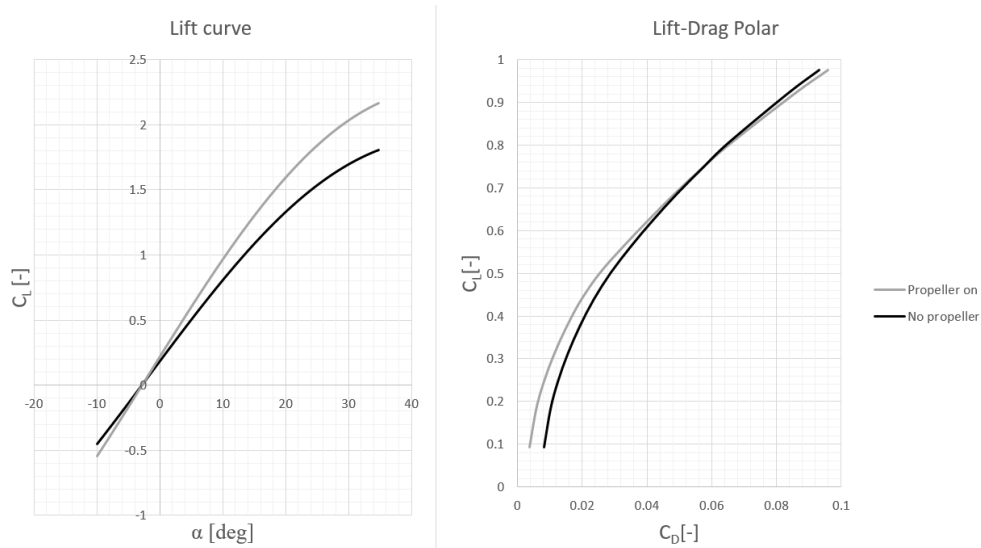
Figure 7.4: Lift polar and Drag polar of the complete aircraft showing the influence of the tip placed propellers Re=$1.3 \cdot 10^6$ M=0.14.

Stability derivatives

For the stability analysis only one method is available, which is a combination of a 3D panel and a ring vortex method. The outputs of this analysis are the moment coefficients and the eigenvalues of the eigenmotions. The former have been used in the stability and control analysis in Chapter 6. However, the accuracy is questionable since these results differ up to 40% from reality [95]. Since this difference is relatively large where possible the values of the stability derivatives have been determined using empirical methods as described in Chapter 6.

Table 7.2: Values of the aerodynamic coefficients.

Coefficient	$C_{l_{max}}$	$C_{L_{max}}$	$C_{l_{design}}$	C_{D_0}	$C_{D_{tilted}}$	$C_{D_{cruise}}$	$C_{D_{vertical}}$	$C_{L_{tilted}}$	$C_{L_{cruise}}$	$C_{L_{vertical}}$
Value	1.7	1.6	0.11	0.012	0.031	0.016	0.8	-0.8	0.010	0

7.3.3 Noise

The SPLs derived by both methods for different altitudes are presented in Table 7.3. These altitudes are chosen in such a way that 1m is the minimum operating distance and 15m (50ft) is the minimum operating altitude (see Chapter 5). The others serve as a reference. From the values from the first two columns from Table 7.3, the SEL could be calculated using Equation (7.9). An combat mission time of 30s and T_1 is equal to 1s are used as input parameters, as the T_1 serves as an scaling factor for the event.

With these SEL known, the amount of daytime and nighttime operations can be determined with the 65 dB DNL requirement taken into account. Note that these operations should then all be executed on the same altitude. As mentioned before, the noise penalty of 10 dB yields between 10pm and 7am. Rewriting Equation (7.8) with SEL (from Table 7.3) and DNL (from the requirement, 65 dB) known, the number of operations can be determined with Equation (7.10). The results can be seen in Fig. 7.5. For choosing the SEL of both methods, the Ruijgrok values are chosen as they are significantly higher compared to the Marte and Kurtz SELs.

Altitude [m]	Ruijgrok SNL [dB]	MK SNL [dB]	Ruijgrok SEL [dB]	MK SEL [dB]
1	76.69	68.10	94.47	85.88
15	53.17	44.58	70.95	62.36
25	48.74	40.14	66.52	57.92
50	42.72	34.12	60.50	51.90

Table 7.3: Sound Pressure Levels and Sound Exposure Levels for different methods at different altitudes, MK is Marte and Kurtz.

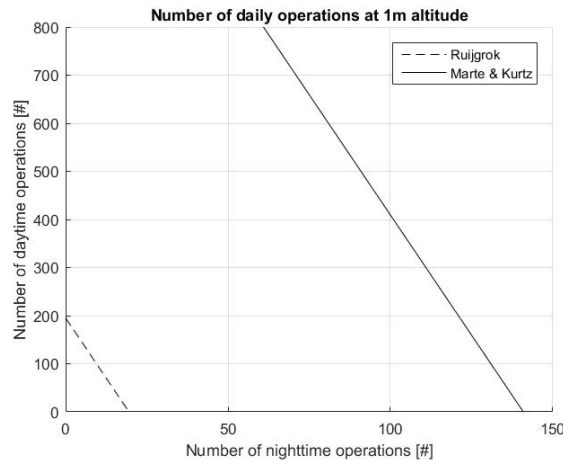$$N_{day} = 10^{11.436 - \frac{SEL}{10}} - 10N_{night} \tag{7.10}$$

Figure 7.5: Number of operations possible at different altitudes.

From Fig. 7.5 it can be noted that the 10 dB penalty has a major influence on the amount of operations possible as the horizontal axis has a significant lower range compared to the vertical axis. It can be concluded that HELIADES can operate as many times it wants, during both day and night. As Fig. 7.5 shows the number of operations at 1 meter altitude for both aforementioned methods, this result in approximately 200 operations during daytime, which is expected to be far more than needed.

Using the altitude scaling of Equation (7.3), the SPLs were investigated at cruise altitude. It turned out that the sound pressure values became negligible at this altitude.

7.4 Verification & Validation

In order to ensure that the methods have been implemented correctly, and to ensure that the applied methods are applicable in practice, verification and validation procedures have to be performed. This section deals with the verification and validation of the applied theory in the aerodynamic analysis of the airfoil, the aircraft and the noise.

7.4.1 Airfoil selection

Verification

The verification process for the airfoil selection follows the following method. The first thing that is checked is the airfoil data. With the software tool that was used XFLR5 NACA airfoils can be generated. To verify these airfoil shapes they were compared to airfoils from a database. If the airfoils were similar it is known the correct shape is inputted. Then the data that was outputted was compared to data with similar inputs available on [2]. If the output data of these two matched the method is verified to be used correctly.

Validation

To validate the data that has been achieved using the method described in Section 7.1 the data has been compared to wind tunnel experiments. Since the method used to analyze airfoils is also used in the analysis of the complete aircraft the 2D software tool is validated in Section 7.4.2.

7.4.2 Aircraft

Verification

To verify that the methods that were used up till now are used correctly, the following method for verification has been applied. The first step in the verification process was to check all the input values. After that the settings for the analysis were checked so that they with the critical situations for either performance, stability and control or the structural loading. After that the geometry inputted in the tool was compared visually to the CAD-model that was made. After the analysis was performed, the forces were visualized on the model and were checked on the expected direction. After the data had been adjusted for the propeller effect, the results were plotted to see if they were as expected. After these steps, the analysis could be considered verified.

Validation of theory

One method to validate the selected method would be to use reference data. However since the design is unique in its kind, no comparable reference aircraft exist. The only aircraft that is similar in looks is the American Dynamics AD-150, however since its propulsion system consists of two ducted fans the propeller wing interaction is completely different from the current design [154]. Other tiltrotor aircraft do use propellers but have completely different fuselage shapes and tail design because of their different purposes. Comparing the acquired data from the methods to these aircraft would give an impression of order of magnitude of what the results should be but would not give accurate data to validate the method used. Therefore, to completely validate the methods used experimental tests should be executed. Since the wing and fuselage can be 3D printed, a scaled model of the aircraft can be made relatively cheap. With this model a wind tunnel test can be executed to exactly determine all aerodynamic coefficients and stability derivatives. In the same test the effect of the propeller can be determined by both testing with and without the propeller running.

For further detailed design more complex CFD software can be used to give more accurate results. This software could also used to validate the first method that was used so far. This more accurate method however is more time extensive and resources to get accurate and reliable results might also need to be validated, especially when considering the fact that it is not yet possible to accurately model the effect of rotating propellers using these types of software. For now, validation is limited to compare a computer-generated heavy lifting tiltrotor design to get an idea of order of magnitude and general lift distributions. The data that was used to validate the aerodynamic analysis is retrieved from a full CFD analysis of a heavy tiltrotor aircraft [109]. The induced velocities and the drag decrease due to the propeller influence were compared and can be found in Fig. 7.6. It can be seen that for the incidence angle of the propeller of 0° the shapes of these velocities look very similar. After that, the values of $\frac{L}{D}$ were investigated that can be achieved by tiltrotors. It was found that values close to 8 during horizontal flight are common. The values that are achieved for the current design are close to 10, meaning it is more efficient. This can be explained by the fact that it is designed for a different purpose than the reference aircraft. These aircraft are mainly build for lifting heavy objects while HELIADES has been designed for maneuverability and speed in horizontal flight.
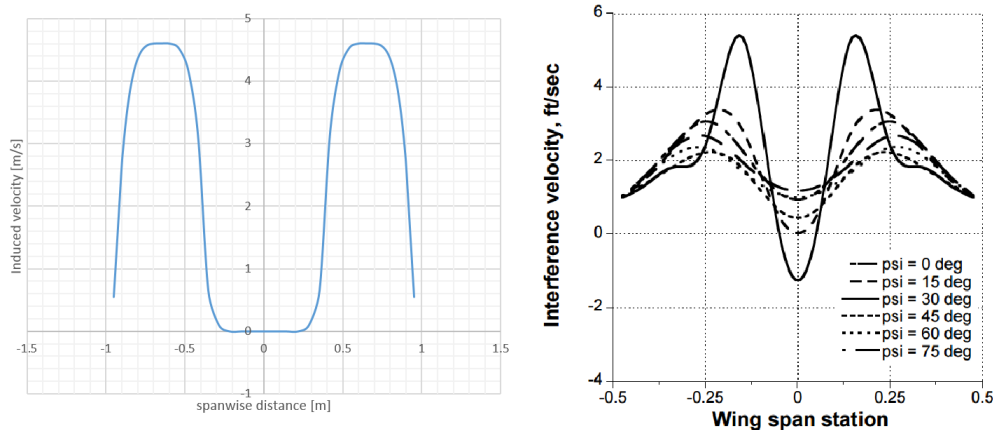

Figure 7.6: On the left the calculated induced velocity, on the right induced velocity from reference data.

Validation of software

As has been stated in the analysis of horizontal flight, XFLR5 only gives accurate results for the linear part of the lift-drag curve and is thus inaccurate at high angles of attack. Additionally, since XFOIL is integrated in the program, the limitations of XFOIL must be taken into account as well. Xfoil only works well at lower Reynolds numbers.[98]

To validate the software tools at low angles of attack, a comparison must be made between real data [125] and the simulated results. To compare the results the input parameters for the software tool need to be exactly the same as for the experimental data. In Fig. 7.7, simulated airfoil data is compared to a wind tunnel test.

What can be seen in Fig. 7.7 is that XFOIL overestimates the lift coefficient and underestimates the drag coefficient. It also overestimates the maximum lift coefficient that can be achieved. When looking at the other experiments conducted at higher Reynolds numbers, the data starts to look more similar to the XFOIL data. From this the suggestion is raised that XFOIL underestimates the the effect of lower Reynolds numbers. However, the lift curve slope is accurate and by taking the maximum lift coefficient of the experimental data a good estimation can be made of the C_{Lmax} of the complete aircraft.
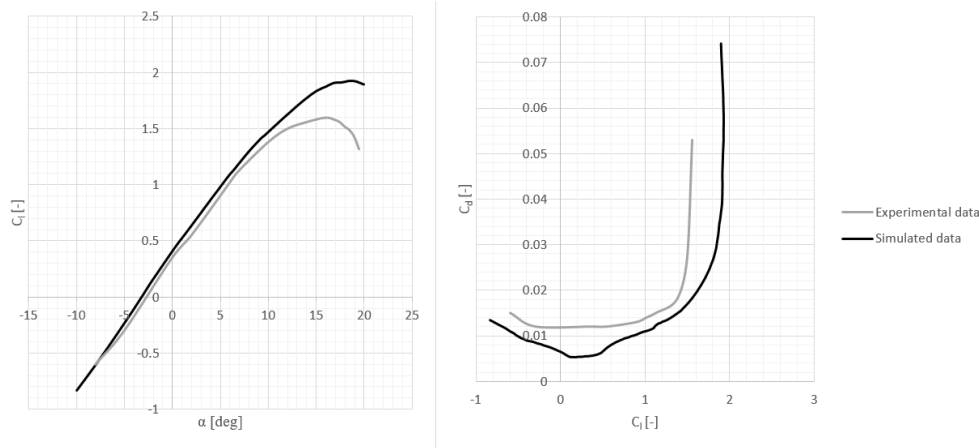
Figure 7.7: Simulated airfoil data compared to a wind tunnel test Re=$2 \cdot 10^6$ M=0.14.

For validation of the XFLR5 software for the complete aircraft research has already been conducted [95]. In this research a real aircraft has been modeled in the software, and simulations were run and compared to test data. A general note that can be made for the XFLR5 software is that the drag coefficient is underestimated by 20-30%. For the airfoil trade-off this discrepancy in drag coefficient does not matter since all airfoils are analyzed by the same software and therefore share this discrepancy. However for the analysis of the complete aircraft this discrepancy should be taken into account. Next to that the program also calculates the moment coefficients for side-slip and roll angles. These differ significantly from realistic data and these values should only be used as guidance and a possible first estimate for the control derivatives.

7.4.3 Noise

Verification

Verification has been performed by eliminating coding errors, adding comments to structure the code and using print statements and manual calculations to verify the calculations. Furthermore, a unit test is done to check consistency in units and correct usage. Lastly, experts in this field were consulted to check the results and from their feedback, more realistic values were obtained as the fly-over time was misinterpreted.

Validation

As there are two methods used, validation is already performed as the SPL levels from Table 7.3 differ just a little for both methods. Furthermore, a small experiment is performed to determine the noise level (A-weighted) of a hovering quadcopter, on which both methods are applied for further validation. Results from this are shown in Table 7.4. The Parrot AR.Drone.2.0 is used to perform this experiment and a Tenma 72-947 decibel meter is used to measure the A-weighted sound level.

Table 7.4: Noise method validation results.

Meas. nr.	Distance [m]	Measured Noise Level [dB]	Ruijgrok method [dB]	Marte & Kurtz method [dB]
1	1	71	75.66	58.59
2	1	70	75.66	58.59

There can be concluded that the empirical Ruijgrok method provides more accurate results for small UAVs at close distance. However, due to time constraint, no perfect experimental setup was used, which could be improved during the post-DSE phase.

8. Structural Analysis

This chapter discusses the static structural analysis of HELIADES. Firstly, the assumptions used are presented. Secondly, the wings and fuselage are analyzed and optimized. The load case considered during aircraft mode is that of a sharp turn with a load factor of 20, and that during helicopter mode is forward flight at a tilt angle of 17.4° and maximum power. These cases were determined to be critical in Chapter 5. Thirdly, additional considerations are discussed following the finalized design. Finally, verification and validation procedures are presented.

8.1 Assumptions

This section elaborates on the assumptions used throughout the chapter.

- **No axial loads in the wing:** there might be some axial loads present due to, for instance, gusts, but these are considered negligible compared to aerodynamic and thrust loads.
- **The aileron does not carry loads:** the wing box is the main load carrying component of a wing, to which the aileron is attached. It will therefore not carry significant loads during flight.
- **Airfoil symmetry:** the airfoil is assumed to be symmetric around the chord line so as to simplify the analysis. In reality, a camber is present, thus leading to an asymmetric airfoil. As this camber is small in this case, this assumption is deemed justified.
- **Skin between booms is straight:** in reality, the skin will be curved. However, by assigning sufficient booms, the curvature can be approximated with only a small error.
- **Thrust acts along the plane of symmetry:** the engines are attached at the end of the wings, providing a concentrated thrust force. As the thickness of the airfoil is relatively small, the thrust can be assumed to act along the plane of symmetry with a negligible error.
- **Engine weight acts through the centroid:** in reality, it will likely cause a torque, forcing the leading edge down. However, the torque caused by the lift is probably significantly greater than the engine weight torque, thus justifying this assumption.
- **The cross sectional shape remains unchanged and the rate of twist of multiple cells is equal:** in reality, some deformation in the shape will be present, albeit small. The moments of inertia and boom coordinates therefore change only slightly, thus justifying this assumption.
- **The skin thickness is assumed to be 1mm:** this value comes from the minimum thickness that can typically be manufactured for plastics and composites [105, 149]. This value is not definitive as the optimal thickness might differ. The latter is considered throughout this chapter.
- **Aircraft symmetry:** HELIADES is assumed to be symmetric about the length of the fuselage in both its geometry as well as its load distribution. The latter might not be true in reality due to, for example, aileron deflections or asymmetric gusts. Nonetheless, the maximum load case occurs in a sharp turn when the aircraft is oriented at the desired roll angle with zero roll rate. In this case, the ailerons are no longer deflected. Therefore, the load symmetry assumption should result in only minor errors.
- **Reaction forces act through the centroid:** in reality, there might be a small eccentricity present, but this would cause only small deviations.
- **The fuselage is modeled as a cone:** as determined in Chapter 6, the fuselage has a decreasing cross sectional area from nose to tail that is approximately conical. In reality though, the shape is more complicated, thus leading to small discrepancies.
- **The fuselage does not produce lift:** in reality, a lift distribution exists over the fuselage, but this is significantly smaller than that produced by the wings. It can therefore be neglected with a limited accuracy penalty.

8.2 Wing Analysis

This section elaborates on the structural analysis of HELIADES' wings. First, FBDs are provided after which loading diagrams are constructed. Next, the stress analysis is presented for both aircraft and helicopter mode, which is followed by material selection. Finally, a buckling analysis and optimization are performed.

8.2.1 Free Body Diagram (FBD)

This subsection provides FBDs of the design, showing all forces acting on it. As HELIADES has the ability to function as both an aircraft and a helicopter, two situations have to be analyzed as shown in Fig. 8.1 and Fig. 8.2. Note that these FBDs display the initial design of the aerial vehicle. In this chapter, the aircraft mode is used to describe the

approach, as the analysis method for helicopter mode is very similar.

There are four main force categories present, being lift (L_w and L_h), weight (W), thrust (T_p), and drag (D_w, D_h, and D_f). Note that the distributions are not necessarily shown with their actual shape, as the main purpose is to visualize the force types acting on the structure. For more specific lift and drag distributions, the reader is referred to Chapter 7.
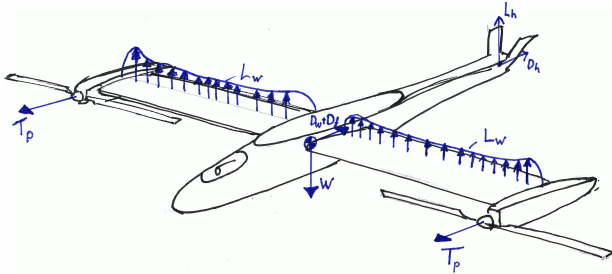

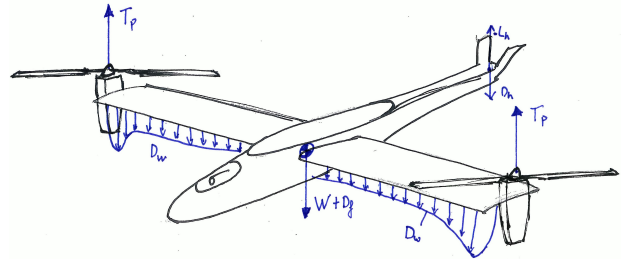Figure 8.1: FBD for HELIADES in aircraft mode.

Figure 8.2: FBD for HELIADES in helicopter mode.

In order to analyze the wing, the present symmetry is used to model the wing and part of the fuselage as a cantilevered beam. The load case presenting itself then is depicted in Fig. 8.3 and Fig. 8.4.
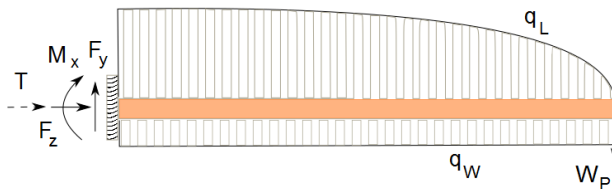
Figure 8.3: FBD for the cantilevered beam model (front view).
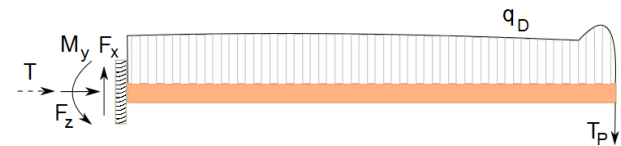
Figure 8.4: FBD for the cantilevered beam model (top view).

Note that the forces, moments, and torques at the location where the beam is fixed represent reaction loads. Torques are represented by dashed arrows, whereas moments and forces are depicted as solid arrows. q_L, q_D, and q_W are the lift, drag, and weight distribution, respectively. The former two were obtained from the aerodynamic analysis in Chapter 7. The weight distribution was assumed to be constant as defined in Equation (8.1). It is justified by the constant chord length/mass distribution over the span.

$$q_W(z) = -W_0 \frac{2}{b} \tag{8.1}$$

Here, W_0 is the total wing weight that is initially considered to equal 1kg so as to comply with the mass budget requirement. Furthermore, T_P and W_P represent engine thrust and weight, respectively. They are modeled as point forces here.

As seen in Fig. 8.3 and Fig. 8.4, the axis system is defined, when viewing the left wing from the tip, as positive x directed toward the trailing edge, positive y directed up, and positive z directed towards the the tip and therefore the spectator. A graphical representation is shown in Fig. 8.5. Note that this axis system differs from the one defined in the stability & control analysis in Chapter 6.
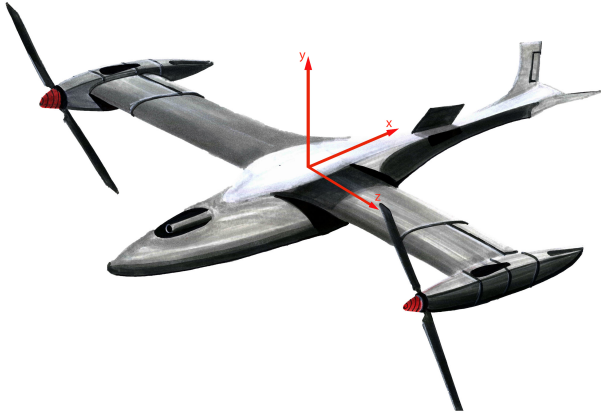
Figure 8.5: The defined axis system

Table 8.1: Reaction forces and their respective values in aircraft mode

Reaction load	Value [Unit]
F_x	15.8 [N]
F_y	-40.5 [N]
M_x	14.2 [Nm]
M_y	14.8 [Nm]
T	8.3 [Nm]

8.2.2 Load Diagrams

Using the FBDs shown in Fig. 8.3 and Fig. 8.4, the load diagrams could be constructed. First, the reaction forces were calculated from static equilibrium, as defined by Equation (8.2).

$$\sum F_x = \sum F_y = \sum F_z = \sum M_x = \sum M_y = \sum T = 0 \tag{8.2}$$

Note that the entries here represent forces, moments, and torques for all axes, so not just the reaction forces indicated in Fig. 8.3 and Fig. 8.4. From this, it can be seen that $F_z = 0$, as it is the only force acting along the z-axis. Substituting all forces from the aforementioned figures into Equation (8.2), the reaction forces shown in Table 8.1 were obtained. For the load distributions (q_L, q_W and q_D), Equation (8.3) and Equation (8.4) were used to obtain the total force induced and the location through which it acts, respectively [151].

$$L, D, W = \int_0^{\frac{b}{2}} q_{L,D,W}\, dz \tag{8.3} \qquad z_{L,D,W} = \frac{\int_0^{\frac{b}{2}} z q_{L,D,W}\, dz}{\int_0^{\frac{b}{2}} q_{L,D,W}\, dz} \tag{8.4}$$

With the reaction forces defined, the internal loads could then be determined by starting at the base of the wing and splitting the wing up into small elements. These elements were then analyzed assuming static equilibrium to determine the internal loads. It resulted in the load diagram shown in Fig. 8.6. Note that the sign of forces is determined by the axis system shown in Fig. 8.5 and that of moments and torques by the right hand rule for these axes. Internal loads were analyzed at the outboard side of each wing element.
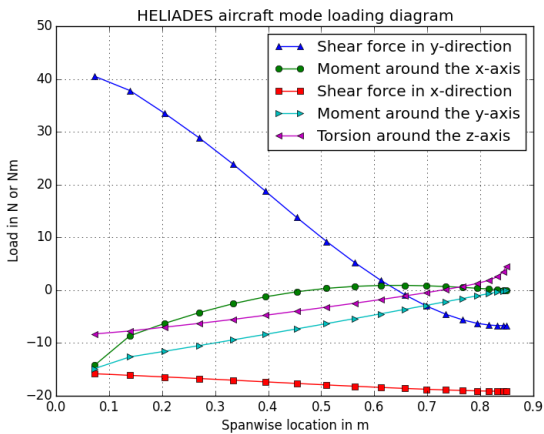

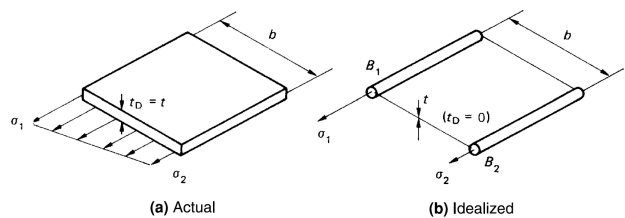Figure 8.6: The loading diagram for the wing of HELIADES.

Figure 8.7: The principal of structural idealization [126].

8.2.3 Stress Analysis

This subsection describes the subsequent stress analysis performed on the wing. In order to allow for easier computational analysis, it was decided to use structural idealization [126]. This method splits the cross section into

so called booms with areas determined by the stress ratio between two adjacent booms as well as the skin thickness. The mathematical definition is shown in Equation (8.5) [126]. A graphical representation is shown in Fig. 8.7 [126].

$$B_r = \frac{t_D b}{6} \left(2 + \frac{\sigma_{r+1}}{\sigma_r} \right) \qquad (8.5)$$

$$\sigma_z = \frac{M_x}{I_{xx}} y - \frac{M_y}{I_{yy}} x \qquad (8.6)$$

Due to the cross section being subjected to bending and no axial loads, the stress ratios can be determined from the difference in bending stress at different locations. The bending stress is defined as shown in Equation (8.6) [126]. Note that the equation has been simplified by setting $I_{xy} = 0$ due to the symmetry assumption. Here, x and y represent coordinates of cross sectional locations and I-terms represent inertia moments. The minus sign is included to ensure compressive (negative) and tensile (positive) stress at the right cross sectional locations in the defined axis system. As the moments of inertia are constant over the wingspan and the applied loads constant over the cross-section, the stress ratio is only dependent on cross sectional location. As such, the boom areas were obtained, yielding the final idealized structure shown in Fig. 8.8. Note that idealization had to take place twice due to the presence of two bending moments that cannot be treated at the same time as the stress ratio would have two values then. This resulted in two shear and normal stress distributions that can be superimposed to obtain the final result.
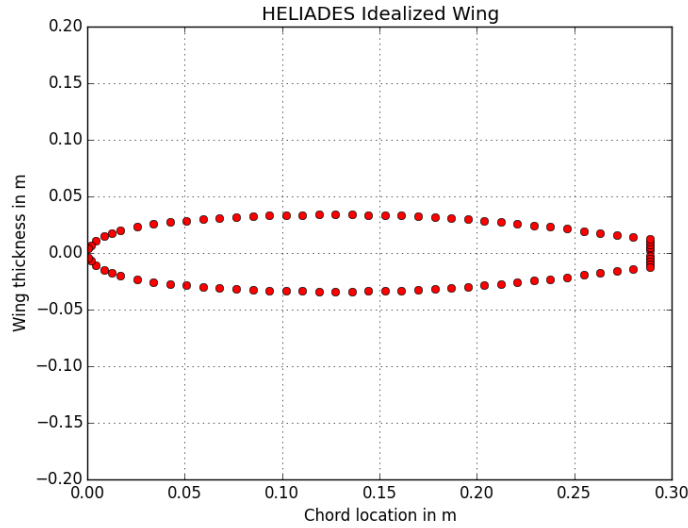
Figure 8.8: Boom locations for the idealized structure

Using the aforementioned areas, the centroid coordinates as well as moment of inertia values were then obtained by using Equation (8.7) and Equation (8.8), respectively [126]. Note that in this case $\bar{y}$ follows from the symmetry assumption.

$$\bar{x} = \frac{\sum B_r x_r}{\sum B_r} \qquad \bar{y} = \frac{\sum B_r y_r}{\sum B_r} \qquad (8.7)$$

$$I_{xx} = \sum B_r y_r^2 \qquad I_{yy} = \sum B_r x_r^2 \qquad (8.8)$$

With the inertia properties determined, the actual stresses could be determined. Three stress categories exist for the case being analyzed, namely bending, torsion and shear. The former is obtained from Equation (8.6), whereas torsional shear stress follows from Equation (8.9) [126]. Note that A_R represents the enclosed area here.

$$\tau = \frac{T}{2 A_R t_D} \qquad (8.9)$$

$$q_s = q_b + q_{s,0} = -\frac{S_x}{I_{yy}} \sum_1^r B_r x_r - \frac{S_y}{I_{xx}} \sum_1^r B_r y_r + q_{s,0} \qquad (8.10)$$

Obtaining the stress due to the shear force is more complicated. The shear flow q_s follows from Equation (8.10) [126]. Here, q_b represents basic shear flow, S-terms represent internal shear forces, and $q_{s,0}$ is a constant shear flow present in closed cross sections. The latter is required to account for the zero shear flow assumed at the starting location by q_b. The starting location on the cross section can be freely selected and terms are added to the summations as booms are passed whilst traversing the cross section. The value for $q_{s,0}$ stems from moment equivalence, meaning that the total moment about any point due to the applied shear forces has to equal the total moment caused by the present shear flows.

In case of a multicell structure, rate of twist equality is used to determine the $q_{s,0}$ values, indicating that each cell has the same twist rate $\frac{d\theta}{dz}$. The required formulas for this are depicted in Equation (8.11) and Equation (8.12)

[126].

$$T = \sum_{R=1}^{N} 2A_R q_R \qquad (8.11) \qquad\qquad \frac{d\theta}{dz} = \frac{1}{2A_R G} \oint_R q \frac{ds}{t} \qquad (8.12)$$

Here, R indicates the cell number and G shear modulus. As both the situations with spars as well as the situation without spars were considered, both single- and multicell structures have to be analyzed. Initially, no spars were assumed, as the spar case was left for the optimization.

Using the aforementioned methods, the maximum normal and shear stresses were determined throughout the wing, yielding the plots shown in Fig. 8.9 and Fig. 8.10.

Figure 8.9: The maximum normal stresses over the wingspan.
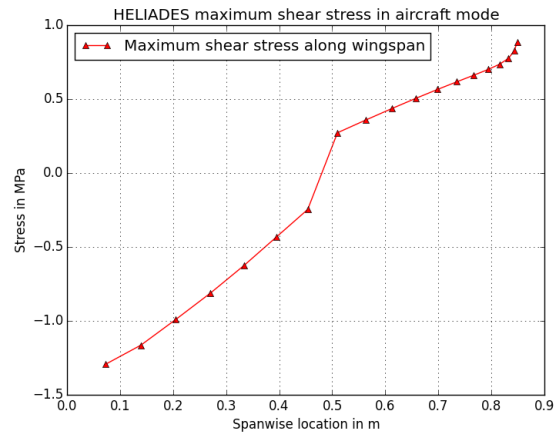
Figure 8.10: The maximum shear stresses over the wingspan.

The overall normal stress distribution makes sense as (absolute) moment loads decrease towards the wing tip, so the stresses should as well. The absolute maximum at the wing root was also expected due to the largest bending arm being present there. The observed jumps are likely the result of the sign change observed in the moment around the x-axis in Fig. 8.6, combined with the changing direction of the total resultant moment and therefore the maximum possible distance away from its line of action.

Moreover, the shear stress changes sign about halfway through the wing. This sign change is also observed in Fig. 8.6 in both shear force in y-direction and in torque. The stress transition is likely due to the change in direction of the resultant shear force and torque, causing their stresses to either amplify or weaken each other. The steep increase at the tip is likely explained by the presence of the thrust force at this location. In conclusion, the maximum normal and shear stress occur at the root of the wing with values of -1.20MPa and -1.29MPa, respectively.

8.2.4 Helicopter Mode

As there exist two separate modes of flight, it is important to consider both of them. In this subsection, a similar analysis is used to analyze the wing in helicopter mode. The critical load case for this mode presents itself at a tilt angle α_T of 17.4° with a thrust value T_P of 51.4N as determined in Chapter 5. The situation is modeled in the FBDs shown in Fig. 8.11 and Fig. 8.12.
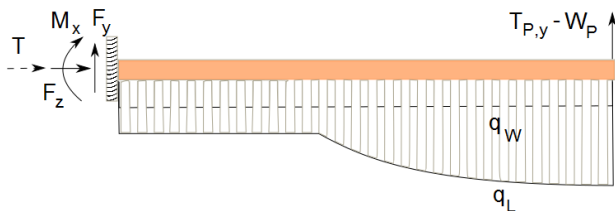
Figure 8.11: FBD for the cantilevered beam model in helicopter mode (front view).
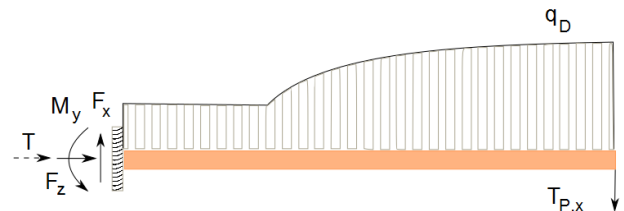
Figure 8.12: FBD for the cantilevered beam model in helicopter mode (top view).

Note that the thrust force was decomposed into an x- and a y-component using the thrust angle. The weight distribution remains the same as in aircraft mode, but the lift and drag distributions change. The latter was obtained in Chapter 7. It is observed that the propeller effect is more prevalent here as the airflow is being pushed against a larger effective wing area than in aircraft mode.

Using the method described in Section 8.2.2, the reaction forces and loading diagrams shown in Table 8.2 and Fig. 8.13, respectively, were determined.

Table 8.2: Reaction forces and their respective values.

Reaction load	Value [Unit]
F_x	13.1 [N]
F_y	-31.6 [N]
M_x	30.3 [Nm]
M_y	11.1 [Nm]
T	≈ 0 [Nm]
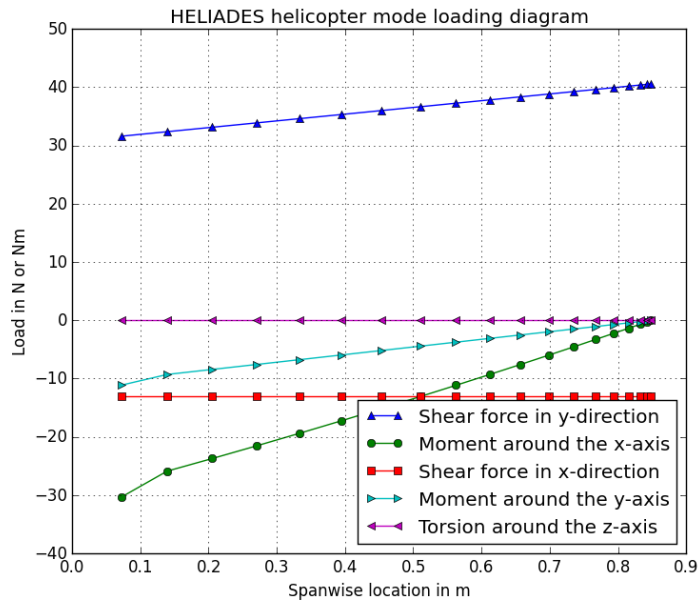
Figure 8.13: The loading diagram for the wing of HELIADES in helicopter mode.

It was observed that the magnitude of the forces and moments was greater than those of the loads experienced in aircraft mode shown in Fig. 8.6. Especially the moment around the x-axis stands out, as expected due to the moment caused by the upward thrust. The stresses were therefore also of a higher order, as seen in Fig. 8.14 and Fig. 8.15. These stresses were determined using the approach described in Section 8.2.3.
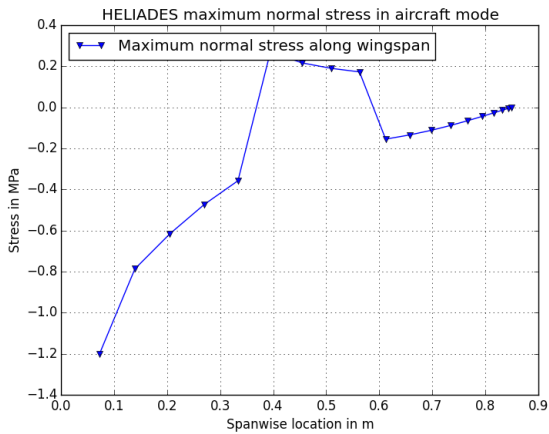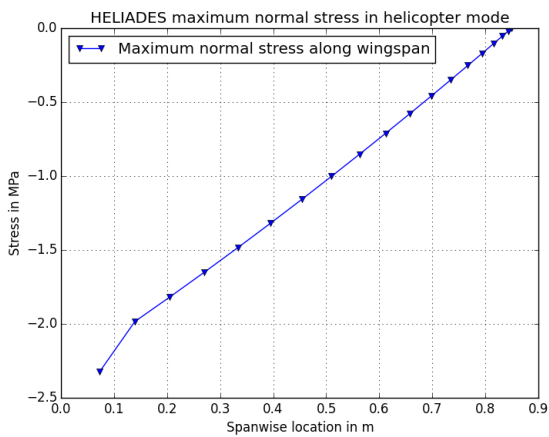

Figure 8.14: The maximum normal stresses over the wingspan.
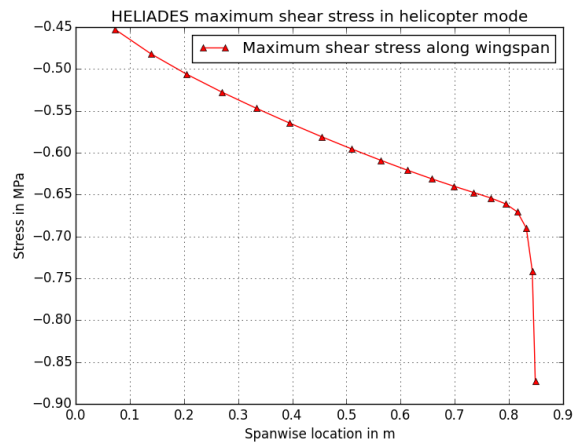
Figure 8.15: The maximum shear stresses over the wingspan.

The normal stress distribution has the expected shape, as its absolute magnitude decreases towards the tip. The shear stress distribution decreases approximately linearly over the wing, as caused by the linear behavior of both shear forces in Fig. 8.13. It is observed that the maximum normal stress equals -2.32MPa at the root and the maximum shear stress equals -0.87MPa near the tip. However, the steep decrease in shear stress near the tip appears to be the result of boundary discretization errors, as it does not follow from the applied shear forces. This was however, not an issue for the material selection as the maximum normal stress is a factor 3 greater, thus causing the maximum stress combination to be located near the root.

8.2.5 Material Selection

In this subsection the material selection is discussed. The main criteria are yield strength, stiffness, and density. It was desired to have plastics or composites due to their favorable sustainability properties and high specific prop-

erties. Firstly, the Von Mises yield criterion was used to determine the yield strength that the material should have. This criterion is shown in Equation (8.13) for planar stress situations [126].

$$\sigma_{yield} = \sqrt{\sigma_x^2 + 3\tau_{xy}^2} \tag{8.13}$$

Substituting in the maximum normal and maximum shear stress found at the wing root from both aircraft and helicopter mode, the aircraft mode was found to be more stringent. It yielded a Von Mises stress of 2.54MPa. Using a safety factor of 1.5 for plastics, due to yield strength and stiffness being the most important property, a required yield strength of 3.81MPa was obtained [116]. For composites, a greater safety factor of 1.9 should be used due to the increased long-time behavioral uncertainty when compared to 'traditional' materials such as metals and plastics [113]. This yielded a required composite yield strength of 4.82MPa.

Based on these results, three material options were selected: polypropylene (PPL), polylactic acid (PLA) and carbon fiber reinforced plastic (CFRP). Here, the latter is a composite, whereas the others are plastics. Pertinent material properties are shown in Table 8.3

Table 8.3: Material properties for all options [105]

Property	Symbol	Unit	PPL	PLA	CFRP
Yield strength	σ_{yield}	[MPa]	34	50	200
Density	ρ	[g/cc]	0.9	1.3	1.5
Young's Modulus	E	[GPa]	0.9	3.5	1.5
Shear Modulus	G	[GPa]	0.42	2.4	53
Specific strength	$\frac{\sigma_{yield}}{\rho}$	[kN m/kg]	36.7	38.5	133.3
Specific stiffness	$\frac{E}{\rho}$	[MN m/kg]	1	2.7	1
Specific cost	C	$/kg	1.10	2.0	110

Note that the yield stresses of these materials are significantly greater than the required strength. However, as the required yield strength was mainly found in foam materials, that lack stiffness, material were selected that both comply with the strength requirement, but are also sufficiently stiff. The stiffness is required to ensure the airfoil keeps its shape throughout the operational lifetime as well as to ensure limited deflections.

Using these values, deflections were determined. Note that mass is not determined as the airfoil shape cannot be changed, so shape optimization is not possible. Therefore, only density and minimum manufacturable skin thickness determined the mass. As the minimum thickness is the same for all these materials, namely 1mm, mass is only dependent on density [105]. In this sense, PPL has the lowest mass, followed by PLA and finally CFRP.

Deflections

The maximum deflections were calculated to check whether these were agreeable with each material option. These are of importance as significant deflections can make the drone harder to control and introduce additional moments due to the thrust vector changing direction. For a beam under bending, Equation (8.14) describes the angle of the beam θ and Equation (8.15) describes the deflection of the beam δ, both at location x [106].

$$EI_x\theta_y = \int_0^z M_x(z)\,dz + C_1 \tag{8.14} \qquad EI_x\delta_y = \int_0^z \left[\int_0^z M_x(z)\,dz + C_1\right]dz + C_2 \tag{8.15}$$

Note that the equations are the same for the beam angle and deflection along the x-axis, but with x and y subscripts inverted. Since a cantilever beam was considered, it is known that the angle and the deflection at the base are zero or, mathematically speaking, $\theta(0) = 0$ and $\delta(0) = 0$. This means that the integration constants C_1 and C_2 can both be omitted. Performing the calculations for all materials yielded the maximum deflections shown in Table 8.4. As expected, all maximum deflections are located at the wing tips.

Table 8.4: Deflections in both the x and y directions.

Deflection	PPL	PLA	CFRP
δ_x [mm]	-1.1	-0.27	-0.6
δ_y [mm]	3.6	0.94	2.2

It can be seen that PLA performs best in terms of deflections, followed by CFRP and finally PPL. This is in line with the stiffness values from Table 8.3, as greater stiffness should lead to smaller deflections.

Conclusion

Having analyzed relevant material and design properties, it was decided to go for PLA. The main issues with the other two materials were the poor stiffness, combined with the poor sustainability of PPL and the high cost and density of CFRP. PLA provides the design with sufficient strength and stiffness at a low cost and mass. Besides, its sustainability performance is excellent as it is fully biodegradable, has limited emissions during manufacturing and consists entirely out of biological products [105]. Furthermore, PLA allows for 3D printing, thus reducing manufacturing cost and complexity [44]. Using PLA results in a total wing mass of 1.39 kg when using the minimum thickness of 1mm.

8.2.6 Optimization

As mentioned before, the helicopter mode concluded to be stringent and is therefore considered in the optimization process. During the optimization process two separate cases were considered: one including an additional spar web in the wing and one without this spar. The purpose of the optimization process was to find lightest wing that was able to withstand the loads (with a safety factor). The thickness was assumed to be constant throughout the cross-section. This was assumed to reduce the computing complexity, besides lowering the manufacturing complexity of the wing. Moreover, due to the relatively small wing dimensions, the impact of having a varying thickness on inertia properties becomes less significant.

In the case with the additional spar, first a thickness was assumed, after which the location of the spar web was varied along the chord in order to find the location which allows for the lowest maximum stress. Then the skin and spar thickness were reduced to find the minimal wing weight. The location of the spar resulting in the minimum stress was found at $0.6 \cdot c$. Together with the minimal possible thickness of 1mm, a maximum Von Mises stress of 1.28MPa was found. This resulted in a cross-sectional area of 734.2mm^2.

The procedure for the case without the spar web consisted of reducing the skin thickness. A maximum stress of 2.54MPa was found at a thickness of 1mm, which still satisfies stress requirement. Further lowering the thickness was not allowed, as this would engender manufacturing issues [105]. Therefore, the optimal cross-sectional area for this case was determined to be 691.1mm^2 with a mass of 1.13kg.

It was found that the case without an additional spar, beside the one to which the aileron is attached, yielded a lighter structure. This makes sense as the yield strength of the selected material is greater than the maximum experienced stress. Therefore, the smallest cross sectional area will close the margin between actual stress and yield stress, thus making the design more efficient.

8.2.7 Buckling

Buckling is a phenomenon that occurs in beams under compression. There exists a certain axial force at which a deflection perpendicular to the loaded axis presents itself. This so called critical buckling force is defined by Equation (8.16) [126].

$$P_{buckling} = \frac{n_{BC}\pi^2 EI}{L^2} \tag{8.16}$$

Here, n_{BC} is a constant that takes into account boundary conditions, such as clamped on one end, clamped on both ends, etc. In case of a cantilever beam, this constant takes on a value of 0.25.

However, the wing itself is not subjected to axial loads, meaning that the buckling analysis had to be performed on separate booms. The latter do experience normal stresses and therefore carry compressive loads. By modeling the top skin booms as one panel subjected to compression, the axial loads due to the applied moments were determined. From the skin panel's moment of inertia the critical buckling load was found from Equation (8.16).

Initially, the maximum allowable compressive load (including safety factor) was 194N in the root section, while a compressive load of 241N was applied. Therefore, the sheet's resistance to buckling had to be increased. This can be done either by adding stringers, or by locally increasing skin thickness. The latter is less efficient in terms of weight though, as more material has to be added compared to adding a number of stringers. Moreover, stringers are specifically made to increase buckling resistance [126]. Therefore, stringers were included in order to minimize the required weight increase.

Several configurations including multiple stringers were considered from which the single stringer configuration, ranging from the root until 0.07m spanwise, concluded to be optimal in terms of weight. The stringer was placed at

0.153m chordwise and attached to the top wing skin. Its configuration was determined to be Z-type due to the ease of manufacturing and the reduction in stress concentration areas due to the single chordwise connection point. The total wing weight increased from 1.13kg to 1.14kg.

Concerning the bottom skin, a similar analysis was performed, modeling the bottom booms as a single skin panel. This panel was analyzed during ground operations, where only the weight introduced a moment resulting in a compressive load in the bottom skin. However, this load concluded to be negligible to the critical buckling load. Therefore, no extra stiffeners were required, thus yielding a fully designed wing capable of withstanding the most extreme loads applied to it.

8.3 Fuselage Analysis

With the wings designed, the fuselage was looked into. A similar approach as described in Section 8.2.1 until Section 8.2.3 was used. Note that, since the helicopter mode case was found to be more stringent than the aircraft mode one, the wing loads for the former case were used to design the fuselage.

8.3.1 Free Body Diagrams (FBD)

Before the stress analysis can be performed, FBDs are constructed to facilitate the aforementioned analysis. Referring back to Fig. 8.1 and Fig. 8.2 and taking into account the weight distribution over the fuselage, the beam model FBD was determined as shown in Fig. 8.16
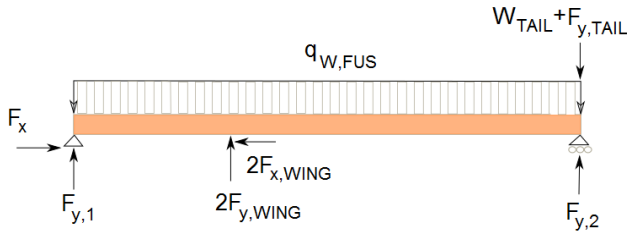
Figure 8.16: FBD of the fuselage beam model (side view)

Table 8.5: Reaction forces and their respective values

Reaction load	Value [Unit]
F_x	26.1 [N]
$F_{y,1}$	-38.9 [N]
$F_{y,2}$	-21.2 [N]

The fuselage was modeled as a beam with a fixed and a roller support. This was done as this way the fuselage deflects realistically due to the induced wing loads, i.e. both the nose and the tail deflect downward relative to the wing position. Another possibility would have been to pick two fixed supports, but this would mean that deflections cause the fuselage length to vary significantly as the supports are at fixed locations. Therefore, a roller support was chosen as this keeps the length approximately constant due to the added degree of freedom. This is deemed to be more realistic as limited length variations are expected due to limited temperature range over the operational altitudes.

Furthermore, $F_{x,WING}$ and $F_{y,WING}$ refer to the reaction forces from Table 8.2. These model the influence of the wing on the fuselage. As only half of the wingspan was considered to obtain these, both are multiplied by two to get the total reaction loads required in the fuselage to ensure the wings remain attached. Note that the moments cancel out due to symmetry.

Moreover, W_{TAIL} and $F_{y,TAIL}$ represent the tail weight and maximum tail force, respectively. Both were determined in Chapter 6. $F_{y,TAIL}$ is assumed to be directed downward, as this causes the largest bending moments and therefore the most stringent load case.

Finally, $q_{W,FUS}$ is the fuselage weight distribution defined by Equation (8.17). It follows from the conical cross section assumption.

$$q_{W,FUS}(x) = \rho_{PLA}\left(\pi a_0 b_0 + (\pi a_L b_L - \pi a_0 b_0)\frac{x}{L_{FUS}}\right)$$

(8.17)

Here, $a_0 b_0$ and $a_L b_L$ are the ellipsoidal parameter products at the noise and at the tail, respectively, and x describes the position along the fuselage length with the origin located at the nose. As PLA had been chosen as wing material, it was used as fuselage material to obtain an initial estimate of the fuselage mass.

8.3.2 Loading Diagrams

Using the static analysis approach described in Section 8.2.2, the reaction forces shown in Table 8.5 were determined as well as the internal load diagrams shown in Fig. 8.17. Note that the axis system used is the one shown in

Fig. 8.5. Moreover, not all data points have been marked due to the plots becoming hard to read otherwise.
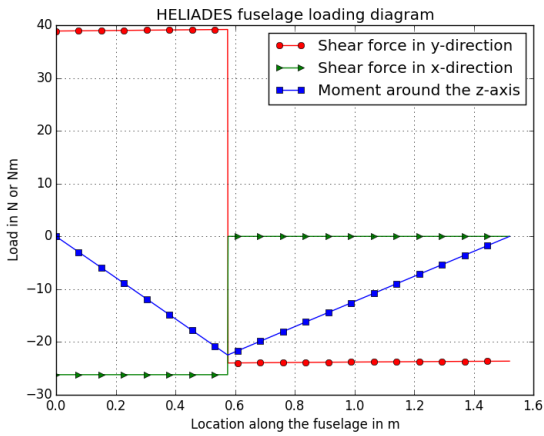
Figure 8.17: Loading diagrams for HELIADES' fuselage.
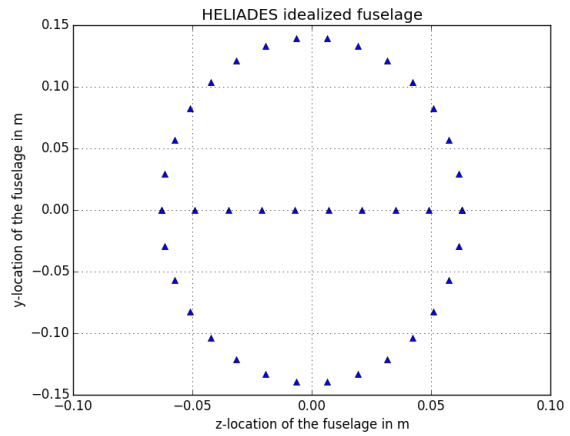
Figure 8.18: Idealized fuselage for HELIADES.

8.3.3 Stress Analysis

With the loads determined, the stress analysis approach described in Section 8.2.3 was applied, resulting in the idealized cross section shown in Fig. 8.18. Using this, the maximum normal and shear stresses over the fuselage length were obtained as shown in Fig. 8.19 and Fig. 8.20, respectively.
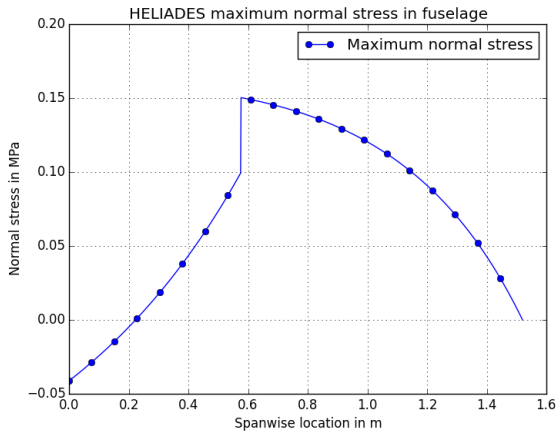
Figure 8.19: The maximum normal stresses over the fuselage length.
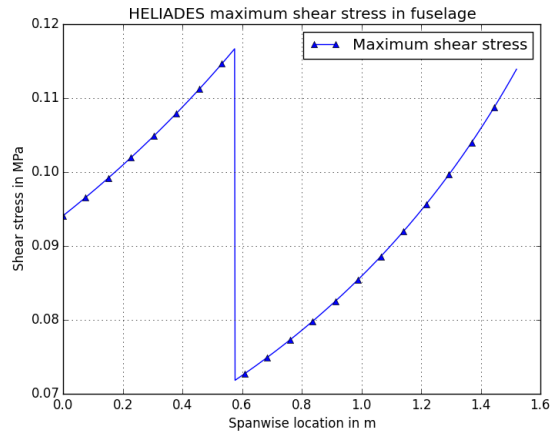
Figure 8.20: The maximum shear stresses over the fuselage length.

It was observed that the maximum normal stress equals 0.15MPa and the maximum shear stress equals 0.116MPa, both occurring at the wing root location. This is logical as the greatest loads are induced here.

8.3.4 Material selection

Substituting the maximum stresses obtained from Fig. 8.19 and Fig. 8.20 into Equation (8.13) yielded a Von Mises stress of 0.25MPa. Applying the safety factor of 1.5 requires the material to have a yield strength of at least 0.38MPa [116]. As mentioned previously, PLA was used as an initial estimate and, from Table 8.3, it was determined that its material strength suffices. Using the same material is more convenient for manufacturing as well as assembly. Moreover, as cut-outs are to be made to improve accessibility, having a stress margin is helpful.

8.3.5 Buckling

Similarly to the wing analysis, the buckling criterion was analyzed for the fuselage using Equation (8.16). The fuselage is subjected to both an axial load and a bending load due to the wing reaction forces in the wing connection and the weight distribution of the fuselage itself. The largest compressive load presents itself in the bottom half of the fuselage due to the downward bending of nose and tail. As determined previously, the highest loads were present at the wing-fuselage connection. The magnitude of these loads however, was significantly lower than the critical buckling loads (a factor 100). Therefore, no stringers had to be included in the fuselage, yielding a total fuselage weight of 0.65kg with a thickness of 1mm.

8.4 Additional Considerations

In this section some additional considerations are discussed resulting from the finalized design. Firstly, PLA is biodegradable, which is good for sustainability, but might cause issues in terms of structural performance. The most prevalent heat source near the wings are the motors. As determined in Chapter 5, the maximum temperature experienced near the engine is 50°C. Comparing this to the glass transition temperature (60°C) and the melting temperature (160°C) of PLA, no heat issues should present themselves during operation [105]. It is recommended though to use light colors when manufacturing the wing, as this will decrease heat absorption and therefore the probability of overheating. Adding a protective coating for increased UV resistance is also suggested, as research has shown that UV light can accelerate the rate of degradation in PLA materials [74].

Secondly, creep is a known issue in the manufacturing and use of PLA [160]. Creep is defined as deformations caused by longterm exposure to stresses and it is desirable to limit the occurrence of this phenomenon. It is mainly present at elevated temperatures, so as long as these are avoided the structure will remain sound. Research has shown that at temperatures below 60° creep can be considered negligible [160]. Therefore, creep is not expected to be an issue for HELIADES during operations. However, it should be noted that limited information on longterm behavior of PLA is available, so it might be possible that over the years eventually some creep occurs. If this is the case, there are several proven methods to ameliorate this issue. One of the possibilities consists of infusing the PLA with hydrocarbon liquid, thus improving creep resistance, whereas another method comprises of a silane treatment that reduces creep strain by enhancing internal material bonds [153, 160].

Thirdly, not all 3D printing methods can be used in combination with PLA materials. As mentioned in the previous paragraph, creep becomes an issue at increased temperatures, thus making heated extrusion methods such as Fused Deposition Modeling (FDM) unfit for use as the extrusion mold will likely clog due to the creeping material [149]. Moreover, FDM builds up the product by winding filament in layers to obtain the final product. This causes local weaknesses at transitions from one layer to another, thus leading to significant strength reduction that cannot be permitted in HELIADES' case. Therefore, Selective Laser Sintering (SLS) should be used [149]. This method uses a laser to heat up and solidify powdered material into a final product. Although heat is added in this process, it does not prevent the printer from working nor does creep play a role as the applied forces are limited compared to extrusion.

Moreover, Chapter 12 contains a discussion on how to transport the system. It is mentioned that the wings and fuselage are taken apart to allow for more convenient transportation. This indicates the need for detachable connection joints at the fairing that connect the wings to the fuselage. For this, bolts are to be used as these joints are easiest to disassemble, are able to carry tensile and shear loads, and are more resistant to fatigue [149]. However, they do introduce stress concentrations, thus requiring greater material strength. As PLA's yield strength compared to the actual stresses experienced (including safety factor) provides a reasonable margin, it is expected that these stress concentrations can be handled by the structure. Nonetheless, a detailed analysis into both stress concentrations as well as optimal bolt positioning should be performed in the post-DSE phase.

Finally, an emerging technology in plastics and composites are so-called Stanford Multi-Actuator-Receiver Transduction (or SMART) materials. It comprises of a layer of piezoelectric sensors embedded between the base material layers [119]. Using these kind of materials would further reduce the weight of the structure, as a large part of the present sensors could be omitted as the SMART material itself would gather the required data. Moreover, HELIADES would be amongst the first designs to incorporate this technology, thus likely resulting in more publicity and therefore increased sales. However, as the technology is at a relatively early stage, it is recommended to go for regular plastics for now, but at a later stage in the design it should be considered to use SMART materials in a future variation on the product.

8.5 Verification & Validation

This section elaborates on the verification and validation procedures used to ensure numerical models were applied correctly and to ensure they provided a realistic approximation. For the structural analysis, a large program of interrelated files was constructed that performed all forms of analysis described in this chapter.

Verification

Firstly, verification was looked into, which was split into code and calculation verification. The former checks for coding errors that cause discrepancies between mathematical and numerical model, whereas the latter checks whether the calculations are executed correctly by comparing results to an analytical solution. As code verification is generally quite straightforward, more emphasis was put on calculation verification through unit and system tests.

Code verification was performed by thoroughly reading through the code with two people and adding print statements to check whether the correct data types were used. This way, it was found that some formulas contained typos, causing them to yield incorrect results. Moreover, some formulas were found to be wrongly determined, such as the weight distribution. These errors were easily fixed, yielding a code verified program. Note that this approach was applied to both separate files as well as to the file incorporating all these separate files.

Calculation verification was performed in a more elaborate way and is described per file. Firstly, unit tests were applied in which small parts of the code were checked to see whether the order of magnitude of the results made sense with regard to the desired output. Furthermore, it was verified whether or not the output of each block corresponded to what was expected. Firstly, the loading diagram block was verified. It was found that the internal loads had the correct order of magnitude, but the moments did not go to zero at the end of the beam, as is required by static equilibrium. This turned out to be due to the internal moment equations being wrongly defined in terms of signs. Furthermore, using a system test that inputs a simplified case of a beam loaded by a constant lift distribution and a point load at the end, it was found that the simulated results were in agreement with the results worked out by hand, thus leading to a verified program.

Next, the structural idealization block was verified. Through unit tests, it was found that inconsistencies between units were present, as mm and m were used together. It was also found that wrong columns of arrays were selected sometimes, causing the x-coordinate instead of the y-coordinates to be used and vice versa. Furthermore, boom areas ended up having the correct order of magnitude. Moving onto a system test, a different airfoil (NACA23018) was used as input to check whether the program still functioned correctly. It was found that the airfoil was imported correctly, but errors presented itself in the idealization of the spar due to the difference in airfoil coordinate format. Therefore, the program was adjusted so that it could handle both symmetric formats (i.e. a top and bottom value are assigned to each x-coordinate) and asymmetric formats (i.e. different x-coordinates are used for the top and bottom surface). Hereafter, the block was deemed verified.

Thirdly, the stress analysis block was analyzed. This file brought all previously described sections together. Unit tests allowed for the group to check whether the shear flows and normal stresses had the correct order of magnitude and sign, besides ensuring the outputs of each block were processed accordingly. Hence, it was found that bending moments were reversed due to an incorrect index. Continuing with a system test, the stress for the idealized wing was calculated along the span. It followed that it had the correct order of magnitude and sign, thus yielding a verified code.

Next, optimization was verified. Due to the complexity of the program, structural optimization had to be performed by changing parameters by hand and checking for both the yield stress and the resulting wing weight. As the code blocks used were already verified, the optimization analysis was also considered to be verified.

Furthermore, deflections were determined using basic equations that were verified by feeding the program a simplified sample case. The result of this case was determined analytically beforehand. Comparing the analytical results with the simulated result, it was found that they were identical, thus deeming the deflection block verified.

Although buckling includes simple equations, initially difficulties were encountered with calculating the centroid and resulting moment of inertia of the modeled skin panel. After correcting these, a sample problem of a beam with a constant transversal load at the end was calculated by hand as well as simulated by the program. A comparison of the results of aforementioned calculations concluded that both were the same. Therefore, the buckling code was verified.

Validation

With the verification completed, validation could be performed. Validation is the process of determining whether a computational model is an accurate representation of reality. This is done through comparisons of simulated data and test data. In this chapter, the main model used for all computations is structural idealization. This model was validated during the Simulation, Verification & Validation project [89]. Here, a fuselage was analyzed using structural idealization, after which it was compared to actual test data. From this, it was found that the maximum Von Mises stress is approximated rather well, whilst the intermediate stresses over the fuselage differ in accuracy. This is due to the linearization aspect that is inherent to structural idealization, thus preventing Von Mises distributions from being non-linear. In reality however, non-linear distributions are likely to occur. Nonetheless, as the maximum Von Mises stresses are the parameter of interest, this is not an issue for the analysis performed in this chapter. Therefore, the fuselage model was considered to be validated.

Regarding the idealized model for the wing, validation data from the Simulation, Verification & Validation project of 2015 was used [78]. Here, a structurally idealized wing was analyzed and compared to test data. Similar to the results described in the previous paragraph, the maximum Von Mises stresses in the structure turned out to be

approximated quite well with a discrepancy of only 4%, whereas the overall distribution was shaped differently. As the maximum stresses are of interest for the design and the material selection, the wing model was considered validated.

Nonetheless, extensive tests are to be performed in the post-DSE phase to ensure a sufficiently reliable validation result. To this end, a test with the prototype has to be performed in which 20g loads are induced on the wing. This can be done mechanically by stress test equipment at relatively low cost. Note that the induced loads have to adjusted to account for bending relief due to the wing weight. Using strain sensors, stresses at locations over the wing and the fuselage can then be determined. Saving these and comparing them to the simulated results, a more reliable validation can be performed. Alternatively, if such a test turns out to be too lengthy or costly, validation can be performed by comparing simulated results to validated results from a detailed FEM analysis. Software to be used for the latter could include Dassault Systemes Abaqus or Ansys.

9. Sensitivity Analysis

In this chapter, the sensitivity analysis is performed. During the design process, as well as in other parts of the product life cycle, certain major system parameters will be subject to change, for example due to design iterations, maintenance or software updates. It is therefore important to test the robustness of the design to changes in these major system parameters, in order to see how feasible the design is. The following major system parameters are changed to this purpose:

- **Power Loading** WP: The power loading will be fixed after the engines are selected and the weight is determined. Engines have already been selected, therefore the power loading might only change due to a change in weight.
- **Wing Loading** WL: A full computational fluid dynamics (CFD) analysis of the aircraft might lead to a more accurate (and different) wing loading. In addition to this, the wing loading might change due to a change in weight.
- **Disk Loading** DL: A more accurate and different disk loading might result from a rotor analysis using blade element theory. The disk loading can also change due to a change in weight.
- **Mission Profile**: Mission profiles can change over time as drones become faster, have increased endurance, can fly higher, etc. They may also change due to a change in 'enemy' tactics: multiple incoming drones, low-altitude flying to evade radar and so on. The mission profile might also change depending on the customer and the area the anti-drone drone has to protect. Finally, different radar systems lead to different detection ranges, and might therefore change the mission profile. System parameters which are be evaluated are altitude, time,
- **Removal System Components**: Different removal system compositions or components lead to different reliabilities due to redundancy, component failure rates, etc. Firstly, the components of the removal system can change depending on the demands of the customer. For example, for operation in remote uninhabited areas a customer might only want the kinetic gun, while a customer that operates in populated areas may only want the net gun to be fitted. Secondly, components of the removal system may be changed due to technology advancements, both in terms of drones as well as in terms of jamming equipment, off-the-shelf net guns, etc.

The effect of changing these major system parameters is assessed through the key performance indicators. While some of the key performance indicators may be analyzed quantitatively, others can only be assessed in a qualitative way. The plots of the quantitative analysis are shown in Fig. 9.1 and Fig. 9.2. The following key performance indicators are used:
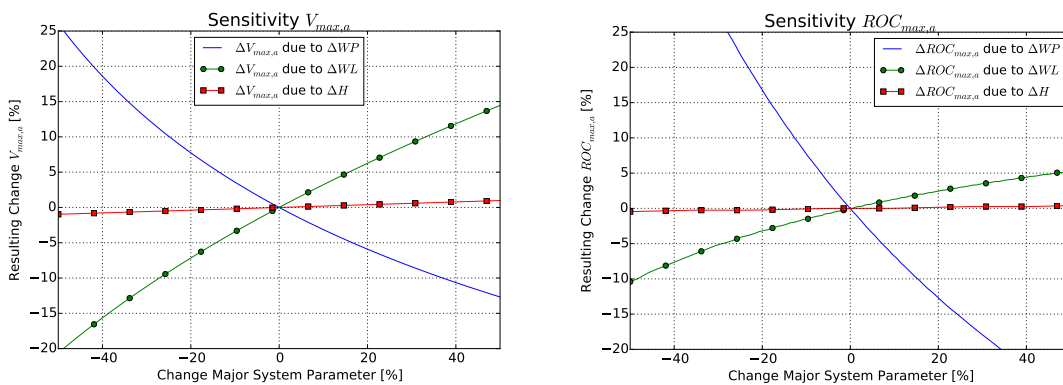
Figure 9.1: Sensitivity plots for the quantitatively assessed key performance indicators $V_{max,a}$ and ROC_{max}.

Max Speed Airplane Mode $V_{max,a}$

Maximum speed is achieved in airplane mode. The analysis is therefore performed for airplane mode. Changes in power loading, wing loading and the mission profile (altitude) lead to changes in maximum speed. This is depicted in the left plot of Fig. 9.1. As can be seen, the maximum achievable speed increases with increasing wing loading and decreases with increasing power loading. Changes in altitude do not affect the maximum speed greatly. The design feasibility in terms of maximum velocity is not very sensitive. Since the current maximum velocity $V_{max,a} = 68.3$m/s, even changes of 40% in wing and power loading will not lead to a maximum velocity below the value

76
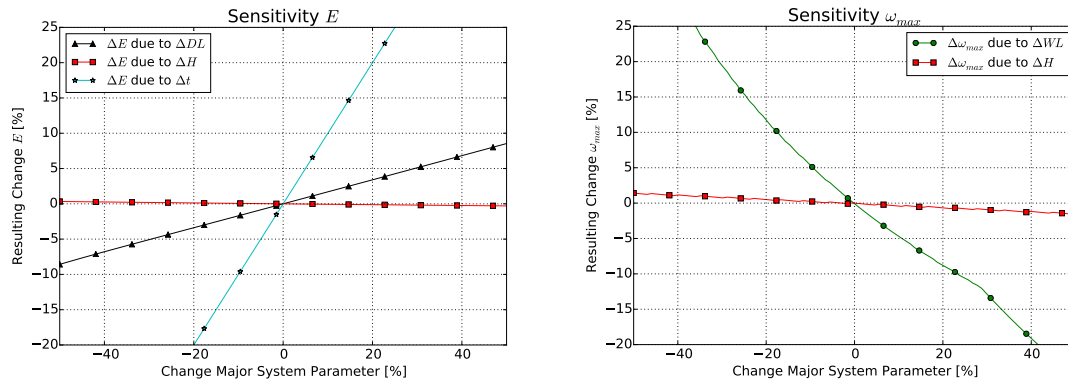
Figure 9.2: Sensitivity plots for the quantitatively assessed key performance indicators E and ω_{max}.

specified in **REQ-PERF-02**.

Max Climb Rate $ROC_{max,a}$
Currently, most climbs in the mission profiles are performed in airplane mode. The analysis shown in the right plot of Fig. 9.1 is therefore performed for airplane mode. Increases in power loading, wing loading and altitude lead to decreases, increases and increases, respectively, in the maximum climb rate. As with the maximum velocity, the design feasibility in terms of maximum climb rate is not very sensitive. The current maximum climb rate in airplane mode is $ROC_{max,a} = 47.2$m/s, well above the value specified in **REQ-PERF-03**. Changes of even 50% will not lead to an insufficient climb rate. Even in the case that most climbs in the mission profile would be performed in helicopter mode, the feasibility of the design would not be compromised, since maximum climb rate for helicopter mode exceeds the one for airplane mode, with $ROC_{maxh,h} = 59$m/s in axial climb.

Battery Energy Required E
In order to assess the sensitivity of both airplane and helicopter mode, the battery energy required is analyzed for the latter. This means that the energy required increases for increasing disk loading and time, while it decreases with increasing altitude. This is shown in the left plot of Fig. 9.2, where a level cruise in helicopter mode at a forward velocity of 20m/s for a duration of 60s is used for analysis. The feasibility of the design in terms of required battery energy is sensitive to changes in the duration of the mission. However, due to using various mission profiles to size the design as well as the fact that the battery used in the design has a reserve energy margin with respect to the missions, this sensitivity is kept as low as possible.

Max Turn Rate ω_{max}
The maximum turn rate is defined here as the maximum instantaneous turn rate in airplane mode. It decreases for an increase in wing loading as well as altitude, as can be seen in the right plot of Fig. 9.2. The feasibility of the design in terms of maximum turn rate is not very sensitive, since the current maximum turn rate $\omega_{max} = 3.25$rad/s is well above the value specified in **REQ-PERF-04**, even in the case of a increase of 40% in wing loading.

Removal Rate
The removal rate is specified to be 99% in **REQ-PERF-19**. It is mostly dependent on removal system components. Wing loading and power loading also influence the removal rate through the performance of the anti-drone drone and its ability to outperform other drones. By utilising multiple removal methods (jammer, net gun, kinetic gun) the removal rate is ensured to be as high as possible, and to meet the required value. However, as drone technology advances the removal rate might decrease. The modularity of the anti-drone drone will then come in handy, as removal system components can be replaced. To conclude, the feasibility of the design in terms of removal rate can be said to be sensitive to changes in removal system components, as well as wing loading and power loading.

Cost
The cost of the entire design is required to be below €50,000, as stated in **REQ-BUDG-02**. The current cost of the design is around €14,000, which is well below the required cost. The cost of the design is most dependent on the removal system components as well as the mission profiles. Since the removal system components are relatively new and have never been integrated in a drone before, their cost is uncertain. The mission profiles might affect the cost through operational costs. However, since the current cost is well below the maximum allowed cost, the feasibility of the design in terms of cost can be said to be insensitive.

To conclude, although HELIADES is a revolutionary product with many new technologies, its feasibility is insensitive in terms of most aspects. Additional detailed analysis is to be performed post-DSE to further improve the design feasibility in terms of mass optimization and removal rate.

10. Removal Systems

In this chapter, the removal systems and their control units are discussed. In Section 10.1, the design of the kinetic cannon and its ammunition are explained. Similarly, in Section 10.2, the design of the net launcher and its custom ammunition is detailed. The design and operation of the RF cannon is then given in Section 10.3. Finally the removal system controllers design and operation are explained in Section 10.4.

10.1 Kinetic Cannon

HELIADES' kinetic cannon was developed around the Rossi Circuit Judge Carbine, a 5 shot revolver chambered for .410 cartridges, having a barrel length of 0.4699m. The advantage of this revolver type system is that the cartridge cases are retained in the cylinder, mitigating some of the shift in center of gravity after firing. Retaining the cartridge case means that a revolver is also a sustainable option, since casings are not dumped in the environment. Further, revolvers are extremely reliable, are not prone to jamming, and offer simple second strike capability in the case of a dud round, without having to extract the said dud from the chamber.

10.1.1 Legality

In the USA, the Bureau of Alcohol, Tobacco, Firearms and Explosives (ATF) [58] proposes rules, makes regulations and enforces legislation with regards to firearms. As HELIADES' kinetic cannon is a firearm, it is necessary that it complies with existing legislation wherever possible.

The main legal restriction is on barrel length, which must be a minimum of 18 inches. Further, in some states the legality of a firearm of this type changes depending on the type of barrel. In California, a smooth bore barrel coupled with a revolving cylinder is banned as an assault weapon, however, as this firearm is also available with a rifled barrel, and the caliber is a handgun caliber, it is legal in California.

According to NFA 26 U.S.C. § 5845(d)[58]:

"The term "shotgun" means a weapon designed or redesigned, made or remade, and intended to be fired from the shoulder and designed or redesigned and made or remade to use the energy of the explosive in a fixed shotgun shell to fire through a smooth bore either a number of projectiles (ball shot) or a single projectile for each pull of the trigger, and shall include any such weapon which may be readily restored to fire a fixed shotgun shell."

With regards to drone mounted weapons, the ATF has not issued a specific notice, but in the few cases where such a system was made, the system was not perceived to violate firearms regulations.

Under the FAA regulations, specifically FAR part 91 Sec. 91 15 [57]:

"No pilot in command of a civil aircraft may allow any object to be dropped from that aircraft in flight that creates a hazard to persons or property. However, this section does not prohibit the dropping of any object if reasonable precautions are taken to avoid injury or damage to persons or property."

In conclusion, the kinetic cannon itself is legal in most states with the exception of California, where it must utilize the rifled barrel to be legal. And provided that the removal systems in general does not pose a hazard to persons or property, it will not breach the FAA rules [13]. However, for a combined aerial and removal system in general there are as yet no rulings.

10.1.2 Design

Ammunition
For a 'hot' round, a .410 loading has a muzzle velocity of 535m/s, firing shot of mass at most 0.0195kg, with a charge mass of 0.78gr, and a charge velocity of 374m/s [4] [62].

Weight Reduction and Modifications
As the device is installed into HELIADES, provisions such as stocks, fore grips and sighting devices are no longer necessary, and are removed. The original judge carbine and the derived kinetic cannon are shown in Fig. 10.1 [58] and Fig. 10.2. The mass of the original carbine is 2.4kg [41], while the derived kinetic cannon has a mass of 1.2kg.

Barrel
The barrel shall be chrome lined so as to improve wear and corrosion resistance, In order to reduce weight, it's

Figure 10.1: Rossi Circuit Judge [58].
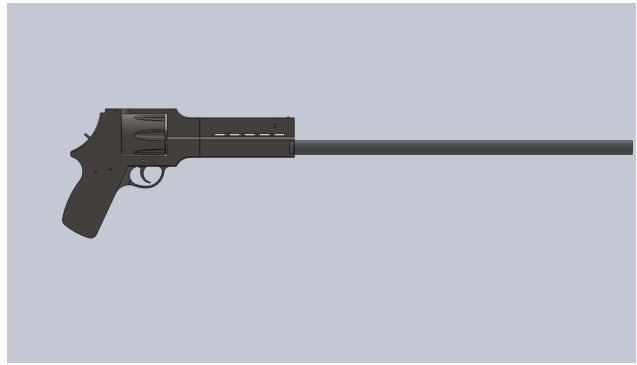
Figure 10.2: HELIADES kinetic cannon.

outside diameter shall be turned down some distance between the throat and muzzle. The resulting shape shall be wrapped in carbon fiber with Thermalgraph DKD particles impregnated in the matrix for heat transfer, as is the state of art for low weight race gun barrels.

10.1.3 Heat Management

As the kinetic cannon is a firearm in the traditional sense, it uses the explosive force of propellant detonation. There are therefore two sources of heat, heating due to the hot gases/ejecta, and friction heating as the projectiles travel down the barrel. As the revolver uses a cylinder having several chambers, each chamber only sees heat flux from one cartridge, and hence the chances of overheating the chamber are minimal. However, there is a gap between the cylinder and barrel through which ejecta flows. Hence a heat shield will be necessary to protect HELIADES' internals.

10.1.4 Recoil

It is necessary to calculate the free recoil of the kinetic cannon, in order to determine if it poses a hazard to the aircraft. It is possible for the recoil velocity to reduce the forward velocity of the aircraft, thereby stalling the wing.

The recoil velocity may be calculated simply via the momentum balance Equation (10.1). The "free recoil" or recoil energy may be calculated via Equation (10.2), this is the energy imparted to the shooter, or in this case HELIADES.

$$M_{HEL}V_{HEL} = M_{bul}V_{bul} \quad (10.1) \qquad E_{gun} = \frac{1}{2}\left(\frac{(m_{bul}v_{bul}) - (m_{charge}v_{charge})}{M_{HEL}}\right) \quad (10.2)$$

Where M_{HEL} is the total mass of the flight vehicle, V_{HEL} is the recoil velocity of the flight vehicle, and the masses in Equation (10.2) are expressed in grams. Using the values for a 'hot' loading, the recoil velocity upon firing the kinetic cannon is 1.04m/s, with a free recoil energy of 3.4J. This means that the fuselage structure should be able to absorb an impact energy of 3.4J, and that the cannon should only be fired at forward flight velocities of 1m/s plus the stall speed. Further, it will be necessary to mount the cannon such that its bore axis lies below HELIADES' center of gravity, such that the recoil causes a nose down pitching moment. Of course, the recoil velocity can be countered by increasing the thrust when firing. These results were checked against published data [19] and formulae for recoil, and found to be in agreement.

10.2 Net Gun

HELIADES' net gun was developed around the Fabrique Nationale d'Herstal FN 303 semi-automatic less-lethal riot gun. This semi-automatic launcher fires an 0.68 caliber 8.5gr round at a velocity of 85.3-91.4m/s, a 15 round magazine and can deliver 60 shots from the 3000psi reservoir before a refill is necessary [20]. The original FN303 has a mass of 2.9kg [20], while the derived net gun has a mass of 940g, of which the reservoir takes up the major part at 494g.

10.2.1 Ammunition

The net launcher uses specially designed shells to launch the net at the target. The shell contains three parts that can be seen in Fig. 10.3: the net (white), a drogue parachute (orange) and a piece of rope (blue) connecting net and parachute. The net shell is spring loaded with a spiral spring (copper) to ensure the net fully unfolds before hitting the target. Once the shell leaves the barrel the shell splits into three parts that are pushed away from each other by

the spring. This causes the net that is attached to the parts of the shell to unfold in flight up to its maximal area and ensures the target is entangled if hit Fig. 10.4.

The parachute is attached to the net using a piece of rope and is also spring-loaded to directly unfold after leaving the barrel. Once unfolded it will slow down and the piece of rope will ensure it does not slow the net before it has traveled a certain distance. The parachute has been designed with an area of 0.9m^2 to ensure a drone of a weight of 2.5kg descends with a velocity of 5m/s. It is assumed that all the drag comes from this parachute, so in reality this velocity will be even lower. The parachute will be made from Terylene which is a thermoplastic polymer very commonly used to make parachutes. The parachute can be folded up into a package to fit inside the shell.

The net inside the shell is made of nylon and has a thickness of 0.25mm. This allows the net to be packed up into an area of 18mm diameter and 100mm length. The corners of the net are attached to the four parts of the shell that are made of PLA.

To prevent any parts from getting lost after being fired all parts are attached to each other. The spring shooting away the parts of the shell is attached to the net and the spring deploying the parachute is attached to the wire. If the net is not damaged by the captured drone and can be untangled the net shells can be put back together and reused. In order to facilitate the retrieval of eliminated drones and missed net shells, a tracker chip is being included into the shell sending out GPS coordinates. These coordinates are being picked up by the ground station for the user to locate the nets.
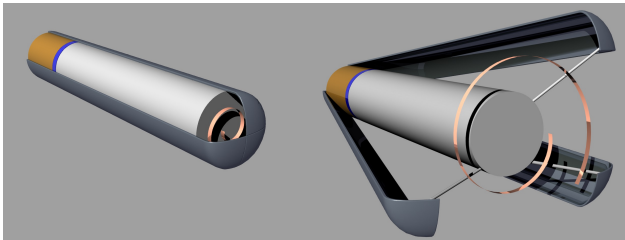
Figure 10.3: Net ammunition consisting of a three part shell surrounding a parachute (most aft part), a rope (middle part) and the net (front part). Left image shows status in barrel, right image status just after leaving the barrel.
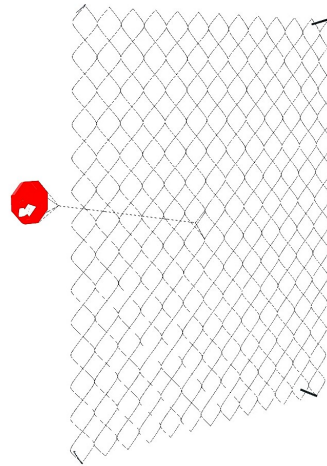
Figure 10.4: Net and parachute after leaving the barrel.

10.3 RF Cannon

The RF cannon is a highly directional radio jammer, utilized to block control signals to the target drone, or to spoof control signals. For jamming action, depending on the target's settings, in the best case it may return home, in the worst case, to some pre-programmed area within the restricted region. In that event, control signal spoofing may be employed in the case of known protocols or GPS guidance, and as a last resort, an increase in jamming power may interfere with the target's electronics and cause it to fall out of the sky.

This is a very sustainable approach to removal, as it utilizes electricity, may be used in multiple engagements, and results in no environmentally harmful byproducts. In this section, the analysis of requirements and design of the RF cannon are elaborated.

10.3.1 Design of RF cannon

The cannon in its most basic form is a radio transmitter, as such it will have an oscillator, a tuning stage to control the oscillator and sweep through the range of desired frequencies, a gain stage to amplify the signal, and an antenna to broadcast it. These components are widely and cheaply available as solid state components, and can be tightly packaged. A simple schematic of HELIADES' RF cannon is shown in Fig. 10.5 with some components shown in Table 10.1.

The tuning stage is provided with a Phased Lock Loop (PLL) as it allows for programmable self tuning. The heart of the circuit is the Voltage Controlled Oscillator (VCO), as they generate the frequencies which sweep through the bands which are to be jammed. This component should first and foremost be capable of sweeping through the desired band, and have a high output gain.
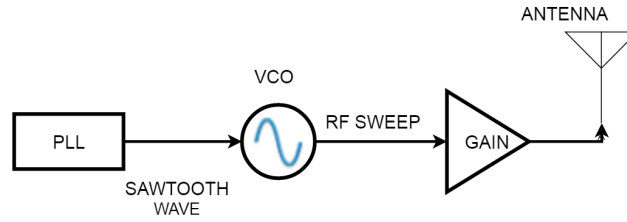
Figure 10.5: Block Schematic of HELIADES' RF jammer.

Table 10.1: RF cannon Main Components.

Component	Model	Quantity	Weight [g]	Cost [$]
VCO 2.4GHz	ROS-2404C-119	1	≤ 2	22
VCO 5.8GHz	ROS-5400+	1	≤ 2	22
VCO GPS	ROS-1700W	1	≤ 2	25
PLL	HMC840LP6CETR-ND	1	≤ 1	17.14
PLL	LMX2433TM	1	≤ 1	4.20
Gain Stage	HMC476MP86-ND	2	≤ 1	3.15

10.3.2 Link Budget and PEIRP

In order to jam or arrest control of a target drone, it is necessary to generate a signal whose strength exceeds that of the target drone's controller. To achieve this, the strength of the target drone's control signal, its bandwidth, protocol, and the distance over which the interfering signal must propagate should be known.

Most commercial hobby systems operate on some form of spread spectrum or frequency hopping protocol, and transmit with a **Peak Effective Isotropic Radiated Power (PEIRP)** of around 100mW to 125mW [14], with a maximum of 4W [18], though this is uncommon. However, depending on the scheme, the actual power is divided over a number of channels.

For a **Frequency Hopping Spread Spectrum technology (FHSS)**, the data is sent over three pseudo-random channels out of around ten, which means that the power is actually 33.33mW. Whereas for **Direct Sequence Spread Spectrum (DSSS)** technology, all data is sent over the ten channels, hence the power is 10mW per channel. This is illustrated in Fig. 10.6.
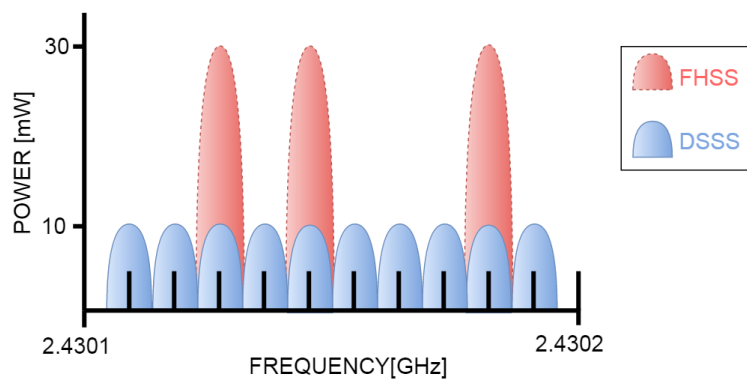
Figure 10.6: Power spectrum of FHSS and DSSS technologies.

For DSSS technology, a PEIRP ≥ 10mW on a single channel would be sufficient to interfere with the target, however FHSS presents a more difficult problem. First the protocol itself is quite robust to interference, as when a channel is blocked, it can hop among the remaining channels. For the case where the three channels in current use are blocked, at least 35 different pseudo-random combinations of channels may be employed from the unblocked portion of the spectrum. This means that the *entire bandwidth* must be polluted in order to knock out the FHSS protocol, hence this represents the *limiting case* for the required on target PEIRP of the RF cannon.

With these considerations in mind, a PEIRP of 600mW across the bandwidth is selected, or 60mW over ten channels.

This ensures that a DSSS system will always be jammed with more than sufficient signal power, and that and FHSS system will also be jammed, as each of the 10 channels is polluted with twice its normal received PEIRP.

Using a schematic representation of the involved transmitters and receivers, Fig. 10.7, it is now possible to calculate the necessary transmitted power, P_{Tx} at the antenna via Equation (10.3).
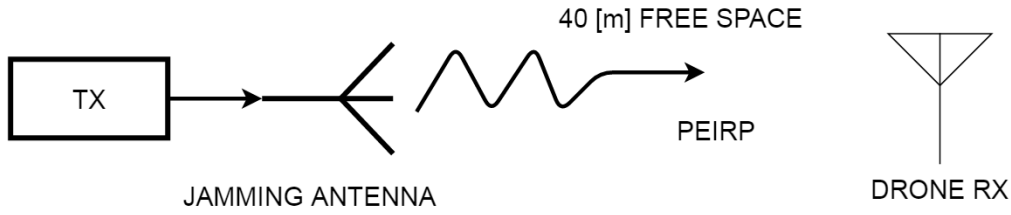
Figure 10.7: Jammer communications link.

$$P_{Rx} = P_{Tx} + G_{Tx} - L_{FS} + G_{RX} \tag{10.3}$$

Where all quantities are expressed in dB. P_{Rx} is the received power, in this case 600mW, G_{Rx}, G_{Tx} are the directions of the receiving and transmitting antennas, and L_{FS} is the Free Space Loss.

First, the directivity of the transmitting and receiving antennas are found. It is assumed that the receiving antenna of a target drone is a standard dipole antenna, with directivity calculated in Equation (10.4) and Equation (10.5), and that a highly directive helical antenna is used with a typical gain of 17dBm [115]. The engagement distance is set to 40m.

$$G_{Rx} = \frac{4\pi A_e}{\lambda^2} \tag{10.4} \qquad\qquad A_{e,dipole} = \frac{1.15\lambda^2}{4\pi} \tag{10.5}$$

$$\lambda = \frac{C}{f} \tag{10.6} \qquad\qquad \text{dBm} = 10\log\left(\frac{\text{Power}}{10^{-3}}\right) \tag{10.7}$$

Where f are the frequencies being jammed -2.4GHz, 5.8GHz and 1.575GHz, λ are the corresponding wavelengths, c is the speed of light, A_e is the Antenna's effective area and G_{Rx} is the directivity of the antenna, which converted to dBm gives 0.6dBm for all the dipole receiver antennas.

The received power in dBm is given by Equation (10.8):

$$P_{Rx} = 10\log\left(\frac{0.6}{10^{-3}}\right) = 27.8\text{dBm} \tag{10.8}$$

The Free Space Loss is calculated via Equation (10.9):

$$LFS = \left(\frac{4\pi d}{\lambda}\right)^2 \tag{10.9}$$

For the used frequencies, this results in values of 71.86dBm, 79.5dBm and 68.2dBm. All values may now be substituted into equation Equation (10.3) and the result solved for the required transmitter power. This yields a required transmitter power, P_{Tx} of 84dBm of 4.44W for 2.4GHz, 91.9dBm or 9.8W for 5.8GHz, and 81.2dBm or 3.36W for GPS.

Clearly the highest of these, 5.8GHz at 9.8W is the necessary power. Indeed, it is possible to minimize the power requirements by reducing the power delivered to the target, and the distance at which the RF cannon should be effective. It is clear from equation Equation (10.9) that the free space loss increases quadratically with the distance, and so reducing the required effective Range will greatly decrease the power required.

10.3.3 Antenna Design

The jammer requires a directional antenna, of which there are several types such as the Yagi-Uda, and variations of the helical antenna [110]. The Helical Antenna in axial mode is chosen because it can be made simply, and is lighter and stiffer in construction than the Yagi. Equations for the design of the helical antenna are given by [115]. For the helical antenna to operate in Axial/End-fire mode, the Circumference C of the antenna must satisfy inequality Equation (10.10), its spacing, S, must satisfy equation Equation (10.11), and the helix angle α must satisfy the in-equality Equation (10.12). Finally, the diameter of the ground plane must satisfy inequality Equation (10.13).

$$\frac{3}{4} \leq \frac{C}{\lambda} \leq \frac{4}{3} \quad (10.10) \qquad S = \frac{\lambda}{4} \quad (10.11) \qquad 12° \leq \alpha \leq 14° \quad (10.12) \qquad D_{GP} \geq \frac{\lambda}{2} \quad (10.13)$$

The Gain of the antenna, provided losses are negligible are given by equation Equation (10.14), where C_λ and S_λ are the wavelength normalized circumference and spacing respectively, and n is the number of turns.

$$G = 12C_\lambda{}^2 n S_\lambda \quad (10.14) \qquad C_\lambda = \frac{C}{\lambda} = \frac{\pi D}{\lambda} \quad (10.15) \qquad S_\lambda = \frac{S}{\lambda} \quad (10.16)$$

Finally, the wire length of the helix antenna is given by simple geometry in Fig. 10.8 and Equation (10.17):

$$L_0 = \sqrt{C^2 + S^2} \quad (10.17)$$
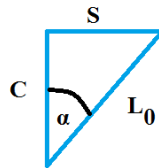
Figure 10.8: Helix antenna angle.

The parameters for the antennas are summarized in Table 10.2. An example of the radiation pattern of the 2.4GHz antenna is shown in Fig. 10.10. The designed helical antenna for the 2.4GHz band is also shown in Fig. 10.9. The copper coil is wound around a main support tube constructed from transparent acrylic, which allows for inspection of the wire element. The disk in the rear is the copper ground plane, which has a concentrically mounted SMA connector, facilitating connection of the antenna to the jammer electronics with a coaxial cable.
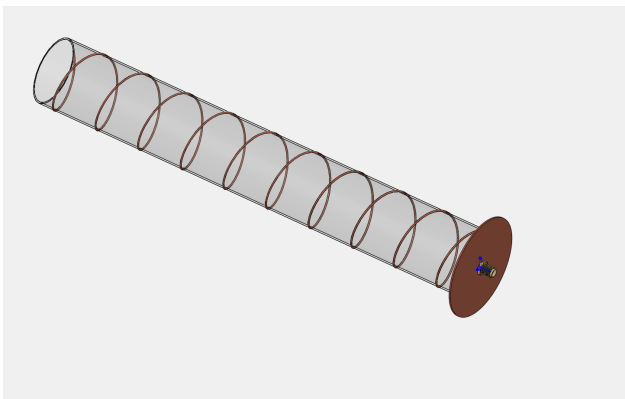
Figure 10.9: 2.4GHz helical antenna.
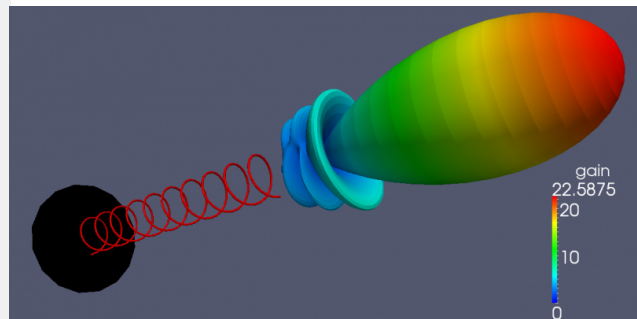
Figure 10.10: Radiation pattern of 2.4GHz jamming antenna.

10.3.4 Verification and Validation

These results are verified and validated using the OpenEMS plugin for MATLAB. It was found that the values of gains given by Equation (10.14) was optimistic, with a predicted gain of 25, 22 and 23 for each frequency respectively.

Table 10.2: Summary of RF cannon antennas.

Frequency	2.4GHz	5.8GHz	1.575GHz
λ [m]	0.1249	0.05168	0.19034
Circumference, C [m]	$0.0937 \leq C \leq 0.16655$	$0.0388 \leq C \leq 0.0689$	$0.142 \leq C \leq 0.253$
Spacing, S [m]	0.03122	0.01292	0.04759
Final RF cannon design parameters			
Circumference, C [m]	0.135	0.055	0.19
Diameter, D [m]	0.04297	0.0175	0.0605
Turns, n	10	10	10
Helix angle α [rad]	13.025	13.22	14
L_0 [m]	0.13856	0.0565	0.2055
L [m]	1.386	0.565	2.055
Antenna length [m]	0.3122	0.1292	0.4759
Ground plane diameter [m]	0.065	0.026	0.0952
Gain	35	33	33.1
Gain OpenEMS	25	22	23

This discrepancy does not adversely affect the previous link budget calculations of Section 10.3.2, as a much lower gain of 17 was used. Using the higher gain predicted by OpenEMS yields new values for Transmitted Power P_{Tx} of 76.3dBm or 2.06W for 2.4GHz, 86.8dBm or 5.88W for 5.8GHz and 64.6dBm or 1.7W for 1.575GHz.

In conclusion, a P_{Tx} of 5.88W is necessary for the RF cannon.

10.4 Removal System Controllers

Each removal system is unique, not only in the removal method, but in operating principle and operating requirements. In order to satisfy each of the armament's unique requirements, controllers tailored to these needs are used. The advantages of using separate controllers are that they reduce the processing load on the main computer by running low-level tasks on a hardware level-removing the need for external interrupts, isolate the main computer from faults, and offer overall system robustness.

HELIADES consists of four removal system controllers. These are:

1. Fire Control System, FCS
2. Stores Management System, SMS
3. Cannon Control Unit, CCU
4. Net Gun Control Unit, NCU

10.4.1 Fire Control System

The fire control system is an independent microcontroller that governs the removal system selection. Its purpose is to communicate between the main computer and the SMS, and coordinate the firing of the selected removal system via its specific control unit. This frees up computational overhead for the main computer, as the FCS can manage the removal mechanisms.

Table 10.3: FCS components.

Component	Model	Quantity	Weight [g]	Cost [$]
Microcontroller	ATMega328P	1	≤ 1	4.30

Design and Operation The system consists of a simple microcontroller, which communicates with the main computer, the SMS, NCU and CCU, as well as turning on the RF cannon. During an engagement, the main computer issues a fire command dictating the use of a specific removal system. The FCS then takes over, communicates with the SMS to see if the specified system is available. Provided that it is, the FCS then commands the specific removal systems controller to fire. If the system is unavailable, the FCS reports this to the main computer, which

may cycle to another removal system, and the FCS repeats the process. Additionally, the main computer may issue several different firing solutions in one command. The FCS stores these firing patterns and executes them when they are possible, cycling through the removal systems based on their availability until the command has been executed.

10.4.2 Stores Management System

The Stores Management System (SMS) is the electronic system which monitors various consumables utilized by the three removal systems. These are specifically the number of remaining rounds for both the Net Gun and the kinetic cannon, the CO_2 pressure for the Net Gun, and the remaining battery power for use with the RF cannon.

These sensors are found in the individual Cannon Control Unit and Net Gun Control Unit. The battery power sensors take the form of a discrete Battery Management Unit (BMU), which monitors cell voltage, temperature, state of charge and cell side impedance. There are several off-the-shelf BMU packages available, hence designing standalone circuits is not necessary. The sensors used in the CCU and NGU are found in their sections specifically.

Table 10.4: SMS components.

Component	Model	Quantity	Weight [g]	Cost [$]
Microcontroller	ATMega328P	1	≤ 1	4.30
Battery Monitoring Unit	TI BQ76930	1	≤ 1	7.00

Design and Operation

The design of the system is simple, it reads the the data from the counters over serial/i2c, and sensor data via serial/i2c or an analog to digital converter where appropriate. Finally the SMS communicates with the FCS, letting it know the status of the stores, again facilitated via serial interface.

The SMS functions by constantly monitoring the state of the stores. When a fire command is issued, the FCS queries the SMS, which reports back whether or not the desired removal system has sufficient materials to function. If the query is positive, then the FCS can continue the fire sequence for the specific removal system, if not, HELIADES must cycle to another removal system.
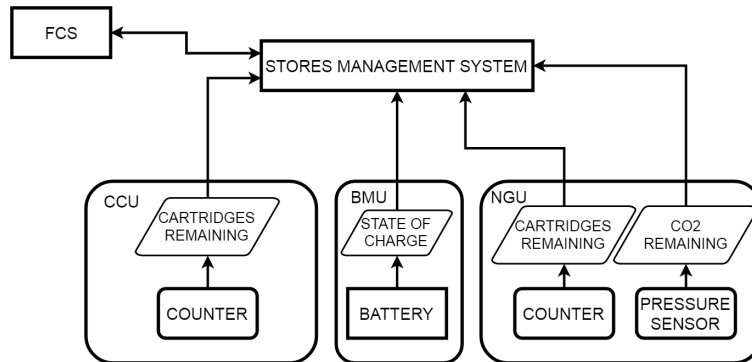
Figure 10.11: Operation of HELIADES' SMS.

10.4.3 Cannon Control Unit

The Cannon Control Unit (CCU) is the electronic system which actuates the shotgun. It consists of a Servo which operates the firing mechanism, Cylinder Position Sensor (CPS) to determine if the cylinder is in battery, and a Counter to decrement the number of rounds remaining. Finally an independent micro controller to coordinate the sequencing and to report sensor information to the SMS. A separate controller frees the main processor, and creates a fault tolerant system.The components are given in Table 10.5.

Design and Operation

The cylinder position sensor is a hall effect sensor, with magnets placed around the perimeter of the cylinder at the location of each chamber. A magnetic sensor was chosen, as there is no wear, and it will be impervious to fouling from dirt and carbon buildup from propellant gases. The micro single pole-double throw (SPDT) switch interfaces with the cylinder lugs, and is depressed with each rotation of the cylinder when it is in battery thereby updating the

Table 10.5: CCU components.

Component	Model	Quantity	Weight [g]	Cost [$]
Servo	MKS HBL575SL	1	53.51	150
Servo	Servo Trigger	1	5	16.95
Cylinder Position Sensor	US1881 Hall sensor	1	≤ 0.5	0.10
Counter	74HC404	1	≤ 0.5	0.74
Counter	SPDT lever switch	1	2	2.95
Microcontroller	ATMega328P	1	≤ 1	4.30

74HC404 decade counter. This component sends a serial output of the round count to the cannon controller and Stores Management System.

When a fire command is issued by the main computer, a signal is sent to the FCS. If the Stores Management System has determined ammunition is still available, the FCS then selects the CCU. Subsequently, the CCU will command the Servo to rotate, actuating the firing mechanism. Once the CPS has determined that the cylinder is in battery, the Servo finishes rotation, and thereby fires a shot shell and the mechanism is then reset. The counter decrements the ammunition count and sends this data to the SMS. This operation is summarized in Fig. 10.12.
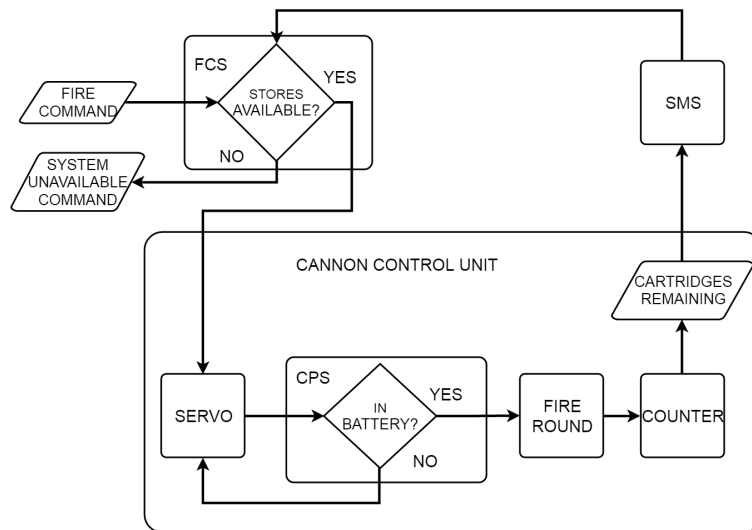
Figure 10.12: Operation of HELIADES' CCU.

10.4.4 Net Gun Control Unit

The Net Gun Control Unit (NCU) is the electronic system which actuates the Net Gun. It consists of a relay triggered Solenoid which operates the FN 303 firing mechanism, a Counter to determine the number of rounds remaining, and an in-line pressure sensor to monitor the CO_2 tank pressure. Finally, an independent micro controller to coordinate the firing, solenoid timing and to report ammunition count to the SMS.

Table 10.6: NCU components.

Component	Model	Quantity	Weight [g]	Cost [$]
Solenoid	MAC 43 R 12 A-3-TB	1	50	50
Solenoid Relay	JZC-11F SPDT	1	10	1.95
Counter	74HC404	1	≤ 0.5	0.74
Counter	SPDT lever switch	1	2	2.95
Pressure Sensor	Honeywell MLH250BSG13B-ND	1	≥ 20	98.78

Design and Operation

The Pressure Sensor is a through-flow type, and is used to monitor the pressure remaining in the CO_2 tank, as well as the pressure loss. This is necessary to estimate the muzzle velocity of the net shell, as with each shot there is a decrease in stored pressure and a decrease in muzzle velocity. The counter is the 74HC04 decade counter, and it is updated by the SPDT switch. This switch's lever interfaces with the ratchet on the back of the magazine, so that each time the cylinder drum advances, it decrements the round count. Finally, the Solenoid which opens the CO_2 valve to launch the projectile is one commonly found in electronic paintball markers. It is controlled through a relay, as the micro controller cannot source sufficient current or voltage to activate it.

When a fire command is issued by the main computer, a signal is sent to the FCS. Once the SMS has determined that ammunition is available, and there is sufficient pressure to launch a net shell, it relays this information to the FCS. The FCS then selects the NCU. Subsequently, the NCU will activate the solenoid, thereby launching the net shell. As the magazine then rotates to chamber the next shell, the counter is updated, as well as the remaining tank pressure. This information is sent to the SMS and the system is reset. This operation is shown in Fig. 10.13.
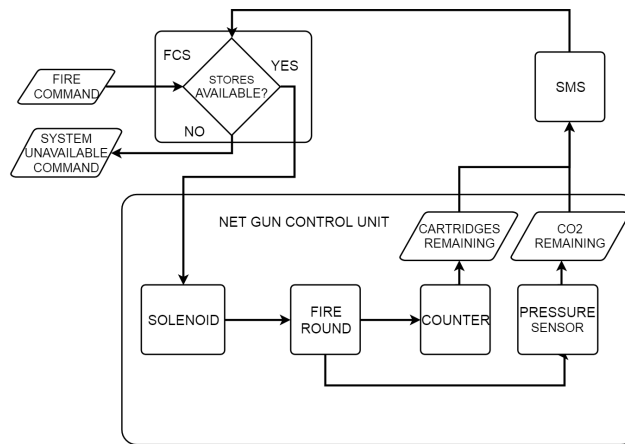
Figure 10.13: Operation of HELIADES' NCU.

10.5 Night Vision

In order to comply with **REQ-PERF-12**, HELIADES must include a Night Vision Device (NVD). There are currently three technologies employed in NVDs, these are:

- **Image Intensification** - This technology utilizes a device called an image intensifier tube, which amplifies the number of photons emitted from passive low light sources.
- **Active Illumination** - This technology relies upon the detection of light reflected back from an active source of illumination such as an LED or laser, often light in the near infrared range. This light is sensed by a standard CCD camera, and displayed.
- **Thermal Imaging** - As the name suggests, this technology detects thermal photons radiated due to temperature differences between objects and the background, and as such do not require an illumination source.

For HELIADES, an Active Illumination system is chosen, in which target illuminations is provided via an infrared tactical flashlight. The stereoscopic cameras are modified to allow their infrared filters to be replaceable, allowing operation at day or night. The rationale for this choice is that in the case of Thermal Imaging systems, they are prohibitively expensive. Devices such as the FLIR AXX series cost on the order of \$10,000 [22], which represents $\frac{1}{5}$ of the total budget. For the Image Intensification technologies, the cost of the image intensifier tube high, around \$3000 each, but the tube may be damaged by bright lights- present at an airport for example, has lower image quality, and high voltage power requirements in [86]. The chosen infrared light and some of its specifications are given in Table 10.7.

Table 10.7: Night Vision components.

Component	Model	Wavelength [nm]	Qty	Weight [g]	Cost [\$]
Infrared Illuminator	IR-75DE	805-830	1	79.38	115

11. Sustainability Approach

Sustainable Development Foreword

We recognize the crucial importance of responsible environmental stewardship so as to mitigate some of the most challenging problems facing humanity, chiefly climate change. Therefore, we aim to incorporate sustainability in every stage of our process so as to achieve and improve upon environmental performance. Our definition of sustainability includes, but is not limited to, minimization of depletion of natural resources and minimization of environmental harm, so as to maintain ecological balance. Through our product, we will proactively ensure a sound biosphere for future generations.' - DSE Group S08

11.1 Sustainable Design

In today's world of ever-increasing consumption, next generation's products need to be designed with sustainability in mind, throughout the entire product life cycle. Reducing the use of resources will not only reduce the production costs and the impact on the environment, but will also make the product a more desirable one on the market.

In order to reduce the environmental impact, the drone shall be made using recyclable materials, unless the design does not allow for it, in case of the Li-Po battery used (although the battery is a more eco-friendly solution in comparison to the alternatives).
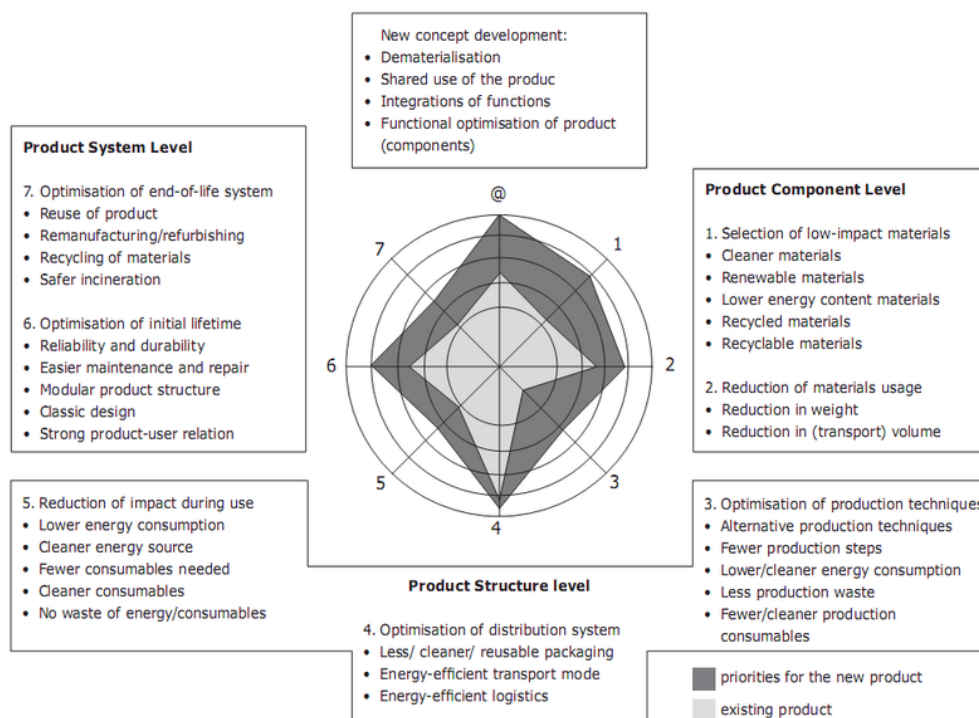
Figure 11.1: EcoDesign Strategy Wheel [92].

The EcoDesign Strategy Wheel (Fig. 11.1, [92]) will be used as a guide for further sustainable design implementation. Though generic in the sense that it can be applied to almost any product, the EcoDesign Wheel does provide a good starting point. A few points of differences - 'Reduction of impact during use' has a relatively low priority on the wheel, whilst in the case of the ADD system, it is as relevant as the other categories of interest. This is elaborated upon in more detail in Section 11.3.

Modularity

One of the driving factors of a sustainable design is the product longevity. A product with a short life time will not be seen as a sustainable one, since its replacement would entail double the energy needed for manufacturing and shipping. Therefore extending the product's life cycle is of crucial importance. In comes the concept of modularity - creating a product with interchangeable components - has been around for quite some time, though mostly underutilized due to the concept of planned obsolescence. A different kind of approach was taken during the design of the ADD system, for a number of reasons:

- Modular components are easier to replace (or *designed* to be easily replaceable)
- Modularity entails easier future upgrades, in case a better component (for example, camera) is available, an existing customer does not have to buy an entire new drone
- Similarly to the above points, repairing the drone is made easier with modules, as the modularity would make it possible for operators, for example, to exchange complex parts they might not have been able to replace otherwise
- A system does not become obsolete with an emergence of new technologies, instead, the system can be upgraded module by module, hence extending product's life cycle

Modularity was one of the driving factor behind design choices. For example, the wings are fully detachable in case a more efficient aerodynamic design is found in the future. All of the electronic components are also modular: CPU and the visual system are due to become obsolete in a few year's time as the technologies evolve, these can be replaced in order to improve performance.

11.2 Materials & Production

The materials used in the production of the ADD system range from metals to plastics, including CFRP. Metals benefit from the ease of recyclability, though require a high amount of energy during manufacturing. Plastics, on the other hand, need to be picked carefully, since their recyclability varies based on the material composition. It was decided to use PLA for the structural frame, due to the ability to 3D print objects, combined with its biodegradability and negligible hazards towards the environment and health of consumers and producers [105]. The biodegradability aspect distinguishes PLA from other plastics, as it can be composted in ten days of treatment in a specially designed unit [105]. Note that PLA does not degrade during regular operation if kept below certain temperatures. The reader is referred to Section 8.4 for more information on additional considerations for using this material. Moreover, PLA's material properties are provided in Table 8.3. The benefits of this material include its low cost, low density, and high specific stiffness, whilst still providing sufficient strength to avoid failure. This allows for decreasing the structural weight, which in turn reduces waste material.

In order to optimize the energy consumption during manufacturing and production, it is necessary to optimize the material selection accordingly. Metals take much more energy to produce, relative to plastics and composites, and will therefore be used only where absolutely necessary. This includes the net gun and shot gun, as well as motor assembly components, manufacturing of which would not be possible using other materials due to the frictional heat and loads exerted during operations. CFRP also requires molding at elevated temperatures, and will therefore be used in locations where stress concentrations exist, such as at the nacelles. Moreover, due to its relatively high heat resistance compared to PLA, it is also auspicious to use it near components that generate significant heat. As mentioned previously, PLA is the main production material being used, which is very favorable for production as it can be 3D printed. This means that the material waste, required heat and gas emissions are minimal. Next to that 3D printing allows the production of shapes that are not possible with conventional production techniques, this means a more efficient design can be achieved.

While material selection is an important step towards sustainable development, another aspect that is equally important is the use of said materials. Picking the most suitable materials would be deemed irrelevant had those materials not been used in a responsible manner. In order to do so, knowledge from Lean Manufacturing is applied [149]. Lean Manufacturing is manufacturing without waste, or, per definition, the dynamic, knowledge driven, customer-focused process through which the whole enterprise continuously eliminates waste in order to create value. Examples of lean manufacturing being implemented into the production process include the use of 3D printers for plastic components (which produces minuscule amounts of wasted matarials), and the use of standardized tools and equipment so that there is no need for specialized tools.

11.3 Sustainable Operations

Making operations of the drone more sustainable involves reducing the energy consumption, alike during production, as well as reducing the noise and emissions by the entire system. The latter was primarily considered during aerodynamic design, since the majority of the noise is generated by the propellers, noise was considered during

trade-off of propellers. A decrease in the noise generated also signifies a more efficient aerodynamic design, hence the energy consumption is (marginally) decreased.

Emissions in terms of environment pollutants have been taken care of by using solar power to produce the required energy for the batteries. Additional batteries are allocated within the ground station in order to enable 'green' operations during night.

Transport

As mentioned in Section 12.2, the shipping package has been optimized to be as tightly-fit as possible, in order to save on the transport costs and indirectly lessen the environmental impact. The system is to be transported via freight shipping, due to the lack of greener alternatives. Following the shipment, a technician is sent to the customer's location in order to install the ground system components. The decision was made not to leave this part of installation to the customer, as an incorrect instalment will lead to a potential mission failure, due to unoptimized radar detection and ground base location.

Lifetime Operations

The energy consumption is mainly comprised of the energy required for operating the radar system. A limitation of current technologies, lowering radar's power consumption has the potential of decreasing system reliability, even compromising the mission. Therefore, renewable energy sources are used in order to balance out the required 'wasted' energy.

Another environmental concern is the battery disposal. Due to the limited number of cycles a battery can be put through, replacement is inevitable. The rest of the drone is designed in a way so as to remain operative for longer than the maximum number of cycles of a battery, therefore multiple batteries will be disposed of during ADD's life cycle.

Furthermore, as mentioned previously, the modular design allows for an extend useful lifetime of the system, contributing to sustainable operations ideology.

Noise

To limit the nuisance for the surrounding and disturbance of the noise level should be limited. A complete analysis of the noise produced by the ADD and the limitations on the number of operations per day and per night has been analyzed for different operating altitudes in Section 7.1.3 .

11.4 End-of-life Solutions

At the eventual end of its service, the ADD system can be re-utilized in different ways. Firstly, the components that can be reused are separated and refurbished, after which they are either used in new products or as spare parts for existing operational systems. This is the case for most electrical components. In case a component (or the entire drone) is beyond the point of repair, it is to be recycled. While metals are easily recyclable (although require plenty of energy in order to be molten and reshaped), composites are harder to recycle.

Due to their heterogeneity, recycling carbon fiber reinforced plastics has to treat fibers and matrix separately. The current solution is to heat up the laminate to the point of melting, and then separate the fibers for reuse. This method does shorten the fibers, deeming them unsuitable for use in aerospace applications. They can however, be repurposed for use in commercial goods that are not as demanding in terms of strength and stiffness. Thermoplastic laminates can be reused in a similar way, as they can be reshaped after the melting process. Furthermore, the entire process consumes only 5% of the energy required to produce 'virgin fiber' [63]. Another alternative is chopping the fibers down to small pieces, that can be used as fillers for body armors or laptop enclosures. A method is also being developed to separate the fibers using wet chemical degradation of the fiber laminate matrix, which could be reserved for use in the future [1].

Finally, as PLA is the main material used for structural elements, its end-of-life solution has to be looked into as well. Due to its biodegradability, it can be recycled in five days of treatment in a dedicated machine [105]. This process uses limited amounts of energy, besides having minimal CO_2 emissions. It should be noted that reusing components fabricated from PLA should not be attempted at this point, as limited knowledge is available on the longterm behavior of this material. Therefore, these components should always be recycled.

12. Operations & Logistics

Operations and logistics describes the delivery and operational processes of HELIADES. This process includes documentation, transport, operations of both aerial vehicle and ground station, inspection and maintenance and finally customer support.

12.1 Documentation

Part List

First of all a part list is provided containing all parts that are included in the system. This will at least include the aerial vehicle and a ground station and their attributes. It also includes spare parts or specific configuration attributes which is dependent on the customer order.

Owner's Manual

Next to the part list, an owner's manual or also called user guide is included. It includes general information on the system and provides instructions for the user. A more elaborate list of contents of the owner's manual is given below. Several important contents are described in this section whereas the first four are described in Section 12.3.

- Installation/assembly instructions
- Setup instructions: setting up restricted area
- Instructions for use
- Product technical specification
- Inspection and Maintenance instructions
- Warranty information
- Certification

- Regulatory code compliance information
- Troubleshooting instructions: Solutions to simple problems including a FAQ which can also be found on the company website.
- Service locations and contact details (described in Section 12.5)
- Emergency Situations

Inspection and Maintenance Manual

The inspection and maintenance manual defines the specific inspection methods and item replacement intervals for each component of the complete system. Directions are given for verifying the condition of specified components, as well as carrying out the necessary cleaning, lubrication and adjustments. A log is being created describing the scheduled and completed maintenance jobs [75]. The maintenance manual also includes an elaborate discussion on resupply and redeployment of HELIADES. Further description of inspection and maintenance processes are given in Section 12.4.

Warranty information

Warranty is defined as a written guarantee, issued to the purchaser of a product by its manufacturer, promising to repair or replace it if necessary within a specified period of time. For HELIADES an initial warranty period of 12 months is being provided to the customer which covers everything unless there is clear evidence of product misuse. An extension of 24 months can be bought by the customer if required.

Certification

By law, for any aircraft operation in the national airspace, a certificated and registered aircraft and an operational approval are required [16]. At the moment there are two methods of gaining FAA authorization to fly civil (non-governmental) UAS: a Section 333 Exemption or a Special Airworthiness Certificate (SAC). The former allows commercial operations in low-risk, controlled environments. Thus this certification does not apply to HELIADES as it aims for operations in the vicinity of airports. The latter applies to UAS in the 'Restricted Category' for special operational purposes. Therefore, the owner's manual includes an SAC which allows carrying out the ADD mission.

Emergency situations

In case of an emergency HELIADES will follow certain protocols. These protocols include the broadcast of a distress message to assure the safety of people and vehicles in the vicinity of the ADD system. The distress message will be broadcasted on the airports specified CTAF/UNICOM frequency in case HELIADES is providing protection at an airport [157]. The message shall include the current position and heading as well as a system status update.

In the emergency procedures outlined below a distinction has been made between "unmanned aircraft emergency", which refers to the aerial vehicle, and "ground control station emergency". These procedures describe how the ADD responds to incidents such as engine-out or power losses as to minimize the threat to surrounding lifeforms or aircraft.

- Unmanned Aircraft Emergency
  - Engine-Out: Standard landing procedure is VTOL. In case of engine failure in aircraft mode, a conventional landing procedure has to be attempted. When engine failure occurs in helicopter mode, the drone shall attempt to perform a safe landing using autorotation. At lower altitudes the drone will also try to autorotate to at least reduce the impact. Even though the landing is to be conducted autonomously, as the system can detect an inoperative engine, care should be taken of property, people, or other manned aircraft in the vicinity. The operator is notified that something has gone wrong and that the drone should be collected.
  - Servo/Actuator Power loss: Actuator loss is only catastrophic in the case of complete control system failure where the drone becomes uncontrollable and maneuvering is impossible. The drone shall initiate a safe descent and perform an emergency landing causing the least damage possible. In case of singular failure the drone returns to base to perform maintenance.
  - Autopilot Power Loss: If autopilot failure occurs due to power loss, a distress message is being sent to ground station. This allows the user to decide if control should be taken over. In the meanwhile a backup system is implemented which lets the drone return to helicopter mode and remain stationary.
  - Degrading Autopilot Performance due to faulty sensors: It is assumed that most failures that are seen as degraded autopilot performance are due to faulty sensors such as the gyros, accelerometers and magnetometers on the inertial measurement unit (IMU) or poor GPS solutions. Similar procedures as with autopilot power loss are applicable in this situation.
- Ground Control Station Emergency
  - Operator Interface Software/Computer Failure: Failure of the user interface results in the inability to control the ADD from the ground system. As it is an autonomous system, the drone is able to continue its mission. If the user requires the drone to return to base, a mechanical button should be pushed which sends a signal to the ADD which allows the ADD to safely terminate the mission and perform an automated landing.
  - Total Power loss: In case of a total power loss, the user is unable to communicate with the drone. This also prevents the user from being able to safely return the drone to the ground station. Should the drone not receive a message from the ground station within 5 minutes, it will automatically return to base.
  - User Abort mission emergency: In case the user prefers to abort the mission at any moment in time, an emergency button on the ground station allows for immediate termination of the mission. HELIADES will interrupt its mission and return to base using the fastest safe trajectory.

12.2 Transport

UAV transportation systems vary greatly, and range from Black Hornet's pocket-sized storage box, to Global Hawk's strategic airlift transport necessary for movement around the globe. With the designed ADD weighing less than 10kg, the transportation of the system (together with the ground station components) does not pose the grandest challenge in comparison to other design elements. Nevertheless, optimizing the transportation process, in terms of the packaging size and delivery routes, will primarily cut down the cost and resources (hence also contributing to the sustainable development aspect), but also make the process of delivering easier and quicker.

HELIADES' modular design enables quick disassembly of the entire drone, which in turn reduces the size of the transport container. One of the concepts featured during concept generation was a 20-foot shipping container equipped with all the necessary ground station electronics inside and photovoltaic panels on the roof. While this method is efficient for constantly mobile operations, most of the expected customers will not move their system around regularly. Hence the system shall be transported in such a way that it consumes the least amount of space possible. In this way, transportation can be done through the regular postal routes.

For shipping purposes, HELIADES' wings detach and can be placed in parallel with the fuselage, as to consume less space. Since the wings are top mounted, the detachment mechanism can be made simple (yet still secure), in order to enable for a quick reassembly time.

A customer might have a need for a mobile ADD system, in case it is used for security purposes at one-time events, or leased out to other institutions for short periods of use. The ground station system is therefore designed to be easily transportable, fully fitting within a specially-made suitcase. The drone itself can be transported alongside, without occupying more than the volume occupied by the ground station suitcase. These 3 suitcases will measure

approximately $1m \times 0.5m \times 0.5m$, $2.0m \times 0.75m \times 0.4m$ and $0.5m \times 0.2m \times 0.5m$, which will, respectively, carry the ground station (including radar system and replacement parts), the drone itself, and the control station.

12.3 Operations

This section discusses operational aspects of the product. In a chronological order, the setup is first discussed after which regular operations are described.

12.3.1 Setup

With the entire system transported and present on site, the customer is left with two cases: one containing the disassembled aerial system and the other containing the ground station. Regarding the former, assembly is a matter of clicking the wing section to the fuselage section and fastening the bolts. The ground station requires a more elaborate approach, as the radar stations have to be distributed over the area in order to ensure full coverage over the entire specified restricted and detection area. All data needs to to be directly streamed to the ground station via a WiFi connection. These stations can be transported to and set up at the desired locations by a technician from the company. Once these are set up, a check at the ground station main unit is performed to verify that the radar signals from all stations are being received. Opening the box and switching on the system, besides verifying the radar connection, is all that is required to set up the ground station.

The operator can be customer's existing employee, who will only need to intervene with normal operations during emergencies. The autonomy of the system does not require a trained person to be present at the system's command at all times, but should be in the vicinity in case, for example, the drone requires approval for using lethal munition, or in case maintenance and servicing need to be conducted.

After the ground station and aerial system have been set up, a secure connection between the two has to be obtained in order to allow for data transmission. To this end, a check has to be performed regularly to ensure the radar data, positioning data and manual control data are transmitted correctly. The latter shall only be used in case of emergencies. Ground station software is included to perform these checks.

Finally, general aerial system functions have to be checked through a system readiness test. Therefore, a short test flight should be performed after the system has been set up. This test flight demonstrates correct functioning of removal system, control system, positioning system and camera system. If this test is performed successfully, the system is deemed ready for regular operation.

12.3.2 Regular Operations

Regular operation requires very limited human interference, as the entire system is autonomous. The system remains in stand-by mode in which only detection functions are constantly active. This decreases the overall power consumption, thus adding to sustainability. Interference is only required when maintenance is due, during which the system can be switched off completely to allow for safe handling. Resupply can be performed whilst the system is in regular operation mode.

12.4 Inspection & Maintenance

Newly developed technologies such as virtual reality and simulators can be used during staff trainings in order to reduce costs, for both the constructor as well as the customer that is to use the product.

Instead of long seminars and thick manuals, both of which would cost plenty of man-hours, an alternative way of staff training would be via a virtual reality environment, in which the operators can both learn and practice their skills before proceeding to the actual aircraft. The initial cost of development of the software to be used pales in comparison to the costs saved for the operator, mainly due to the ease of conducting maintenance.

The virtual reality guide is to be structured as follows:

- Visual guide to maintenance: this section of the simulator will demonstrate in detail how to inspect and conduct maintenance for each part of the drone. Categories within this section include
    - End-of-Mission Procedure
    - External Inspection Procedure
    - Component Calibration & Replacement Procedure
    - System Upgrade Procedure
- Maintenance simulation: an environment in which the operator can try out the above mentioned maintenance tasks without the fear of damaging the aircraft.

- Flight simulation: In case the autonomous pilot becomes inoperative, manual override is possible. This simulator woud serve to get the operator acquainted to the manual operation mode, once agian, without exposing the aircraft to any potential damage.

In terms of the maintenance schedule, the drone shall be checked on a regular basis for wear-and-tear damage that is accumulated over time. Furthermore non-scheduled maintenance must be taken into account, in case of a main component failure or software and component updates. Software updates are not considered a part of the scheduled maintenance; further justification presented in Section 12.5. The maintenance schedule is to be integrated in the ground station user interface, in the form of a pop-up notification, in order to inform the operator in due time.

In order to keep HELIADES operative and to reduce the risk of component failure, inspection and maintenance has to be performed regularly. In terms of the maintenance schedule, the battery has to be replaced and ammunition has to be resupplied after every mission and the drone shall be checked on a regular basis for wear-and-tear damage that is accumulated over time. Furthermore non-scheduled maintenance must be taken into account, in case of component failure or software and component updates. The complexity and rate of maintenance strongly depend on the accessibility of the components under inspection or maintenance and the simplicity of the described procedures. Therefore the design includes hatches to access internal components. The remainder of the section will expand on the various maintenance procedures listed below that will form the foundations of detailed final procedures being created following the final design. Example procedures on replacement and calibration will be given for certain components as of now. As stated before, these maintenance procedures are provided on the GUI and can be practiced using the virtual reality guide. Furthermore, during the actual maintenance, the procedures are provided as support for the licensee.

- End-of-Mission Procedure
- External Inspection Procedure
- Component Calibration & Replacement Procedure
- System Upgrade Procedure

End-of-Mission Procedure

PURPOSE:
To establish the steps to be followed for effective replacement of battery and resupply of ammunition.

SCOPE:
This procedure describes the process for replacing the battery and resupplying the ammunition for either the net gun or the kinetic cannon at the end of a mission. Replacing the battery is done by removing the wing fairing while the ammunition is resupplied by opening a hatch underneath the fuselage. The procedure is to be performed by qualified personnel in order to meet the product quality requirements and prevent premature failure [55][59].

PROCEDURE

    I General Procedure:
       A. Equipment and materials
          1. The equipment required for battery replacement includes a wrench and a fully charged spare battery.
          2. The ammunition replacement does not require specific equipment beside the spare ammunition.
       B. Battery Replacement
          1. Once HELIADES has landed, wait for the propellers to come to a standstill.
          2. Visually inspect possible damage to wing fairing.
             - If damage is present, report the findings to the supervisor. If the fairing is unharmed, proceed with the next step.
          3. Unlock the latch for the fuselage hatch.
          4. Open up the hatch
          5. Locate the battery and disconnect it from the HELIADES.
          6. Store the battery in the recharging pods.
          7. Connect the charged battery to the HELIADES in the fuselage using the battery hardware diagram.
          8. Close the wing fairing.
       C. Ammunition Resupplying
          1. Once the HELIADES has landed, wait for the propellers to come to a standstill.
          2. Visually inspect possible damage to the removal system hatch.

- If damage is present, report the findings to the supervisor. If the hatch is unharmed, proceed with the next step.
3. Unlock the latch and open the removal system hatch.
4. Take spare ammunition.
5. Resupply the ammunition in the gun magazine.
6. Close the hatch and lock the latch.
    D. Reboot HELIADES system
        1. Boot the HELIADES system on the GUI of the ground station.
        2. Check if system boots as usual.
            - If the system boots properly, proceed with the next step. If error messages show up, check the documentation for a solution and report the findings to the supervisor.
        3. Document a maintenance report.

External Inspection Procedure

PURPOSE:

To establish steps to be followed for inspection of the exterior of the HELIADES flight vehicle.

SCOPE:

This procedure describes the process for inspecting the flight vehicle's exterior which is done to detect cracks before these reach critical size. This procedure is to be completed by the operator.

PROCEDURE

I General Procedure:
    A Equipment and materials
        1. Equipment required for detecting cracks includes magnifying devices delivered to the customer.
    B Crack Inspection
        1. Inspect critical areas for cracks.
            - These critical areas include the wing-fuselage and wing root connections, landing gear, nacelle attach points and the propellers. Visually present damage shall be documented and reported to the supervisor. If these cracks are within 2 mm of the critical size, HELIADES should be taken out of service for repairs.
        2. Inspect less critical areas for cracks.
            - These areas include the wing and tail-planes and their control surfaces. Again, the presence of cracks shall be documented and repaired when within 2 mm of the critical crack size.
        3. Finally inspect the remaining skin parts of the vehicle.

Component Calibration & Replacement Procedure

PURPOSE:

To establish steps to be followed for effective calibration and replacement of components.

SCOPE:

This procedure describes the steps to be followed for calibrating and/or replacing specific components on the HELIADES flight vehicle. These procedures have to be executed by qualified personnel.

PROCEDURE

I General Procedure:
    A Equipment and materials
        1. Equipment required for these procedures include wrenches and screwdrivers applicable to specific bolts and fasteners.
    B Component Calibration & Replacement
        1. Check the instrument carefully to determine if the component:
            a Has been operating under adverse environmental conditions like high vibrations, temperature, humidity, etc.
            b Has any broken parts or cables.
            c Has worn-out parts, etc.
        If any of the above conditions apply, document them and report the findings to the supervisor. If none of the conditions apply, proceed with calibration & replacement.
        2. Refer to the following sections for specific component procedures:
            a Section II: CPU (BeagleBone Black) (Replacement)
            b Section III: Battery (Thunderpower RC TP5000-12SM70S) (Replacement)

       c Section IV: IMU Module (Razor 9dof IMU) (Calibration and Replacement)

       d Section V: Net gun (Replacement)

II CPU (BeagleBone Black)

  A Replacement

     1 Unlock the latch of the fuselage hatch.

     2 Open up the hatch.

     3 Remove the CPU connections.

     4 Loosen the CPU bolts.

     5 Remove the CPU.

     6 Position the new CPU.

     7 Tighten the CPU bolts.

     8 Reconnect all cables to the CPU using the CPU hardware diagram.

     9 Close the hatch and lock the latch.

   10 Reboot the complete system.

        • If error messages show up, check the documentation for a solution and report the findings to the supervisor.

   11 Report the replacement.

III Battery (Thunderpower RC TP5000-12SM70S)

  A Replacement

     1. Follow battery instructions in the End-of-Mission Procedure.

IV IMU module (Razor 9dof IMU)

  A Calibration

     1 Unlock the latch of the fuselage hatch.

     2 Open up the hatch.

     3 Disconnect the cabling and connections from the IMU.

     4 Loosen the bolts connecting the IMU to the fuselage.

     5 Take out the IMU.

     6 Perform calibration using instructions from [81].

     7 After calibration tighten the bolts again to connect the IMU to the fuselage.

     8 Then reconnect the wiring to the IMU using the IMU hardware diagram.

     9 Close the hatch and lock the latch.

   10 Finally tighten the fairing bolts again.

  B Replacement

     1 Follow Calibration instructions beside Item 6 and replace existing IMU with new one.

V Net Gun

  A Replacement

     1 Open up hatch.

     2 Remove wings for better accessibility.

     3 Close the valve of the compressed air tank.

     4 Remove the net shell ammunition.

     5 Unscrew compressed air tank.

     6 Remove air tank.

     7 Place new filled up air tank.

     8 Tighten screws and bolts.

     9 Insert full set of net shell ammunition.

   10 Place and fix wings.

System Upgrade Procedure

PURPOSE:

To establish steps to be followed for system upgrade, both software- and component-wise.

SCOPE:

This procedure describes the process for upgrading the system software or system components. Upgrading the software is done through the ground station while system components refer to the HELIADES flight vehicle. The procedure is to be executed by qualified licensees.

<u>PROCEDURE</u>

I General Procedure:
  A Equipment and materials
    1. The tool required for the upgrade is component dependent, based on the level of complexity of the upgrade.
  B Upgrading system software
    1. Make sure the HELIADES is positioned on the landing platform.
    2. Make sure the HELIADES has more than **50%** battery life left.
        • Else replace the battery using the "Battery Replacement" procedure.
    3. Open up the user menu of the GUI.
    4. Open up the Software Upgrade tab.
    5. Initiate the firmware or software upgrade.
    6. Follow the provided instructions.
    7. Check if the upgrade is properly installed.
        • If warning messages show up, consult the documentation and report to the supervisor.
    8. Reboot the complete system.
    9. Document the System Upgrade.
  C Upgrading system components
    1. Identify Component designated for upgrade.
    2. Follow provided instructions for upgrade.

12.5 Customer Support

Nowadays, customer support forms a major contributor to customer satisfaction. It is important for a company to incessantly provide its customers with adequate support. Therefore, a platform has to be provided in which customers can easily ask questions, can easily report problems and can easily obtain updates for ground station and aerial system software. This section elaborates on the customer support that is to be provided.

Direct Contact

Firstly, customers should be able to contact the company at any time. Preferably, the majority of media platforms are covered for this, being phone lines, websites, email and Facebook. The latter is especially important as an increasing number of companies is shifting most of its customer support resources to this medium, so as to ensure short response times. This is mainly due to it being a convenient way for customers to get into touch with companies besides also being one of the largest platforms currently available. Moreover, the group aims for 24/7 support throughout the year. In order to achieve this, it is intended to make use of bots, i.e. automated algorithms that are able to respond to the majority of questions received. Nevertheless, it is important to still have a human aspect to customer support, so a dedicated team should be focused on addressing all inquiries. Apart from that, having an extensive FAQ available in both the manuals as well as on the company website is likely to decrease the number of questions received, thus decreasing the size of the aforementioned team.

Software support

Regular software updates, if deemed necessary, should be scheduled to ensure appropriate use of the system throughout time as well as to account for encountered bugs. By notifying customers whenever an update is available, it can be ensured that they are distributed accordingly. The use of a system in which updates are automatically installed through 3G/4G was considered, but decided against due to security concerns. Note that software updates are only issued in case changes are necessary, as otherwise a situation might present itself in which the performance is actually decreased due to updates.

Furthermore, customers should be able to communicate bugs and other software issues to the company. This allows the company to resolve issues as soon as they arise. Besides that, it is beneficial for customer satisfaction, as customers can voice their concerns and subsequently experience a better product.

13. Risk Management & RAMS

In this chapter, possible hazards are anticipated by performing risk management. Furthermore, the reliability, availability, maintainability and safety (RAMS) are discussed.

13.1 Risk Management

In the Baseline Report and Mid-term Report, risk management was already performed on a general and conceptual level, respectively [66, 67]. In these, mainly functional risks were discussed as well as some general system risks. Here, the full risk map was generated for the HELIADES for both its functionalities as well as its subsystems. This is done using the same risk process as in previous reports, see Fig. 13.1 [66, 67].

Figure 13.1: The process of risk management.[91]

This section follows the systems engineering approach shown in Fig. 13.1. Risks are identified, assessed, analyzed, and finally handled.

Identification

Risks have been identified with respect to functions of the system [66] [67]. However, as a concept has since been selected and analyzed in more detail, specific component risks are also analyzed. The functions which are identified follow from the functional diagrams in Chapter 2. Therefore, it should perform ground operations, fly, eliminate the threat, provide power, and handle the data. More specific functions underlying the aforementioned functions were used for the risk analysis and can be found in Fig. 2.1. The investigated components follow from the component list from Chapter 14.

Assessment

Both the assessment of the probability and the consequence of occurrence are discussed in this section. In the baseline report, five probability categories were distinguished [66]. These are almost certain (>90% probability), likely (65-90% probability), possible (35-65% probability), unlikely (10-35% probability) and remote (<10% probability). These risk probabilities are given per 100 flight hours [76]. For the consequence of occurrence, also five categories were distinguished, being catastrophic, critical, moderate, marginal, and negligible [66].

Analysis

All identified functions and components were then analyzed and classified in terms of probability and consequence. First, the functions and components are discussed. For this analysis, it is assumed that solely the particular function will fail. The codes shown in the list below were used as identifiers in the risk map. Note that the detection function is divided in radar detection [r] and visual detection [v]. Moreover, removal is divided in mechanical failure [m] and net failure [n].

Functions

- **[F01] Pick Up Target:** As picking up the target is done by the human operator, failure of this is *unlikely* as most places on Earth that require an ADD for safety are accessible. Moreover, all nets are equipped with a GPS tracker, allowing them to be easily located. The consequence of not picking up the target drone is *negligible*, as it does not affect HELIADES' primary purpose.

- **[F02] Maintain Stores:** Keeping stocks up to date is also a task to be performed by the human operator. Failure probability is *remote* as the operator should have a good overview of the current stocks via the ground station. Moreover, the consequence is *negligible* as well, as the ground system should have a large stock and threats are assumed to appear once a day.
- **[F03] Inspect System:** Inspecting the system is another function performed by the human operator. The probability of failure of this system is *unlikely*, as the human operator should have sufficient knowledge on how to perform this inspection. As it is assumed that inspection will reduce the failure probability of other systems, its consequence is *moderate*.
- **[F04] Attach Aerial System to Charger:** The last function performed by the human operator, but the most critical as the aerial vehicle of the HELIADES fully depends on its available power. However, as the operator is most likely aware of this threat, its failure probability is classified as *remote*. Note that a battery swap is performed, rather than actually attaching the system to a charger. Moreover, its consequence is *critical*, as the mission could be performed once, but not repeated.
- **[F05] Provide Lift:** Lift is provided by the wings in aircraft mode, depending on the wing condition and velocity, and the propulsive system in helicopter mode. Both modes are proven to be a reliable design. However, as the wing and rotor are significantly smaller compared to conventional aircraft or helicopters, interference from dirt or insects has a greater effect on performance. Therefore, the probability is expected to be *possible*. If lift loss occurs, the vehicle cannot remain airborne, thus having *catastrophic* consequences.
- **[F06] Provide Propulsion:** Propulsion has to be provided to ensure the vehicle remains airborne. A proven design is used, but the tilting function can be fragile, so its failure *likely*. As the mission cannot be performed without propulsion, its consequence is *catastrophic*.
- **[F07] Provide Stability & Control:** Stability and control is provided by the rudder, elevators, and ailerons as well as by the pitch control mechanisms. The inverted V-tail has two control surfaces combining the functions of elevators and rudders. Therefore, if one of aforementioned control surfaces fails, the other control surfaces provide redundancy. Moreover, these conventional control surfaces have proven to be reliable and therefore their probability of failure is *unlikely*. The consequence is *marginal* due to the present redundancy.
- **[F08] Detect Drone: [r]** Initially, the target drone is detected by the radar system. When HELIADES approaches the target, the visual system is used to detect the drone. If the radar system fails, the detection of the drone is expected to fail *almost certain*. As the incoming drones are expected to have a relative small amount of conducting elements, their detection area is small and comparable with, for example, birds. Therefore, the radar system will give a false alarm in most cases. However, this can be checked if the visual system is used to identify the drone or the drone is close enough to the radar to confirm its identity. The consequence of this failure is *moderate*, as time could be wasted by returning to base and swapping the batteries, but if there is a sufficient battery level, the mission could be performed faster as the HELIADES is already in the air. **[v]** The visual detection system is *unlikely* to fail, as it just depends on a few subsystems and reliable off-the-shelf products are available on today's market. However, the consequence of this possible failure is *critical*, as the target drone's exact position cannot be estimated and therefore the accuracy of capturing the drone will decrease drastically.
- **[F09] Remove Drone:** For the removal of the drone, a few points of failure are pointed out. **[m]** The mechanical part of the system depends on a few subsystems and is an newly designed system, which results in a *possible* failure probability. The consequence of this failure is *catastrophic*, as the mission cannot be completed. **[n]** The net system can fail as well if unfolded in an improper way or weather conditions are harsh. Its probability is possible and again the consequence is catastrophic for the same reason as the mechanical failure.
- **[F10] Provide Power:** By providing power is mainly meant the correct supply and distribution of the available power. As reliable off-the-shelf products exists and the function is not dependent on other functions, the probability of failure is *remote*. However, the consequence is *critical*, as incorrectly regulating the power might result in overheating, and failing if maintained for a significant period, components or shortening of power required, which is a significant risk for performing the mission properly.
- **[F11] Handle Images:** Handling of images mainly depends on computer processing speed and transceiving abilities, which depends on the processor and power required. Failure probability is *remote* as off-the-shelf products have proven to be able to handle images at appropriate speed. The consequence of failure is *critical* for the same reasoning of failure of the visual detection function. Moreover, improper image handling speed might result in undesired lag, decreasing the accuracy as well.
- **[F12] Handle Position Data:** For position data handling, the same yields as for the image handling considering the probability of failure, being *remote*. Despite using the visual detection system, its consequence is *catastrophic*. The human operator might be able to orientate itself, being able to perform the mission but HELIADES' position might be in the restricted area, thus failing the mission.
- **[F13] Handle User Commands:** For handling user commands, probability of failure is considered to be *un-*

likely, as off-the-shelf products can be used. But it is much more dependent on several other functions. The consequence of failure is *catastrophic*, as the mission will probably fail if commands are handled improperly.

Components

- **[C01] CPU:** With the BeagleBone Black, a solid and reliable CPU choice has been made. If properly installed and programmed, probability of failure of this component (hardware/software failure) is considered to be *remote*. Nevertheless, the consequences of failure are *catastrophic* as the CPU can be seen as the heart of the HELIADES, being essential towards mission success.
- **[C02] IMU:** Like the CPU, an off-the-shelf component is used for the IMU. These components have been extensively tested delivering a sufficient reliability [71, 108, 111]. Therefore failure of the sensors in the IMU are *remote*. As the IMU is a fundamental aspect in chasing the threat, consequences are seen as *critical* depending on the reset capability of the IMU. If the IMU is able to function again after reset, the mission can still be completed.
- **[C03] GPS:** Performing routine checks on the accuracy of the sensor and re-calibrating it if required keeps the reliability of the sensor readings up to a satisfactory level [120]. Therefore probability of failure is kept low and seen as *remote*. If GPS signals are unavailable due to failure for example, the IMU is able to take over the GPS function. Consequences due this failure are thus seen as *marginal*.
- **[C04] Battery:** Although the used LiPo batteries are off-the-shelf, a questionable reliability is present due to both performance and safety issues. [39, 42]. The expected lifetime of these batteries is around 300-400 charge/discharge cycles [146]. However, performance is highly dependent on the batch number and the number of cycles and depth of discharge. If mistreated the battery can burst and/or catch fire because of the high energy storage. The likelihood is therefore quantified as *possible*. The battery is the crucial component and mission cannot be ensued in case of failure, thus seen as *catastrophic* for the mission.
- **[C05] Propulsion System:** The propulsion system includes the propellers as well as the gearbox of the engine. As failure in the propellers mainly occurs due to impact which is prevented by collision avoidance by the control system, this failure is being neglected in the risk analysis. Nevertheless it should be noted that if impact occurs propeller blades possibly fail which results in an emergency landing. The designed gearbox uses a two stage gearbox like the PT6 which has a reputation for excellent reliability [53]. Although there is major scale difference between these two systems, the team considers the comparison valid for now and identifies the probability of failure as *unlikely*. Without the propulsion system, the HELIADES is not able to continue its mission thus seen as *catastrophic*.
- **[C06] Stereoscopic Camera System:** This system uses an off-the-shelf component which is a proven design in drone flight. Therefore an *unlikely* probability is assumed. Although failure is *unlikely*, it will still be *catastrophic* for the mission as aiming at the target is becoming immensely difficult.
- **[C07] Laser Range Finder:** The laser range finder is seen as an assurance for accurate aiming at a target. Though it might not work without the previously discussed camera system because the laser is not able to identify what it is aiming at. Furthermore the range finder is a simple sensor with a *remote* failure probability if installed correctly and supplied with sufficient power. As the laser is mainly seen as a redundancy to target finding, consequences of failure are quantified as *marginal*.
- **[C08] Ultrasonic Range Finder:** The sensor used for landing is an off-the-shelf low complexity ultrasonic range finder. Therefore, like the laser range finder, the probability is modest and seen as *remote*. Furthermore, landing failure is not considered detrimental for mission output. Thus *negligible* consequences in case of failure.
- **[C09] Infra-red Sensor:** Like the previous mentioned components, the infra-red sensors are extensively tested and include a low level of complexity. Therefore it also has a *remote* probability. The consequences towards the mission are *marginal* as hovering (sidewards) flight is only a small slight portion of the mission.
- **[C10] Barometer:** The off-the-shelf Bosch BMP180 barometer is a highly accurate pressure sensor calibrated on beforehand [7]. If the sensor readings are check regularly and re-calibrated is necessary, the probability of failure is considered to be *remote*. In case of sensor failure, the system will have to base it's altitude data on the less accurate GPS readings. Therefore consequences are deemed *marginal*.
- **[C11] Pitot Tube:** Initially the pitot tube's probability of failure is dependent on it's mission environment. If the pitot tube is covered during ground operations and being inspected before flight, failure is seen as being *remote*. Like the barometer, if the pitot tube produces faulty readings, the less accurate GPS readings are to be used. Thus also following *marginal* consequences.
- **[C12] Cabling/Wiring:** The cables themselves are very reliable, the connections of the cabling might introduce risks. Depending on the type of connections, cables might disconnect or come loose due to vibrations. If connected or soldered properly, cabling issues/risks should be avoided. Thus failure is seen as *unlikely*. The consequences though are *catastrophic* as it might cut off the power to mission critical components.

Handling

If the risk of a specific function or component is too high, meaning in the red zone indicated in Fig. 13.2, actions should be taken to decrease the probability and/or level of consequence and therefore decreasing the risk. This risk mitigation is discussed in this section. For the functions and components in the yellow zone, action is taken if deemed necessary or when quick and cheap solutions are available. The functions which are discussed are providing lift, providing propulsion, detecting by radar and drone removing. For the components, the risk in battery failure is being mitigated to prevent the system from having risks in the red zone. The updates are visualized in the updated risk map from Fig. 13.3.

Functions

Necessary Adjustments

- **[F05] Provide Lift:** The lift function can be enhanced by choosing an robust airfoil for the wing and rotors to overcome dirt or bugs. Furthermore, de-icing equipment can be considered for the wing. These methods should decrease the probability of failure to unlikely.
- **[F06] Provide Propulsion:** To decrease the almost certain probability of the propulsion function, a robust airfoil is selected which is still capable of providing propulsion when dirt is on the rotor. Moreover, multiple spare rotor parts are added to the product, which also decreases the likelihood of failure of providing propulsion after the HELIADES had a rough landing or has crashed. It is expected that these alterations lead to an unlikely probability.
- **[F08r] Detection by Radar:** To decrease both probability and consequence, multiple radar systems at different locations or very expensive ones could be used. Although, cost will increase significantly for the customer, but this is not a concern for the design of the HELIADES but for the customer. Expected is that using one of these methods will decrease the probability to possible and decrease the consequence to marginal. For example, market analysis shows that the Elvira of Robin Radar Systems [139] is able to detect drones specifically.
- **[F09] Drone Removing: [m]** The shooting mechanism can be tested thoroughly which decreases its probability from possible to unlikely. **[n]** To increase the accuracy of drone removing, and thus decrease the likelihood of failure, multiple net shots are carried and reloaded automatically if a shot is fired. Though the probability of failing will remain possible, its consequence is less dramatic and is reduced to marginal, as four additional shots can be fired after the first one.

Possible Adjustments

- **[F08v] Detection by Visual System:** A redundant camera could be added if deemed necessary. This would decrease the consequence of failing to marginal.
- **[F12] Handle Position Data:** A redundant GPS sensor is added to the ground station, which can be used to compare position data. This will decreasing the consequence to marginal.
- **[F13] Handle User Commands:** HELIADES' level of autonomously performing the mission could be increased by using thoroughly tested algorithms, decreasing the consequence to moderate.

Components

Necessary Adjustments

- **[C04] Battery:** First of all, the type of battery being used requires extensive testing. Furthermore, taking sufficient care of the charge and discharge level will reduce the risk. Having a considerable number of batteries will reduce the number of discharge cycles per battery over a certain amount of time reducing the probability of failure. As a general rule, it is time to retire the pack when the battery no longer holds more than 80% of its original capacity, and certainly if there is excessive puffing [60]. Applying these measures all together will reduce the probability from *possible* to *unlikely*.

Possible Adjustments

- **[C01] CPU:** Adding redundancy by implementing a second CPU which is able to take over the main tasks the main CPU in case of sudden failure. The method on how this would is described in [23]. This would reduce the severity of the consequences to *marginal*.
- **[C04] Battery:** In order to reduce the consequences of failure, an extra battery can be incorporated to take over in case the main battery fails which will reduce the consequences to *marginal*. This adjustment is not advisable though as it will massively increase the total weight of the drone which might not be possible as other components might have to be scaled up.
- **[C06] Propulsion system:** Reducing the consequences of single gearbox failure can be done by including the possibility of actuating both engines by both gearboxes. So if one would fail, the other can actuate both

engines. Although this would increase both weight and complexity, consequences would be reduced to *moderate*.

- **[C07] Stereoscopic Camera System:** Implementing a second high resolution camera which is able to identify targets from considerable distance will be able to take over the aiming function of the camera system. However collision avoidance can not be done with this camera and therefore greater care has to be taken in flying at lower altitudes. The severity of the consequences becomes *critical*.
- **[C13] Cabling/Wiring** Again by introducing redundancy into the system, consequences can be mitigated. Implementing redundancy in this case would mean that the total distance of the wiring is being doubled which is unfeasible. Therefore the consequences remain *catastrophic*.
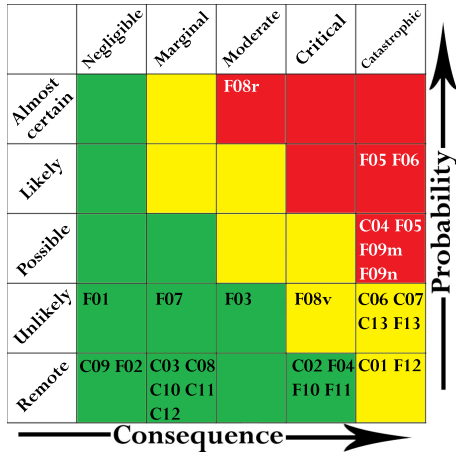

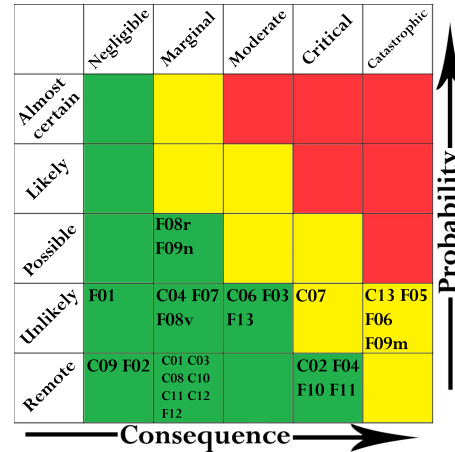Figure 13.2: Risk map of functions and components.

Figure 13.3: Mitigated risk map of functions and components.

13.2 Reliability, Availability, Maintainability, Safety (RAMS)

Reliability

Reliability denotes a product or system's ability to perform a specific function over a given amount of time and may be given as design reliability or operational reliability. Design reliability describes the ability to function as intended directly after production, whereas operational reliability is described as the ability to fulfill its function over a specified period of time [38].

The cost to design and operate a drone safely may include safeguards such as redundant sensors, logic controllers, and reserve battery capacity in order to be able to provide the desired reliability. Implementing redundancy though, adds complexity, weight, and cost to the drone. Therefore, risks that could compromise the mission have been identified and a certain level of redundancy has been realized. Furthermore, after the first deployment and testing of the HELIADES, it is likely that unique unforeseen failure mechanisms are revealed, which are to be addressed to assure the set reliability [145].

Reliability goal statement

The initial reliability goal statement is based on and addresses four elements: mission function, operating environment, probability of success, and the duration over which the reliability is to be ensured.

- Function: Prevent any fixed wing and rotary wing drones whose mass is smaller than 2.5kg and velocity smaller than 35m/s from entering a restricted area of 1 km in diameter (**REQ-PERF-01**).
- Environmental elements: This covers location, circumstances, conditions, etc.) as well as potential stress factors, such as dust. As mentioned in the function description, a 1 km diameter restricted area shall be protected which can be located at a myriad of locations. Equal reliability is ensured during night and certain weather conditions, such as rain and moderate wind, as compared to regular conditions. In case of heavy winds, hail, and snowstorms, a reduced reliability arises and the system should not be operated under such conditions. Stress factors such as dirt and dust do not reduce the reliability.
- Probability and duration: These are described together in a couplet. Multiple product specific couplets are allowed. In this case, a distinction is made between a single mission and yearly operation. According to a reliability synthesis conducted by Reliability Consultants Ltd a Mean Time Between Failures (MTBF) of 625 flight hours is found for UAVs [76]. Substituting this into Equation (13.1) yielded the reliability after t hours of

operation and produced the following mission and yearly reliabilities.

$$P(t) = e^{\frac{-t}{MTBF}} \tag{13.1}$$

- – Single removal mission (Design reliability): **99%** reliability over an average 2.5 minutes of flight.
- – First Operating Year (Operating reliability): **88.54%** reliability in the first year of operation.

These elements combined result in the reliability goal statement below:

HELIADES will prevent any fixed wing and rotary wing drone whose mass is smaller than 2.5kg and velocity smaller than 35m/s from entering a restricted area of 1 km in diameter with a 99% reliability for a single mission over an average flight time of 2.5 minutes and with a reliability of 88.54% over the first year of operation.

Availability

Availability denotes the ability of a system to be kept in a functioning state. The availability of a system depends on the system's design reliability, its maintainability, and its maintenance support. Due to the nature of the ADD mission, HELIADES is required to provide perpetual availability to prevent threats from compromising the restricted area. The operational availability A_O is defined by Equation (13.2) [141].

$$A_O = \frac{MTBM}{MTBM + MDT} \tag{13.2}$$

Here, MTBM is the Mean Time Between Maintenance and MDT is the Maintenance Down Time, which includes reset time, active maintenance time, logistic delays, and administrative delays. The MDT accounts for considerations on minimizing repair time and costs to improve system availability, especially for elements that are known to wear out more quickly, such as bearings, engines, and batteries. Furthermore, the MDT is dependent on availability of spare parts and personnel, as having sufficient number of spare parts and an easily accessible system is essential for keeping the MDT low. It is assumed to to be 1 hour each day. These considerations will be further explained in Maintainability. An expected availability of **95.8%** was found with an MDT of 1 hour and an MTBM of 23 hours. It is expected though, that the actual MDT will be lower due to fewer engagements a day than simulated. Therefore, the actual availability will likely be higher.

Maintainability

The ease at which the product or system can be repaired is described as the maintainability of the HELIADES. Maintainability is governed by the accessibility, standardization, and modularization of the complete system.

Accessibility is crucial for performing efficient maintenance operations. By opening a hatch on the side/top of the fuselage, quick access to the internal components, including batteries, is possible, thus allowing for short reset times. For performing maintenance on the engines, the nacelles open like a hatch. This provides the engineers with full access to the gearbox and shaft of the engine. Finally, the removal system can be accessed through another hatch at the bottom of the fuselage. Through this opening, the ammunition can be resupplied and the actual gun be taken out for inspection and cleaning. All three access points lead to competitive reset times and efficient maintenance shifts.

By introducing standardization and modularity in the form of using off-the-shelf components and universal tooling, the replacement and repairs of HELIADES are drastically shortened. Furthermore, the training of ground personnel is significantly simplified. Due to HELIADES' modular design and the interchangeability of components, specifically the sensors, maintenance times are kept low and the implementation of system upgrades becomes more straightforward.

Furthermore, an outline of the maintenance activities is presented. In general, maintenance can be split into two categories: scheduled and nonscheduled. Scheduled maintenance involves taking preventive measures in order to ensure the drone remains operative. Nonscheduled maintenance takes place in emergency situations, where the drone is no longer able to fulfill its mission due to, for example, components failure or software bugs. For detailed maintenance procedures, the reader is referred to Section 12.4.

Safety

In order to prevent the system from causing harm to people, the environment, or any other assets during its life cycle, adequate safety during normal use and foreseeable misuse has to be provided. Safety is governed by the requirement stating that HELIADES shall not form a threat to manned aviation, and lifeforms on the ground and in the air. Therefore, critical safety points were identified besides discussing methods of use to prevent exacerbation of the aforementioned criticalities.

First, operating the drone in areas with increased temperatures should be avoided as this might cause material problems. PLA has a glass transition temperature at 60°, which has been taken into account with engine heat and ambient temperature, as described in Section 8.4 [105]. However, if the drone is to operate at higher temperatures in, for example, deserts, degradation issues might present themselves, potentially causing cracks and/or ultimately structural failure.

Secondly, the tilting function of the engines is essential to ensure proper operation of the drone. It is required to switch between helicopter and aircraft mode, thus allowing efficient forward flight as well as VTOL capabilities. The tilting concept has been proven to work, but it adds complexity and is therefore a critical point for safety. Therefore, special attention should be paid to the tilting mechanism during maintenance.

Thirdly, issues might present themselves with deflections of the rotor blades during operations. If these blades are not sufficiently stiff, deflection might become great enough for the blades to hit the wings. This should be prevented at all costs, as it would be detrimental to the aerodynamic performance, structural health, and the mission as a whole. Therefore, a separate structural analysis should be conducted on the rotor blades in the post-DSE phase to ensure they are designed such that these deflections can never pose a threat to the mission.

Furthermore, as described in Chapter 6, HELIADES has a slight longitudinal stability, indicating that the aircraft's response to a disturbance causes this disturbance to decrease slightly. During landing, such a disturbance could change the drone's attitude in such a way that safe touchdown can no longer be guaranteed. Therefore, a control algorithm should be developed such that a landing disturbance is compensated quickly with limited oscillations. To this end, a detailed stability & control analysis of the landing stage should be conducted in the post-DSE phase.

Another important point for safety is the removal of the target. What if the net or pellet fails to hit the target? What if the net's parachute fails to deploy or the target is flying too close to the ground to allow for parachute deployment? In principle, the net is safe to fire anytime due to the parachute ensuring a soft, slow landing. However, if this parachute fails to deploy or if the target flies too close to the ground, this could cause danger to lifeforms, buildings, and vehicles. Use of the removal system is therefore not recommended at lower altitudes in areas densely populated with the aforementioned stakeholders. The control algorithm should therefore be designed such that the customer can make the drone aware of this, leading to adjusted drone behavior. This can be done by, for example, importing a detailed map of the area in question with information on population density. Moreover, this algorithm should have a chase function that attempts to push the target drone to a greater altitude at which the parachute has sufficient time to deploy when a net is fired. Forcing the target to a greater altitude is also beneficial to structures and lifeforms on the ground, as the risk of the threat crashing into something or someone, or of it being in range to perform hostile activities is limited. Finally, special attention should be paid to the removal system and the associated ammunition during maintenance, so as to ensure proper functioning of it.

14. Final Design

Following the technical analyses a final design is presented. This chapter serves as a summary of the HELIADES final characteristics and components as well as providing the configuration and layout and budget breakdown for both the drone and the ground station.

14.1 Design Characteristics

Aerial Vehicle Characteristics and Layout

Most of the electronics can be placed close to each other in the nose of the aircraft. This is favorable as less cabling was needed and thus a lighter design was achieved. The components that are placed together in a casing are the BeagleBone Black embedded computer, the GPS module, and the pingRX. The IMU should be placed as close to the center of gravity as possible to get accurate data. Therefore, the IMU was placed in a different position than the embedded computer. An overview of all components and their respective positions in the fuselage can be found in Fig. 14.2 and Fig. 14.1.
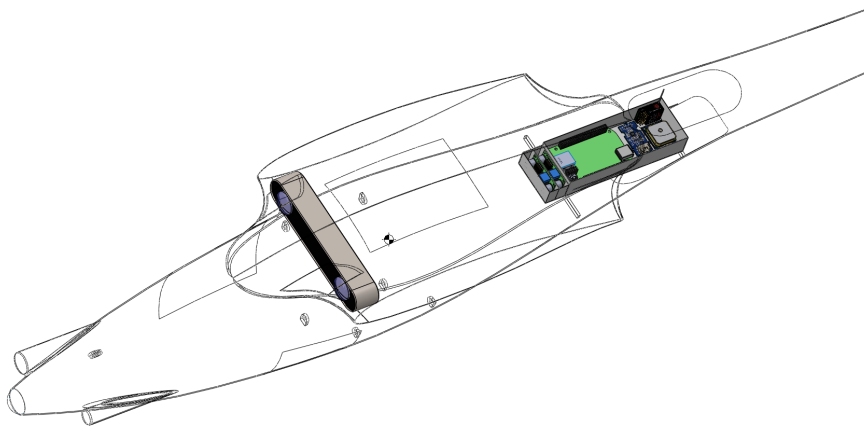

Figure 14.1: Layout of the aerial vehicle electronics.

The stereoscopic camera system is used for detection and tracking of targets. It should therefore be pointed in the direction of flight. Next to the stereoscopic camera system, a laser range finder is used to accurately determine the distance to the target. This laser range finder is therefore also placed in the front of the fuselage.

Not only is it important to be able to detect and track a target, it is also necessary to avoid collisions. To provide guidance during landing, an ultrasonic range finder is used at the bottom of the nose to measure the distance to the ground. Next to that, there are three IR sensors that are used for detection of obstacles in hovering flight. These are placed in the wings and the fuselage. They are pointed in such a way that they cover the blind spots of the camera system.

All these components are connected with the BeagleBone Black, that performs all the calculations and sends the control signals to control surface actuators and motors. Separate cables are required for power and control signals. In total 17 actuators are used and most of them are placed inside the wing. They are connected to the stiffening structure using bolts inside the wing. All the cabling runs from the fuselage through the wing towards the ailerons and nacelles. As the propellers use cyclic/collective pitch there need to be three actuators in the fuselage to provide both the pitching of the propellers as well as the tilting of the nacelles Fig. 14.3.

The antennas that are used for jamming the GPS and WiFi signals are high accuracy antennas, that need to be pointed in the direction of the target. It is therefore convenient to place the antennas pointing in the direction of the nose, such that during a chase the jammer can easily be aimed at the target.

The landing gear consists of struts that come out during the vertical landing. They are controlled using a linear actuator to extend both the struts. The struts are placed in front of the center of gravity and together with the tail it is made sure the aircraft does not tip over when standing on the ground.

The removal systems are placed in the front of the fuselage to be able to shoot down the target during a chase and by aiming using the camera system. The systems are controlled using two actuators that are connected to the Beaglebone Black. The exact workings of the removal system are described in Chapter 10.
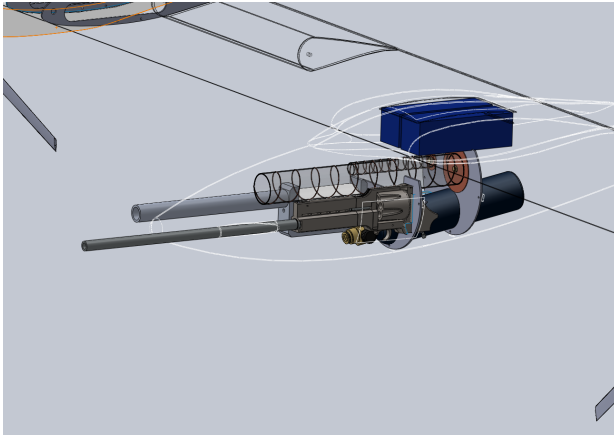
Figure 14.2: Layout of the fuselage.
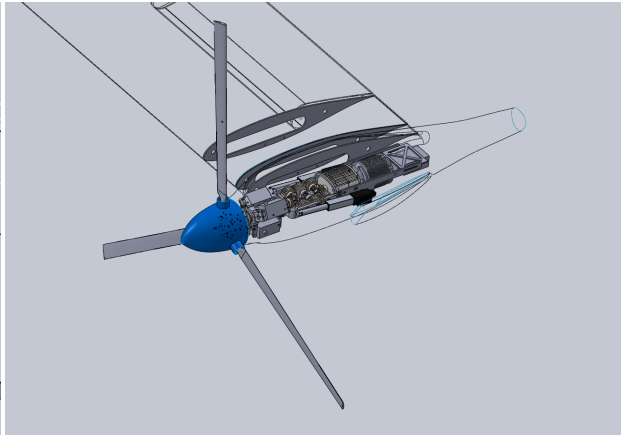
Figure 14.3: Layout of the nacelle.

Ground Station Characteristics and Layout

The ground station needs to be operational at all times in order to meet the detection requirements. Hence, the power is supplied off the local power grid, as opposed to the initially designed power supply through photovoltaic cells. The latter is still an option for remote operations, but is not the most convenient choice with readily-available power supply at most operating locations.

The ground system comprises of a radar system, and a suitcase including a control system/device capable of controlling the aerial system. The suitcase includes a fixed Dell Latitude 14 Rugged Extreme laptop [11] incorporated with a joystick to control the drone if necessary. The laptop is ruggedized to withstand extreme conditions, and the screen is readable in bright sunlight. Furthermore, components like the hard drive and battery are swappable in the field with a long battery life, thus being perfect for remote missions without power supply. An example of such a system, that is also used by Delft Dynamics, is shown in Fig. 14.4 [94].

Figure 14.4: Ground Station layout [94].

Figure 14.5: Ground Station laptop [11].

Furthermore, boxes are provided in order to transport the drone and the ground station components (except for the suitcase). These components include antennas and recharging pods. The wings of HELIADES had to be detached for it to fit in the box. Accompanying tools for the detachment are integrated in the box. A more elaborate description of the transportation of the system is provided in Section 12.2.

The antenna consists of the TUALLINK Ground Terminal which is compatible with the provided laptop [54]. It allows for communications with the drone at a range of 200km. Like the drone transceiver from the same company, it operates in the L and S bands. An example of a operational TUALLINK antenna is shown in Fig. 14.6.

Figure 14.6: TUALLINK ground terminal antenna [54].

By designing the battery as complete module, the ease of swapping is increased, thus reducing reset times. A rendering of the battery swap system is shown in Fig. 14.7 and Fig. 14.8. The top component in Fig. 14.7 is the actual battery module, while the bottom component represents the pod used for charging at the ground station as well as the battery connection in the drone. The battery swap system is accessible via a hatch that is hinged and locked using a spring loaded latch. The hatch can be opened using a simple screwdriver by turning the latch 90°. The system itself consists of the bay in which the battery is plugged in.
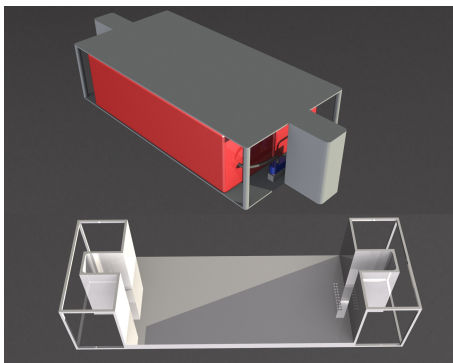
Figure 14.7: Battery swap system (top: battery module, bottom: connector frame) (top view).

Figure 14.8: Battery swap system (side view).

The radar detection system was not examined due to the level of complexity and lack of expertise on this subject. Several companies producing such systems have been approached for HELIADES' mission, but a final decision has to be made in the post DSE phase [139] [12]. Furthermore, if the location of system installation features a radar system, this system can be adjusted such that it fits HELIADES' purpose. An example would be the radar systems at airports, such as Schiphol.

14.2 Budget Breakdown

This chapter discusses the final mass and cost budget breakdown for HELIADES. This is an update of the budget breakdown from the mid-term report presented in Chapter 4. The major updates with respect to the budget breakdown of the mid-term are the disregarding of the radar subsystem of the ground station, addition of cost margin and production costs, higher propulsion power and consideration of spare batteries and ammo. The disregarding of the radar significantly lowers the potential system cost.

14.2.1 Mass

The mass of the ADD is set at a maximum of 10kg, following **REQ-BUDG-01**, while the maximum mass of the ground station is not set. See column 4 of Table 14.1 for an overview of the system components with their mass allocation. Column 5 shows the mass margin, this is the upper bound of the deviation from the target mass. A margin is given to components whose mass is not sufficiently detailed. third-party products bought from suppliers thus do not have a mass margin. Structural elements for instance can still increase in mass due to changes in design

of connection/detaching elements to provide modularity of the ADD.

The wing mass is 1.077kg, which is comprised of the wing structure, ailerons and nacelle shrouds. The mass of the fuselage is 0.524kg and pertains the hull, wing and tail fairings and maintenance hatches. Following the components of the CAD design in Section 10.2, the mass of the net gun is 1.928kg and the mass of the kinetic cannon is taken at 1.31kg. The motor assembly is the collection of all components inside both motor nacelles including the nacelles, rotor blades and spinners. Its mass is derived from the CAD drawings of the motor from Section 5.5.1. The computer of the GS is a Dell Latitude 14 Rugged with SSD hard drive for robustness.

Looking at the mass allocation of the aerial vehicle and comparing it to the mid-term allocation, the wing increased from 1kg to 1.077kg, actuator mass increased from 0.1kg to 0.868g, the removal system went from 1.5kg to 2.417kg, while the fuselage decreased from 2kg to 0.524kg and battery increased from 2.8kg to 2.82kg. All electronics are relatively light, adding a total of 0.76kg, excluding the battery.

Looking at the mass allocation of the GS and comparing it to the mid-term allocation, transportation cases are taken into consideration which add a mass of 50kg. Spare batteries and spare ammo are also considered, adding 7.57kg. The target ADD mass is within the mass requirement at 9.653kg, including upper margin the 10kg requirement is also satisfied at 9.84kg.

14.2.2 Cost

The cost margin per component is, analogous to the mass margin, existent only for components whose price is not stated in detail.

The structural components are cheap as they are made of PLA, which is $2 per kg [105]. 3D printing of PLA however costs around $0.4 per gram[147], amounting to the values depicted in Table 14.1. All electronic components are budgeted into detail as their price is clearly stated. Their cost margin is thus also not existent. The manufacturing costs margin is set to anticipate professional services. In principle, the prototype will be manufactured by students, resulting in free manufacturing costs. The cost of manufacturing of the GS is also comprised of only 3D-printing. The cost for software development is also set at 0 as students will be employed to code the software of the system.

The shipping costs are the total of shipping plus import taxes of all components, resulting in a upper boundary cost of €1,715. Import taxes are considered at 0.21% of product value of products whose value is above €150 [79]. Since shipping costs fluctuate, a margin of €200 is assigned. The largest contributor to the shipping cost is the transportation case of the ADD. Its shipping costs are €140, as this has a mass of 45kg excluding packaging and must be shipped from China [69].

The main differences of cost allocation with the mid-term are the lower production cost for the structural components, as 3D printed PLA is used. The cost for the kinetic cannon including spare ammo is reduced from €2,000 to €1,636. The cost for the motor assembly is reduced from €1,000 to €624 excluding manufacturing. Though the ESC's for the motors, which were not considered in the mid-term, add €1,069 to the total. The cost of the actuators were underestimated during the mid-term, they increased from €480 to €2,059. Furthermore, the cost of the communications antenna of the GS adds a significant cost amount of €8021 [54].

The cost of a fully functioning prototype including development and ground station shall be no more than €50,000, following **REQ-BUDG-02**. The total cost including margin of the ADD following Table 14.1 is €9106, of the ground station including the transportation case of the ADD is €11,241, shipping plus import duties of components is €1,715. This amounts to a total upper bound system break-even price of €22,415. This is taken at a Euro value of $1.10640 on 28-06-2016 [99].

14.2.3 Power

The power stated per component in Table 14.1 is the maximum stated power consumption. However, during operation it will not be likely that this power consumption is experienced as not all actuators will be in use at the same time. The motor assembly accounts for the largest ADD contribution because the motors are situated in this group. The ESC's use a significant portion assuming they have an operating efficiency of 0.99 [88] in providing the motors with 4.8 kW of power at peak thrust. The actuators also use a significant portion as each actuator uses 8 watts of power in operation [70]. The recharger is a 20A, 50.4V Li-Po battery charger, using 1200W[152].

Table 14.1: Budget breakdown of the ADD system

	Group	Component	Mass		Cost		Power [W]
			Target mass [kg]	Margin [kg]	Target cost [€]	Margin [€]	
Aerial vehicle	Structure	Wing	1.0770	0.05	398.9	18.5	-
		Fuselage	0.5243	0.025	194.2	9.3	-
		Landing Gear	0.0414	-	15.3	0	-
		Tail	0.1592	0.01	59.0	3.7	-
	Removal system	Net gun	0.9283	0.05	784	0	-
		ammo	0.0425	-	50	20	-
		Kinetic cannon	1.3103	0.05	463.4	0	-
		ammo	0.1360	-	8.0	0	-
	Propulsion	Motor assembly	0.9879	-	623.8	50	4752
	Electronics	Battery	2.82	-	374.3	0	-
		Cabling	0.05	0.0025	10.0	5	-
		ESC	0.256	-	1069.4	0	48
		CPU	0.04	-	55.0	0	1.7
		GPS receiver	0.01	-	44.6	0	0.135
		IMU	0.005	-	66.8	0	0.005
		Stereo camera	0.1	-	400.1	0	1.9
		Infrared sensors	0.0035	-	37.4	0	0.06
		Laser range finder	0.105	-	665.7	0	0.015
		Ultrasonic range finder	0.004	-	74.9	0	0.01
		Barometer	0.005	-	3.6	0	0.000025
		ADS-B transceiver	0.0015	-	156.0	0	0.15
		Telemetry transceiver 5.8Ghz	0.02	-	26.7	0	0.6
		Comms transceiver 2.4Ghz	0.01	-	62.4	0	0.4
		VCO	0.0018	-	65.1	0	0.4
		Pitot tube	0.01	-	62.4	0	0.015
		Jammer + amplifier	0.1363	-	106.9	0	5.88
	Actuators	Collective/cyclic control	0.321	-	802.1	0	48
		Nacelle	0.2411	-	525.8	0	16
		Removal	0.0637	-	133.7	0	8
		Ailerons	0.107	-	267.4	0	16
		Tail	0.107	-	267.4	0	16
		Landing Gear	0.028	-	62.4	0	8
	Manufacturing		-	-	0	1000	-
	ADD total		**9.653**	**0.188**	**7936.8**	**1106.5**	**4923.3**
Ground station		Transp'n case ADD	45	-	150	50	-
		Transp'n case laptop	5	-	13.4	0	-
		Transp'n case components	10	-	26.7	0	-
		Dell Latitude 14 Rugged	2.95	-	1425.9	0	36.8
		GPS receiver	0.01	-	60	0	0.135
		Telemetry transceiver 5.8Ghz	0.02	-	26.7	0	0.6
		Comms transceiver 2.4Ghz	0.01	-	62.4	0	0.4
		Housing	0.5	0.1	0.18	0	-
		TUALLINK Ground Terminal	11	-	8020.7	-	N/A
		Recharger	5	-	240.6	0	1200
		Spare battery x2	6	-	873.4	0	-
		Spare net gun ammo x5	0.213	0.5	250	100	-
		Spare kinetic cannon ammo	1.360	-	80.2	0	-
		Manuals	0.5	0.5	10	5	-
	Manufacturing		-	-	0	200	-
	GS total		**87.203**	**1.100**	**11115.3**	**355.0**	**1237.9**
Shipping + import duties			-	-	1515	200	-
System total			**96.856**	**1.288**	**20541**	**1661**	**6161.2**

15. Compliance Matrix & Feasibility Analysis

The purpose of this chapter is to check whether the design meets each requirement and elaborates on the requirements that have not been met by the anti-drone system. This chapter starts off with an updated list of the requirements set in the midterm report ([67]) in Section 15.1. Section 15.2 displays the compliance matrix, a large table which shows the compliance of both the initial and the final design with the imposed requirements. In Section 15.3, a feasibility analysis is conducted which rationalizes the unmet requirements.

15.1 Updated Requirement

During the detailed design, some requirements were added and some were altered. These additions and alterations are discussed here.

- **REQ-PERF-17**: The operational ceiling was lowered from 7km to 4km due to the very low probability that non-military drones fly at altitudes above 4km.
- **REQ-PERF-22**: A maximum structural load factor of 20 was imposed based the fact that the aircraft is unmanned and therefore in theory not limited to a certain maximum load factor. A load factor of 20 is a typical value for an Unmanned Combat Aerial Vehicle (UCAV) [101].
- **REQ-PERF-23**: A temperature range ranging from -10°C to 50°C for operation is added. This range is based on the glass transition temperature of 60°C of PLA [105], the degradation of battery performance with temperature [162] and the maximum temperature of the engines (based on the efficiency [114]).
- **REQ-PERF-24**: A pitch rate of 60°/s is imposed based on the following: assume that the target drone is at 5m distance from the anti-drone drone, and that it suddenly increases altitude at a vertical climb rate of 10m/s (which is higher than for most commercial as well as professional drones [97, 127]). In order to keep up with the target, the pitch rate should be at least equal to the specified number.
- **REQ-PERF-25**: A roll rate of 150°/s is required based on the roll performance of fighter aircraft in air-to-air combat phases [159].
- **REQ-PERF-26**: Gust velocities up to 15 m/s shall not destabilize HELIADES in helicopter mode [140], in airplane mode HELIADES is assumed to float with the wind.
- **REQ-PERF-27**: The pneumatic guns recoil shall not destabilize HELIADES, neither in helicopter nor airplane mode.
- **REQ-PERF-28**: HELIADES shall be stable in Dutch roll.
- **REQ-PERF-29**: HELIADES shall be stable in spiral.
- **REQ-SAFR-04**: For the one engine inoperative case, a maximum angle of sideslip of 5° is imposed [24].
- **REQ-SAFR-05**: This requirement was mainly imposed based on the sensitivity of the airfoil to dirt [125]. Since operations could take place in for example sandy environments, the performance of the anti-drone drone should not be decreased greatly by dirt or other contaminations.
- **REQ-SAFR-06**: Based on regulations imposed by the Civil Aviation Authority (CAA, United Kingdom) a flight termination system has to be present aboard civil UAVs [104].
- **REQ-SUST-06**: A maximum day-night average sound level of 65 dBA is imposed based on [30], which states that the average noise level of aircraft around airports is equal to this value. Therefore, as long as the anti-drone drone produces less noise, it will not be a nuisance to nearby residents.

15.2 Compliance Matrix

The compliance matrix displaying the met and unmet requirements for both the initial and final design is displayed in Table 15.1.

Table 15.1: Requirement Compliance Matrix of the initial and final design

		Compliance	
Identifier	Requirement	Initial Design	Final Design
Performance			

REQ-PERF-01	Prevent any fixed wing and rotary wing drones whose mass is less than 2.5kg and velocity less than 35m/s from entering a restricted area with a diameter of 1km.	✓	✓
REQ-PERF-02	The anti-drone drone shall have a horizontal velocity of at least 50m/s.	✓	✓
REQ-PERF-03	The anti-drone drone shall have a climb rate of at least 8m/s.	✓	✓
REQ-PERF-04	The anti-drone drone shall have a rate of turn of at least 0.29rad/s.	✓	✓
REQ-PERF-05	The reset time after end of engagement shall be less than 5 minutes.	✓	✓
REQ-PERF-06	The anti-drone drone shall be able to perform its mission autonomously when airborne.	-	✓
REQ-PERF-07	The anti-drone drone shall be able to hit a circular target with a diameter of 0.35m at a distance of 13m.	✓	✓
REQ-PERF-08	The anti-drone system shall detect intruding aerial vehicles at a distance of 2250m from the center of the restricted area.	✓	✓*
REQ-PERF-09	The anti-drone drone shall intercept the intruding aerial vehicles at a distance of 2250m from the center of the restricted area.	✓	✓
REQ-PERF-10	The anti-drone drone shall be able to accelerate horizontally with at least 8m/s^2 during normal weather conditions.	✓	✓
REQ-PERF-11	The anti-drone drone shall be able to accelerate vertically with at least 2.8m/s^2 during normal weather conditions.	✓	✓
REQ-PERF-12	The anti-drone system shall be operational at night.	-	✓
REQ-PERF-13	The anti-drone system shall be able to track the target UAV.	-	✓
REQ-PERF-14	The anti-drone drone shall be able to remove the target UAV.	✓	✓
REQ-PERF-15	The anti-drone drone shall be able to communicate with the ground station.	✓	✓
REQ-PERF-16	The anti-drone drone shall be able to avoid collisions with anything other than the target.	-	✓
REQ-PERF-17	The anti-drone drone shall have an operational height of at least 4km.	✓	✓
REQ-PERF-18	The rate of successful removal shall be at least 99%.	-	✗, 89%
REQ-PERF-19	The deployment time shall be less than that of current ground-based solutions.	-	✓
REQ-PERF-20	The anti-drone system shall be operational in the presence of wind gusts of at least 15m/s.	✓	✓
REQ-PERF-21	The anti-drone drone shall have an endurance of 10 minutes in nominal operation.	✓	✓
REQ-PERF-22	The structure of the anti-drone drone shall be able to sustain a load factor of at least 20.	✗	✓
REQ-PERF-23	The anti-drone system shall be operable in outside air temperatures ranging from -10°C to 50°C.	-	✓
REQ-PERF-24	The anti-drone drone shall be capable of a minimum pitch rate of 60°/s.	-	✓
REQ-PERF-25	The anti-drone drone shall be capable of a minimum roll rate of 150°/s.	-	✓

REQ-PERF-26	Gust velocities up to 15 m/s shall not destabilize HELI-ADES in helicopter mode.	-	✓
REQ-PERF-27	The pneumatic guns recoil shall not destabilize HELI-ADES, neither in helicopter nor airplane mode.	-	✓
REQ-PERF-28	HELIADES shall be stable in Dutch roll.	-	✓
REQ-PERF-29	HELIADES shall be stable in spiral.	-	✓
Safety and Reliability			
REQ-SAFR-01	The anti-drone system shall not form a threat to manned aviation.	✓	✓
REQ-SAFR-02	The anti-drone system shall not form a threat to life forms.	-	✓
REQ-SAFR-03	The anti-drone system shall require maintenance after no less than 50 engagements.	-	✗, 4
REQ-SAFR-04	The anti-drone drone shall be capable of maintaining altitude with a maximum sideslip angle of 5° with one engine inoperative.	-	✓
REQ-SAFR-05	The anti-drone drone shall be capable of nominal operation in dirty environments.	-	✓
REQ-SAFR-06	The anti-drone system shall include a Flight Termination System.	-	✓
Sustainability			
REQ-SUST-01	The anti-drone system shall have an end-of-life solution.	✓	✓
REQ-SUST-02	The anti-drone drone shall have a carbon emission rate of no more than that of currently available anti-drone technologies.	✓	✓
REQ-SUST-03	The operational power requirements of the anti-drone system shall be met with sustainable energy sources.	✓	✗
REQ-SUST-04	The waste during the entire design and production process shall be minimized.	-	TBD
REQ-SUST-05	The operational costs of the anti-drone system shall be minimal [TBD].	-	TBD
REQ-SUST-06	The anti-drone system shall produce a day-night average sound level of at most 65 dBA.	-	✓
Budgets			
REQ-BUDG-01	The anti-drone drone shall have a mass of less than 10 kg.	✓	✓
REQ-BUDG-02	The anti-drone system shall have a fully functional prototype cost of no more than €50,000.	✓	✓*
Legislation			
REQ-LEGN-01	The anti-drone system shall comply with U.S. and Asian regulations.	-	✓**
Other			
REQ-OTHR-01	The anti-drone drone shall stay outside of the restricted area at all times.	✓	✓
REQ-OTHR-02	All aspects of the design shall be combined using design integration and systems engineering tools.	✓	✓
REQ-OTHR-03	The design shall be finished within 10 weeks.	-	✓
REQ-OTHR-04	The design process shall be performed by a group of ten prospective aerospace engineers.	✓	✓

From Table 15.1 it can be concluded that the final design meets most of the requirements and shows significant improvement over the initial design.

15.3 Feasibility Analysis

This feasibility analysis serves to elaborate on the requirements that the anti-drone system was not able to meet, see Table 15.1. The requirements marked with an * or ** are conditional, since they depend on the availability of a radar and the current indefinite legislation, respectively.

REQ-PERF-08 and **REQ-BUDG-02**
If a radar is included at the anti-drone system, it would not fulfill REQ-BUDG-02. However, it would be able to detect the target and thus comply with REQ-PERF-08. If the anti-drone system does not include a radar, REQ-BUDG-02 can be met, but system could not detect the target and thus violate REQ-PERF-08. As has been stated in Section 14.1, it has been assumed that a radar system designed by other companies will be used. This radar can then be integrated with the anti-drone system. Tracking of the enemy drone is independent from the radar, given that HELIADES is within 14m of the target.

REQ-LEGN-01
As explained in Section 10.1, the kinetic cannon does meet the regulations set by the American government, although at the time of writing, no regulations have been imposed on autonomous UAVs in the USA. Depending on future changes in legislation, a restriction might be imposed and negatively affect the operation of the anti-drone system. Additionally, no information were found on the Asian drone regulations.

REQ-PERF-18
The probability of removal failure is stated in the RAMS section in Chapter 13. In this analysis, it has been stated that the probability of succesful removal is 89 %, ten % below the required 99 %.

REQ-SAFR-03
In Fig. 7.5 it has been visualized that the anti-drone system is capable of a maximum of four engagements per day, considering the worst case scenario. To comply with this requirement, this implies maintenance approximately once a fortnight. In Section 12.4 is determined a maintenance of 30 minutes every 24 hours, this requirement could not be met.

REQ-SUST-03
The ground station explained in Chapter 14 does not make use of solar panels. Therefore, the power to recharge the batteries must be delivered by the power supply of the customer. In the USA, only 13% of the electricity is generated by renewable methods [156]. Therefore, the anti-drone system is not able to comply with requirement REQ-SUST-03. One option to improve the sustainability is to provide the customer with a portable solar array pack. This way the battery energy can be provided in a renewable way, provided there is enough time and space to set up the solar panels.

REQ-SUST-04 and **REQ-SUST-05**
For these requirements, no standards has been determined. The maximum acceptable waste as well as the maximum operational costs will be determined in the post-DSE stage of the prototype design.

HELIADES is entirely manufactured by bio-degradable PLA plastic, which minimizes the environmental impact and waste during the production process.

As for the mission, although the net launcher described in Section 10.2 uses a standard fishing net, which is neither bio-degradable or eco-friendly, the nets can be recovered and recycled and are thus not classified as waste.

The shell of the net gun, although not recoverable, is made of bio-degradable PLA plastic as well, so that it does not harm the environment. The ammunition used by the kinetic cannon (see Section 10.1) is made of ceramics. This has a minimal impact on the environment, when compared to traditional bullets from lead or steel.

As explained for REQ-SUST-03, most of the energy required for the mission is generated from nonrenewable energy sources. To minimize the environmental impact of the battery charging, a portable solar array system can be provided to the customer if desired.

The autonomy of HELIADES also reduced the operating costs compared to a pilot-controlled UAV. As of now, no estimate on operating costs are made.

16. Post-DSE Planning

In this chapter, activities for the post-DSE phase are investigated. First, a project design and development flow chart is presented. Then, the identified activities are shown in a preliminary Gantt chart. Hereafter, the cost breakdown structure for these activities is shown. Lastly, verification & validation procedures are elaborated on.

16.1 Project Design and Development

In Fig. 16.1, the activities are shown that are to be performed after the end of the DSE. Most activities are self-explanatory or have been elaborated on earlier. For example, creep and SMART structures were discussed in Chapter 8.

It is worth mentioning that a significant amount of time has to be spent on further testing and analysis, as seen from the size of the block in Fig. 16.1. These are required mainly for validation and detailed design, so as to ensure a reliable product that performs its functions accordingly. Some examples of tests include a spin recovery test and a deep stall test for stability & control of HELIADES. Deep stall will likely not be an issue as an inverted V-tail is used, causing the tail to be out of the wake of the main wing in most cases. Regarding the structural tests; bending, fatigue, and impact tests should be performed to ensure the design remains intact under operational conditions. For performance, specifications should be validated by experimental measurements. For example, climb rate and maximum velocity should be measured to validate the used models.

The activities flow down to the actual sale of the product. However, there are still activities left to be performed after this point, such as maintenance and customer support. These could lead to possible additions to the product, which should be investigated. Therefore, these activities are iterative.
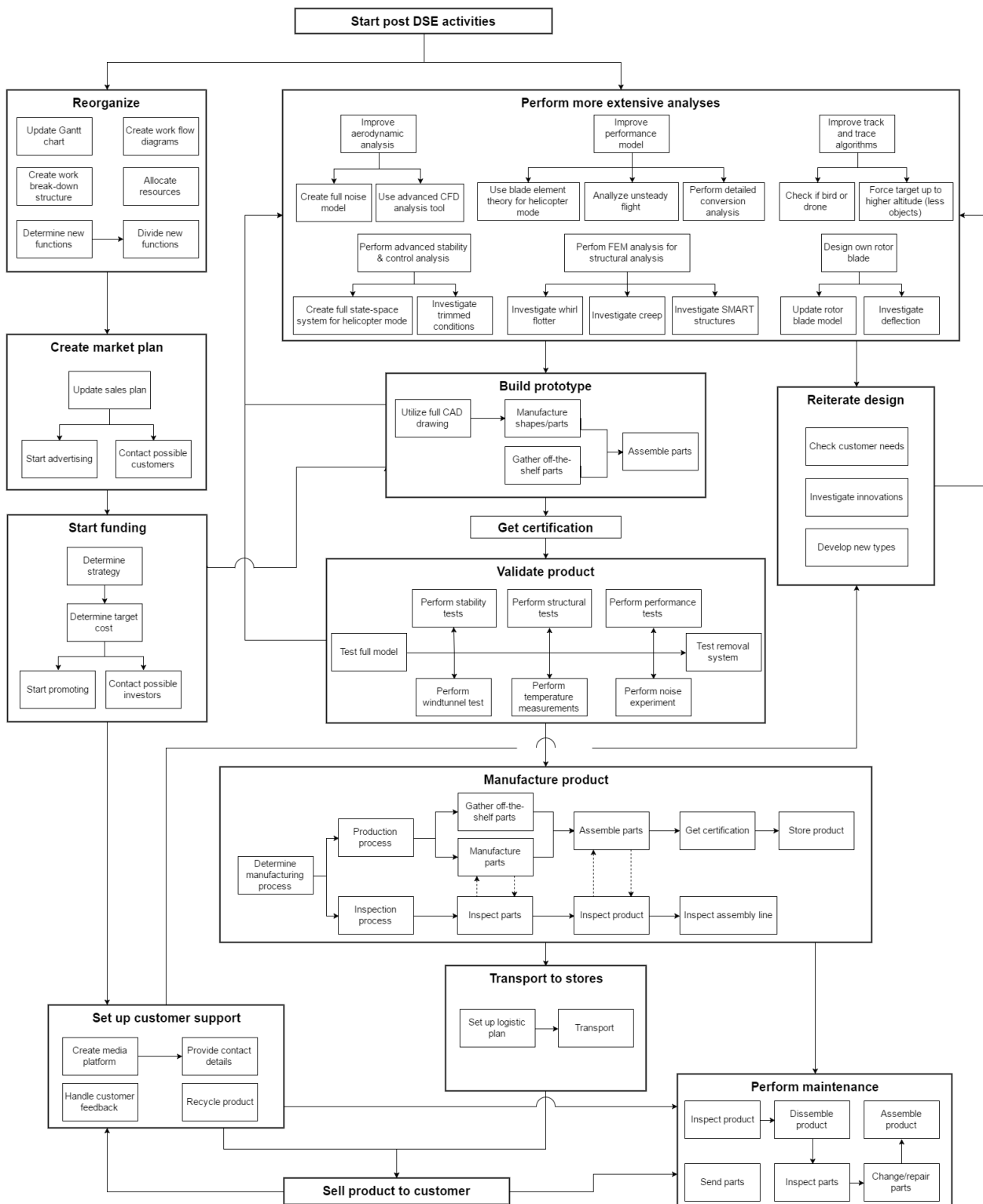
Figure 16.1: Post DSE activities.

16.2 Gantt Chart

The activities from Fig. 16.1 were scheduled in a preliminary Gantt-chart, as can be seen in Fig. 16.2. This serves as an initial schedule for post DSE activities. The duration of most activities was based on Gantt-charts from the Project Plan and Mid-term Report as well as on experience gained during the DSE [67, 68]. Others were estimated after deliberation with the group. Concurrent engineering should be performed whenever possible. Nonetheless, the certification process is likely to consume a significant amount of time, thus hindering the progress. As HELI-ADES can be 3D printed, manufacturing time is relatively low [29].

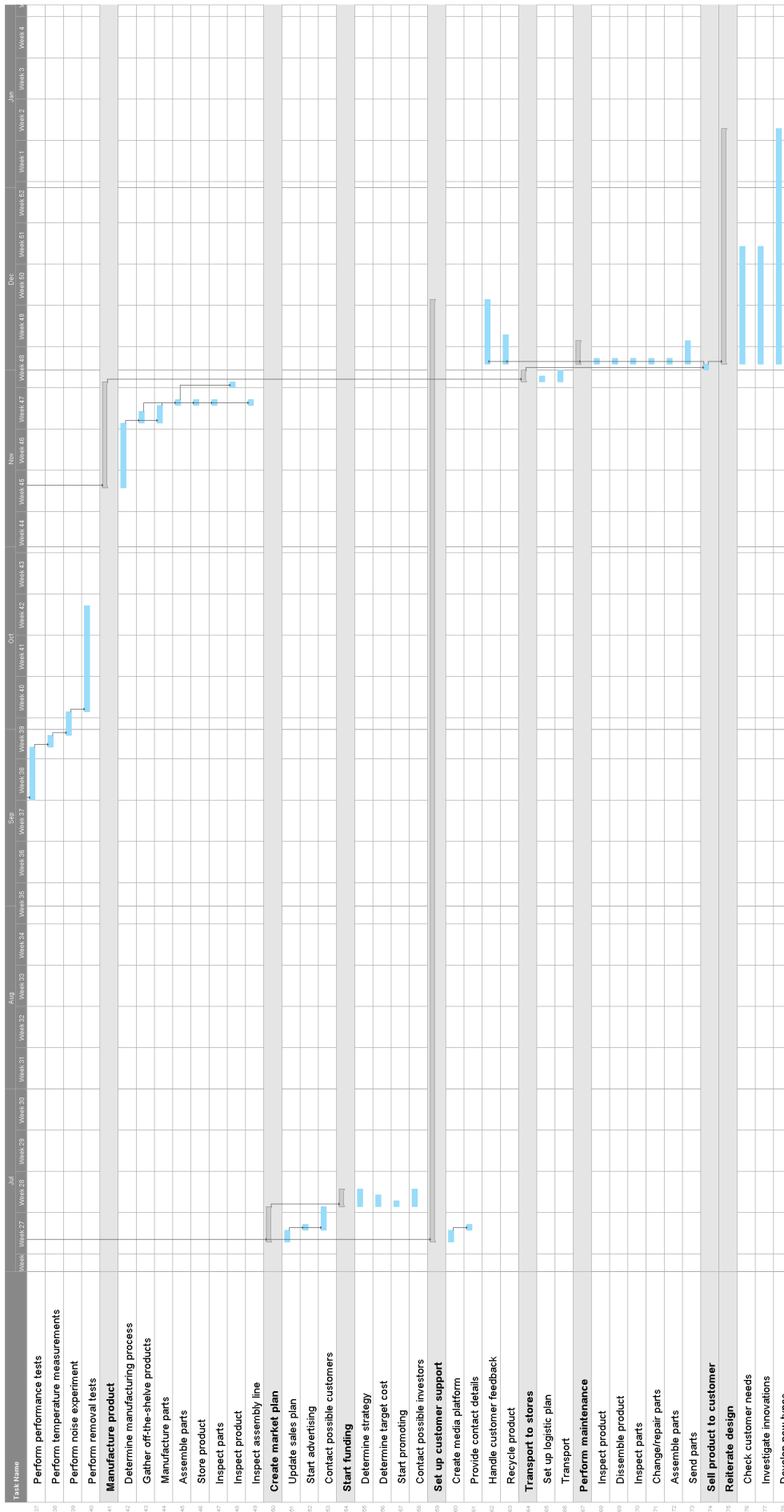|	Task Name
1	**Reorganize**
2	Update Gantt chart
3	Create work flow diagrams
4	Create work break-down structure
5	Allocate resources
6	Determine new functions
7	Divide new functions
8	**Perform more extensive analysis**
9	Use advanced CFD analysis tool
10	Develop advanced noise model
11	Use blade element theory for helicopter mode
12	Use differential equations instead of simplifications
13	Perform detailed transition phase analysis
14	Develop detailed track and trace algorithm
15	Investigate radar design
16	Develop drone/bird distinction algorithm
17	Force target up to high altitude (less objects)
18	Perform advanced stability & control analysis
19	Create full state-space system for helicopter
20	Investigate trimmed conditions
21	Perform FEM analysis for structural analysis
22	Investigate whirl flutter
23	Investigate creep
24	Investigate use SMART structures
25	Update rotor blade model
26	Investigate deflection
27	**Build prototype**
28	Check full CAD drawing
29	Manufacture shapes/parts
30	Gather off-the-shelve products
31	Assemble parts
32	**Get Certification**
33	**Perform tests and experiments**
34	Perform windtunnel tests
35	Perform stability tests
36	Perform structural tests
37	Perform performance tests
38	Perform temperature measurements
39	Perform noise experiment
40	Perform removal tests

Figure 16.2: Post DSE Gantt chart.

16.3 Cost Breakdown

A preliminary cost breakdown structure can be seen in Fig. 16.3. The cost breakdown structure is an AND tree consisting of cost elements for the post DSE phase. As of now, the process is subject to quite some uncertainty, thus making it difficult to predict exact costs. It is however, possible to determine cost elements. These are split up into overhead costs and development costs.

Overhead costs are split up in facilities, marketing, and customer support. The former relates to, amongst others, the cost of project rooms, storage space, and company taxes. Marketing is required to bring the product to the attention of potential customers. Examples include promotion team costs and the cost for the development of a media platform. Finally, customer support has to be guaranteed. Once a prototype has been developed and full scale production has initiated, this kind of service is important for maintenance, transport, and recycling. The former is especially important, as maintenance has to be organized at regular intervals to ensure the customer's product preserves its functionality. Moreover, professionals have to be hired to perform maintenance activities. Maintenance will likely be one of the larger contributions to cost. Recycling should also be taken into account, as special machines might be required to facilitate this process. Finally, if the product is repurposed, additional costs have to be taken into account for, amongst others, the purchase of new components and refurbishing of old components.

Development costs are split up in design, manufacturing, and testing costs. The former is mainly computer based and is thus determined by software development and the purchase of existing software. Furthermore, resources to facilitate the design process are required, such as post-its, white boards, and markers. Manufacturing is also a large contributor to cost. It is not only used for prototyping and production; it is also important for maintenance, as spare parts have to be manufactured. Moreover, professionals have to be hired to handle the equipment. Finally, testing will take up a significant amount of time. Besides, facilities such as wind tunnels and heat testing areas are costly to hire. It should also be noted that certification can significantly push the cost of development due to the time, documentation, and testing required.
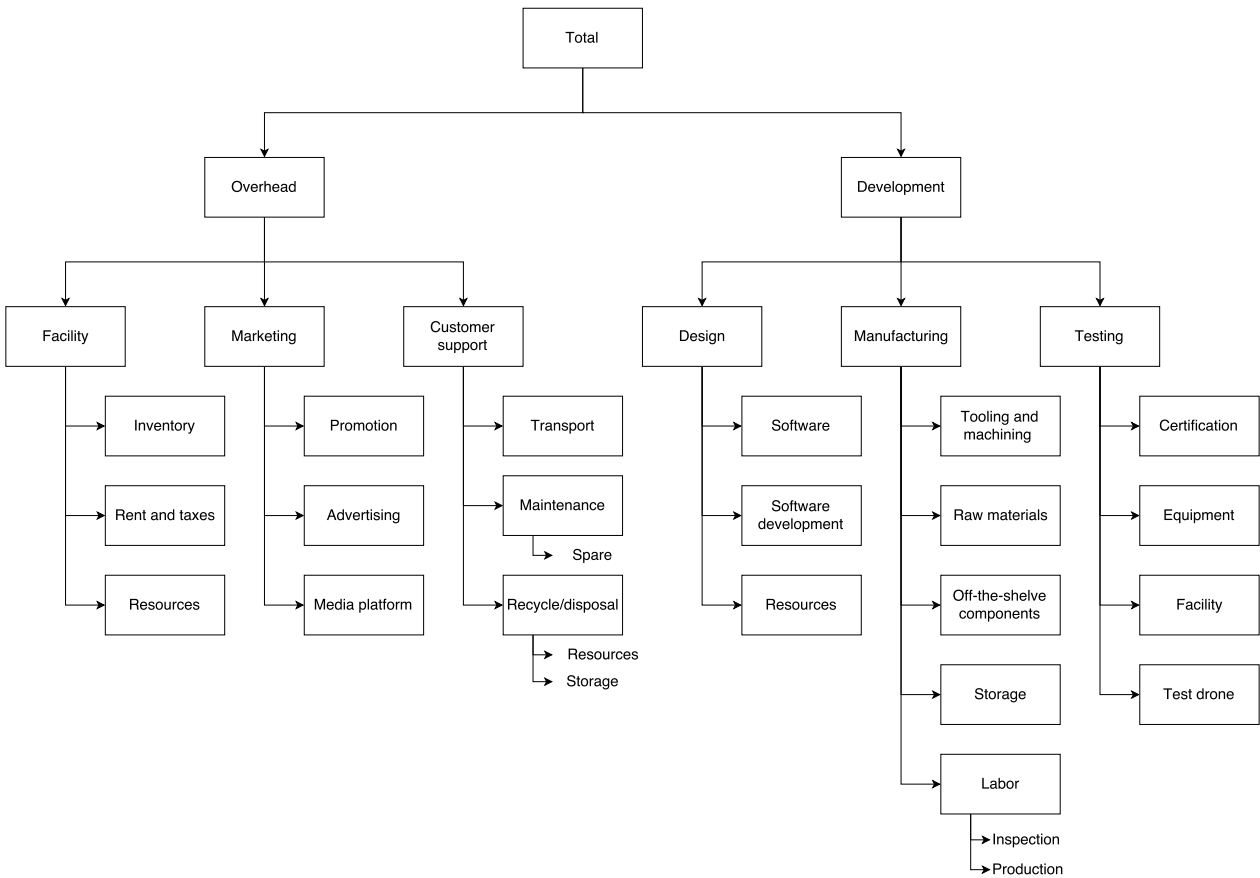

Figure 16.3: Preliminary cost break-down structure of post DSE activities.

16.4 Verification & Validation Procedures

This section describes the verification and validation procedures that are to be used to obtain proof that the system meets the requirements and performs the mission successfully. These parts are an important aspect of any design process, as it proves to the stakeholders that the product satisfies their needs. Note that this differs from the compliance matrix in the sense that it is performed once a detailed design has been obtained. All methods discussed are in accordance with the Systems Engineering approach described in [103].

Verification Procedures

Verification of the design establishes whether or not the defined requirements imposed on the system have been met. There are four possible ways to accomplish this, as described below.

- **Inspection -** This comprises of inspection of the system or the documentation. For example, the total mass could be inspected to ensure it complies with set requirements.
- **Analysis -** This entails performing a mathematical or computational analysis. For instance, this can be used to look into fatigue to verify whether operational lifetime requirements are met.
- **Demonstration -** The system, or part of it, is used in a demonstration to show that it meets the requirements. This method could be used to verify the reset time requirement, for instance.
- **Test -** This method encompasses performing a test under specific design conditions with a representative system model. This would, for example, be used to verify whether the system can operate in the defined temperature range.

Validation Procedures

Validation determines whether the product fulfills its purpose in practice, so as to comply with stakeholder needs. Procedures available are listed below.

- **End-to-End Information System Testing -** This method is used to check whether all information systems are compatible. Once a prototype has been developed, it can be validated whether radar data, GPS data, and control commands are correctly exchanged between subsystems.
- **Mission Scenario Testing -** This demonstrates that the hardware and software can execute the mission under realistic flight circumstances for each phase without a real timeline. This means testing take-off, intercept, removal, and landing phases separately to ensure hardware and software components are correctly functioning over the duration of all of them.
- **Operations Readiness Testing -** This method demonstrates that the ground segment is able to accomplish the mission using a real timeline. For HELIADES, this means demonstrating maintenance, reset, radar detection, and net retrieval, amongst others.
- **Stress-Testing and Simulation -** This is done to assess the sensitivity to variations in performance and fault conditions. This is conducted through, for example, fatigue testing or by exposing the system to elevated temperatures for extended periods of time.

Planning

Adequate planning of the aforementioned activities is important to achieve the desired outcome. The following approach is to be used: 1) The verification or validation objective is defined. 2) One of the aforementioned methods is chosen to achieve the defined objective. 3) Control variables, constants, and desired outputs of the activity are determined. 4) Facilities, resources, and personnel required are determined. 5) The plan is documented and discussed with the stakeholders. 6) The activity is set up. 7) Verification or Validation is executed. 8) The result is documented and the process iterated if necessary.

17. Conclusion

This report discussed the preliminary design phase of HELIADES, a drone capable of preventing other drones from entering a specified area. It was previously selected from a group of six concepts, due to its maneuverability, versatility, and efficiency.

It was found from the market analysis that there are ample opportunities for anti-drone systems. This is evidenced by an expected market growth rate of 23.89% between 2017 and 2022. As HELIADES operates autonomously and has a significantly greater detection range than existing solutions (5km), it is expected to be favored over other products. Moreover, its development cost of €50,000 is negligible compared to the millions of euros customers such as airports could otherwise lose due to drone incidents. Therefore, a final system cost of €200,000 is set, as this way a break even margin is included besides also ensuring remunerative sales.

Furthermore, an elaborate technical analysis was performed to ensure the system met the requirements imposed on it. Attention was paid to maneuverability to ensure intruding drones could be intercepted, to control to ensure complete autonomy in flight, and to structural design to ensure all loads could be sustained. Regarding the former; HELIADES uses tiltrotors to switch between helicopter and aircraft mode, thus allowing for efficient flight whilst omitting the need for a runway. Moreover, autonomy is ensured through the use of a combination of mostly existing software programs for obstacle avoidance, trajectory planning, and target tracking. The latter is done by using a stereoscopic camera that keeps the target in sight and determines when it is close enough to attempt removal. For the latter, a jammer, a net gun, and a kinetic cannon are used, thus providing the system with multiple options to take out the target. This makes it effective against the majority of hobby drones available. Furthermore, HELIADES is built using mainly Polylactic Acid (PLA), a biodegradable plastic produced from renewable resources such as corn starch. This allows for the structure to be 3D printed, resulting in a total aerial system weight of 9.7kg.

Following the technical analysis, the detailed design took place. In this phase, operational aspects and risks were assessed. It was ensured that the system broadcasts a distress message in case of emergency, so as to ensure safety in the vicinity of the drone. Moreover, the design is such that the wings and fuselage can be detached to allow for convenient transport. Note that only one operator is required to keep the system operational. This does not have to be a professional as the operator's tasks are relatively straightforward. They include maintaining stores and switching batteries, besides performing inspections one hour a day. The reliability of the system was also analyzed, yielding a probability of successful removal of 89% during the first year of operations.

Finally, a preliminary planning for future phases was set up. This identified activities, cost elements, and verification and validation procedures. The main focus will be on more extensive analysis and testing, so as to obtain a more detailed design that has been reliably validated. Recommendations for this phase are included in the next chapter.

Summarizing, HELIADES is revolutionary in the sense that it is capable of autonomously performing its mission. Moreover, it outperforms existing solutions in terms of maneuverability and cost. Besides, its sustainability is unmatched, as carbon emissions are limited during manufacturing and operations. It is also easily recycled due to its biodegradable structure. In conclusion, the group is confident that HELIADES will experience a successful market introduction due to the design's potential as well as the team's drive to deliver a sound product. This report marks another milestone in the path leading up to this introduction, but certainly not the last one.

18. Recommendations

During the preliminary design process, not all design aspects could be investigated due to them being too complex or detailed to be thoroughly analyzed in the time available to the group. These should however, be addressed in future design phases as elaborated on in Chapter 16. This chapter serves as a summary of recommendations that are to be taken into account for further development of HELIADES.

Firstly, a detailed analysis of the transition from helicopter to aircraft mode and vice versa should be conducted. A preliminary analysis has been performed, showing that the transition can be performed safely. Nonetheless, this phase can cause difficulties for stability and control due to the disparity between operation modes. Therefore, a state space model should be set up that accurately models this transition phase and the resultant change in attitude. To this end, validation tests should also be performed to ensure the transition can be safely performed in reality.

Secondly, the removal system should be tested extensively to ensure it functions correctly and provides the desired reliability. Components have been selected or designed, but should be validated both on the ground as well as in the air. The former allows for general checking of whether the individual components work, whereas the latter allows for checking of the functioning of the combination of jammer, net gun, and kinetic cannon when used on an aerial vehicle.

Thirdly, radar system options should be looked into. The preliminary design mainly focused on the aerial system, and used the assumption of a functioning radar detection system. The Faculty of Electrical Engineering, Mathematics, and Computer Science at Delft University of Technology was approached to set up an experiment to test the effectiveness of existing radar systems for drone detection. Due to legislation issues however, drone flight exemptions had to be arranged and therefore these experiments could not be performed in time. It should be performed at a later point in time though, after which either an existing system should be selected or a customized system should be designed.

Moreover, validation tests should be performed for the used computational models in the preliminary design. Most of the validation procedures in this design phase were conducted using data that was not specific for HELIADES. Although these do allow for an initial verdict on the validity of aforementioned models, they are not as reliable as data obtained from concept specific tests. Examples of the latter include wing bending tests, stall tests, and flight tests. Note that more advanced computational methods, such a Computational Fluid Dynamics (CFD) and Finite Element Analysis (FEA), should be used for detailed analysis. These should also be validated using aforementioned tests.

Furthermore, the developed system remains in a gray area when it comes to legality. This is due its use of firing mechanisms and jammers, that are usually not allowed for commercial use. As of now, some legislative requirements have been taken into account, but a detailed legislative analysis should be performed to ensure the drone is allowed to operate as intended in every aspect.

Finally, a marketing strategy should be defined for both sales as well as development funding. As a phase is entered in which profuse tests will be performed, investors have to be found and convinced of the potential of HELIADES to ensure sufficient resources are available for further development.

Websites

[1] Adherent Technologies, Inc. Recycling Technologies, 2016. URL http://www.adherent-tech.com/recycling_technologies. Cited on 27-05-2016.

[2] airfoiltools. airfoiltools.com, N/A. URL http://airfoiltools.com/search/index. cited on 25-05-2016.

[3] Allen Gears. Efficiency of Epicyclic versus Parallel Shaft Gearboxes, N/A. URL http://www.allengears.com/pdf/epicyclic-revenue-advantage.pdf. Cited on 19-06-16.

[4] Alliant Powder. Reloaders guide 2014, N/A. URL http://alliantpowder.com/resources/catalog/alliantpowder-reloadersguide/2014_Alliant_Powder_Catalog.pdf. cited on 20-06-16.

[5] Bahrami, M. Forced convection heat transfer, N/A. URL http://www.sfu.ca/~mbahrami/ENSC%20388/Notes/Forced%20Convection.pdf. Cited on 18-06-16.

[6] Blighter Surveillance System Ltd. Blighter AUDS Anti-UAV Defence System, 2016. URL http://www.blighter.com/products/blighter-auds-anti-uav-defence-system.html.

[7] Bosch. BMP180 Digital Pressure Sensor, 2015. URL http://cdn.sparkfun.com/datasheets/Sensors/Pressure/BMP180.pdf. Cited on 02-06-2016.

[8] C.W. Acree, R. P., Jr. and Johnson, W. Improving tiltrotor whirl-mode stability with rotor design variations. NASA Ames Research Center, N/A. URL http://ntrs.nasa.gov/archive/nasa/casi.ntrs.nasa.gov/20000114842.pdf.

[9] De Staatssecretaris van Infrastructuur en Milieu. Regeling op afstand bestuurde luchtvaartuigen, 2015. URL http://wetten.overheid.nl/BWBR0036568/2015-11-07. Cited on 02-06-2016.

[10] Delft Dynamics. DroneCatcher continues, 2015. URL http://www.delftdynamics.nl/index.php/en/news-en. Cited on 02-06-2016.

[11] Dell. Dell Latitude Rugged, 2016. URL http://www.dell.com/en-us/work/learn/rugged#Overview. cited on 27-06-16.

[12] DeTect Inc. Drone surveillance & interdiction systems, N/A. URL http://www.detect-inc.com/drone.html. Cited on 19-06-16.

[13] Detective Halstead, Sacramento Police Department. Circuit Judge in .410/.45 Colt by Rossi, N/A. URL http://www.hoffmang.com/firearms/Sacramento-PD-Bulletin-Circuit-Judge-2011-03-31.pdf. Cited on 19-06-16.

[14] DJI. Main Page, 2016. URL http://wiki.dji.com/en/index.php/Main_Page. cited on 20-06-16.

[15] DriveCalc. Drive Caculator - DC Motor Analysis Tool, N/A. URL http://www.drivecalc.de. Cited on 19-06-16.

[16] Federal Aviation Administration. Aircraft certification, 2016. URL https://www.faa.gov/licenses_certificates/aircraft_certification/. cited on 20-06-16.

[17] Federal Aviation Administration. UAS Sighting Report November 2014 - August 2015, 2016. URL https://www.faa.gov/uas/media/UASEventsNov2014-Aug2015.xls. Cited on 24-06-16.

[18] Federal Communications Commission Office of Engineering and Technology. Understanding the fcc regulations for low-power, non-licensed transmitters, N/A. URL https://transition.fcc.gov/Bureaus/Engineering_Technology/Documents/bulletins/oet63/oet63rev.pdf. cited on 20-06-16.

[19] Hawks, C. Shotgun recoil table, N/A. URL http://www.chuckhawks.com/shotgun_recoil_table.htm. cited on 20-06-16.

[20] HEADQUARTERS, DEPARTMENT OF THE ARMY. Operator and field maintenance manual for firing device, non lethal: Fn303 launcher, N/A. URL http://www.liberatedmanuals.com/TM-9-1095-212-13-and-P.pdf. cited on 20-06-16.

[21] HobbyTown. KBDD International 325 mm Carbon Fiber Extreme Flybarless Main Blade, N/A. URL https://www.hobbytown.com/kbdd-international-325mm-carbon-fiber-extreme-flybarless-main-blade-orange-kbd3 p273377. Cited on 17-06-16.

[22] Infrared Camera Warehouse. Flir a65 w/ 45° lens, N/A. URL http://www.infraredcamerawarehouse.com/flir-a65-w-45-lens/. cited on 20-06-16.

[23] Krause, B. Use processor redundancy for maximum reliability, 2002. URL http://www.eetimes.com/document.asp?doc_id=1277540.

[24] La Rocca, G. AE3221-I Systems Engineering & Aerospace Design: Requirement Analysis and Design Principles for A/C Stability & Control. Delft University of Technology, 2008. URL https://blackboard.tudelft.nl/bbcswebdav/pid-2524902-dt-content-rid-8585886_2/xid-8585886_2. Cited on 14-06-16.

[25] Lighware. SF11/C 120m LighWare Optoelectronics Pty Ltd, 2016. URL http://www.lightware.co.za/shop/en/drone-altimeters/51-sf11c-120-m.html. Cited on 01-06-2016.

[26] LOCOSYS. Datasheet of GPS smart antenna module, LS20030 3, 2015. URL https://cdn.sparkfun.com/datasheets/GPS/LS20030~3_datasheet_v1.3.pdf. Cited on 02-06-2016.

[27] M.A.L.O.U. tech - Groupe Assmann. MPI 200 commercial offer, 2015. URL http://www.psa-entreprise.fr/malou-tech/Documentations/OffreMpi200_US.pdf. Cited on 25-05-2016.

[28] Marcus, B. Proposed faa small uas rules, N/A. URL https://medium.com/future-of-flight/proposed-faa-small-uas-rule-what-is-class-b-c-d-and-e-airspace-81e760a36db1. cited on 20-06-16.

[29] MASSIVit 3D. Technology and products, N/A. URL http://www.massivit3d.com/technology-and-products. Cited on 15-06-16.

[30] Massport. Environmental Reporting - Noise Monitoring, N/A. URL http://www.massport.com/environment/environmental-reporting/noise-abatement/noise-monitoring/. Cited on 14-06-16.

[31] MaxBotix. LV-MaxSonar -EZ™ Series , 2015. URL http://maxbotix.com/documents/LV-MaxSonar-EZ_Datasheet.pdf. Cited on 02-06-2016.

[32] MEGA-DCS. Megapixel digital stereo head, 2012. URL http://users.rcn.com/mclaughl.dnai/sthmdcs.htm. Cited on 01-06-2016.

[33] OpenCV. Disparity map post filtering, 2010. URL http://docs.opencv.org/3.1.0/d3/d14/tutorial_ximgproc_disparity_filtering.html. Cited on 05-06-16.

[34] OpenCV. Depth Map from Stereo Images, 2016. URL http://docs.opencv.org/master/dd/d53/tutorial_py_depthmap.html. Cited on 13-06-16.

[35] OpenWorks Engineering. Skywall, N/A. URL http://openworksengineering.com/skywall. Cited on 16-06-16.

[36] PixHawk. PX4 Airspeed Sensor, 2016. URL https://pixhawk.org/peripherals/sensors/px4airspeed.

[37] Point Grey. Bumblebee Stereo Vision Camera Systems, 2012. URL https://www.ptgrey.com/support/downloads/10132. Cited on 01-06-2016.

[38] RAMS-group: Department of Production and Quality Engineering, NTNU. System safety: Reliability, availability, maintainability, safety, 2016. URL http://www.ntnu.edu/c/document_library/get_file?uuid=ae1f2570-1191-4d7c-b4c3-9686aaeccaf8&groupId=151572.

[39] RC Groups. Finding reliable lipo brands, 2011. URL http://www.rcgroups.com/forums/showthread.php?t=1561939.

[40] Rogers, D. F. Propeller Efficiency, 2010. URL http://www.esoteric-david.eu/prilohy/HPB_3.pdf.

[41] Rossi. Rossi Circuit Judge, 2016. URL http://www.rossiusa.com/product-details.cfm?id=15452&category=15&toggle=&breadcrumbseries=. cited on 27-06-16.

[42] Salt, J. Understanding rc lipo batteries, 2008. URL http://www.rchelicopterfun.com/rc-lipo-batteries.html.

[43] Selex ES. Falcon shield counter unmanned aerial vehicle (c-uav) system, N/A. URL http://www.us.selex-es.com/documents/6283866/64370908/body_Falcon_Shield_LQ_mm08605_.pdf. Cited on 16-06-16.

[44] Shapeways. PLA Material Information, 2016. URL http://www.shapeways.com/materials/pla. Cited on 06-06-2016.

[45] Sharp. GP2Y0A21YK General Purpose Type Distance Measuring Sensors, 2015. URL https://www.sparkfun.com/datasheets/Components/GP2Y0A21YK.pdf. Cited on 01-06-2016.

[46] SparkFun. 9 Degrees of Freedom - Razor IMU, 2015. URL https://www.sparkfun.com/products/10736. Cited on 02-06-2016.

[47] SparkFun. BeagleBone Black Rev C, 2016. URL https://www.sparkfun.com/products/12857.

[48] StereoLabs. Zed, 2012. URL https://www.stereolabs.com/zed/docs/ZED_Datasheet_2016.pdf. Cited on 01-06-2016.

[49] The Engineering Toolbox. Air properties, N/A. URL http://www.engineeringtoolbox.com/air-properties-d_156.html. Cited on 18-06-16.

[50] The Engineering Toolbox. Dry air properties, N/A. URL http://www.engineeringtoolbox.com/dry-air-properties-d_973.html. Cited on 18-06-16.

[51] The World Bank Group. GNI per capita, Atlas method (current US$), 1 2016. URL http://data.worldbank.org/indicator/NY.GNP.PCAP.CD/countries?display=default. Cited on 25-05-2016.

[52] Theiss UAV. Research and development, N/A. URL http://www.theissuav.com/researchanddevelopment/. Cited on 16-06-16.

[53] Transport Canada. Evaluation-single-engine turbine airplanes transporting passengers in ifr flight or night vfr, 2016. URL http://www.tc.gc.ca/eng/civilaviation/publications/tp185-3-07-feature-3772.htm.

[54] TUALCOM Communication & RF technologies. Tuallink ground terminal, N/A. URL http://www.tualcom.com/en/products/tuallink-ground-terminal. Cited on 19-06-16.

[55] Turner, S. Maintenance Procedures Templates, N/A. URL http://www.maintenance.org/topic/maintenance-procedures-templates. Cited on 14-06-16.

[56] uAvionix. Ping-2020 ads-b transceiver, 2016. URL http://uavionix.com/downloads/ping2020/docs/uAvionix-ping2020-data-sheet-ap0.pdf.

[57] US Government. PART 91—GENERAL OPERATING AND FLIGHT RULES, N/A. URL http://www.ecfr.gov/cgi-bin/text-idx?c=ecfr&sid=3efaad1b0a259d4e48f1150a34d1aa77&rgn=div5&view=text&node=14:2.0.1.3.10&idno=14#se14.2.91_115. Cited on 19-06-16.

[58] US Government. NFA, 26 U.S.C. Chapter 53 THE NATIONAL FIREARMS ACT TITLE 26, UNITED STATES CODE, CHAPTER 53 INTERNAL REVENUE CODE, N/A. URL https://www.atf.gov/firearms/docs/atf-national-firearms-act-handbook-appendix/download. Cited on 19-06-16.

[59] U.S.NRC. Maintenance Procedures, N/A. URL http://www.nrc.gov/reading-rm/doc-collections/insp-manual/inspection-procedure/ip42451.pdf. Cited on 14-06-16.

[60] Vaszary, Z. The ultimate drone battery care guide, 2016. URL http://www.dronethusiast.com/ultimate-drone-battery-care/.

[61] Whatson. Drone halts air traffic at dubai international for over an hour, N/A. URL http://whatson.ae/dubai/2016/06/drone-halts-air-traffic-at-dubai-international-for-over-an-hour/. Cited on 16-06-16.

[62] Winchester. Shotshell ammunition, N/A. URL http://www.winchester.com/Products/shotshell-ammunition/Innovative/PDX1-Defender-Shotshell/Pages/default.aspx. cited on 20-06-16.

[63] Wood, K. Carbon Fiber Reclamation Going Commercial, 2010. URL http://www.compositesworld.com/articles/carbon-fiber-reclamation-going-commercial. Cited on 27-05-2016.

Bibliography

[64] Aerostudents. Nonlinear dynamic inversion, . URL http://aerostudents.com/files/advancedFlightControl/nonlinearDynamicInversion.pdf. Cited on 19-06-16.

[65] Aerostudents. Backstepping, . URL http://aerostudents.com/files/advancedFlightControl/backstepping.pdf. Cited on 19-06-16.

[66] Aerts et al. Anti-Drone Drone Baseline Report DSE 2016 Group S08. Technical Report 1, Delft University of Technology, Faculty of Aerospace Engineering, Kluyverweg 1, 2629 HS Delft, 5 2016.

[67] Aerts et al. Anti-Drone Drone Mid-term Report DSE 2016 Group S08. Technical Report 1, Delft University of Technology, Faculty of Aerospace Engineering, Kluyverweg 1, 2629 HS Delft, 5 2016.

[68] Aerts et al. Anti-Drone Drone Project Plan DSE 2016 Group S08. Technical Report 1, Delft University of Technology, faculty of Aerospace Engineering, Kluyverweg 1, 2629 HS Delft, 4 2016.

[69] Alibaba.com. Aluminium flight case dual plasma display led lighting, . URL http://boryflightcase.en.alibaba.com/product/60313840418-801925991/aluminum_flight_case_dual_plasma_display_led_lighting.html. Cited on 17-06-16.

[70] Alibaba.com. Hbl575sl, . URL http://www.mksservosusa.com/product.php?productid=199&cat=27&page=1. Cited on 17-06-16.

[71] Analog Devices, Inc. Digital accelerometer adxl345. Technical report, P.O. Box 9106, Norwood, MA 02062-9106, U.S.A., 2009.

[72] Anderson, J. *Aircraft Performance and Design*. WCB/McGraw-Hill Boston, 1999.

[73] Anderson, J. *Fundamentals of Aerodynamics*. McGraw Hill, 5 edition, 2011. SI Edition.

[74] Araújo, A., Botelho, G. L., Silva, M., and Machado, A. V. UV Stability of Polyactic Acid Nanocomposites. *Journal of Materials Science & Engineering*, 178(3):75–83, 2 2013.

[75] Austin, R. *Unmanned Aircraft Systems: UAVS Design, Development and Deployment*, volume 1, chapter 14, pages 197–199. John Wiley & Sons, Ltd, 1 edition, 2010.

[76] Austin, R. *Unmanned aircraft systems: UAVS design, development and deployment*, volume 54. John Wiley & Sons, 2011.

[77] Barry, A. and Tedrake, R. Pushbroom stereo for high-speed navigation in cluttered environments. *Computer Science and Artificial Intelligence Lab Massachusetts Institute of Technology*, 2014.

[78] Becx, T. et al. Technical Report: Structural. Technical Report 1, Delft University of Technology, Kluyverweg 1, 2629 HS Delft, 2 2015. Simulation, Verification & Validation: Wing Idealization.

[79] Belastingdienst. Hoe bereken ik de belasting bij invoer? URL http://www.belastingdienst.nl/wps/wcm/connect/bldcontentnl/belastingdienst/prive/douane/goederen_ontvangen_uit_het_buitenland/van_organisaties_en_bedrijven/hoe_bereken_ik_de_belasting_bij_invoer_internetaankopen. Cited on 17-06-16.

[80] Blom et al. TECHNICAL REPORT - FL 3 11-03-16. Technical Report 1, Delft University of Technology, faculty of Aerospace Engineering, Kluyverweg 1, 2629 HS Delft, 3 2016.

[81] Bouchier, P. Sensor Calibration. URL http://wiki.ros.org/razor_imu_9dof#Sensor_Calibration. Cited on 14-06-16.

[82] Burmeister, L. *Convective Heat Transfer*. Wiley-Interscience, 1 edition, 1983. ISBN 0-471-09141-3.

[83] Carlson, D. H. . J. *USAF Stability and Control Handbook*. Dayton OH, 1961. ISBN -.

[84] Carrier, G. and Gebhardt, L. A joint dlr-onera contribution to cfd-based investigations of unconventional empennages for future civil transport aircraft. 2005.

[85] Caughey, D. Introduction to aircraft stability and control. Sibley School of Mechanical & Aerospace Engineering Cornell University, 2011. URL https://courses.cit.cornell.edu/mae5070/Caughey_2011_04.pdf.

[86] Chrzanowski, K. Review of Night Vision Technology. *Opto-Electronics Review*, 21(2):153–181, 7 2013.

[87] Civil Jet Aircraft Design. Data A: Aircraft data file, Table 8: Miscellaneous manufacturers, 2016. URL http://booksite.elsevier.com/9780340741528/appendices/data-a/table-8/table.htm. Cited on 23-06-2016.

[88] Clayton Green. Modeling and Test of the Efficiency of Electronic Speed Controllers for Brushless DC Motors, 2016. URL https://aero.calpoly.edu/static/media/uploads/green,c_grad_seminar.pdf. cited on 28-06-16.

[89] Colijn, R. et al. Simulation Report: Structural. Technical Report 1, Delft University of Technology, Kluyverweg 1, 2629 HS Delft, 2 2016. Simulation, Verification & Validation: Fuselage Idealization.

[90] Crowell, G. A. The Descriptive Geometry of Nose Cones, 1996. URL https://web.archive.org/web/20110411143013/http://www.if.sc.usp.br/~projetosulfos/artigos/NoseCone_EQN2.PDF. Cited on 17-06-2016.

[91] Curran, R. and Verhagen, W. AE3211-I Systems Engineering & Aerospace Design slides: Risk Management and Reliability Engineering. Delft University of Technology, 2014. URL https://blackboard.tudelft.nl/bbcswebdav/pid-2524917-dt-content-rid-9170170_2/courses/35051-151603/AE3221-L08-Risk%20%26%20Reliability%20%282015-2016%29.pdf.

[92] Daalhuizen et al. *Delft Design Guide: Design Strategies and Methods.* BIS Publishers, 2014. ISBN 9063693273.

[93] de Croon, G. C. H. E. Monocular distance estimation with optical flow maneuvers and efference copies: a stability-based strategy. *Bioinspiration & Biomimetics*, 11(1):016004, 2016. URL http://stacks.iop.org/1748-3190/11/i=1/a=016004.

[94] Delft Dynamics. RH2 'Stern' Ground Station. URL http://www.delftdynamics.nl/index.php/nl/producten/robothelikopter. Cited on 17-06-16.

[95] Deperrois, A. Results vs Prediction, 2009. URL http://www.xflr5.com/docs/Results_vs_Prediction.pdf.

[96] Dimchev, M. Experimental and numerical study on wingtip mounted propellers for low aspect ratio uav design. Master's thesis, TU Delft, Kluyverweg 1, Delft, 3 2012.

[97] DJI. Phantom 4 Specifications. URL http://www.dji.com/product/phantom-4/info#specs. Cited on 14-06-16.

[98] Drela, M. Xfoil: An analysis and design system for low reynolds number airfoils., N/A. URL http://web.mit.edu/drela/Public/papers/xfoil_sv.pdf. cited on 20-06-16.

[99] European Central Bank. US dollar (USD), 5 2016. URL https://www.ecb.europa.eu/stats/exchange/eurofxref/html/eurofxref-graph-usd.en.html. Cited on 25-05-2016.

[100] Filippone, A. *Flight Performance of Fixed and Rotary Wing Aircraft.* Elsevier, 2006.

[101] Fischer, A. et al. Design of an Extremely Maneuverable UCAV. MAElab, University of California, San Diego. URL http://maelabs.ucsd.edu/mae155/classes/SP_03/Extremely_Maneuverable_UCAV.ppt. Cited on 14-06-16.

[102] Gaffey, T. The efect of positive pitch-flap coupling (negative delta-3) on rotor blade motion stability and flapping. *Journal of the American Helicopter Society*, 14(2), 1969.

[103] Gill, E. and Hoevenaars, T. AE3211-I Systems Engineering & Aerospace Design slides: Verification and Validation for the Attitude and Orbit Control System. Delft University of Technology, 2 2014.

[104] Haddon, D. and Whittaker, C. Aircraft Airworthiness Certification Standards for Civil UAVs. *Aeronautical Journal*, 107(1068 Spec):79–86, 2003.

[105] Harper, C. *Modern Plastics.* McGraw-Hill, 2010. ISBN 9780070267145.

[106] Hibbeler, R. C. *Mechanics of Materials*. Pearson Education, Ltd, 7 edition, 7 2008. ISBN 9789810679941.

[107] Hoak, D. e. a. *USAF Stability and Control DATCOM*. Global Engineering Documents, Clayton, MO, 1978.

[108] Honeywell. 3-axis digital compass ic hmc5883l. Technical report, 12001 Highway 55 Plymouth, MN 55441, 3 2011.

[109] Hyeonsoo, Y. and Johnson, W. Performance and design investigation of heavy lift tilt-rotor with aerodynamic interference effects. *Journal of Aircraft*, 46(4):1231–1239, 7 2009.

[110] Imbriale, W. e. a. *Space Antenna Handbook*. Wiley, 2012. ISBN 978-1119993193.

[111] InvenSense, Inc. Itg-3200 3-axis gyro evaluation board application note rev 1.1. Technical report, 1197 Borregas Ave., Sunnyvale, CA 94089, USA, 3 2010.

[112] J. Marte, D. K. A review of aerodynamics noise from propellers, rotors, and lift fans. Technical Report N7015224, Jet Propulsion Laboratory, 1 1970.

[113] Kassapoglou, C. *Design and Analysis of Composite Structures: With Applications to Aerospace Structures*. John Wiley & Sons, Ltd, 2 edition, 5 2013. ISBN 978-1-118-40160-6.

[114] Kontronik. Katalog 2014 - PYRO 650 65-L. URL http://www.kontronik.com/fileadmin/kontronik-sobek/Public/Content/Images/Content/Sonstiges/Katalog_2014.compressed.pdf. Cited on 14-06-16.

[115] Kraus, J. and Marhefka, R. *Antennas For All Applications*. McGraw-Hill Science, 2001. ISBN 978-0072321036.

[116] Krishnamachari, S. and Broutman, L. *Applied Stress Analysis of Plastics: A Mechanical Engineering Approach*, chapter 4, pages 174–196. Springer, 2 1993.

[117] La Rocca, G. AE3211-I Slide: Requirement Analysis and Design principles for A/C stability & control (Part 1). Lecture materials: TU Delft Faculty of Aerospace Engineering, 2014.

[118] Leishman, J. G. *Principles of Helicopter Aerodynamics*. Cambridge University Press, 2006.

[119] Lin, M. and Chang, F.-K. The manufacture of composite structures with a built-in network of piezoceramics. *Composites Science and Technology*, 62(7):919–939, 6 2002.

[120] LOCOSYS Technology Inc. Datasheet of gps smart antenna module, ls2003x series, 2006. URL http://pdf.datasheetarchive.com/indexerfiles/Datasheet-035/DSA0015933.pdf.

[121] M. Lowson, J. O. Studies of helicopter rotor noise. Technical Report AD684394, U.S. Army Aviation Materiel Laboratories, 1 1969.

[122] Maisel, M. et al. *The History of the XV-15 Tilt Rotor Research Aircraft: From Concept to Flight*. National Aeronautics and Space Administration, Office of Policy and Plans, NASA History Division, 2000.

[123] Majumdar, A. and Tedrake, R. Funnel libraries for realtime robust feedback motion planning. *Computer Science and Artificial Intelligence Lab Massachusetts Institute of Technology*, 2016.

[124] MarketsandMarkets. Anti-drone market by technology, vertical, and region - global forecast to 2022. Technical report, MarketsandMarkets, 2016. Summary available at http://www.reportlinker.com/p03681937-summary/Anti-Drone-Market-by-Technology-Vertical-and-Region-Global-Forecast-to.html.

[125] McGhee, R. J. and Beasley, W. D. Low-speed aerodynamic characteristics of a 17-percent-thick medim-speed airfoil designed for general aviation applications. Technical Report 1786, National Aeronautics and Space Administration, Washington, DC 20546, 12 1980. Langley Research Center.

[126] Megson, T. *Aircraft Structures for Engineering Students*. Elsevier, Ltd., 5 edition, 2013.

[127] Microdrones. MD4-000 Specifications. URL https://www.microdrones.com/en/products/md4-3000/. Cited on 14-06-16.

[128] Mulder, J., van Staveren, W., van der Vaart, J., de Weerdt, E., de Visser, C., in 't Veld, A., and Mooij, E. *Flight Dynamics*. Faculty of Aerospace Engineering, 2013.

[129] NDARC. NASA Design and Analysis of Rotorcraft, 2015. URL http://rotorcraft.arc.nasa.gov/Publications/files/NDARCTheory_v1_6_938.pdf.

[130] Pavel, M. AE3-021: Guidelines for a First Dimensioning of Helicopter Rotor.

[131] Phillips, W. and Hansen, A. Effects of tail dihedral on static stability. *Journal of Aircraft*, 43(6), 2006.

[132] Prouty, R. W. *Helicopter Performance, Stability, and Control.* Krieger Publishing Company, 1995.

[133] Queijo, T. T. . M. Approximate relations and charts for low-speed stability derivatives of swept wings. Technical Report 1, NACA T.N., 300 E. Street SW, Suite 5R30 Washington, DC 20546, 5 1948.

[134] Raffo, G. et al. Backstepping/nonlinear H control for path tracking of a quadrotor unmanned aerial vehicle. Technical Report 1, University of Seville, Camino de los Descubrimientos, 6 2008.

[135] Raymer, D. *Aircraft Design: A Conveptual Approach.* AIAA, 1989.

[136] Remple, M. T. . R. *Aircraft and Rotorcraft System Identification.* AIAA, 2 edition, 1 2012. ISBN 978-1-60086-820-7.

[137] Ren, B. e. a. *Modeling, Control and Coordination of Helicopter Systems.* Springer Science & Business Media, 2012. ISBN 9781461415633.

[138] Rhinoceros. Rhino 5 features, 2016. URL https://www.rhino3d.com/features. Cited on 20-06-16.

[139] Robin Radar Systems BV. Brochure Drone Detection, 2016. Brochure provided by a contact of Robin Radar Systems BV.

[140] Rocca, G. L. V-n diagram. Delft University of Technology Blackboard course page, 2 2016. Document describing the construction of maneuver and gust diagrams.

[141] Roskam, J. *Preliminary calculation of Aerodynamic, Thrust and Power Characteristics.* Darcorporation, 1987. ISBN 1884885527.

[142] Ruijgrok, G. *Elements of Aviation Acoustics.* Delft University Press, 2004. ISBN 90-407-2560-8.

[143] Sadraey, M. Tail design. Lecture materials: Daniel Webster College, 2013. URL http://faculty.dwc.edu/sadraey/Chapter%206.%20Tail%20Design.pdf.

[144] Sadraey, M. H. *Aircraft Design: A Systems Engineering Approach.* Wiley, 2012. ISBN 978-1-119-95340-1.

[145] Schenkelberg, F. How reliable does a delivery drone have to be. Jan 2016. doi: 10.1109/RAMS.2016.7448054.

[146] Schneider, B. A guide to understanding lipo batteries, 2016. URL http://rogershobbycenter.com/lipoguide/.

[147] Shapeways. Pla material information, N/A. URL http://www.shapeways.com/materials/pla. Cited on 17-06-16.

[148] Simons, D. Ae4445 introduction to aircraft noise, elements of aviation acoustics, noise measures. Lecture slides, Delft University of Technology, 6 2016.

[149] Sinke, J. AE3211-II Production of Aerospace Systems reader. Technical report, Delft University of Technology, 2016.

[150] Stach, B. A. *Clinical Audiology An Introduction.* Delmar, Cengage Learning, Clifton Park, NY 12065-2919, 2 edition, 2010. ISBN 978-0-766-86288-3.

[151] Stewart, J. *Calculus: Early Transcendentals.* Cengage Learning Inc, 7 edition, 10 2011. ISBN 9780538497879.

[152] SuPower Battery. 43v 44v 50.4v 20a lithium ion lipo battery charger 12s 12x 3.6v, N/A. URL http://www.batterysupports.com/43v-44v-504v-20a-lithium-ion-lipo-battery-charger-12s-12x-36v-p-442.html. Cited on 17-06-16.

[153] Takemura, K., Takada, Y., and Katogi, H. Effect of treatment using silane coupling agent on creep properties of jute fiber reinforced composites. *High Performance Structures and Material VI*, pages 417–424, 2 2012.

[154] The future of things. Ad-150, N/A. URL http://thefutureofthings.com/6403-american-dynamics-ad-150-uav/. cited on 10-06-16.

[155] Torenbeek, E. *Synthesis of subsonic design.* Nijgh-Wolters-Noordhoff, 1976. ISBN 90 298 2505 7.

[156] U.S. Energy Information Administration. U.S. electricity generation by energy source, 2015. URL https://www.eia.gov/tools/faqs/faq.cfm?id=427&t=3. Cited on 17-06-2016.

[157] Valavanis, K. P. and Vachtsevanos, G. J. *Handbook of Unmanned Aerial Vehicles*, volume 5. Springer, 1 edition, 2015. ISBN 978-90-481-9706-4.

[158] Veldhuis, L. L. M. *Propeller Wing Aerodynamic Interference.* PhD thesis, TU Delft, Kluyverweg 1, Delft, 6 2005.

[159] Whitford, R. *AE4245 Reader: Design for Air Combat.* Faculty of Aerospace Engineering, 2014.

[160] Widiastuti, I., Sbarski, I., and Masood, S. Creep behavior of PLA-based biodegradable plastic exposed to a hydrocarbon liquid. *Journal of Applied Polymer Science*, 127(4):2654–2660, 2 2013.

[161] Wzorek, M. and Doherty, P. Reconfigurable path planning for an autonomous unmanned aerial vehicle. *Department of Computer and Information Science Linkoping University, Sweden*, 2006.

[162] Zhang, S., Xu, K., and Jow, T. The low temperature performance of li-ion batteries. *Journal of Power Sources*, 115(1):137–140, 2003.

[163] Zitnick, C. L. and Kanade, T. A Cooperative Algorithm for Stereo Matching and Occlusion Detection. *IEEE Transactions on Pattern Analysis and Machine Intelligence*, 22(7):675–684, 7 2000.

A. Technical Diagrams

This chapter contains technical diagrams describing the relations between different components of the design. First, the Electrical Block Diagram (EBD) is presented, containing all electrical equipment and its relations. Next, Hardware and Software Block Diagrams (HWBD and SWBD) illustrate all system components and their relations. Finally, a Communication/Data Flow Chart (CDFC) shows the interaction between system and environment in terms of data flow.

A.1 Electrical Block Diagram

The EBD is shown in Fig. A.1. Here, black, straight arrows represent general relations, yellow, dashed arrows represent low voltage currents, and red, dotted arrows represent high voltage currents.
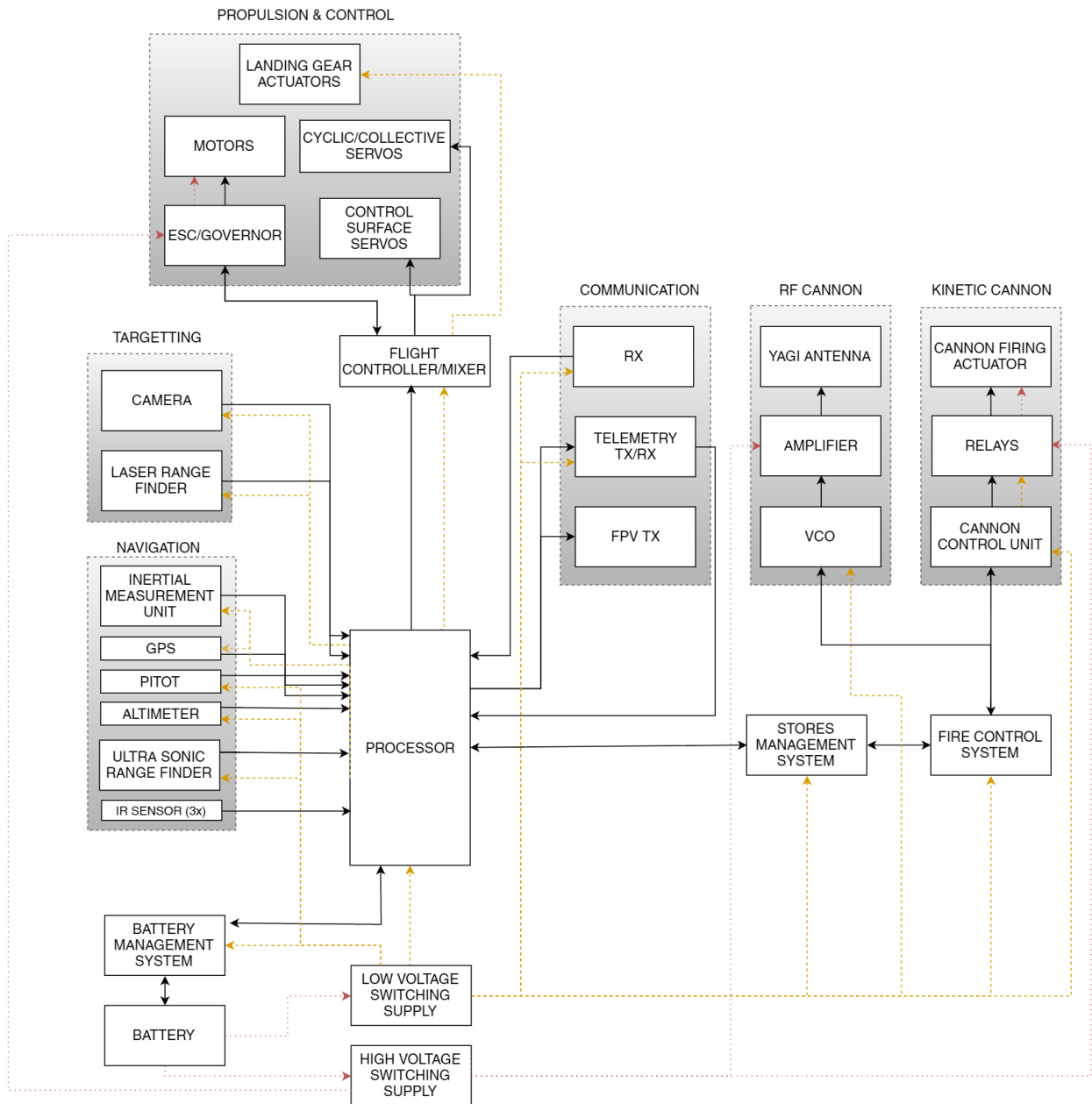

Figure A.1: Electrical Block Diagram

A.2 Hardware and Software Block Diagrams

The HWBD and SWBD are depicted in Fig. A.2 and Fig. A.3, respectively. The hardware components include in the HWBD were previously determined in Chapter 5 and Chapter 6.
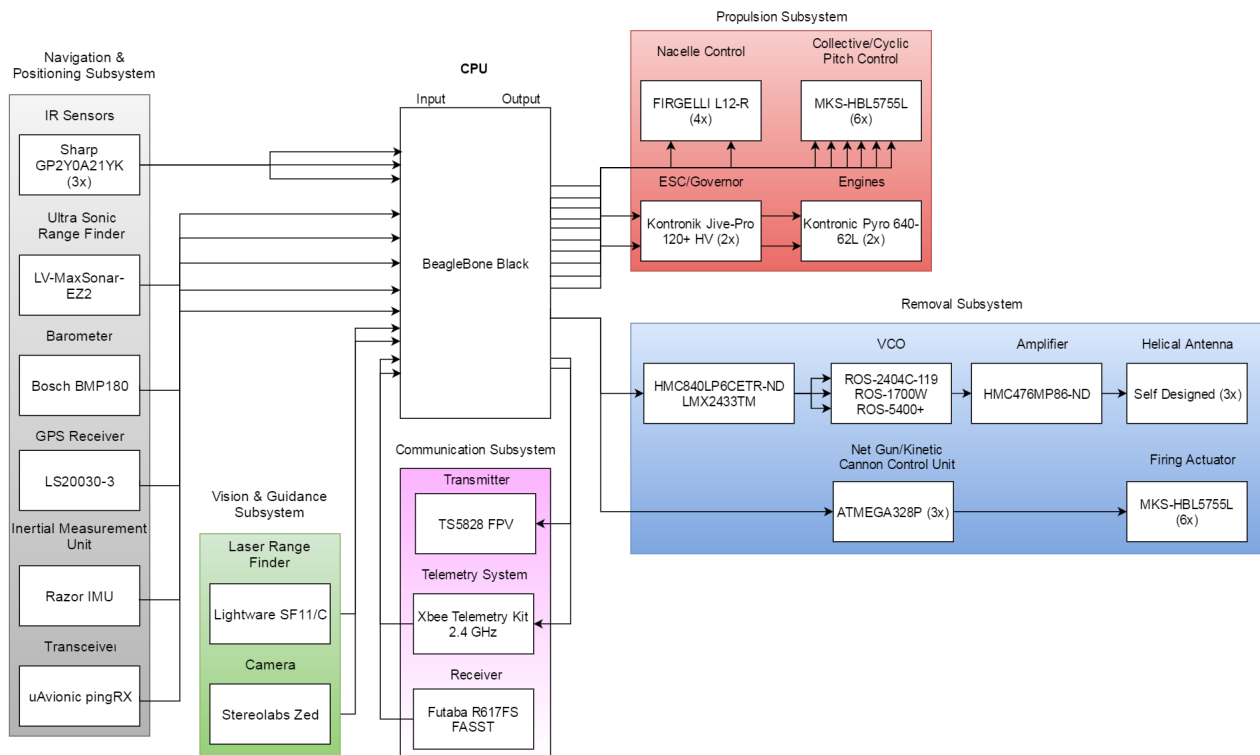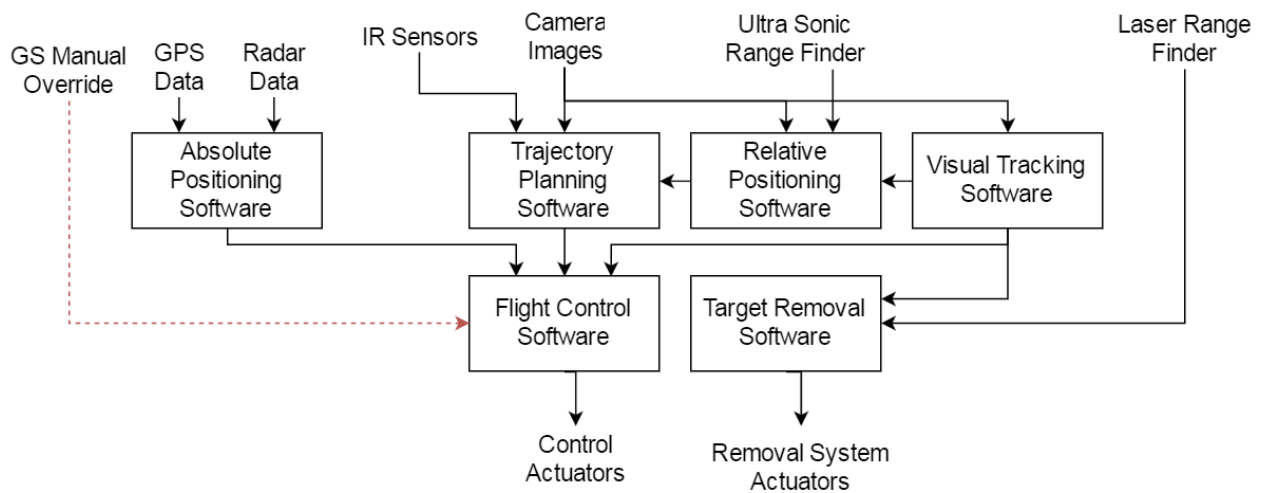

Figure A.2: Hardware Block Diagram

Figure A.3: Software Block Diagram

A.3 Communication/Data Flow Chart

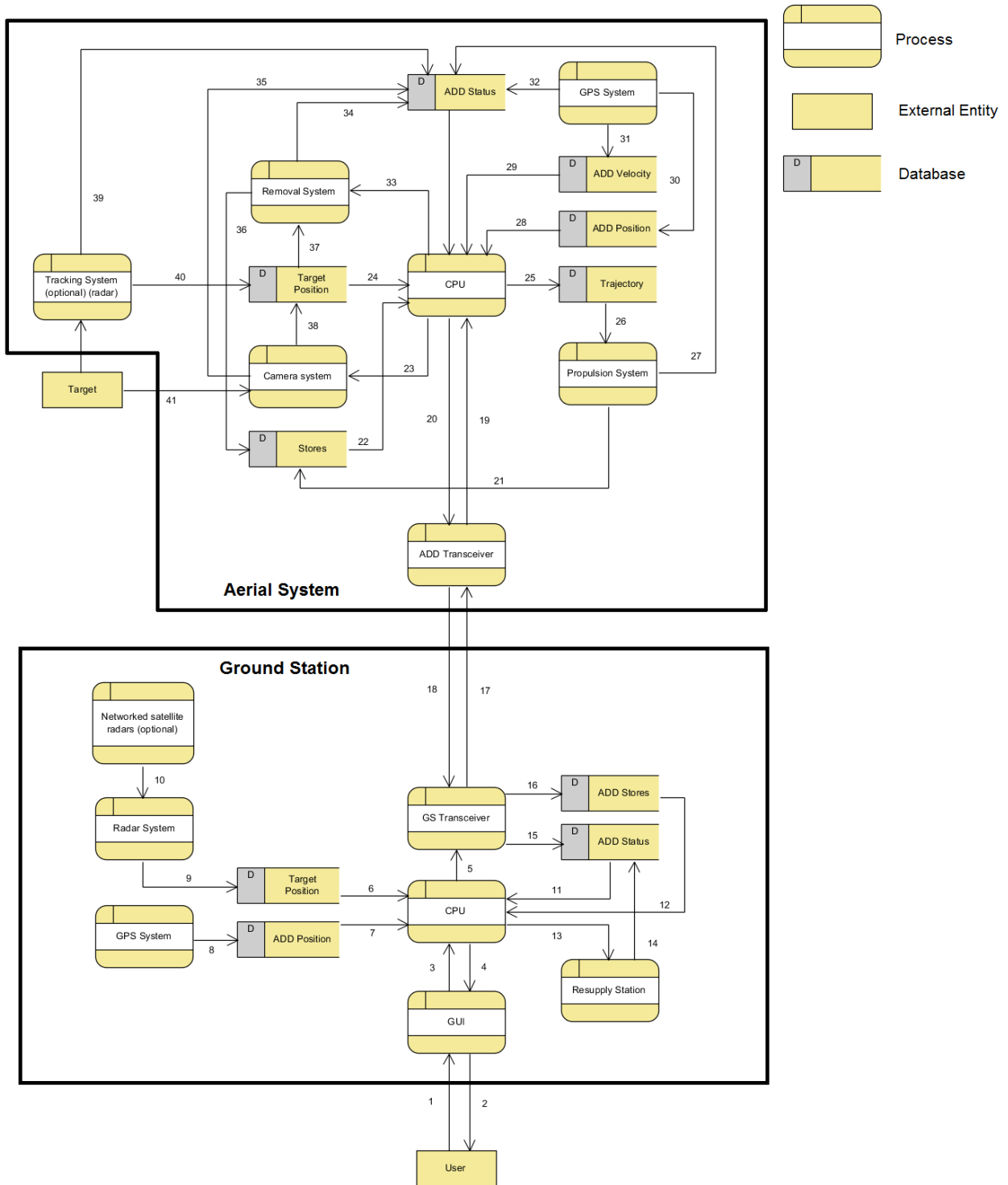The CDFC is provided in Fig. A.4 with the data flow descriptions in Table A.1.

Figure A.4: Communication/Data Flow Chart

Table A.1: Communication data as shown in the Communication/Data Flow Chart

	Data			Data
1	Position restricted area		22	Current remaining stores
2	System status		23	Camera System readiness
3	Incoming User Input		24	Current Target position
4	Outgoing System feedback		25	Required ADD trajectory
5	Outgoing GS message		26	Read required ADD trajectory
6	Current Target position		27	Propulsion System status
7	Current ADD position		28	Current ADD position
8	ADD position		29	Current ADD velocity
9	Target position		30	ADD position
10	Target position		31	ADD velocity
11	Current ADD status		32	GPS System status
12	Current remaining ADD stores		33	Removal readiness
13	Resupply readiness		34	Removal System status
14	Resupply Station status		35	Camera System status
15	Received ADD status		36	Update remaining removal stores
16	Received ADD stores data		37	Current Target position
17	Target detected, operational commands		38	Target position
18	ADD status, ADD stores data		39	Tracking System status
19	Incoming GS message		40	Target position
20	Outgoing ADD message		41	Target sighting
21	Update remaining propulsion stores		42	Target sighting

336.17

1885

337.62

1520

1704.50

80.92

369.11

UNLESS OTHERWISE SPECIFIED:
DIMENSIONS ARE IN MILLIMETERS
SURFACE FINISH:
TOLERANCES:
   LINEAR:
   ANGULAR:
	FINISH:			DEBUR AND
				BREAK SHARP
				EDGES
						DO NOT SCALE DRAWING		REVISION

	NAME	SIGNATURE	DATE			TITLE:		
DRAWN								
CHK'D								
APPV'D								
MFG								
Q.A			MATERIAL:			DWG NO.	HELIADES	A4
			WEIGHT:			SCALE:1:25	SHEET 1 OF 1	